STUDY OF THE DRELL-YAN PROCESS $qq \rightarrow Z/\gamma^{*} \rightarrow \mu^{+} \mu^{-}$ IN p-p COLLISIONS USING CMS DETECTOR AT LHC

A THESIS

Submitted to the
FACULTY OF SCIENCE
PANJAB UNIVERSITY,CHANDIGARH
for the degree of

DOCTOR OF PHILOSOPHY

2018

GENIUS WALIA

DEPARTMENT OF PHYSICS
CENTRE OF ADVANCED STUDY IN PHYSICS
PANJAB UNIVERSITY, CHANDIGARH, INDIA

DEPARTMENT OF PHYSICS
Centre of Advanced Study in Physics
PANJAB UNIVERSITY, CHANDIGARH-160 014 (INDIA)
Fax: ++91-172-2783336
Phone: ++91-172-2541741
EPABX: ++91-172-2534466, 2534446
Email: casphypu.ac.in

CORRECTION CERTIFICATE

It is certified that there were no specific corrections recommended by the examiner of Ms. Genius Walia in her Ph.D. thesis entitled '**STUDY OF THE DRELL-YAN PROCESS $q\bar{q}\rightarrow Z/\gamma^*\rightarrow\mu^+\mu^-$ IN p-p COLLISIONS USING CMS DETECTOR AT LHC'** .

The thesis submitted by Genius Walia, in the present form, is acceptable.

MKaur
(Prof. Manjit Kaur)
Dept. of Physics,
P.U., Chandigarh
(Supervisor)

26/11/18
(Prof. Rajeev K. Puri)
Dept. of Physics,
P.U., Chandigarh
Chairman

Chairperson
Department of Physics
Panjab University
Chandigarh-160014

Acknowledgement

Words are often too frail to express ones inward emotions of ineffable indebtedness. The same perplexity haunts inside me in expressing my inner feelings even though I fumble for them to articulate my heartiest gratitude to all those who have been a source of my inspiration and been there for me at every step.

It is a great privilege to express my sagacious sense of gratitude and admiration towards my esteemed venerable supervisors, Prof. Manjit Kaur and Prof. Slawomir Tkaczyk for their valuable constructive guidance, firm and clear convictions meticulous efforts and persistent motivation. I owe my sincere gratitude to Prof. Manjit Kaur for giving me the opportunity to work in the world's largest accelerator. Due to her constant support, I was able to work at Tata Institute of Fundamental Research in Mumbai.

During my PhD tenure, I have been blessed to work with leading experimentalist from India. I am highly obliged to Prof. Kajari Mazumdar for triggering the ϕ^* *analysis. She has been mentoring me in the best way possible and the discussion with her on any aspect, were always enlightening and motivating. Her enthusiasm towards research was stimulating and her thorough understanding of high energy physics helped a lot during the course of this study.*

I owe my heartiest respect to Prof. Sunanda Banerjee for giving me the opportunity to work with him. He has always been an inspiration and it was privilege working with him. I have learnt a lot from his sincere, patient, systematic and professional attitude towards research. Working under his adroit guidance has been an enriching experience both at professional and personal level.

I am also thankful to India-CMS Collaboration and Panjab University Experimental High Energy Physics group for friendly environment and helping me in various stages of Ph.D. I extend my sincere thanks to Dr. Rajdeep Chatterjee from TIFR for his invaluable help at every stage of this study.

I owe my sincere gratitude to the European Council for Nuclear Physics

(CERN) and Fermi National Lab (FNAL) for providing me the computing resources and also hosting me at different points of time. I have thoroughly enjoyed going through all the intricacies of acquisition, retrieval, analysis and presentation of experimental data. Also, I wish to express my gratitude towards the dielectron ϕ^* *analysis team for their help and innumerable discussion sessions which has helped me to improve my knowledge of the subject.*

I am deeply thankful to all my friends in Physics department and in High-Energy Physics lab at Panjab University. I wish to express my thanks to Dr. Bhawandeep, Dr. Shilpi, Priyanka, Rajat, Rathijit, Ruchi and Shamik who were always there for helping me and ensuring fun filled time during my CERN visits.

Life has been tough during the Ph.D. years, but the company of true and supportive friends made this journey a lot easier. I owe my debt to my best friend, Sukhwant Kaur, for helping me stay sane through these difficult years. The stay at Panjab University was refreshing and adventurous in the company of my close friends, Devinder, Rajinder, Maninder and Ujjwal.

All of my work would have been impossible without the patience and incredible support of my family. I am indebted to my parents for tolerating my behaviour during the rough phases of life and for believing in my abilities. I also wish to acknowledge my brother for his encouragement and constant support. I am greatly thankful to my extended family for their support and care during thesis writing phase. I am highly grateful to my husband, Amanpreet Singh, for his unwavering emotional support, understanding and patience. He has been great source of inspiration for completing this project successfully.

I can't forget to express my thankfulness to the greatest search engine Google, without whom it was impossible to do the research work. It always had either an idea or a solution to various computing problems.

I am thankful to Chairman, Department of Physics, Panjab University for providing the infrastructural support in the department. The financial support by INSPIRE, DST, India, is highly acknowledged without which it would have been

impossible to finish this work.

Last but not the least, I wish to pay my sincere regards to Almighty God for bestowing upon me the courage to face the complexities of life and complete this project successfully.

Finally, I wish to thank everybody who was important to the successful realization of this thesis, as well as express my apology that I could not mention everybody personally who contributed in my endeavour to complete the thesis.

Date: **(Genius Walia)**

Abstract

The Large Hadron Collider, LHC at CERN, Geneva, Switzerland is the most powerful circular particle accelerator and has been delivering proton-proton collision data with unprecedented energy and luminosity. The proton beams are made to collide at four interaction points along the LHC ring. At these collision points, four giant detectors are installed to record every possible outcome of the collision. The Compact Muon Solenoid (CMS) is a multipurpose hermetic detector among four LHC experiments. The high precision detection of particles from collision events in the CMS detector, makes it a powerful tool for both Standard Model measurements and new physics searches.

In this thesis, measurements of single and double-differential cross sections for the Drell-Yan (DY) process are presented. The DY process unravels significant characteristics of the proton-proton collisions at the LHC. At high energies, the theoretical calculations for the DY production rate are fairly accurate, since the Quantum Chromodynamics effects dominate only at the initial state, hence, these predictions can be used to validate the SM. In addition, Drell-Yan lepton-pair production is a major source of background for various physics analyses, such as $t\bar{t}$ and diboson measurements, as well as for the searches for new physics beyond the standard model, such as the production of high-mass dilepton resonances.

The work has been done using the LHC data collected by the CMS experiment at $\sqrt{s} = 8$ TeV, corresponding to an integrated luminosity of 19.7 fb^{-1}. The study is focused on inclusive Z boson production with a subsequent decay into pair of oppositely charged muons. The single-differential cross section has been measured with respect to phistar (ϕ^*) and for double-differential measurements, in addition to ϕ^*, the dependence on Z boson rapidity $|y|$ have also been taken into account.

The measured differential cross sections are compared with various theoretical predictions from Monte Carlo event generators , such as, MADGRAPH, POWHEG, ResBos and aMC@NLO. None of the theoretical predictions matches the measure-

ments perfectly for the entire range of ϕ^* covered in this analysis. However, the analysis validates the overall theoretical description of inclusive Z boson production at LHC energies by the perturbative formalism of the Standard Model.

This thesis also presents the results of various studies performed for the Hadron Outer (HO) upgrade during Long Shutdown Phase 1. The photodetectors of Hadron Outer (HO) calorimeter were replaced by silicon photomultipliers (SiPMs). The quality tests performed pre and post installation of SiPMs are presented along with installation details of the SiPMs in the CMS detector.

The hadron calorimeter (HCAL) has a nonlinear energy response, and must be calibrated to increase the energy response to unity for the charged hadrons of energy around 50 GeV. The absolute calibration is being done regularly using the isolated charged hadrons from the collision data. Dedicated HCAL calibration triggers have been set up to provide adequate number of charged hadrons to calculate the correction factors. The effect of pileup on the isolated track trigger efficiency was studied using simulation samples generated with 13 TeV data-taking scenario and it was concluded that a larger bandwidth for data transfer at lower luminosity or at low pile up events will benefit the overall rate of isolated track event selection.

Contents

List of Figures

List of Tables

---

3 Event Generation, Simulation and Reconstruction 67

List of Figures

List of Tables

Chapter 1

The Standard Model and The Drell Yan Process

The field of Particle Physics seeks to establish a profound understanding of the fundamental constituents of matter and the interactions between them. It challenges our preconceptions, inspires and seeks to move human knowledge forward at a basic level - wherever that may lead to. The precise understanding of the matter constituents is significant to apprehend the fundamental physics laws that shape our universe. Since the dawn of civilization, scientists and philosophers have been engaged in solving the mysteries related to the formation of the universe. What initially started in the early civilizations as a predominantly philosophical problem has today led to a wide spectrum of scientific research programs involving huge experiments and worldwide collaborations. During the past century, numerous ever-evolving experiments discovered more and more particles, which led to a formulation of the Standard Model of interactions of particles.

1.1 History of Particle Physics

During the classical era of Particle Physics, from 1897 to 1932, a major breakthrough came with discovery of the electron. J.J.Thomson discovered this elementary particle in 1897 [1], thereby authenticating the substructure of the atom. Later in 1911, the famous Rutherford scattering experiment [2, 3], exhibited that atom has most of its mass concentrated in the small, dense, positively charged "nucleus". The discovery of neutron in 1932 by J.Chadwick [4] seemed to complete the picture and to allow the explanation of matter formed in atoms by fundamental particles. In 1930, Pauli predicted the existence of neutrino in order to explain the continuous energy spectrum of electrons in β-decay. The neutrinos were detected experimentally in late 1956 [5]. In 1928, Dirac predicted the presence of anti-particle states to explain the negative energy quantum states obtained by solving the Dirac equations. The first anti-particle "positron" was experimentally observed in 1933 by C. Anderson, in a cosmic ray experiment [6].

In 1934, Yukawa Heidki proposed the presence of "π" mesons as the transmitter of short range strong nuclear forces. These force carriers were later observed in 1947 by Powell and his coworkers at Bristol [7], who discovered that there are actually two middle-weight particles in cosmic rays, which they called π (or pion) and μ (or muon). The other members of meson family, e.g. kaons and B mesons were discovered by G. D. Rochester, C. C. Butler (1947) [8] , and C.Bebek, J.Haggerty (1981) [9], respectively. In 1961, Murray Gell-Mann proposed the concept of "Eight-fold Way" [10], for classification of these subatomic particles into groups on the basis of their symmetry properties (i.e. charge and strangeness). A spectrum of new particles discovered in different collider experiments during 1960/70s is shown in figure 1.1.

Gell-Mann and Zweig in 1964, independently proposed that baryons and mesons are the bound states of their elementary constituents, known as "quarks". According to the quark model, each baryon is made up of 3 quarks while the mesons originate from quark-antiquark combinations. The model was later verified in 1986, by the deep inelastic scattering experiments conducted at SLAC (Stanford Linear Accelerator Center) and CERN [11], when the substructure of the proton consisting of three lumps was observed, as shown in figure 1.2. In 1983, the force carriers of

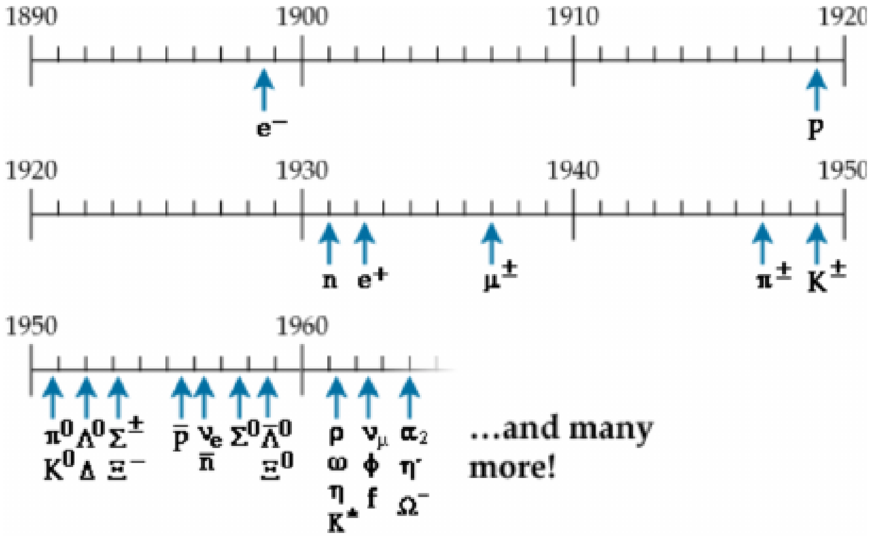

Figure 1.1: Spectra of particles discovered up to 1970's. Figure source : http://www.particleadventure.org/other/history/quantumt.html.

strong interactions, "gluons", were discovered at DESY [12]. Similarly, the mediators of weak interactions, W and Z bosons, were discovered at CERN [13–16] in 1983. A more detailed and readable account of the history of Particle Physics is found in [17–19].

1.2 The Standard Model

The Standard Model (SM) [20,21] is a comprehensive framework which provides the best theoretical description of the elementary particles and the interactions between them. According to the SM, all visible matter in the universe is made up of basic building blocks called "fundamental particles", categorized in three generations of quarks and three generations of leptons, which interact via four fundamental forces. Since the early 1970's, several theoretical predictions given by the SM have been verified experimentally to high precision. Mathematically, the SM is a gauge theory based on Quantum Field Theories (QFT) [22] and is defined by local symmetry group :

$$\mathrm{SU(3)_C \times SU(2)_L \times U(1)_Y} \tag{1.1}$$

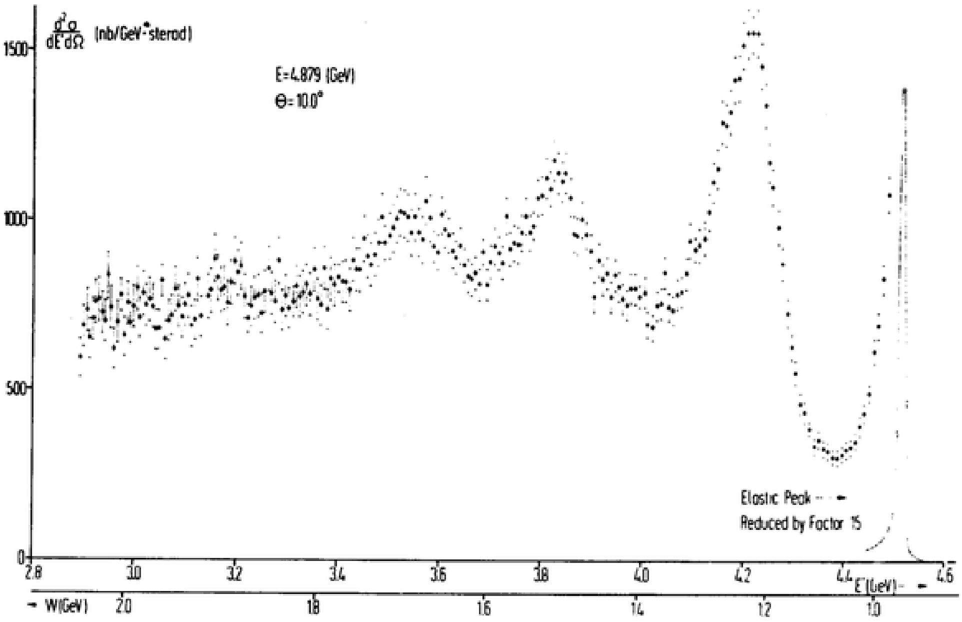

Figure 1.2: Three lumps showing existence of three quarks as proton's substructure. Figure source : https://sidquarkphysics.quora.com/Can-we-see-a-quark-by-Viktor-T-Toth.

where Y stands for hypercharge (Y = B + S, where, B represents Baryon Number and S the Strangeness), L for weak isospin and C for color charge. The Quantum Chromodynamics (QCD) is the basis of SU(3)$_C$ term and represents the strong interactions of quark and gluons while the $SU(2)_L \times U(1)_Y$ term unifies the electromagnetic and the weak interactions. At sufficiently high energies i.e. at the electroweak scale[1], the QED and the weak interactions are unified in an electroweak theory, described by the symmetry group SU(2)$_L$xU(1)$_Y$.

1.2.1 Fundamental Particles

In the SM, the fundamental particles are broadly categorized as :

- **Matter Particles** : Building blocks of the visible matter and are referred as the *fermions*. The fermions are spin $\frac{1}{2}$ particles, further classified into 6 *leptons*

---

[1] The electroweak scale is the energy scale around 246 GeV, a typical energy of processes described by the electroweak theory. The particular number 246 GeV is taken to be the vacuum expectation value.

and 6 *quarks*, as shown in figure 1.3. All quarks and leptons obey Fermi Dirac Statistics, thus known as fermions.

- **Force Carriers** : Mediators of the fundamental interactions between SM particles. The fundamental forces of nature are characterized by their strength and the range over which they are effective, which in turn depend upon the mass of their mediators exchanged between the particles. There are 4 vector bosons in the SM, which are mediators of interactions and a scalar "Higgs boson".

The twelve different fermions and their corresponding antiparticles have the same masses with equal but opposite charges. They are grouped into three generations and each generation further has two leptons and two quarks. The leptons of the first generation are the electron (e) and the electron neutrino (ν_e), while the corresponding quarks are the up (u) and the down (d) quark. Similarly, the leptons of the second and third generation are the muon (μ) and the tau lepton (τ) as well as the corresponding neutrinos ν_μ and ν_τ, while the quarks are denoted charm (c) and strange (s) top (t) and bottom (b). In general, the fermions get progressively heavier with each generation e.g., the electron is lighter than the muon, which is lighter than the τ. Electrons are the most stable, and the most common charged lepton found in nature, while the heavier muons and taus are formed from high energy collisions and quickly decay down to the electrons and neutrinos. The stable matter of the universe is made of electrons and quarks of first generation : up (u) and down (d). The constituents of atomic nuclei, protons and neutrons are composites of u and d quarks and the atomic shell is formed by electrons.

1.2.2 Fundamental Forces

All matter in the Universe interact through four forces: Strong, Electromagnetic, Weak and Gravitational, listed in table 1.1 and shown in figure 1.4. Each force is characterized by its strength and the range over which it is effective which in turn

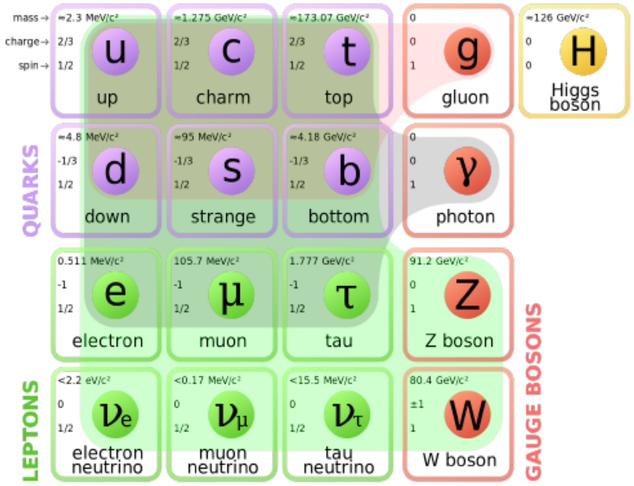

Figure 1.3: Particles of the standard model represented in three generations. Figure source : https://en.wikipedia.org/wiki/Standard_Model.

depends upon the mass of the mediator(s) exchanged between the particles. A brief description of these fundamental forces is given below.

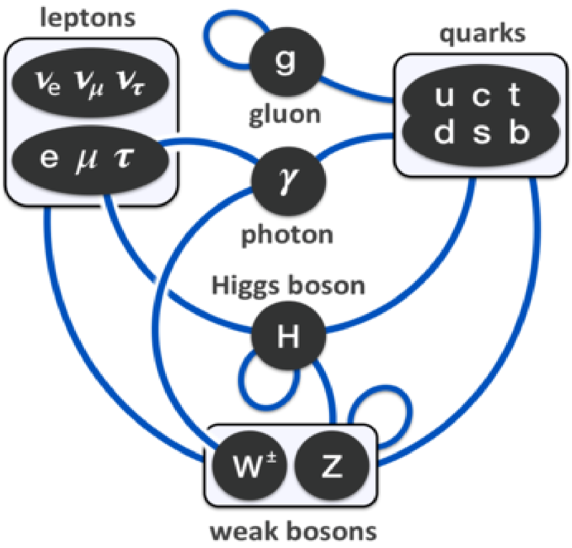

Figure 1.4: The four fundamental interactions of nature.

- **Strong Interaction** : It is the force experienced by the quarks and is the strongest of the four fundamental forces, and has a very short range of the order of 1 femtometer (10^{-15} m). The strong interaction is described by the QCD which is based on $SU(3)_C$ symmetry group. The properties of the particles and their corresponding interactions are represented by “Quantum Numbers”. The strongly interacting particles i.e. quark and gluons have specific quantum number known as “color”. Each quark has an associated color, while anti-quark holds an anti-colour. In two-quark states, a color and its anti-color combine to make a colorless state. The corresponding triplet representation results in eight gluons, which are the force carries of the strong interaction. Gluons are bi-coloured and at the same time carry a color and anti-color. The strength of strong interaction is governed by the size of the strong coupling constant g_S or equivalently $\alpha_s = \frac{g_s^2}{4\pi}$ and varies from large to low energies, α_s ($Q = m_{hadron}$) ~ 1 up to the vanishing asymptotic limit α_s ($Q \to \infty$) $\to 0$, Q represents the momentum transfer). This last limit indicates that the quarks behave as free particles when they are observed at infinitely large energies or, equivalently, infinitely short distances. This is known as the property of asymptotic freedom.

- **Electromagnetic (EM) Interaction** : It is mediated between particles with electric charge by the exchange of photons (γ), which themselves are electrically neutral and massless. For example, two electrons can scatter via the exchange of a photon, or they can annihilate into a photon which in turn can again produce an electron and its antiparticle, a positron (pair production). It is a long range force and is governed by U(1) local gauge group.

- **Weak Interaction** : It is a short range force and is effective only at subatomic scale. However, this force is stronger than the gravitational force at subatomic level. All fermions in the SM carry a weak charge, the weak interaction is mediated by the exchange of the massive Z and $W^{\pm}$ bosons. As a consequence, the weak interaction is suppressed compared to the electromagnetic interaction below the $Z/W^{\pm}$ mass scale.

- **Gravitational Interaction** : It is the weakest in magnitude and is experienced even at infinite distances. It is attractive in nature and is responsible

Force	Particles	Mediators	Relative Strength	Range
Strong	Quarks, Gluons	Gluons	10^{38}	10^{-15} m
Electromagnetic	Charged particles	Photon	10^{36}	∞
Weak	Quarks, Leptons	$W^{\pm}$,Z^0	10^{25}	10^{-18} m
Gravitational	all particles with mass	Graviton	1	∞

Table 1.1: Various properties of the fundamental interaction of nature.

for holding the planets inside the solar system. It is hypothesized that gravitational interactions are mediated by a massless spin-2 particle called the graviton, which however has not been discovered so far.

1.2.3 Electroweak Theory

The main goal of the study of the fundamental particles is to provide the most universal laws, which would describe as many aspects of the Universe as possible. For example, the electricity and magnetism are already unified to a common theory of electromagnetism. The unification of the electromagnetic and the weak interactions was achieved by Glashow, Salam and Weinberg providing a theory of the electroweak interactions [23–25]. Although the weak and the electromagnetic forces behave differently at low energies, the electroweak theory models them as two different aspects of the same force. Eventually they discovered that at very short distances (about 10^{-18} meters) the strength of the weak interaction is comparable to that of the electromagnetic [26].

The electroweak interactions were experimentally verified by the discovery of neutral currents in neutrino scattering by the Gargamelle collaboration at the CERN [27] in 1973, and by the UA1 [28] and the UA2 [29] Collaborations with the discovery of the W and Z gauge bosons in $p\bar{p}$ collisions at the CERN in 1983.

The electroweak interactions are represented by two quantum numbers : weak isospin and hypercharge. The third component of weak isospin T_3, signifies the arrangement of left handed (negatively chiral) fermions within the SM generations. The weak hypercharge (Y_w) relates third component of weak isospin (T_3) and electric charge (e) as given below :

$$e = T_3 + \frac{Y_w}{2} \tag{1.2}$$

The weak interaction through charged current is associated with $SU(2)_L$ gauge symmetry group, which has three generators $T_i = \sigma i\ /2$, σ_i are the Pauli matrices. The $SU(2)_L$ (L represents left handed) local gauge invariance is satisfied by introducing three fields, which correspond to three gauge bosons : W_μ^1, W_μ^2 and W_μ^3. Similarly, the symmetry group associated to the weak hypercharge is the group $U(1)_Y$ which has one generator and thus one gauge field $B\mu$. These two groups build up the symmetry group of the electroweak theory $SU(2)_L \times U(1)_Y$. Hence, parity violating weak force and parity conserving electromagnetic force are unified using $SU(2)_L \times U(1)_Y$ gauge theory. This group allows for the collective four force-carrying bosons : photon, positively charged and negatively charged W's and neutral Z to be described as compositions of the same underlying states.

1.2.4 Quantum Chromodynamics

The strong interactions are represented by the Quantum Field Theory or QCD [30, 31] theory. In the SM, the strong force arises by requiring local gauge invariance under the non-Abelian group $SU(3)_C$ between the colored states of quarks. In QCD, the quarks are described by ψ_i field, i varies from 1 to 3, i representing "color" quantum number. The behaviour of quarks and gluons in particle collisions is determined by two peculiar features of QCD : Asymptotic Freedom and Quark Confinement.

- **Asymptotic Freedom** : The quarks interact weakly at high energies and can be considered as free, since the strength of strong interactions tends to decrease at such energies. This property of strong interaction is known as asymptotic freedom [32], discovered by Gross, Politzer, and Wilczek in 1973 [33, 34]. The quark interactions occur through the exchange of gluons with a

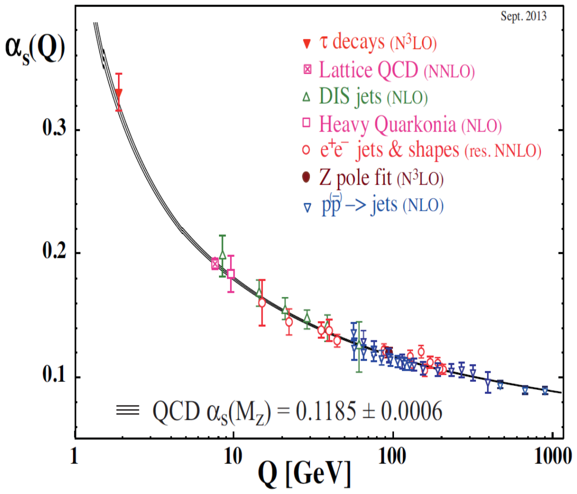

Figure 1.5: Plot representing the measured values of α_s (Q^2) as a function of the respective energy scale Q. Figure reproduced from [36].

definite momentum transfer Q. Hence, the strong force coupling constant α_s is dependent on the momentum transfer and defined as :

$$\alpha_{\mathrm{s}}(\mathrm{Q}^2) = \frac{12\pi}{33 - 2\mathrm{n_f}\ln(\frac{\mathrm{Q}^2}{\Lambda^2})} \tag{1.3}$$

where, n_f represents the number of quark flavors and Λ is the QCD scale, Q denotes the momentum transfer. The dependence of strong coupling constant on momentum transfer makes the QCD complex. Figure 1.5 shows the variation of strong coupling constant α_s with Q, obtained from various experimental observations [35]. The world average value of the strong coupling constant is 0.1181 ± 0.0011 [35].

- **Quark Confinement** : It is the phenomenon due to which the color charged particles, quarks and gluons, cannot be isolated or cannot be directly observed in normal conditions. Thus, quarks are confined in groups with other quarks to form color neutral composites, hadrons, as shown in figure 1.6. Every attempt to kick a quark free from a hadron, via high-energy collisions, only results in the formation of new color-singlet hadrons.

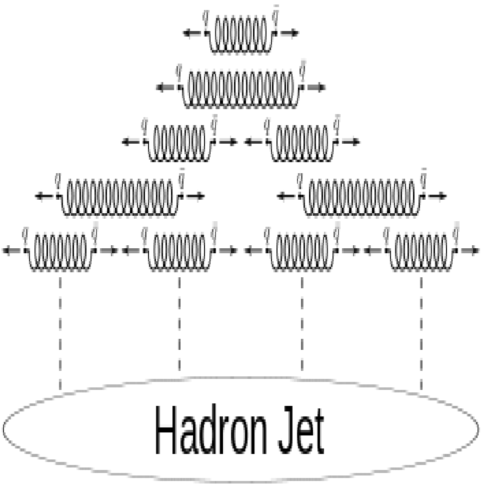

Figure 1.6: Diagram representing color confinement and formation of hadronic jets. Figure source : https://en.wikipedia.org/wiki/Color_confinement.

1.2.5 Spontaneous Symmetry Breaking

The major drawback in establishing the electroweak theory was the fact that weak force carriers, $W^{\pm}$ and Z boson, are massive particles, whereas, the mediators of EM interactions, photons, are massless. These particles are accurately described by SU(2) gauge theory, but bosons in gauge theory have to be massless. To get massive particles, the electroweak symmetry must be broken in such a way that all symmetry predictions remain preserved. The classical solution to this problem is the Electroweak Symmetry Breaking Higgs mechanism [37–39], which leaves the Lagrangian, but not the vacuum state, invariant under electroweak transformations, a principle called spontaneous symmetry breaking. A canonical example of a spontaneous symmetry breaking is that of a ferromagnetic system. Above the Curie temperature, T_C, the system shows SO(3) rotational symmetry, with all dipoles randomly oriented in the three dimensional space, yielding a null overall magnetization. For $T < T_C$, the configuration of minimum energy is reached when all dipoles are aligned in arbitrary directions (spontaneous magnetization) and the rotational symmetry is hidden.

In the Higgs mechanism an additional scalar field, the Higgs field, is introduced into the theory, which has a potential function of a form allowing degenerate vacuum solutions with a non-zero vacuum expectation value. In its simplest structure, an SU(2) doublet, the Higgs field is given below :

$$\Phi = \begin{pmatrix} \Phi^{+} \\ \Phi^{0} \end{pmatrix} \tag{1.4}$$

The corresponding Higgs potential is given below and its pictorial representation is given in figure 1.7 :

$$\mathrm{V}(\Phi) = \mu^{2}\Phi^{+}\Phi + \lambda(\Phi^{+}\Phi)^{2} \tag{1.5}$$

where, μ and λ are real constants with $\lambda > 0$ and $\mu^{2} = 0$. V has degenerate, non-trivial minima Φ_0 defined by :

$$\Phi_0^{+}\Phi_0 = \frac{\mu^{2}}{2\lambda} \equiv \frac{\mathrm{v}^{2}}{2} \tag{1.6}$$

here, v represents the vacuum expectation value (VEV). The choice of any particular minimum (vacuum state) breaks the $\mathrm{U}(1)_Y \times SU(2)_L$ symmetry of the system. The vacuum state is chosen electrically neutral as :

$$\Phi = \frac{1}{\sqrt{2}} \begin{pmatrix} 0 \\ v \end{pmatrix} \tag{1.7}$$

It is quantised by expansion around the minimum, resulting in one massive and three massless bosons, the later being known as the Goldstone bosons [40]. By the choice of a suitable gauge, the Goldstone boson fields are eliminated and the Higgs field becomes :

$$\Phi = \frac{1}{\sqrt{2}} \begin{pmatrix} 0 \\ v + H(x) \end{pmatrix} \tag{1.8}$$

with the massive Higgs boson H(x). Substitution of Eq. 1.8 into 1.7 results in

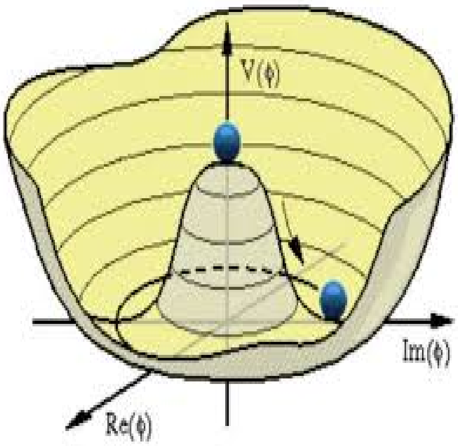

Figure 1.7: Pictorial view of Higgs potential. Source : https://www-cdf.fnal.gov/physics/new/hdg/results/combcdf_080801.

the mass terms :

$$m_H = \sqrt{2}\mu m_W = \frac{1}{2} g v m_z = \frac{m_W}{\cos\theta_W} \tag{1.9}$$

By virtue of the chosen neutral vacuum state, the photon does not acquire mass. In addition, there are also terms describing interactions between the H and the $W^{\pm}$ and Z bosons with couplings proportional to the vector boson masses, as well as self-coupling terms of the H.

1.3 Limitations of the Standard Model

Although the SM is the most outstanding theory in explaining the fundamental particles and their interactions, several theoretical issues and experimental observations have proved that it is still incomplete and at some higher energy it must be embedded into a wider new theory. Many searches for beyond the Standard Model (BSM) physics are motivated by some inherent limitations of the SM. Some unanswered questions are discussed below :

- **Gravity** : The SM does not include gravity, one of the four fundamental forces. It also fails to explain why gravity is so much weaker than the electromagnetic or strong nuclear forces. Since, the gravitational force is $\sim 10^{32}$ times weaker than the weak force, the absence of gravitation force does not affect SM theory. However, this fundamental force cannot be ignored at the Planck scale $M_P \sim (10^{19}$ GeV).

- **Neutrino Mass** : The SM and the Higgs mechanism predict neutrinos as massless, hence neutrino flavor oscillations are forbidden. However, the neutrino oscillations have been confirmed by several neutrino based experiments [41–43]. Although the absolute masses of neutrinos are not measured yet their squared mass differences have been measured to be non-zero.

- **Matter-AntiMatter Symmetry** : According to SM, 13.8 billion years ago, at the time of creation of Universe, the equal amounts of matter and antimatter must have been created. But it has been observed that there is large asymmetry between matter and antimatter content. Several theorists have recommended that three conditions can be responsible for this asymmetry : Baryon number violation, Charge, C and Charge-Parity, CP symmetry violation, and the interactions out of thermal equilibrium.

- **Dark Matter** : The SM also leaves many open questions in the context of cosmology. While several astrophysical observations have indicated the existence of dark matter [44, 45] which accounts for the majority of the known mass of the universe, the SM offers no viable candidates for this dark matter. Furthermore, the SM does not provide a mechanism for the observed expansion of the universe and the large amount of dark energy which contributes to this expansion.

- **Hierarchy Problem** : The SM is capable of explaining the relative strength of the electromagnetic, weak, and strong forces. It offers no explanation for the relative difference in the strength of the electroweak and gravitational forces. This observed difference, known as the Hierarchy Problem [46], is also fundamentally related to the problem of fine-tuning of the radiative corrections

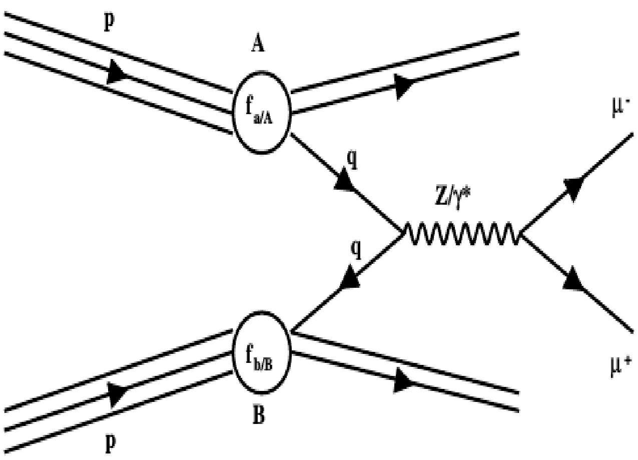

Figure 1.8: Feynman diagram of Drell-Yan process

of the Higgs mass, which has been observed to be much lighter than the Planck mass.

1.4 The Drell-Yan Process

During hadronic collisions, the production of lepton-antilepton (l^+l^-) pair via quark-antiquark ($q\bar{q}$) annihilation is known as Drell-Yan (DY) process, as shown in figure 1.8. The annihilation of $q\bar{q}$ pair results in the production of either a virtual photon(γ^*) or Z boson, which subsequently decays into a pair of lepton-antilepton. In 1970, this process was discussed by Sidney Drell and Tung-Mow Yan [47] in order to describe the presence of lepton pairs in hadronic collisions in the context of Feynman's parton model [48]. The DY process was experimentally confirmed at Brookhaven National Laboratory (BNL) in US, by hitting protons on a fixed target uranium and examining the lepton pairs produced [49]. In figure 1.9, the dimuon yield as measured at BNL is shown, where the kink near the muon pair mass of 3 GeV/c^2, corresponds to J/ψ particle.

The work presented in this thesis is based on the study of Drell-Yan production

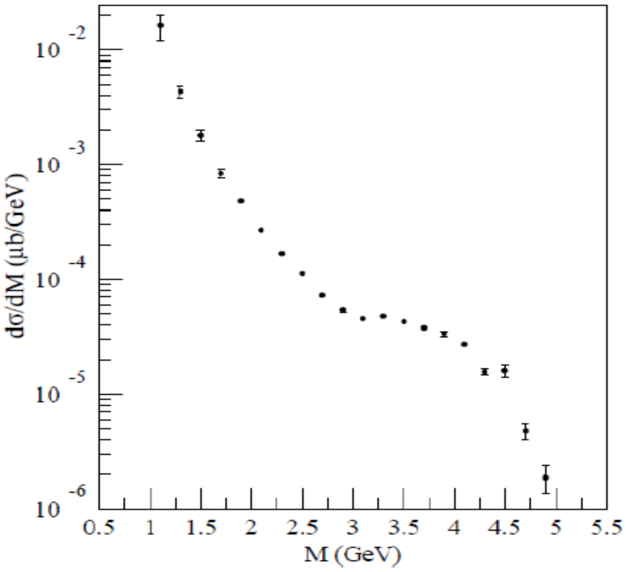

Figure 1.9: The measured dimuon cross section at the Brookhaven National Laboratory. Figure reproduced from [49].

with muon-antimuon final state, as shown in figure 1.8 and in Eq. 1.10.

$$q\bar{q} \rightarrow Z/\gamma^* \rightarrow \mu^+\mu^- \tag{1.10}$$

1.4.1 Z boson decay modes

Z bosons have been extensively studied at the CERN LEP e^+e^- collider [55] and at the Fermilab Tevatron collider [56, 57]. Z boson has no electric charge and is its own antiparticle. The most precise current values of Z boson mass M_Z and its decay width Γ_Z are [58]:

$$M_Z = 91.1876 \pm 0.0021 \text{ p/c}^2$$
$$\Gamma_Z = 2.4952 \pm 0.0023 \text{ GeV}$$

Using the Heisenberg principle, the mean lifetime of the boson was estimated of order of $3{\times}10^{-25}$s, hence its production is instantaneously followed by the decay. Hence, to study DY production, the resulting particle must therefore be detected through Z decay products. Z boson decays into a fermion and its antiparticle. The decay of the

Z boson can occur in several ways as listed in table 1.2. The Z boson prefers to decay hadronically, with almost 70% of the decays being to strong interacting particles. Invisible decays to neutrinos account for 20% of the decays and the remaining are leptonic decays to electrons, muons and taus in almost equal amounts. The leptonic decays have the cleanest signature.

Decay Mode	**Fraction**
Z→ e^+e^-	3.363±0.004 %
Z→ $\mu^+\mu^-$	3.366 ±0.004 %
Z→ $\tau^+\tau^-$	3.370 ±0.008 %
Z→ $\nu\bar{\nu}$	20.00±0.06 %
Z→ $q\bar{q}$	69.91±0.06 %

Table 1.2: Branching fraction of the Z Boson decay modes.
Source : http://pdg.lbl.gov/2012/listings/rpp2012-list-z-boson.pdf

1.4.2 Motivation to study DY process

- The DY process unravels significant characteristics of the hadronic collisions, i.e. pp collisions at LHC. At high energies, the theoretical calculations for the DY production rate are fairly accurate, since the QCD effects dominate only at the initial state [50], hence, these predictions can be used to validate the SM.

- Drell-Yan lepton-pair production is a major source of background for various physics analyses, such as $t\bar{t}$ and diboson measurements, as well as for searches for new physics beyond the standard model, such as the production of high-mass dilepton resonances. Thus a systematic understanding of this background is necessary.

- The DY events can be used to study the Initial State Radiation (ISR) effects. These can be used in the measurement of top-quark mass M_t by $t\bar{t}$ production, where it is difficult to differentiate the ISR hadrons from the Final State Radiation hadrons. Thus, DY data provides a unique opportunity to study ISR effects.

The theoretical calculations of the differential cross section are well established up to the next-to-next-to-leading order (NNLO). Comparisons between theoretical calculations and experimental measurements, provide tests of perturbative quantum chromodynamics (QCD) and constraints on the parton distribution functions (PDFs) $Q^2 \sim M_{ll}$, Q being the momentum transfer and M_{ll} represents the dilepton mass. The detailed knowledge of the PDFs of the incident protons can be extracted by understanding the forward and backward angular asymmetry of the charged leptons. In addition, these angular measurements will eventually lead to a precise calculation of effective weak mixing angle, $\sin^2\theta_w$. A thorough understanding of the origin of transverse momenta of the Z bosons is essential for future high precision measurement of W-mass. The DY events around the Z-mass can be used for accurate extrapolation of the boson transverse momentum from the Z-mass scale to the W-mass scale.

1.4.3 Drell-Yan cross section

For experiments with large center of mass energy, the kinematics and cross section of various physics processes are explained by the parton model [48]. The model holds for the processes involving large momentum transfers Q^2 between colliding particle. The parton model treats the constituent partons of the incident (or target) hadrons as autonomous particles.

The DY total production cross section (figure 1.8) is calculated by summing the cross sections of sub-processes involving the partons in one hadron and those in the other hadron. For instance, consider the proton A colliding with second proton B for some fixed Q^2. The longitudinal momentum fraction of parton ‘a’ in A denoted by x_a and the parton distribution function, PDF of ‘a’ in A to be $f_{a/A}$ (x_a) and by x_b and $f_{b/B}(x_b)$ for parton ‘b’ in proton B. Let the protons collide and result in the reaction given below:

$$A + B \rightarrow c + X, \tag{1.11}$$

where, ‘c’ corresponds to a fermion and X denotes arbitrary final state particles. Let the subprocess be given as :

$$\mathrm{a} + \mathrm{b} \rightarrow \mathrm{c} + \mathrm{X}, \tag{1.12}$$

Then, the total cross section $\sigma \equiv \sigma(AB \rightarrow cX)$ is calculated by multiplying the subprocess cross section $\hat{\sigma} \equiv \hat{\sigma}(ab \rightarrow cX)$ by dx$_a$ f$_{a/A}$ (x$_a$) and dx$_b$ f$_{b/B}$ (x$_b$), summing over all parton types of ‘a’ and ‘b’, and integrating over x$_a$ and x$_b$. The DY total production cross section σ_{tot} is calculated as :

$$\sigma_{\mathrm{tot}} = \sum_{\mathrm{a,b=q,\bar{q},g}} \mathrm{C}_{ab} \int_0^1 \mathrm{dx_a} \int_0^1 \mathrm{dx_b} [\mathrm{f_{a/A}(x_a) f_{b/B}(x_b)} + (\mathrm{A} \leftrightarrow \mathrm{B}, \text{if } \mathrm{a} \neq \mathrm{b})]\hat{\sigma} \tag{1.13}$$

where, the term C$_{ab}$ represents the initial colour-average factor. To account for the feasibility of parton ‘a’ coming from proton B and parton ‘b’ coming from parton A the following term is introduced :

$$\mathrm{A} \leftrightarrow \mathrm{B} \equiv \mathrm{f_{a/B}(x_b) f_{b/A}(x_a)}, \tag{1.14}$$

which is zero if a = b.

The relationship between the variables x and Q^2 and the kinetic variables corresponding to a final state of mass M and produced with rapidity ‘y’ is shown in figure 1.10. In addition, the phase space regions for various high energy experiments are shown. The predicted cross sections of different processes, including Z bosons, as a function of centre of mass energy $\sqrt{s} = \mathrm{E}$ are shown in figure 1.11.

1.5 Thesis Organization

In this thesis, studies performed using the proton-proton (pp) collision data collected with the Compact Muon Solenoid (CMS) detector at $\sqrt{s}$=8 TeV to measure the single and double differential cross section of Drell-Yan process are presented in the

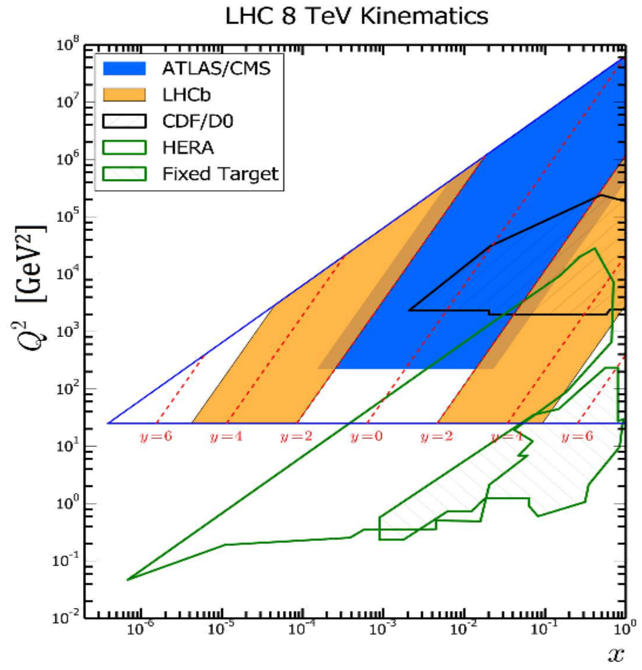

Figure 1.10: Comparison of phase space available for Drell-Yan production cross section at HERA and LHC. Figure reproduced from [59].

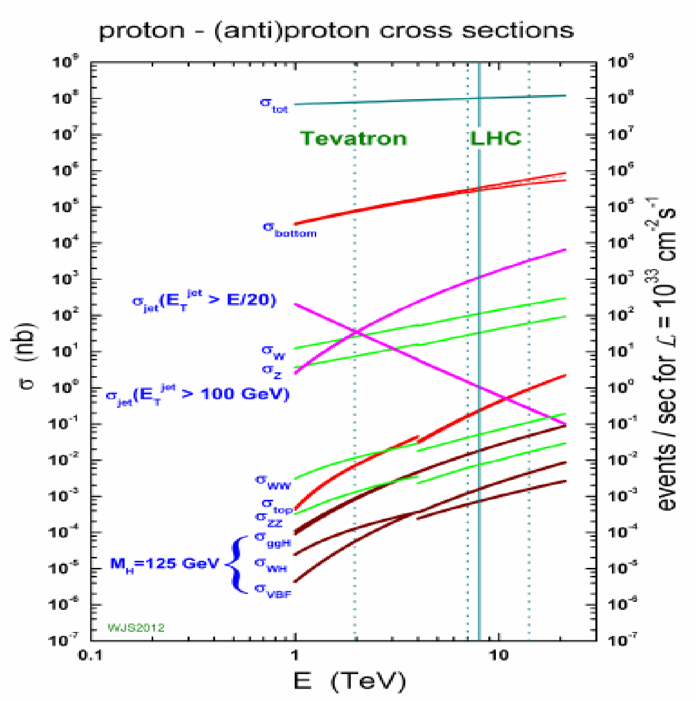

Figure 1.11: Cross sections for different processes in hadron colliders as a function of centre of mass energy. Figure source : http://inspirehep.net/record/834830/plots

final state consisting of two muons In addition, various aspects of CMS detector have been studied to improve the detector performance through precise calibration procedures. The layout of the thesis is :

- The present chapter gives an overview of the Standard Model of particle physics and its shortcomings. It further explains the Drell-Yan process and its historical perspective.
- **Chapter 2** gives an overview of the LHC machine at CERN. Various experimental facilities at CERN are described briefly along with the setup of the CMS detector used for the present work.
- **Chapter 3** explains all the steps for Monte Carlo simulation of a high energy physics experiment. Simulated events are required for better understanding of the detector. The last part of the chapter covers the reconstruction techniques of all types of physics objects. Muon reconstruction is discussed in detail as it is important for the topic of this thesis.
- **Chapter 4** covers the work done during the upgradation of LHC during Phase 1. The photodetectors of Hadron Outer (HO) were replaced by silicon photomultipliers (SiPMs). The detailed description of the HO along with the analysis performed to study thermal stability of SiPM is covered in this chapter. Also, the quality tests performed pre and post installation of SiPMs are discussed. The second part of the chapter covers the studies performed for evaluating the calibration constants of the Hadron Calorimeter (HCAL). In addition, the performance of the dedicated calibration triggers was also studied.
- **Chapter 5** describes in detail the analysis performed to measure the Drell-Yan production cross section. This chapter includes description of data and Monte Carlo (MC) samples, event selection, detector level comparison, unfolding to correct for the detector effects and the main sources of systematic uncertainties for single and double differential measurements. The comparison

of the measurements made for Drell-Yan events with predictions from various Monte Carlo samples is discussed in the chapter. The comparisons are made in different ranges of ϕ^* and rapidity. These comparisons highlight regions where parton shower Monte Carlo generators do not explain the measurements from data.

- The summary and conclusions are given in **Chapter 6**.

Bibliography

[1] J.J.Thomson, “XL. Cathode Rays”, Philosophical Magazine Series 5,vol. 44, no. 269, pp. 293-316, 1897.

[2] E. Rutherford, “The Structure of the Atom”, Nature, vol. 92, pp. 423, 1913.

[3] E. Rutherford, “The scattering of alpha and beta particles by matter and the structure of the atom”, Phil. Mag., vol. 21, pp. 669-688, 1911.

[4] J. Chadwick, “Possible Existence of a Neutron, Nature, vol. 129, pp. 312, 1932.

[5] F. Reines and C. L. Cowan, “Detection of the free neutrino”, Phys. Rev., vol. 92, pp. 830-831, 1953.

[6] C. D. Anderson, “The positive electron”, Phys. Rev., vol. 43, pp. 491-494, 1933.

[7] C.M.G Lattes, “Observation on the Tracks of Slow Mesons in Photographic Emulsions”, Nature, vol. 160, pp. 486-492, 1947.

[8] G. D. Rochester and C. C. Butler, “Evidence for the Existence of New Unstable Elementary Particles”, Nature, vol. 160, pp. 855-857, 1947.

[9] C.Bebek et. al, “Evidence for New Flavor Production at the Γ(4S)”, Phys. Review Lett., vol. 46, issue 2, pp. 84-87, 1981.

[10] M. Gell-Mann, “A Schematic Model of Baryons and Mesons”, Phys. Lett., vol. 8, pp. 214-215, 1964.

[11] David J. Griffiths, “Introduction to elementary particles”, Book published by Wiley, 2008.

[12] B. R. Stella and H.-J. Meyer, “Υ(9.46 GeV) and the gluon discovery (a critical recollection of PLUTO results)”, Eur. Phys. J., vol. H36, pp. 203-243, 2011.

[13] UA1 Collaboration, “Experimental observation of isolated large transverse energy electrons with associated missing energy at $\sqrt{s}$=540 GeV”, Physics Letters B, vol. 122, no. 1, pp. 103-116, 1983.

[14] UA2 Collaboration, “Observation of Single Isolated Electrons of High Transverse Momentum in Events with Missing Transverse Energy at the CERN anti-p p Collider”, Phys. Lett., vol. B122, pp. 476-485, 1983.

[15] UA1 Collaboration, “Experimental Observation of Lepton Pairs of Invariant Mass Around 95-GeV/c^2 at the CERN SPS Collider”, Phys. Lett., vol. B126, pp. 398-410, 1983.

[16] UA2 Collaboration, “Evidence for $Z^0 \to e^-e^+$ at the CERN $p\overline{p}$ Collider”, Phys. Lett., vol. B129, pp. 130-140, 1983.

[17] S.Weinberg, “Subatomic Particles”, Scientific American Library, New York, 1983.

[18] A. Kellers, “The Infancy of Atomic Physics”, Book published by Oxford University Press, Oxford, 1983.

[19] Leon M. Lederman and David N. Schramm, “From Quarks to the Cosmos: Tools of Discovery”, Scientific American Library, 1989.

[20] M. J. Herrero, “The Standard Model” arXiv:hep-ph/9812242.

[21] D. H. Perkins, “Introduction to High Energy Physics”, Book published by Addison-Wesley, 1987.

[22] M. E. Peskin and D. V. Schroeder, “An Introduction to quantum field theory”, Book published by Addison-Wesley, 1995.

[23] .L.Glasow, “Partial Symmetries of Weak Interactions”, Nuclear Physics, vol. 22, issue 4, pp. 579-588, 1961.

[24] A.Salam and J.C.Ward, “Electromagnetic and Weak Interactions”, Physics Letters, vol. 13, issue 2, pp. 168-171, 1964.

[25] S.Weinberg, “A Model of Leptons”, Phys. Rev. Lett., vol. 19, issue 21, pp. 1264-1266, 1967.

[26] http://www.particleadventure.org/electroweak.html.

[27] F.J.Hasert, “Observation of Neutrino Like Interactions without Muon or Electron in the Gargamelle Neutrino Experiment”, Nucl.Phys. B73, pp. 1-22, 1974.

[28] The UA1 Collaboration, “Experimental observation of isolated large transverse energy electrons with associated missing energy at $\sqrt{s}$=540 GeV”, Phys. Lett. B, vol. 122, issue 1, pp. 103-116, 1983.

[29] The UA2 Collaboration,“Observation of single isolated electrons of high transverse momentum in events with missing transverse energy at the CERN pp collider”, Phys. Lett. B, vol. 122, issue 5-6, pp. 476-485, 1983.

[30] R.K.Ellis, W.J.Stirling and B.R.Webber, “QCD and Collider Physics”, Cambridge University Press, 1996.

[31] D.J.Gross and F.Wilczek, “Asymptotically Free Gauge Theories”, Phys. Rev. D, vol.8, issue 10, pp. 3633-3652, 1973.

[32] H.D.Politzer, “Asymptotic Freedom: An Approach to Strong Interactions”, Physics Reports, vol. 14, pp. 129-180, 1974.

[33] D.J.Gross and F.Wilczek, “Ultraviolet Behavior of Nonabelian Gauge Theories”, Phys.Rev.Lett., vol. 30, issue 26, pp. 1343-1346, 1973.

[34] H. D. Politzer, “Reliable Perturbative Results for Strong Interactions?”, Phys. Rev. Lett., vol. 30, issue 26, pp. 1346-1349, 1973.

[35] C. Patrignani et al., “Review of Particle Physics”, Chin. Phys., vol. C40, no. 10, p. 100001, 2016.

[36] http://webific.ific.uv.es/web/en/content/lattice-qcd-numerical-approach-strong-force.

[37] P. W. Higgs, "Broken Symmetries and the Masses of Gauge Bosons", Phys. Rev. Lett., vol. 13, issue 16, pp. 508-509, 1964 .

[38] F. Englert and R. Brout, "Broken Symmetry and the Mass of Gauge Vector Mesons", Phys. Rev. Lett., vol. 13, issue 9, pp. 321-323, 1964.

[39] G. Guralnik, C. Hagen, and T. Kibble, "Global Conservation Laws and Massless Particles", Phys.Rev.Lett., vol. 13, issue 20, pp. 585-587, 1964.

[40] J. Goldstone, A. Salam, and S. Weinberg, "Broken Symmetries", Phys.Rev., vol. 127, issue 3, pp. 965-970, 1962.

[41] M. P. Decowski, "KamLANDs precision neutrino oscillation measurements",Nucl. Phys., vol. B908, pp. 52-61, 2016.

[42] OPERA Collaboration, "Observation of tau neutrino appearance in the CNGS beam with the OPERA experiment", PTEP, vol. 2014, no. 10, pp. 101C01, 2014.

[43] T2K Collaboration, "Precise Measurement of the Neutrino Mixing Parameter θ_{23} from Muon Neutrino Disappearance in an Off-Axis Beam", Phys. Rev. Lett., vol. 112, issue 18, pp. 181801, 2014.

[44] F. Zwicky, "On the Masses of Nebulae and of Clusters of Nebulae", Astrophys. J., vol. 86, pp. 217-246, 1937.

[45] "Planck 2015 Constraints on Dark Energy and Inflation", https://darkmatterdarkenergy.com/tag/planck-2015/.

[46] N.A.Hameda, "The hierarchy problem and new dimensions at a millimeter", Phys. Rev. Lett. B, vol. 429, issue 3-4, pp. 263,272, 1998.

[47] S. D. Drell and T.-M. Yan, “Massive Lepton-Pair Production in Hadron-Hadron Collisions at High Energies”, Phys. Rev. Lett., vol. 25, issue 5, pp. 316-320, 1970.

[48] R. P. Feynman, “Very High-Energy Collisions of Hadrons”, Phys. Rev. Lett., vol. 23, issue 24, pp. 1415-1417, 1969.

[49] J. Christenson et al., “Observation of Massive Muon Pairs in Hadron Collisions”, Phys. Rev. Lett., vol. 25, issue 21, pp. 1523-1526, 1970.

[50] Y. K. Kim, et al., “Initial state gluon radiation studies on Drell-Yan data for top-pair production in hadron collider”, CDF/PHYS/CDFR/6804, 2004.

[51] ATLAS Collaboration, “Measurement of the transverse momentum distribution of Z/γ^* bosons in proton-proton collisions at $\sqrt{s}$ = 7 TeV with the ATLAS detector, Phys.Lett. B705, pp 415-434, 2011.

[52] CMS Collaboration, “Measurement of the Rapidity and Transverse Momentum Distributions of Z Bosons in pp Collisions at $\sqrt{s}$ = 7 TeV, Phys.Rev. D, vol.85, issue 3, 032002, 2012.

[53] CMS Collaboration, “Measurement of the transverse momentum distributions of Z Bosons decaying to dimuons in pp collisions at $\sqrt{s}$=8 TeV”, Technical Report CMS-PAS-SMP-12-025, CERN, Geneva, 2013.

[54] CMS Collaboration, “Measurement of Z production as a function of p$_T$, Y”, Technical Report CMS-PAS-SMP-13-013, CERN, Geneva, 2014.

[55] LEP and SLD Collaborations, “A combination of preliminary electroweak measurements and constraints on the Standard Model”, CERN-EP-2001-021, arXiv:hep- ex/0103048, 2001.

[56] D0 Collaboration, “Measurement of W and Z production cross-sections in p$\bar{p}$ collisions at $\sqrt{s}$ = 1.8 TeV”, arXiv:hep-ex/9412016, 1994.

[57] CDF Collaboration, “Observation of WZ Production”, Physics Review Letters , vol.98, issue 16, 161801, 2007.

[58] K.Nakamura et al.,(Particle Data Group) “Review of Particle Physics”, J.Phys.G 37, no. 075021, 2010.

[59] W.Barter, “A brief review of measurements of electroweak bosons at the LHCb experiment in LHC Run 1”, Mod. Phys. Lett. A, vol. 31, issue 38, 1630044, 2016.

Chapter 2

The Large Hadron Collider and the CMS Experiment

The European Organization for Nuclear Research (CERN) was established in 1954 with a mandate of understanding the constituents of atomic nuclei. In due course of time, the understanding of the matter has gone much deeper and nowadays, the research at CERN is dedicated to decode the fundamental constituents of matter and their interactions.

In CERN's quest to explore the complexity of matter, several discoveries have been made in the field of particle physics. The discovery of weak neutral currents in 1973 inside Gargamelle bubble chamber, first observation of W and Z bosons in 1983, production of first anti-atoms in 1995 and the discovery of the Standard Model Higgs boson in 2012 are some of the revolutionary achievements accomplished at CERN.

Hadron colliders are well suited to the task of exploring new energy domains. By colliding protons at TeV energies, the Large Hadron Collider (LHC) aims to recreate the conditions which we assume to have existed immediately after the creation of the Universe. The beam energy and the design luminosity of the LHC have been chosen to enable the study at the TeV energy scale. A wide range of physics is potentially possible with the seven-fold increase in energy and hundred-fold increase in integrated luminosity over the previous hadron collider experiments. The detailed description of the LHC is given in the following sections.

2.1 Large Hadron Collider

The Large Hadron Collider [10] is the world's largest circular particle accelerating machine that collides protons and lead (Pb) beams at the highest controlled energies and instantaneous beam luminosities. The LHC is installed in a tunnel with a circumference of 26.7 km and 40-170 m underneath the Swiss-French border in Geneva, Switzerland. This tunnel was built earlier for housing the Large Electron Positron Collider (LEP).

The LHC tunnel has two adjacent beamlines in which protons or heavy ions are injected after being accelerated to desired energies. For escorting the hadronic beams inside the beamlines, 1200 superconducting dipole magnets provide 8.33 T magnetic field under ultra high vacuum conditions. The steering and focussing of the beams are achieved using 392 quadrupole magnets. There are four beam intersection points inside the tunnel, where the proton beams are made to collide. At these intersection points, four major detectors are installed to track the outcomes of collisions happening at the center of the each detector.

2.1.1 LHC Operations

The first batch of real pp collisions at the LHC were delivered on November, 2009 at $\sqrt{s}$ = 900 GeV. Soon after that the centre of mass energy was increased to 2.36 TeV, exceeding the centre of mass energy achieved at the Tevatron (1.96 TeV) [2]. The data collected at $\sqrt{s}$ = 900 GeV was inadequate to explore the potential of major advancements in our understanding of particle physics, but it was extensively used for calibrating various detectors at LHC along with the development of data acquisition chain through the re-discovery of known standard model (SM) signals. The first prolonged period of data taking began in March 2010 and continued till November 2010. The LHC operated at centre of mass energy of $\sqrt{s} = 7$ TeV and, delivered roughly 47 pb^{-1} of integrated luminosity to both the ATLAS and CMS experiments, out of which CMS commissioned 36 pb^{-1} of data for several physics analyses and to narrow down most of the existing limits on supersymmetric (SUSY) signatures [3, 4], as well as to reveal new characteristics of the QCD production at low energies [5]. In addition, the first proton-lead collisions were delivered at LHC in 2010, before the technical stop of the collider.

The major breakthroughs for the LHC were witnessed in the year 2011. LHC started taking data on 14th of March and delivered $\sim$ 6 fb^{-1} of data. 5.5 fb^{-1} of data was recorded by CMS and physics analyses were done for 5 fb^{-1}. In April 2011, LHC became the world's highest luminosity accelerator, with a peak luminosity of $4.67\times 10^{32}\ cm^{-2}s^{-1}$, surpassing the record of highest luminosity of $4.024\times\ 10^{32}\ cm^{-2}s^{-1}$ achieved by the Tevatron. In 2012, the beam-energy was increased to 4 TeV, to gain both in luminosity and in Higgs production cross-section. Figure 2.1 shows clearly the corresponding increase in integrated luminosity for the years 2010, 2011 and 2012 for proton-proton collisions. The total integrated luminosities delivered by the LHC as measured by the CMS for these three years of running are 44.2 pb^{-1}, 6.1 fb^{-1} and 23.3 fb^{-1} respectively. Figure 2.2 shows the corresponding increase in integrated luminosity during data-taking period of the year 2012. On 4 July 2012, the two main experiments at the LHC, ATLAS and CMS, independently reported the discovery of a new resonance with a mass of about 125 GeV/c^{2} [7, 8].

In early 2013, the LHC went through a long technical stop for the purpose of essential upgrades and repairs, referred to Phase I upgrade or LS1. LHC restarted again in 2015 and currently, it is operating at a center of mass energy of $\sqrt{s} = 13$ TeV before eventually reaching its design energy and luminosity. This upgrade

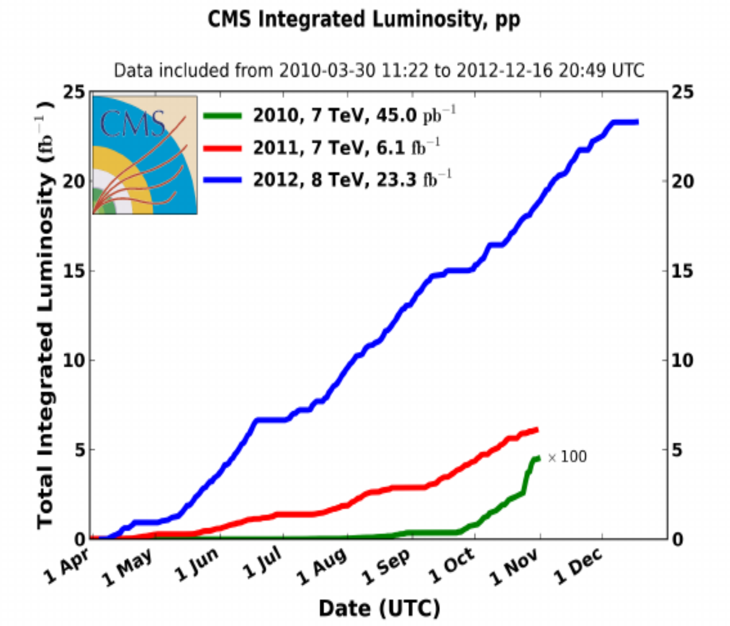

Figure 2.1: Summary of the integrated luminosity for the three different years of the data taking at the LHC. Plot reproduced from [20].

reduced the colliding bunch spacing of the protons down to 25 ns that is equal to the design value.

2.1.2 Accelerator Complex

- **LINAC2** (figure 2.3), 30m in length, is the introductory facility of the CERN accelerator complex, where the protons are accelerated to 50 MeV. The acceleration is preceded by stripping of protons from hydrogen gas by applying strong electric field. For reaching the desired energy, an array of alternating charged cylindrical conductors is used, which provides the acceleration when the field behind the proton yields a push and the field in front of the proton yields a pull.

- Four ringed **P**roton **S**ynchroton **B**ooster, 25m in length, is the next accelerator in the chain, which increases energy of protons to 1.4 GeV.

- Proton beams are then directed to **P**roton **S**ynchroton facility, a synchroton

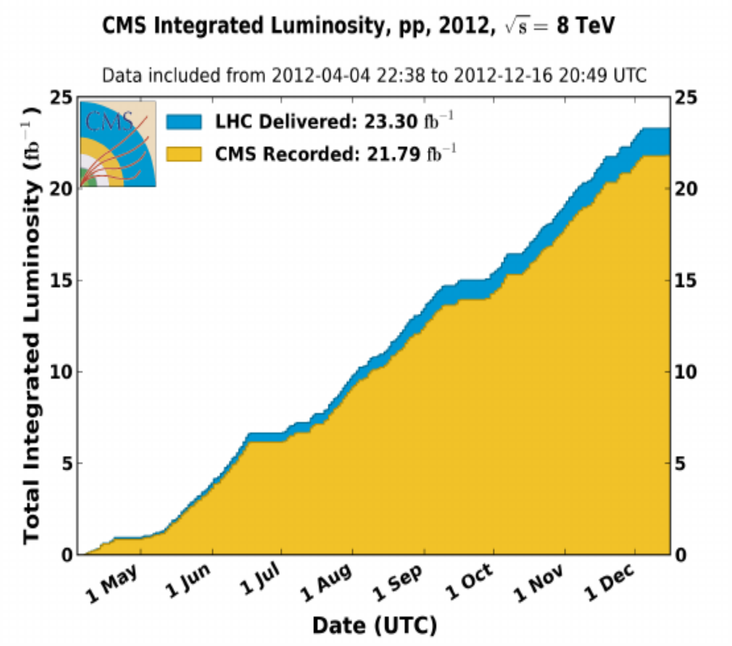

Figure 2.2: Delivered versus recorded luminosity for proton-proton collisions in CMS at a center of mass energy of 8 TeV during 2012. Plot source : https://twiki.cern.ch/twiki/bin/view/CMSPublic/LumiPublicResults.

ring with a circumference of 628 m. The PS facility accelerates the injected beams to 25 GeV.

- **S**uper **P**roton **S**ynchroton is fourth in the chain and is the second largest accelerator at CERN. A network of 1317 conventional magnets and 744 dipoles, accelerates the proton beams to 450 GeV, before directing them towards the LHC ring.

The proton acceleration process gets completed in 16 minutes, after which they are injected into the two separate vacuum filled beam pipes. Each proton beam is further accelerated to the desired energy, by eight superconducting radiofrequency cavities within the LHC ring. The network of 1232 superconducting Niobium Titanium (NbTi) dipole magnets is used to steer the proton beams, by creating a magnetic field of 8.3 Tesla. To keep the beams focused, 392 quadrupole magnets are used, which control the beam to micrometer(μm)dimension. Higher-pole magnets (sextupole, decapole) magnets are used to correct for small imperfections in the magnetic field at the extremities of the dipoles. The entire magnetic system is kept at -271.3 °C with 96 tonnes of liquid helium.

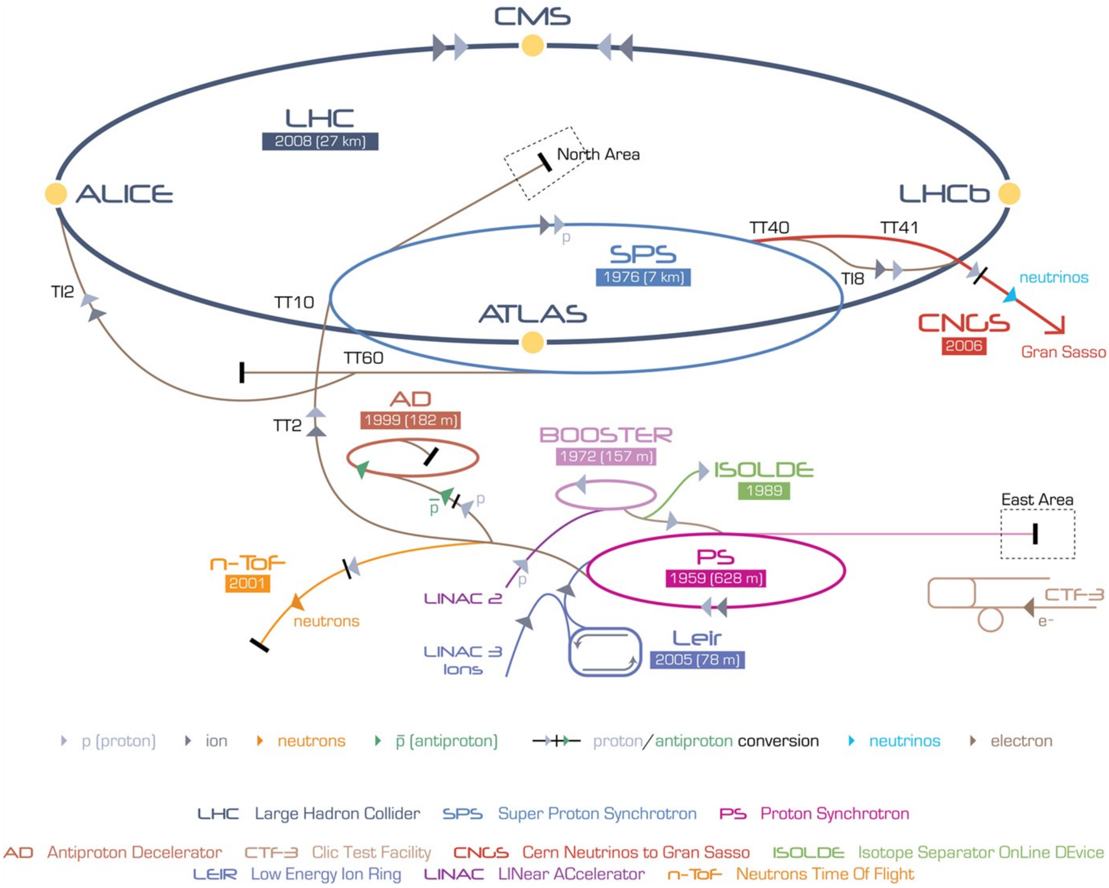

Figure 2.3: Schematic representation of CERN accelerator complex. Figure source : http://www.stfc.ac.uk/research/particle-physics-and-particle-astrophysics/large-hadron-collider/cern-accelerator-complex.

2.1.3 Machine Parameters

2.1.3.1 Luminosity

The luminosity, $\mathcal{L}$ is an important parameter to characterize the performance of a collider. It measures the ability of a collider to produce the required number of interactions. It is the proportionality factor between the event rate dN/dt and the cross-section of the observed event σ:

$$\mathrm{dN/dt} = \mathcal{L}\sigma \tag{1}$$

In order to compute the instantaneous luminosity $\mathcal{L}$ for two colliding bunched beams, several parameters have to be taken into account. The density distribution of each beam in the transverse and longitudinal planes along with the longitudinal position of each crossing beam with time has to be considered. If two bunches containing N_1 and N_2 particles collide with frequency f, then :

$$\mathcal{L} = f\tfrac{N_1 N_2}{4\pi\sigma_x\sigma_y}\mathcal{F}(\theta) \tag{2}$$

where $\mathcal{F}(\theta)$ is luminosity reduction factor due to the crossing angle θ and is 0.85 for LHC, σ_x, σ_y are the standard deviations of beam profile in x and y directions, defined as : $\sigma_{x,y} = \epsilon_{x,y}\ \beta_{x,y}$ typically measured by Van Der Meer scan method, developed for ISR (Intersecting Storage Rings). According to Van Der Meer method, it is possible to measure the effective height h_e of the colliding ISR beams by observing the counting rate R in a suitable monitor system while sweeping the two beams vertically through each other. h_e is equal to the area under the curve defined by the evolution of the counting rates divided by its ordinate for zero transverse displacement. The underlying assumption of this method is that the beam density functions are uncorrelated such that it is possible to factorize the 2D transverse density function into two independent functions of x and y. The values of $\sigma_x, \sigma_y = 17$ μm , the no. of particles per bunch (N_1,N_2) are 10^{11} in LHC. The frequency of revolution f is given by :

$$f = \text{c/bunch spacing} = 3 \text{ x } 10^8/7.5 \text{ (in m)} = 40 \text{ MHz} = 1/(25 \text{ nsec}) \tag{3}$$

Using the above values in (2), $\mathcal{L}$ at nominal LHC energy of 14 TeV is calculated as :

$$\mathcal{L} = \tfrac{(10^9/25)(10^{11})^2}{4\pi(17\text{x}10^{-4})^2\text{cm}^2\text{sec}} \text{ x } 0.85 \approx 10^{34}\text{cm}^{-2}\text{sec}^{-1} \tag{4}$$

The relative precision of the luminosity calibration at LHC for $\sqrt{s} = 8$ TeV, was calculated as 1.47% using Van Der Meer scan method and the overall error on the calibration is dominated by the uncertainty from intensity measurements.

The integral of the delivered luminosity over time is called integrated luminosity. The integral is taken over the sensitive time, i.e., excluding possible dead time of the LHC. It is a measurement of the collected data size, and it is an important value to characterize the performance of an accelerator. It is defined as :

$$\mathrm{L} = \int \mathcal{L} dt$$

Usually, L is expressed in inverse of cross section (i.e. 1/nb or nb^{-1} - $\mathrm{nanobarn}^{-1}$; 1/pb or pb^{-1}- $\mathrm{picobarn}^{-1}$; 1/fb or $1\mathrm{fb}^{-1}$ - $\mathrm{femtobarn}^{-1}$). For instance, if LHC had an average luminosity of $\sim 0.85\times10^{34}\mathrm{cm}^{-2}\mathrm{sec}^{-1}$, the integrated luminosity over an hour will be :

$$\mathrm{L} = (0.85\times10^{34})\times\ 60\times60\ \mathrm{cm}^{-2} = 30.6\ \times10^{36}\ \mathrm{cm}^{-2} = 30.6\ \mathrm{pb}^{-1}.$$

In CMS, the luminosity measurement is done using signals from its two subdetectors : (i) the forward hadronic calorimeter (HF), and (ii) the silicon pixel detector. The online measurement of luminosity is performed using HF which is capable of estimating the luminosity per bunch, whereas, the offline measurement is done using the silicon pixel detector which is characterized by very low occupancy and excellent stability over time.

For online measurement of instantaneous luminosity, “zero counting” method is used, in which the average fraction of empty Hadron Forward (HF) towers is used to infer the mean number of interactions per bunch crossing. For detection of the signal from towers Photo Multiplier Tubes (PMTs) were used. As a result of gain changes in the PMTs, the HF luminosity measurement was affected due to time dependent changes. In addition, the detector response has been proved to be non-linear with pileup in the luminosity range of the 2012 LHC run. These two effects together make the usage of HF difficult to measure the luminosity with a high accuracy.

The offline luminosity calculation is based on the Pixel cluster counting (PCC) method. A cluster is a group of pixels with signal higher than the threshold and associated with one particle hit. The number of pixels is about 7×10^7, which means that the probability of a given pixel being hit by two different tracks from the same bunch crossing is exceedingly small. The high fraction of fully live channels, which minimizes variance in detector acceptance, and low occupancy at high event rate, which means count rates are linear with event rate, make it especially suited for use as a luminometer. The pixel tracker can only operate in stable running conditions, which means it cannot provide an online luminosity measurement. However, it is stable and precise and therefore used as the reference luminometer for CMS.

Figure 2.2 shows the delivered and recorded luminosity for the CMS during 2012 data taking period, at an instantaneous luminosity of $7.7\times10^{33} cm^{-2}s^{-1}$. The luminosity by the LHC is referred as delivered, whereas, the recorded luminosity includes only the luminosity actually logged by a detector, such as, CMS. Ideally, the delivered and recorded luminosity should be the identical, but due to various reasons, for instance the absence of one or more sub-detectors during data taking period or because the data acquisition chain of CMS being busy, the CMS detector is unable to take data and these two values are different.

2.1.3.2 Pileup

At high luminosity, the probability that one single bunch crossing producing several independent events is non-negligible. These additional interactions occur during each beam crossing due to the very high instantaneous bunch-by-bunch collision luminosity. An example of one such event recorded by CMS is given in figure 2.4 for 2012 data taking period, where, for one bunch crossing, 72 vertices are reconstructed for a single event. These events are called pileup events, or average number of events per crossing, and are given by :

$$<N_p> = \sigma_{inel} \cdot \mathcal{L} \cdot \tau_b \tag{5}$$

In convenient units,

$$<N_p> = \frac{\sigma_{inel}}{(1barn)} \cdot \frac{\mathcal{L}}{(10^{33}cm^{-2}s^{-1})} \cdot \frac{\tau_b}{(1ns)} \tag{6}$$

where, σ_{inel} is the inelastic pp cross section, $\mathcal{L}$ is the instantaneous luminosity and τ_b is the bunch spacing. The typical values of LHC at $\sqrt{s}$ = 8 TeV, $\mathcal{L}$ = 0.75x$10^{34}cm^{-2}s^{-1}$, σ_{inel} = 71.5 mb and τ_b = 50 ns, hence eq.(4) gives $<N_p>$ = 27. Similarly, at nominal LHC collision energy $\sqrt{s}$ = 14 TeV ,the inelastic pp cross section σ_{inel} is 76 mb, $\mathcal{L}$ = $10^{34}cm^{-2}s^{-1}$, and if we keep τ_b = 50 ns, then number of pileup events will be ∼38. However, keeping all other parameters fixed, if we reduce τ_b to 25 ns, then $<N_p>$ will be reduced to 19. Hence, during the Long shut down 1 (LS1) of the LHC, the sub detectors and the DAQ have been upgraded to improve their performance at the 25 ns bunch spacing. Figure 2.5 shows the estimate of the observed number of pileup interactions over the whole data taking period of 2012.

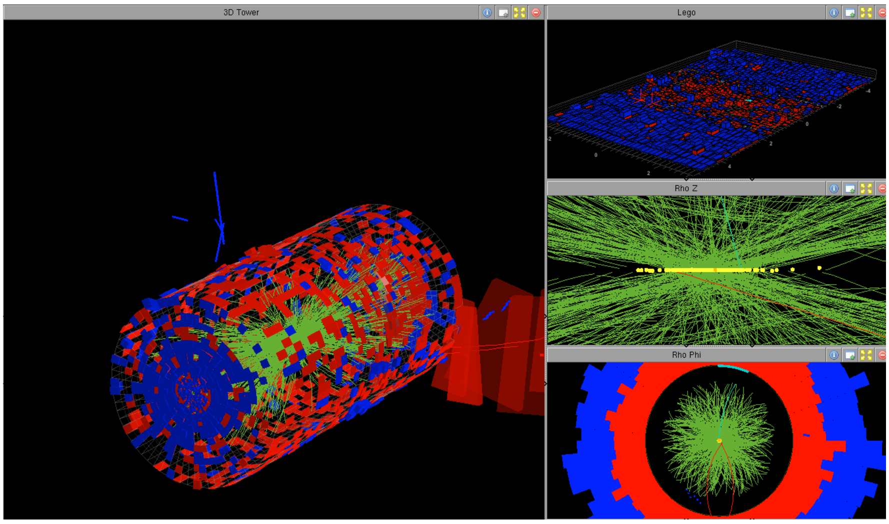

Figure 2.4: Event display showing 78 reconstructed vertices in one beam crossing, obtained from a special high pileup run. Figure source : https://cms.cern/tags/pile.

The pileup can be categorized as in-time and out-time pileup, depending on the time at which the additional energy enters the calorimeters :

- In-time : It refers to additional energy recorded in the calorimeters to multiple interactions within the same bunch crossing and is the largest source of pileup.
- Out-time : The energy left from last bunch crossing or the energy from later

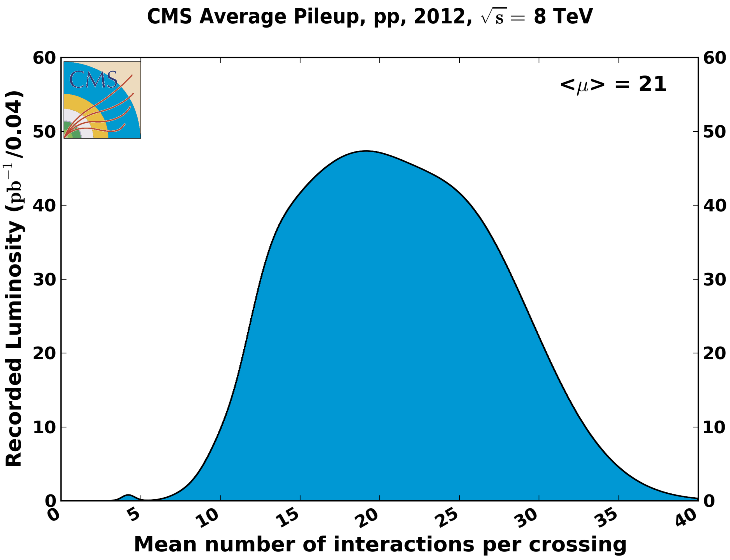

Figure 2.5: Mean number of interactions per bunch crossing at 8 TeV. Plot source : https://twiki.cern.ch/twiki/bin/view/CMSPublic/LumiPublicResults.

bunch crossing that is integrated with the current events energy, may also alter the object reconstruction.

The main parameters of the machine are listed in table 2.1.

2.2 Experiments at the LHC

The proton beams are made to collide at four interaction points along the LHC ring. At these collision points, four giant detectors are installed to record every possible outcome of the collision, as shown in figure 2.6 :

- **A Toroidal LHC ApparatuS (ATLAS)** [11] is one of the two general purpose 4π hermetic detectors at the LHC. The detector targets the validation of Standard Model and exploration of Beyond Standard Model regime. It is the largest detector at the LHC with a length of 45 m, height of 25 m and a diameter of 25 m. ATLAS uses wide range of sub detectors for particle detection : an inner Tracker, a Hadron and Electromagnetic calorimetry system

Parameter	**Designed**	**Achieved (2012)**
Proton Energy per beam [TeV]	7	4
Peak Luminosity [cm^2 s^1]	1.1x10^{34}	7.7x10^{33}
Number of bunches	2808	1374
Bunch spacing [ns]	25	50
Number of collisions per bunch crossing	19	40
Number of protons per bunch	1.15x10^{11}	1.6-1.7x10^{11}
β at interaction point (β^*)	0.55	0.6
Transverse normalized emittance [μm]	3.75	2.5
Beam current [A]	0.582	0.369
Beam size at IP [μm]	16.7	19

Table 2.1: Comparison between LHC design parameters and achieved parameters in 2012. Table source : http://cerncourier.com/cws/article/cern/54381.

and outer Muon detector. The experiment resides 100 m below ground near the main CERN site, close to the Meyrin village in Switzerland.

- **Compact Muon Solenoid (CMS)** [12] is another multipurpose hermetic detector at the LHC. The detector is located in an underground cavern at Cessy, France. The detailed description of the detector will follow in section 2.3.

- **A Large Ion Collider Experiment (ALICE)** [13] is adhered to explore the Quark Gluon Plasma and to track the particles produced during lead-lead (Pb-Pb) collisions. The ALICE detector has dimensions 26 m long, 16 m high and 16 m wide and weighs 10000 tons. The detector sits in a vast cavern 56 m below ground close to the village of St Genis-Pouilly in France, receiving beams from the LHC.

- **Large Hadron Collider beauty (LHCb)** [14] is single-sided spectrometer installed in the forward beam direction. The detector is built for resolving the mystery of imbalance between the matter and anti-matter in the universe and to study the decay modes of the B-mesons. The detector has dimensions of 21 m long, 10 m high and 13 m wide and weighs 5600 tonnes. The experiment sits in Ferney-Voltaire, France just over the border from Geneva.

- **Large Hadron Collider forward (LHCf)** [15] is the smallest experiment at the LHC and is housed near the ATLAS detector. This special detector aims to measure production cross section of the neutral particles (e.g. π^0,γ and neutrons) in the very forward region. These particles carry huge fraction of collision energy and hence play major role in understanding the particle shower development in the atmosphere by high-energy cosmic rays.

- **TOTal Elastic and diffractive cross section Measurement (TOTEM)** [16] is designed for elastic low angle scattering of protons and is installed on the both sides of the CMS detector, close to the beam axis. It targets the precise measurement of the proton-proton interaction cross section in the very forward direction of the LHC experiment.

- **Monopole and Exotics Detector at the LHC (MoEDAL)** [17] shares the intersection point with LHCb detector. It is built for exploring the signatures of magnetic monopoles and massive pseudo-stable charged particles.

2.3 Compact Muon Solenoid

The CMS is a hermetic, multi-purpose detector located in an underground cavern at Cessy, France. The main volume of CMS detector is a multi-layered cylinder, 21.6 m long and 14.6 m in diameter, weighing around 14,000 tonnes. It consists of several sub-detectors, arranged in an onion-like structure around the beam interaction point, in order to identify and to measure the properties of different particle types produced in the collisions. The collision products interact with the various sub-detectors, leaving behind charge and energy deposits that are subsequently readout and algorithmically combined to reconstruct a comprehensive picture of the original collision. The striking feature of the detector is a giant, superconducting solenoid magnet, with a diameter of 6 m and length of 13 m, that provides a uniform, 3.8 T, axial magnetic field. The strong magnetic field bends the trajectories of the

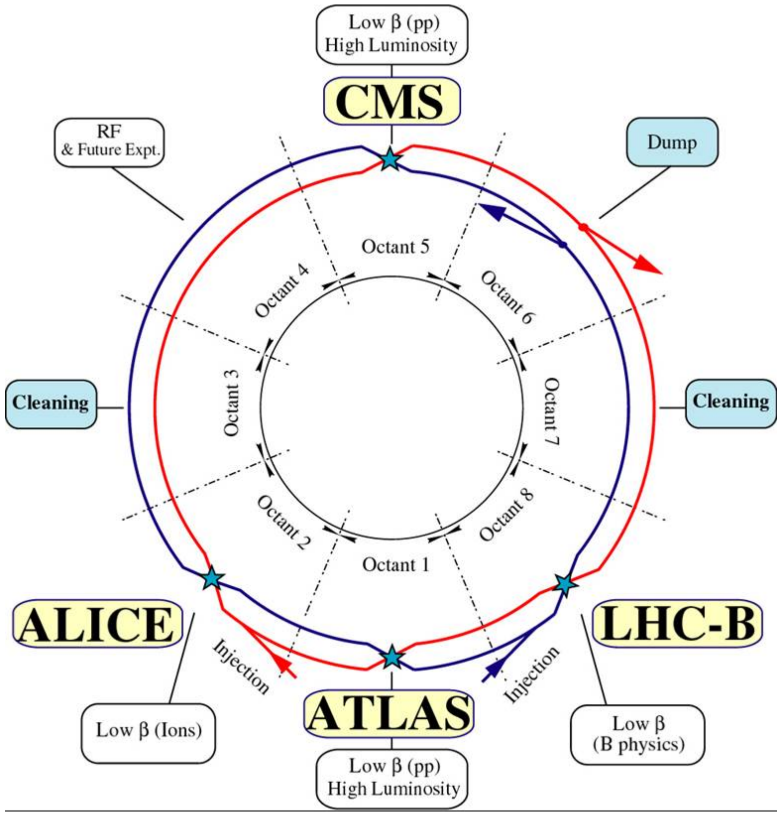

Figure 2.6: Schematic view of the LHC ring, divided into eight octant arcs with four crossings housing the ALICE, ATLAS, LHCb and CMS detectors. Figure source : https://lhc-machine-outreach.web.cern.ch/lhc-machine-outreach/lhc_in_pictures.html

charged particles, allowing precise measurement of their momenta. The schematic illustration of CMS detector is shown in figure 2.7.

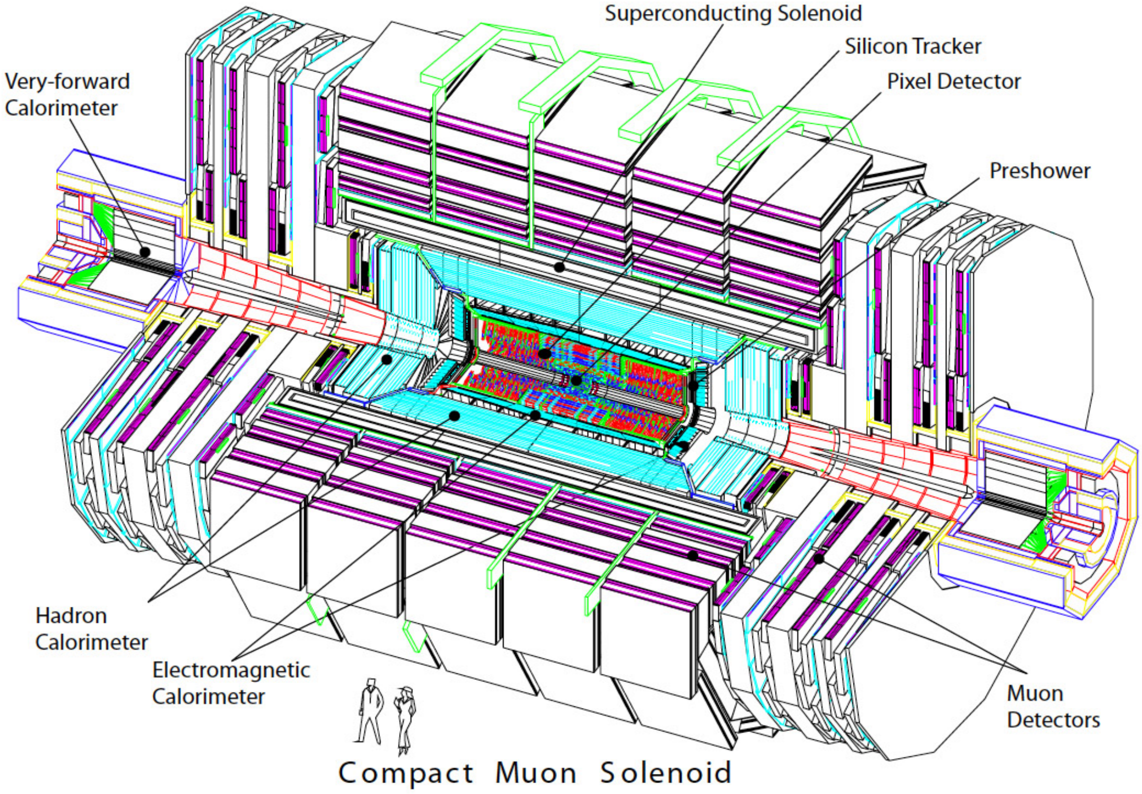

Figure 2.7: Layout of Compact Muon Solenoid detector at CERN. Figure source : http://cms.ciemat.es/alignment.

The peculiar features of the CMS detector are :

- Robust tracking system with the best charged-particle momentum measurement and reconstruction efficiency.
- Efficient triggering and offline tagging of top quarks and b-jets, which is achieved by positioning pixel detectors close to interaction region.
- An excellent electromagnetic calorimeter with good energy resolution and wide geometric coverage. It has good diphoton, dielectron mass resolution ($\approx 1\%$ at 100GeV) and excellent electron, photon isolation with efficient rejection of π^0's.

- Good muon identification and momentum resolution, covering a vast range of angles and energy ranges. It has the capability of measuring the muon charge with p_T upto 1 TeV.
- Hadronic calorimeters are hermetic with large geometric coverage to ensure good dijet mass resolution and missing transverse energy measurement.

2.3.1 CMS Co-ordinate System

At the CMS detector, the interaction point of two counter-rotating proton beams is chosen as the centre of coordinate system. In a right handed Cartesian coordinate system, the x-axis is pointed radially to the detector center, the y-axis is pointed perpendicular to the LHC plane and and the z-axis is pointed along the beam direction. The z-plane along the beam direction is referred to as longitudinal plane and the x-y plane, orthogonal to the beam line, is called transverse plane. More often, CMS uses cylindrical co-ordinates, defined by azimuthal angle ϕ, radial distance r and the z coordinate, or spherical co-ordinates, defined by an azimuthal angle ϕ, radial distance ρ and polar angle θ. ϕ is measured from the x-axis in the x-y and θ is measured from +z axis.

The longitudinal momenta of the scattered particles at hadron colliders suffer from large and variable uncertainties. This is due to the fact that initial momentum in the -z direction of the interacting parton of incident protons is unknown. Hence, the kinematic variables defined in the transverse plane are more used for particle definition. Moreover in hadron collisions, the most suitable event description is provided by using quantities which are either invariant or transform simply under longitudinal boosts, for instance, rapidity (y) and transverse momentum (p_T). y and p_T are defined as :

$$\mathrm{p_T} = \sqrt{\mathrm{p_x}^2 + \mathrm{p_y}^2} \tag{2.1}$$

and,

$$y = \frac{1}{2}\ln(\frac{\mathrm{E} + \mathrm{p_z}}{\mathrm{E} - \mathrm{p_z}}) \tag{2.2}$$

where,

$$E = \sqrt{p^2 + m_0^2} \tag{2.3}$$

$$p_z = p\cos\theta \tag{2.4}$$

In equations 2.3 and 2.4, m_0, E, p_z and p corresponds to rest mass, energy, longitudinal momentum and total momentum of the scattered particle, respectively.

To skip the energy dependence, pseudorapidity (η) is used, defined as :

$$\eta = -\ln(\tan\frac{\theta}{2}) \tag{2.5}$$

The physical relation between η and θ is depicted in figure 2.8. The difference between rapidities, i.e., $\Delta y = y_1$ - y_2 is constant under Lorentz transformation and hence, in CMS experiment, y is preferred over θ as particle production is mostly flat as a function of rapidity. For relativistic particles, $p^2 >> m_0^2$, Equation 2.3 gives :

$$E = \sqrt{p^2 + m_0^2} = \sqrt{p_T^2 + p_L^2 + m_0^2} = \sqrt{p_T^2 + p_L^2} = p \tag{2.6}$$

Using the relation E=p in equation 2.2 gives :

$$y \sim \frac{1}{2}\ln(\frac{p + p_z}{p - p_z}) = \frac{1}{2}\ln(\frac{1 + \cos\theta}{1 - \cos\theta}) = -\ln(\tan\frac{\theta}{2}) = \eta \tag{2.7}$$

Since, pseudorapidity is equal to the rapidity in the limit m<<p, hence η approximates y in case of light particles. For jets, the mass is not expected to be small and therefore the rapidity is a more convenient choice.

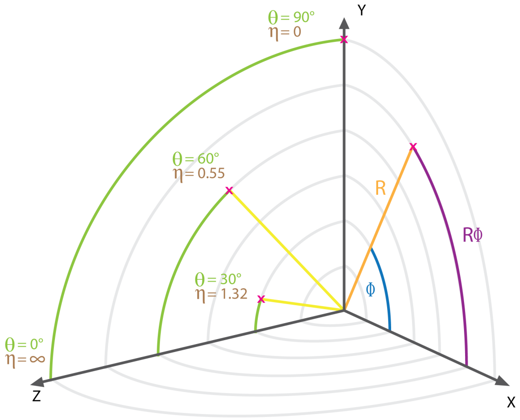

Figure 2.8: Pseudorapidity η and azimuthal angle ϕ are used for tracking particles inside detector. Figure reproduced from [9].

2.4 CMS sub-detectors

In order to identify and to measure different particle types produced in the collisions, CMS is a composite system of different sub-detectors. The Tracker is the innermost part and measures the momenta of charged particles by tracing their trajectories in the magnetic field. Outside the tracking system, the calorimeter is placed for energy measurement. Both the tracking system and the calorimeter are confined by the solenoid magnet. The outer most part of the detector, the muon system, measures the momentum of muons and identifies them. The detailed description of each CMS sub-detector is given in the following sections :

2.4.1 Tracker

The silicon tracker [18] (figure 2.9) is the innermost layer of the CMS detector and is close to the beam interaction point. It serves the purpose of measuring trajectories and momenta of the produced charged particles, with high precision. The tracker is 5.8 m long, has radius of 5 m and extends upto $\eta \leq \pm 2.5$. For muons with p_T=100 GeV, $|\eta|$ <1.4, tracker has momentum resolution of 2.8%, which further reduces for muons with $p_T >$ 100 GeV/c, due to smaller curvature of the tracking system.

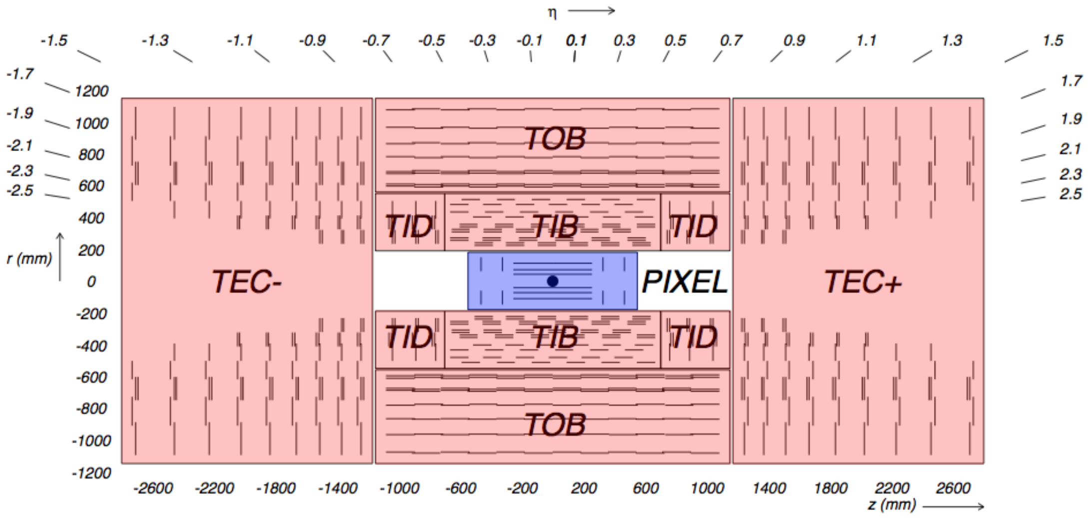

Figure 2.9: Detailed view of CMS tracker in the r-z plane, showing the location of pixel and silicon strip detectors. Figure reproduced from [9].

The particle flux varies inversely as square of distance from the interaction point. Hence, silicon is chosen to be tracking material, due to its high granularity and fast response. The tracking system consists of two subdetectors : the pixel detector and silicon strip tracker, which work as ionization detectors. When a charged particle passes through the pixel tracker or the strip detector, the electrons gets ejected from the silicon atoms, creating electron-hole pairs. Each pixel uses an electric current to collect these charges on the surface as a small electric signal or "hit". The tracks of charged particles are reconstructed by combining hits from various subdetectors. In the case of the strip detector, a hit is considered to be found if it is on the same module in which the hit was expected to be observed. In the case of the pixel detector, the hit must be found within a 500 μm radius of the expected intersection point. In both cases, the only particle trajectories that are considered are those which have reconstructed hits on adjacent layers. The charged hadrons reconstruction facilitates the application of relative isolation requirements for rejection of "fake" leptons or photons. The trajectories of the charged particles are curved due to the strong magnetic field and the radius of curvature for each particle is used to measure its momentum and charge.

2.4.1.1 The Pixel Tracker

The silicon pixel detector is installed within 10 cm of the CMS interaction point, covering η range of ± 2.5. 1440 pixel modules with 65 million pixels embedded in the pixel tracker provides excellent tagging of primary and secondary vertex. The vertex tagging information is useful in identification of b-quark jets. For three-dimensional measurement of the hits, the silicon sensors with pixel dimensions of 100 x 150 μm^2 are arranged in barrel (768 pixel modules) and endcap (672 pixel modules) regions. The barrel region (BPiX) has three cylindrical layers (53 cm long) at radius of 4.4 cm, 7.3 cm, and 10.2 cm respectively with a total of 48 million pixels. The endcap region (FPiX) has two disks on each side, each extending from 6 to 15 cm in radius, located at ±35.5 cm and ±48.5 cm from the nominal vertex position. The endcap region has 18 million pixels in total to accomplish a spatial resolution of 10 μm and in z direction, 20-40 μm in r-ϕ direction.

2.4.1.2 Silicon Strip Tracker

The silicon strip detector is housed beyond the pixel detector, and covers the radial region from 10 to 110 cm along beam axis. The sub-detector has ten layers in barrel and nine discs in endcap region. 9.3 million silicon strips covering a total area of 198 cm^2 are used as ionization detectors. Due to increased distance from the interaction point, the particle flux and occupancy is comparatively low, hence, silicon strip sensors are used instead of pixels. On the basis of strip modules positions, the subsystem is further classified into four regions : Tracker Inner Barrel (TIB), Tracker Inner Disk (TID), Tracker Outer Barrel (TOB) and Tracker Endcaps (TEC).

The TIB and TID extend upto 65 cm on both sides of vertex position and have four layers in barrel and three discs in endcap region. The layers of TIB and TID are made of silicon sensors, with 320 μm thickness and variable strip pitch, ranging from 80-120 μm. Each barrel layer is 140 cm long and these layers have diameters of 510 mm, 678 mm, 837 mm and 996 mm respectively. The single point resolution of TIB in r-ϕ region is 16-28 μm and 230 μm in z plane. TOB has an outer radius of 116 cm and covers the TIB and TID.

The TECs extend upto the region of 22.5 cm < r < 113.5 cm and 124 cm $<|z|<$ 282 cm. Each side of TECs (TEC+ and TEC-) consists of 9 disks, out of which two disks serve as front and back terminator and seven consists of silicon micro strip sensors. Thus, TEC provides 9 measurements per particle trajectory.

2.4.2 Electron Calorimeter

The Electromagnetic Calorimeter (ECAL) [19] is a hermetic homogeneous calorimeter which quantifies the electron and photon energies, upto $|\eta| \leq 3.0$ (figure 2.10). It also measures any partial energy deposits by the charged particles while traversing the calorimeter. ECAL has been designed to well elevate the discovery of Higgs

(M_H <150 GeV/c^2), decaying into photon pair. A total of 61,200 lead tungstate ($PbWO_4$) crystals are installed in the barrel region ($|\eta| < 1.479$) and 7,324 crystals are mounted in endcap region ($1.479 < |\eta| \leq 3.0$).

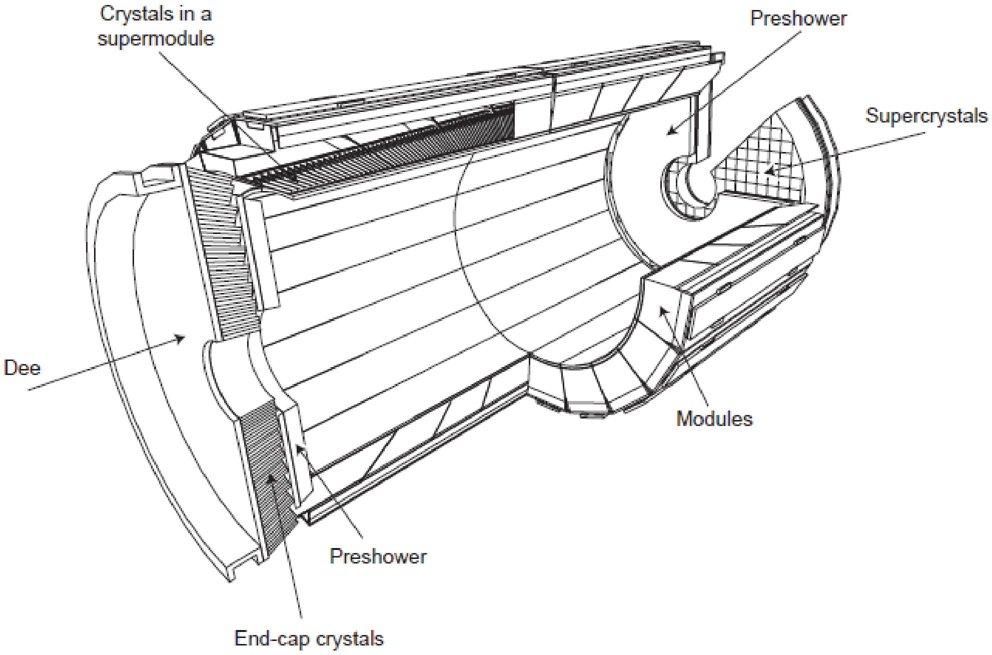

Figure 2.10: Transverse slice of the ECAL showing the position of its various components. Figure source : https://www.researchgate.net/figure/258309853_fig1_figure-1-The-CMS-Electromagnetic-Calorimeter-ECAL-The-barrel-section-comprises-36.

The electron and photons while traversing through ECAL, interact with $PbWO_4$ crystals and build electromagnetic showers via pair production and bremsstrahlung. These electromagnetic showers produce green-blue light, which travels through the entire transparent crystal before reaching the readout modules. Avalanche photodiodes (APD) are the light readout devices in the barrel region, while in the endcap Vacuum Phototriodes (VPT) are used. At the operating temperature of -18°C, both the photodetectors measure ≈4.5 photoelectrons, for each MeV energy deposition in the crystals.

Lead tungstate was chosen as ECAL material, as it has following advantages :

- It has short radiation length (X_0=0.89 cm) and high density (8.28 g/cm^3). Each crystal in barrel(endcap) has the front area of 2.2 x 2.2 cm^2 (2.9 x 2.9

cm^2) and is 23 cm (22 cm) long. The small size of the $PbWO_4$ crystal permits the compact dimensions of the calorimeter, which fits well within the solenoid magnet.

- $PbWO_4$ has very small Molière radius, which signifies better position resolution and well separated electromagnetic showers.
- The scintillation decay time is short, with 80% of light emitting in less than 25 ns which is the the design bunch-spacing of the LHC.
- $PbWO_4$ is radiation resistant, ensuring lesser signal losses, event at high luminosities.

ECAL uses PreShower (PS) detector for electron identification against the background of minimum-ionizing particles (MIP), and to improve the position resolution of electrons and photons in the calorimeter. It is installed infront of the endcap, in the detector region $1.653 < |\eta| < 2.6$. The PS also rectifies the photon identification, provides precise spatial measurement of electrons and photons and enhances background rejection rate in the forward region. It is composed of 1,072 silicon strip sensors interleaved with lead radiators. The energy of electromagnetic showers formed in the radiators, is measured using the strip sensors.

2.4.2.1 Energy Resolution in the Electromagnetic Calorimeter

For photons with energies less than 500 GeV, the ECAL energy resolution $\sigma(E)$ is given as :

$$(\frac{\sigma}{E})^2 = (\frac{S}{E})^2 + (\frac{N}{E})^2 + \mathrm{C}^2$$

where, first term represents the stochastic contributions, due to shower containment and preshower measuremental errors. The second term represents the contribution coming from the various noise sources,e.g. electronics, digitization etc. The constant term incorporates the effect of non-uniformity of longitudinal light collection, energy leakage from the scintillators and various inter-calibration errors. The terms have been calculated using the test beam data at $\sqrt{s} = 7$ TeV and are approximately 2.8%, 12%, and 0.3% respectively, for electrons with energy between 20 MeV and 240 GeV. In the CMS, the real energy resolution is measured using known resonances, Z$\rightarrow$e$^{+}e^{-}$ and H$\rightarrow \gamma\gamma$ for both electrons and photons. At $\sqrt{s} = 7$ TeV using 60 GeV electrons, the ECAL resolution was measured to be 1.1% in barrel and 5% in the forward region.

2.4.3 Hadron Calorimeter

The next calorimeter in succession is the hermetic Hadronic Calorimeter (HCAL) [6], with the angular coverage upto $|\eta| \leq 3.0$. It allows the precise energy and position measurement of the hadrons produced in the collisions. The calorimeter distinguishes all the products of hadron decay (i.e. pions and nucleons), hence any energy imbalance would manifest the existence of neutrinos. The forward hadronic calorimeter (HF) extends the HCAL coverage upto $|\eta| \leq 5.0$ with enhanced hermeticity, to ensure precise measurement of missing transverse energy ($\not{E}_T$). Due to the size constraints, two parts of the HCAL lie inside the solenoid and HF is located beyond the magnet. The HCAL is divided into four regions, on the basis of η : HCAL Barrel (HB) upto $|\eta| \leq 1.3$, HCAL Endcap (HE) covering the range $1.3 < |\eta| < 3.0$, HCAL Outer (HO) for $0 < |\eta| < 1.2$ and HCAL Forward extending from $|\eta| < 3.0$ to $|\eta| < 5.0$. Figure 2.11 shows the quarter slice of the HCAL, where the color indicates the optical grouping of scintillator layers into different longitudinal readouts.

The HCAL is built using brass as absorber material, since it has short interaction length. The barrel and endcap regions are sampling calorimeters, which use brass as the absorber and plastic scintillator as the active material. The neutral pions, produced due to hadron interaction with absorber, decay instantly into

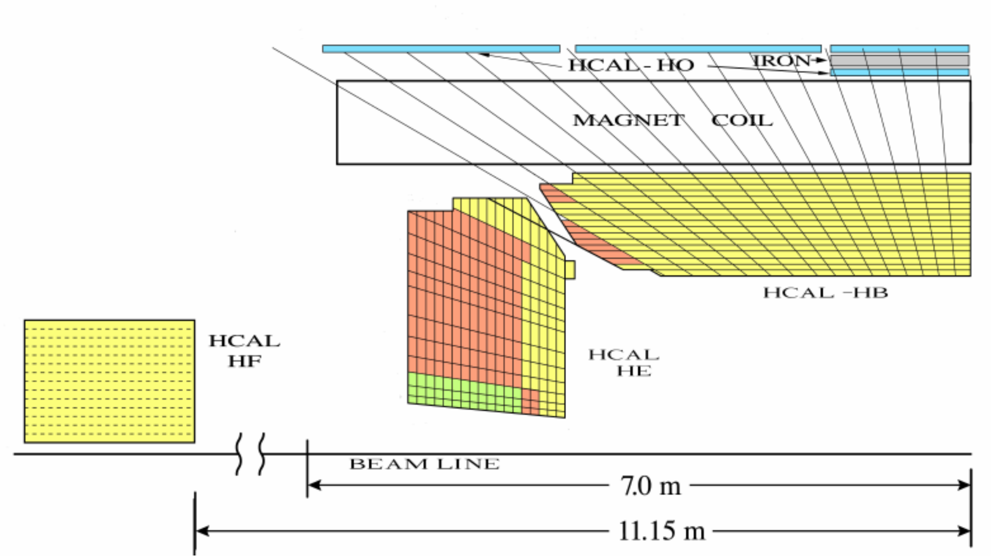

Figure 2.11: Quarter view of the CMS hadron calorimeter. Figure source : https://www.researchgate.net/figure/236896164_fig1_Figure-1-Quarter-view-of-the-CMS-hadron-calorimeter-The-shading-indicates-the-optical.

photons, which further give rise to electromagnetic showers. On the other hand, the charged pions while traversing through the absorber material produce hadronic showers. The showers emit blue-violet light, when passing through the alternating layers of active scintillators and are readout using Wavelength Shifting Fibres (WLS). The WLS shift the blue-violet light into the green region of the spectrum. Next, the clear optical fibres, spliced to WLS, channel this light to the readout boxes and the Photodetectors convert the optical signal into the electrical signal.

The charged pions are used to measure the resolution of the calorimeter. However, the fluctuations in sampling and signal leakage deteriorate the HCAL resolution, which is given by :

$$(\frac{\sigma}{E})^2 = (\frac{S}{\sqrt{E}})^2 + \mathrm{C}^2$$

where, S is the stochastic term and C is a constant which includes contributions from non-uniformity of the calorimeter, mis-calibration and electronic noise . The resolution was evaluated using charged pions of 20-300 GeV. For HB, S = 84.7%, C = 7.4% and for combined HB and HO system, the term C improves to 6.6%. Similarly, for HF, S = 279.9% and C = 11.4% and for HE, S = 153% and C =

6.3% [6].

2.4.3.1 Hadron Barrel

The Hadron Barrel extends radially between $|1.81|<r<|2.95|$ meters and has 16 absorbing layers along with plastic scintillators. To ensure structural strength, the innermost and outermost layers of HB are made of stainless steel and for rest 14 layers, brass (70% copper, 30% zinc) is used as absorber material. The space constraints of the CMS detector limits the thickness of the sampling calorimeter.

The barrel region is divided into two parts : (HB^+ and HB^-) and each part has 18 identical 20° wedges in azimuthal sectors (ϕ). The front steel absorber layer is 40 mm thick and last layer has thickness of 75 mm , with radiation length (X_0) of 1.68 cm and a nuclear interaction length, λ_0 of 16.8 cm. The absorber itself consists of a 40 mm thick front steel plate, followed first by eight 50.5 mm thick brass plates, and then six 56.5 mm thick brass plates, with a final 75 mm thick steel back plate.

For both HB^+ and HB^-, the absorber layer is followed first by eight 50.5 mm thick brass plates, and then six 56.5 mm thick brass plates, with $X_0 = 1.49$ cm, $\lambda_0 = 16.42$ cm. The plastic scintillators are mounted on 70,000 megatiles in between the absorber material, arranged radially over 16 η divisions and 36 ϕ divisions. Each scintillator has 0.087 x 0.087 η-ϕ coverage.

2.4.3.2 Hadron Outer

At low η range, the thickness of HB is relatively thin due to size constraints. Hence, an additional layer of hadron calorimeter is installed outside the magnet, which uses magnetic bulk as absorber material and scintillator tiles as detectors. The Hadron Outer Calorimeter (HO) acts as tail catcher, by measuring the energies of the hadronic showers that leak out the barrel part of HCAL. HO is partitioned in z, into 5 rings and resides in first sensitive layer within the iron return yoke. The nominal z positions of the five rings are centered at -5.342 m, -2.686 m, 0, +2.686 m and +5.342 m respectively. The central ring, Ring 0 covers the $|\eta|$ range upto 0.35, Rings ± 1 cover the pseudorapidity range $0.35 < |\eta| < 0.87$ and Rings ± 2 cover the pseudorapidity range for $0.87 < |\eta| < 1.2$. Two layers of the scintillators are installed in the central ring, to increase the overall interaction length. The granularity of the scintillator tiles in the HO is the same as that in the HB and the tiles are arranged in such a way as to roughly map the layout of the HB tiles. This allows consistent clusters to be created throughout the subdetectors of the HCAL.

2.4.3.3 Hadron Endcap

The Hadronic Endcap (HE) overlays the HB to establish hermeticity and is mounted onto the iron yoke of muon endcap. The HE uses brass as absorber material, since it is mounted onto the iron yoke of muon endcap system and lies under the influence of the magnetic field. The brass plates are 79 mm thick with 9 mm gaps to accommodate the plastic scintillators. The gaps between the scintillators are painted with reflective material to prevent the emitted light from escaping the detector. Layer 0 of the HE measures the extended showers that originate in the dead material between the ECAL endcap and HE and other layers have multiple depths for precise re-calibration of individual HE towers to mitigate the impact of radiation damage. The granularity of HE in $\Delta\eta$ x $\Delta\phi$ is 0.087 x 0.087 for $1.2 < |\eta| < 1.6$ and it reduces to 0.17 x 0.17 at higher $|\eta|$ range.

2.4.3.4 Hadron Forward

The Hadron Forward (HF) is cylindrical steel structure with an outer radius of 130.0 cm and a cylindrical hole for the beampipe with a diameter of 25.0 cm. The front face of HF is located at distance of 11.1 m from the interaction point. At low pseudorapidity range, the HF towers granularity in η - ϕ plane is 0.175 x 0.175, which reduces to 0.175 x 0.35 at $|\eta| > 4.7$. The particle flux is more at high η region and almost 90% of the particles deposit their energy in the HF. For this reason, different technologies are implemented to ensure the radiation hardness of the HF. HF is used for identification and reconstruction of very forward jets and to improve the missing transverse energy (E_T^{miss}) measurement.

The HF uses steel as an absorber material having a depth of approximately $10\lambda_I$. Radiation-hard quartz fibres are embedded parallel to the z axis as active component, which are suited for operation in the high particle flux in the forward region. Charged shower particles generate Cherenkov light in the fibres, bundles of which are readout by a common photomultiplier.

Since the electrons, photons and hadrons all deposit their energy in the HF, hence it uses quartz fibres of two variable lengths. One set of fibres is spread over the entire HF length while the other set of fibres start at the depth of 22 cm from the detector's center. The signal is produced when charged shower particles above the Cherenkov threshold ($E \leq 190$ KeV for electrons) generate Cherenkov light, thereby rendering the HF mostly sensitive to the electromagnetic component of the shower.

2.4.4 Magnetic Coil

The CMS superconducting magnet [21] is built around 12.5 m long solenoidal Nb-Ti coil, with 6 m diameter and weighing 220 metric tons. It is designed to produce 4T magnetic field at operating temperature of 4 K. The magnet has three major components : the superconducting coil, the magnet yoke and the vacuum tank. The superconducting coil provides an axial magnetic field and the yoke returns the magnetic flux. The CMS tracking system and calorimeters are enclosed within the large magnet system and this improves the energy resolution of electrons and photons as well as the missing transverse energy.

The return yoke comprises 5 wheels in barrel, with 2 endcaps (3 disks in each endcap) on either side of barrel. The strong magnetic field permits the precise measurement of particle momentum upto $|\eta| < 2.4$ and reduces the pileup by restricting

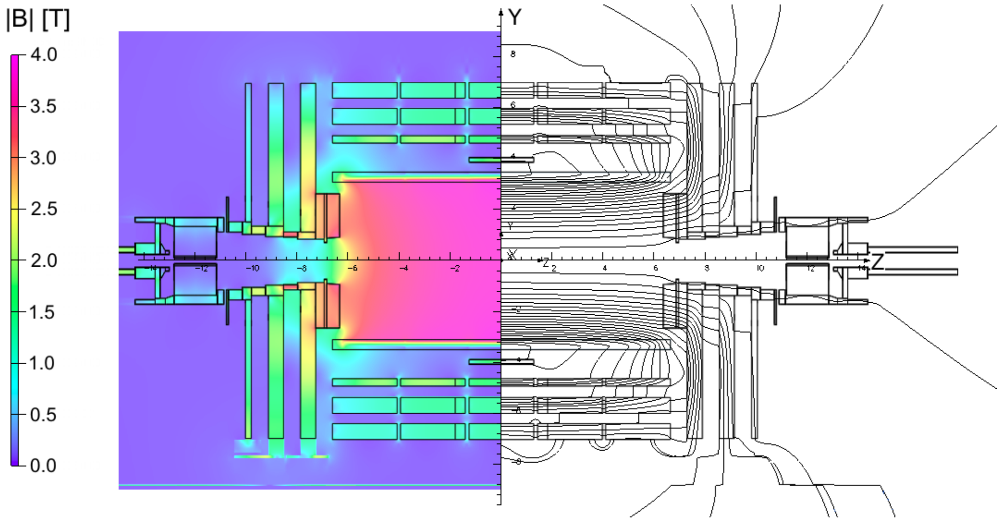

Figure 2.12: Field map of the CMS magnet system. Figure reproduced from [9].

the low momentum particles ($p_T < 0.75$ GeV/c) from reaching ECAL. For handling large current, Nb-Ti are the chosen materials for the solenoidal coil. The superconducting coil is housed in the vacuum tank for thermal insulation of the coil. All the barrel subdetectors are located in the inner cylinder of the vacuum tank. The field map of solenoidal magnet measured using cosmic rays is depicted in figure 2.12.

2.4.5 Muon Detectors

Muons leave their signatures very far from the interaction point and deposit ≈ 3 GeV of energy in the calorimeters. Hence, the muon detectors are placed outside the CMS magnet and in between the return yoke plates, as shown in figure 2.13. The muon system aims at good identification, momentum measurement and muon triggering. The muon system has three subsystems at different pseudorapidity ranges : Drift Tubes (DT) covers the central $|\eta|$ region ($|\eta| < 1.2$), Cathode Strip Chambers (CSC) are in the forward $|\eta|$ region ($0.8 < |\eta| < 2.4$) and Resistive Plate Chambers (RPCs) extend over $|\eta| > 2.1$.

2.4.5.1 Drift Tube Chambers

The Drift Tubes are installed in the barrel region of the muon detector along the interaction point, where the muon rate is relatively low along with uniform magnetic field. The DT detectors are tube like structures with anode wires placed between the cathode strips. A gaseous mixture of 85% Argon (Ar) and 15% Carbon dioxide (CO_2) is filled inside the DT tubes. The muon traversing through the tube, ionizes the gas mixture and resulting electric current is measured at the anode.

Four stations of DT chambers (MB1 to MB4) are interspersed within the return yoke to form concentric cylinders around the beam pipe. Eight chambers are separately installed in first three muon stations for azimuthal co-ordinate (in r-ϕ plane), and four chambers for longitudinal co-ordinate measurement. The detection wires of chambers are orthogonally positioned for measurements in both planes. Each DT chamber has the 100 μm position resolution in bending plane (r-ϕ plane),which increases to 150 μm in longitudinal plane. The overall muon direction resolution is $\approx$ 1 mrad.

2.4.5.2 Cathode Strip Chambers

In the endcap region, Cathode Strip Chambers are used for muon measurements. The muon flux is high in this region along with varying magnetic field. The CSCs have better signal response time than DT, are robust against the radiation effects and provide more precise measurements which are needed to muon triggering. A total of 468 CSCs of trapezoidal shape are installed in six layers of the muon endcap.

The CSC chambers are filled with 40% Ar, 50% CO and 10 % CF_4, latter has been added to inhibit polymerization of anode wires. Each anode wire in chamber is equipped with segmented and non-segmented cathode strips. The non-segmented strips measure the muon position in r - θ plane due to electric current produced by the gas ionization. The positive ions produced in this process get drifted towards the segmented cathode, positioned orthogonal to anode wires, and help to measure the r-ϕ co-ordinate of the muons. The CSCs have better position resolution than DTs, i.e. 75 - 150 μm in the bending plane, which increases to 200 μm in longitudinal plane.

2.4.5.3 Resistive Plate Chambers

For fast triggering of the muons, parallel plate gaseous detectors (RPCs) are installed in the muon barrel and endcap region. The response time of a typical RPCs is 1.26 ns which is way smaller than LHC bunch crossing of 25 ns. Hence, they can instantaneously associate a muon track with its bunch crossing time, irrespective of the high background rates in the endcap region. In the barrel region, six RPC stations are installed and three RPC stations are mounted in both the endcaps.

The RPC chambers are filled with 96.2% $C_2H_2F_4$, 3.5% iC_4H_{10}, and 0.3% SF_6 along with water vapors.

2.4.6 CMS Trigger and Data Acquisition System

A huge amount of data, at a rate of about 40 MHz, is produced during pp collisions within the CMS detector. However, due to performance limitations of the mass storage hardware, it is unfeasible to store all the information of collisions. Hence, the CMS detector uses a two-fold triggering system [23] to reduce the event rate to approximately 100 Hz, and to retain only potentially interesting events :

- Level-1 Trigger
- High Level Trigger

- **Level-1 Trigger** : The Level-1 (L1) trigger hinges on custom-made electronics and is situated in the service and experiment caverns of the detector. It is designed to scale down the event rate to 100 kHz, by using the information

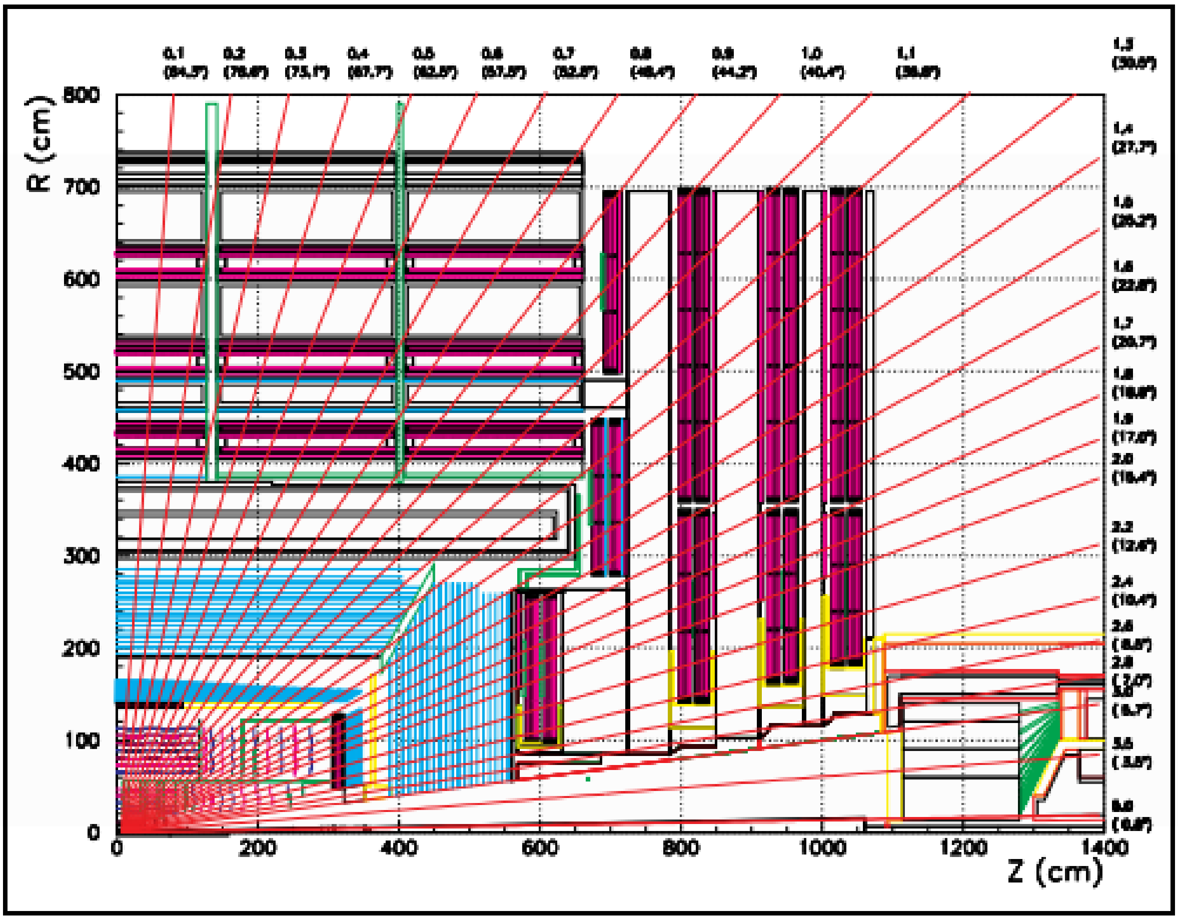

Figure 2.13: Layout of one quarter of the CMS muon system showing the location of the drift tube (DT), resistive plate chamber (RPC) and cathode strip chambers (CSC). Figure reproduced from [9].

collected in the calorimetry and muon systems. The L1 decision has to be swift, hence, event acceptance/rejection is accomplished within 3.2 μs. The event selection relies on the presence of Trigger Primitives Objects (TPO) such as electrons, photons, jets and muons above certain p_T threshold. The information of the L1 accepted events is saved in pipelines and passed to next level (HLT) for further processing. The architecture of the L1 Trigger is shown in figure 2.14.

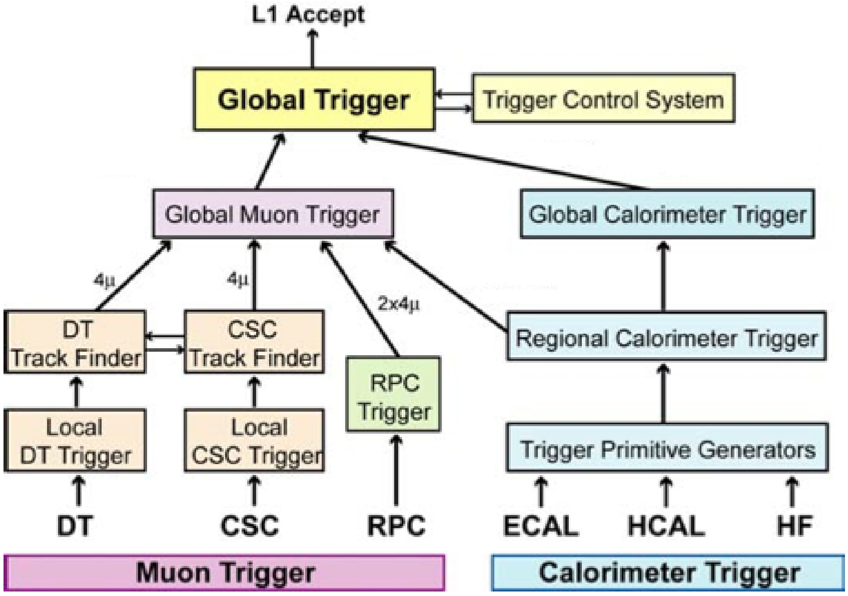

Figure 2.14: Detailed view of the CMS L1-trigger system. Figure reproduced from [9].

- **High Level Trigger** : High-Level Trigger (HLT), is designed for a further reduction of the rate down to 100 Hz. The HLT software contains more sophisticated algorithms which are very close to the ones applied in the offline analysis. The decision made at each stage of the trigger to keep or reject a specific interaction is based on the reconstruction and identification of the physics objects at the final state of that particular interaction. Because processes of physics interest, such as production and decay of rare particles like Higgs bosons, contain highly energetic objects, such as electrons, photons, muons and jets, various trigger streams are defined, each of which requires some configurable physics conditions. An interaction which fires at least one of the trigger streams is archived permanently and kept for the offline analysis.

The triggers with lower p_T threshold has high event selection rate and hence can saturate the data taking bandwidth. These trigger paths are throttled in a way, every N^{th} event to pass a trigger path is recorded, giving the trigger a prescale factor of N.
The CMS trigger system had excellent performance during the 2012 LHC run. The L1 Trigger system maintained rates up to 100 kHz with only 3% dead time. The HLT system maintained rates up to 1 kHz, utilizing only 200 ms on average to process events.

- **Data Acquisition and Storage** :After the online event selection by L1 trigger, the data from each sub-detector is then recorded by CMS Data Acquisition System (DAQ). The system consists of front-end drivers, the readout system and online event builder filter, as shown in figure 2.15. The prime responsibility of the DAQ system is to collect the data from each subdetector and process the information to reconstruct the complete event at a rate of 100 kHz.

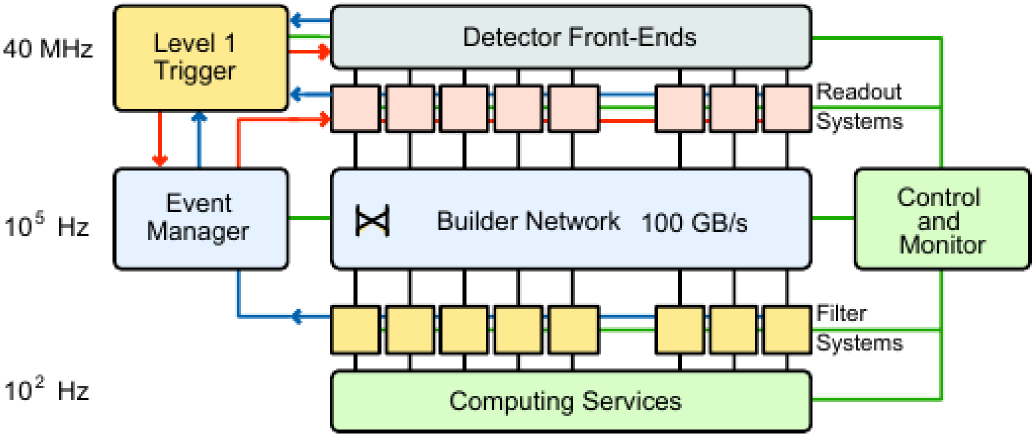

Figure 2.15: CMS Trigger and Data Acquisition System. Figure source : https://www.researchgate.net/figure/35216310_fig16_Figure-37-Overview-of-the-CMS-DAQ-system-From-ref-35.

The data from each subdetector is transferred via front end electronics to the Event Builders for complete event reconstruction. At the next stage, the events are filtered using the HLT software, which consists of dedicated trigger menus for event filtering. Finally, the HLT passed data is shifted to Tier 0, for storing the analog and digital prints of the events. The events are further classified as Primary Datasets (PD), depending on the trigger they fired, e.g. all events that triggered a muon path are stored in the muon PD.

2.4.6.1 Physics Goals and role of muon detectors

As the name Compact Muon Solenoid implies, muons are one of the main particles to detect with the CMS. Muons can penetrate large detector regions without being absorbed by interaction with the detector material. They cross the iron return yoke and are not stopped by the calorimeters. They only dispose a small amount of energy in the calorimeter, that is why the muons are embraced by the term minimum ionizing particle (MIP). The muons leave a characteristic signal in the muon chambers, which can be used to discriminate to other particle decays.

Muon detection is the most natural and powerful tool to detect interesting events over the background. A gold plated signal of the Higgs Boson is its decay into Z-Z or Z-Z^* which in turn decays into four charged leptons. If the leptons are muons, the best 4-particle mass resolution can be achieved, as the muons are less affected than electrons by radiative losses in the tracker material.

The LHC allows the discovery or exclusion of new gauge bosons with masses below ∼4 TeV - more than an order of magnitude heavier than the W and Z. For the highest discovery reach, precision measurements of high energy muons ($p_T > 1$ TeV) in $Z^{'} \rightarrow \mu^+\mu^-$ are important. Lepton and photon isolation criteria are essential to extract most of the signals searched for at the LHC. Since muons can be measured within jets, which is generally not the case for electrons and photons, muons make it possible to determine directly the lepton and photon isolation rejection factors. The possibility of measuring muons in jets is also a powerful tool for b-jet tagging, exploiting the b→ μ decay, which is essential in a number of Higgs studies, top studies, and SUSY searches.

The muon system of the CMS detector has three purposes: muon identification, muon trigger, and muon momentum measurement. The muon particle is measured by fitting a curve to hits among the four muon stations, which sit outside the magnet coil and are interleaved with iron return yoke plates . The trajectory and the momentum of the muon candidate is determined by tracking its position through the multiple layers of each station, combined with tracker measurements. The detailed description of muon reconstruction, identification and trigger is given in Section 3.3.4.

The work presented in this thesis is based on cross section measurement of the Drell-Yan process in dimuon final state. In this study, measurements of single and double-differential cross sections for the DY process are presented. The work has been done using the LHC data collected by the CMS at $\sqrt{s} = 8$ TeV, corresponding to an integrated luminosity of 19.7 fb^{-1}. The study is focused on inclusive Z boson production with a subsequent decay into pair of oppositely charged muons. The single-differential cross section has been measured with respect to phistar (ϕ^{*}), a kinematical variable which has better experimental resolution than p_T and correlates with transverse momentum of the Z boson (p_T), whereas for double-differential measurements the dependence on Z boson rapidity ($|y|$) has also been taken into account.

Bibliography

[1] L. Evans and P. Bryant, "LHC Machine", Journal of Instrumentation, vol. 3, S08001, 2008.

[2] R. R. Wilson, "The Tevatron", Fermilab, FERMILAB-TM-0763, 1978.

[3] CMS Collaboration, "Search for supersymmetry in pp collisions at $\sqrt{s}$=7 TeV in events with a single lepton, jets, and missing transverse momentum, Journal of High Energy Physics, vol. 2011, no. 08, pp. 156, 2011.

[4] CMS Collaboration, "Inclusive search for squarks and gluinos in pp collisions at $\sqrt{s}$= 7 TeV", Phys. Rev. D, vol. 85, issue 1, pp. 012004, 2012.

[5] CMS Collaboration, "Observation of Long-Range, Near-Side Angular Correlations in Proton-Proton Collisions at the LHC", Journal of High Energy Physics, vol. 2010, no. 9, pp. 091, 2010.

[6] CMS Collaboration, "Projected Performance of an Upgraded CMS Detector at the LHC and HLLHC: Contribution to the Snowmass Process", CMS-NOTE-13-002, 2013.

[7] CMS Collaboration, "Observation of a new boson at a mass of 125 GeV/c with the CMS experiment at the LHC", Phys. Lett. B, vol. 716, issue 1, pp. 30-61, 2012.

[8] ATLAS collaboration, "Observation of a New Particle in the Search for the Standard Model Higgs Boson with the ATLAS Detector at the LHC", Phys. Lett. B, vol. 716, issue 1, pp. 129, 2012.

[9] T. Lenzi and G. De Lentdecker, "Development and Study of Different Muon Track Reconstruction Algorithms for the Level-1 Trigger for the CMS Muon Upgrade with GEM Detectors", arXiv:1306.0858, 2013.

[10] https://lhc-machine-outreach.web.cern.ch/lhc-machine-outreach.

[11] ATLAS Collaboration, G . Aad et al., "The ATLAS Experiment at the CERN Large Hadron Collider", JINST, vol. 3, no. 08, pp. S08003, 2008.

[12] CMS Collaboration, S . Chatrchyan et al., "The CMS experiment at the CERN LHC", JINST, vol. 3, no. 08, pp. S08004, 2008.

[13] ALICE Collaboration, K . Aamodt et al., "The ALICE experiment at the CERN LHC", JINST, vol. 3, no. 08, pp. S08002, 2008.

[14] LHCb Collaboration, A . Augusto et al., "The LHCb Detector at the LHC", JINST, vol. 3, pp. S08005, 2008.

[15] LHCf Collaboration, O. Adriani et al., "The LHCf detector at the CERN Large Hadron Collider", JINST, vol. 3, no. 08, pp. S08006, 2008.

[16] TOTEM Collaboration, G. Anelli et al., "The TOTEM Experiment at the CERN Large Hadron Collider", JINST, vol. 3, no. 08, pp. S08007, 2008.

[17] https://home.cern/about/experiments/moedal.

[18] CMS Collaboration, "The Tracker Project, Technical Design Report", CERN-LHCC-98-006; CMS-TDR-5, 1998.

[19] CMS Collaboration, "The Electromagnetic Calorimeter Project, Technical Design Report", CERN-LHCC-97-033; CMS-TDR-4, 1997.

[20] CMS Collaboration, "The Hadron Calorimeter Project, Technical Design Report", CERN-LHCC-97-031; CMS-TDR-2, 1997.

[21] CMS Collaboration, "The Magnet Project, Technical Design Report", CERN-LHCC-97-10; CMS-TDR-1, 1997.

[22] CMS Collaboration, “The CMS muon project: Technical Design Report”, CERN-LHCC-97-032; CMS-TDR-3, 1997.

[23] S. Cittolin et al., “CMS The TriDAS Project : Technical Design Report, Volume 2: Data Acquisition and High-Level Trigger”, CERN-LHCC-2002-026; CMS-TDR-6, 2002.

Chapter 3

Event Generation, Simulation and Reconstruction

A thorough understanding of the physics of pp collisions and of the experimental setup plays a crucial role in scrutinizing the data collected from the LHC. The complete chain of collision event evolution is simulated numerically with the help of Monte Carlo (MC) event generators, which rely on repeated random sampling of the theoretical predictions. The events simulated by various MC generators are then compared to the real events (data) collected by the experiment, in order to validate the Standard Model and its possible extensions. The complete chain of event simulation, shown in figure 3.1, is segregated into following steps:

- Event Generation : A collision event of interest is simulated in the event generator starting from particle interaction to the final products of the collision.

- Detector Simulation : It includes full detector geometry simulation along with complete evolution of the event through space and time, along with interaction of particles within the detector volume.

- Event Reconstruction : The raw data collected by the various sub-detectors of the CMS are combined to reconstruct tracks and calorimeter clusters.

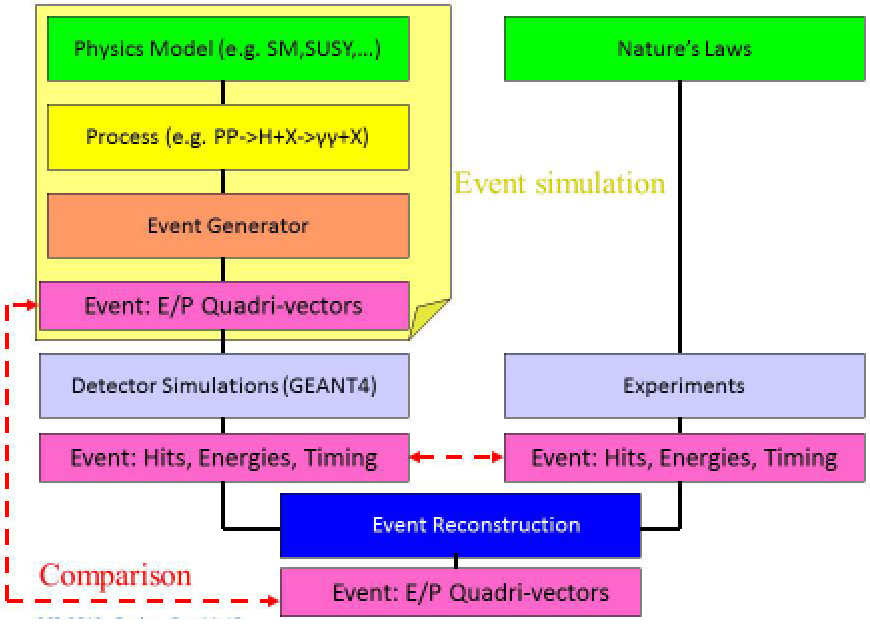

Figure 3.1: Basic steps in simulation and data analysis.

3.1 Event Generation

The hadronic collisions are complex, as protons are composite particles, and precise knowledge of their partonic structure is essential for cross section measurements. Hence, the event generation includes clubbing the information from various simpler steps involved in particle collision, e.g. to generate a hard process :

- Feynman diagram of the physics process is generated.
- The parton level cross sections are calculated using the matrix element (ME) of the hard process, also referred to as the scattering matrix, which relates the initial state and the final state of a physical system.
- Random generation of the events is done in coherence with the full differential cross section.
- Eventually, set of four-momentum vectors associated with each of the final state particles is provided.

A schematic representation of the different components that are implemented in event generators is shown in figure 3.2. The red blob represents the hard physics process of interest. At large momentum scale, the hadronic interactions result in production of thousands of fundamental particles. The quarks (or antiquarks) and the gluons from the incoming hadrons participate in the hard scattering, and gluons, quarks (or antiquarks) and a boson (subsequently decaying into a quark-antiquark pair), are produced. The softer multiple interactions are represented by purple balls and the fragments of the initial hadrons are represented by cyan balls in the figure. The additional radiations attached to the incoming partons are referred to as initial state radiations (ISR), while, the additional radiations attached to final state partons are referred to as final-state radiations (FSR). The accelerated coloured partons emit QCD radiation in the form of gluons. The gluons themselves emit further radiation, leading to parton showering. This process repeats itself until the collision energy has been converted and the stable final state particles are produced. This results in a stream of collimated particles -jet and the phenomenon is referred to as hadronization. Hence, complete chain of hadronic interactions can be separated into various steps which makes it easier for different programs to handle each step. For example, one program may simulate the hard process, while another program might exclusively produce parton showering and hadronization process.

3.1.1 Parton Showering

During the hard scatter process, incoming and outgoing partons emit gluons, which further radiate off quark-antiquark pairs and gluons, hence creating the parton showers [1]. These gluons radiated from the partons carry a fraction of energy of the mother particle and the associated color connection. The parton showering continues until the radiated partons have energy above an infrared cutoff. The final state parton showers are described by subsequent splitting of the gluons with a decrease in energy after each splitting. The initial-state radiation is produced in the similar way to the final state radiation, but inverting the process such that the colored ob-

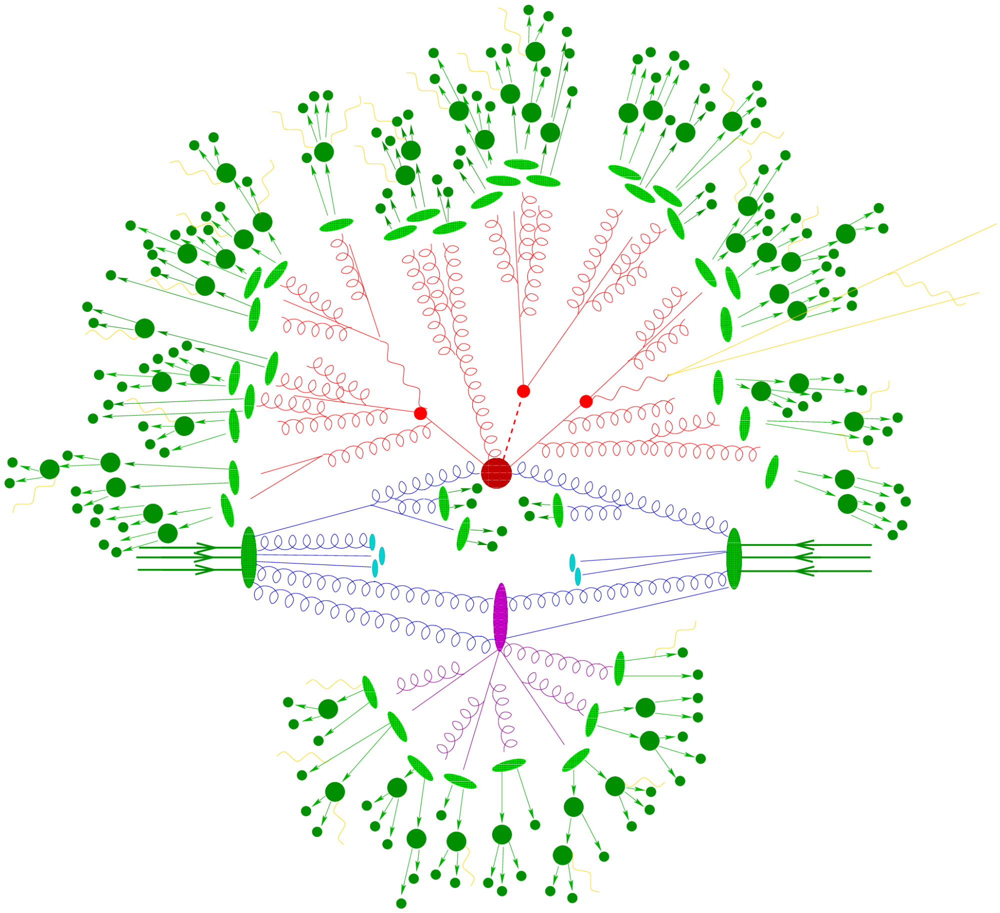

Figure 3.2: A schematic representation of a pp collision generated by a typical event generator where the different colors indicate the different stages involved in event generation. Figure reproduced from [1].

jects out of the shower collapse back to the initial partons out of the protons. The parton showers populate the regions of phase space where emissions are collinear or infrared divergent. The infrared divergences are difficult to calculate as they include some virtual contributions. Hence, an approximation scheme is used for considering the dominant contributions.

3.1.2 Hadronization Models

The development of parton shower stops, at momentum scale of 1 GeV/c, where the strong coupling constant α_s becomes too large. In this QCD regime, the perturbative models are replaced by the nonperturbation models, which explains the colored partons confinement into colorless hadrons. In general, hadronization refers to the transition of final state to actual final state hadrons [2]. There are two hadronization models which are widely used : Lund String Model and Cluster Model. While the String model transforms color connected partons directly into hadrons, the Cluster model uses an interposed stage of cluster objects, with typical mass scale of a few GeV/c^2 :

- Lund String Model : This model uses string dynamics to represent color flux stretched between q$\overline{q}$ (figure 3.3) [2, 3]. It considers a string or a colored flux tube holding the two quarks having linearly confined potential. The string breaks when the energy of string exceeds the mass of quark-antiquark pair forming another quark-antiquark pair. The procedure is repeated multiple times until the color-connected partons form on-shell hadrons.
- Cluster Model : The cluster hadronization model [2, 3] (figure 3.3) is based on preconfinement, that the color structure of a perturbative QCD shower evolution at any scale Q$_0$ is such that the partons clusters occur with a universal invariant mass distribution that depends only on Q$_0$. At the end of the parton shower, the gluons are forced to split into a quark-antiquark pair and the

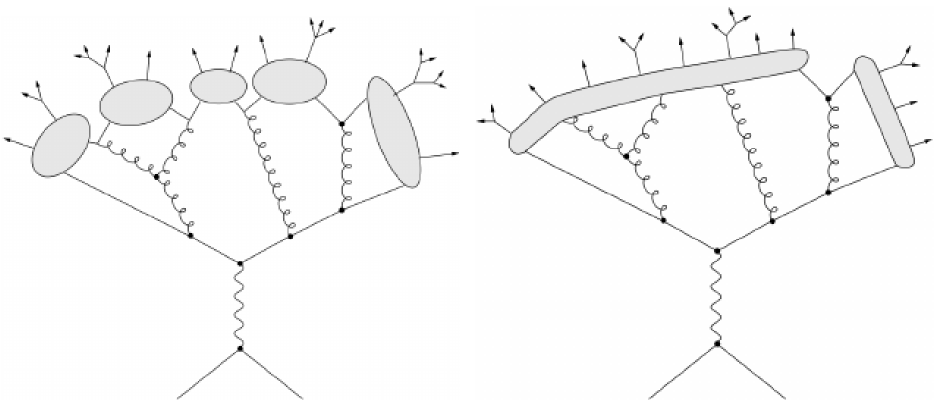

Figure 3.3: Illustration of cluster (left) and string (right) hadronization models. Figure reproduced from [4].

clusters formed by the gluon splitting are then forced to decay into on-shell hadrons. More details on the hadronization models can be found in [2,3].

3.1.3 Parton Distribution Function

Parton Distribution Functions (PDFs) represent the probability density of ascertaining a parton inside the proton. Each parton (quark or gluon), depending on the energy scale Q^2, has a definite value of the longitudinal momentum x associated with it. A precise knowledge of the PDFs is crucial for new predictions for the Standard Model and beyond the Standard Model processes at hadronic colliders. Furthermore, the discovery of new exciting physics relies on precise knowledge of PDFs.

The cross sections of hard scattering processes are calculated by convoluting the cross section calculated at the parton level with the PDFs. Since the PDFs parametrise soft effects, they cannot be computed in perturbative QCD and are obtained experimentally. Usually, the results from different experiments and processes, such as deep-inelastic ep scattering at the HERA collider [5], are combined to extract the PDFs. These PDFs are calculated most accurately by globally fitting the available deep inelastic scattering (DIS) and related hard scattering data from HERA and Tevatron [6] experiments. The fitting can be done at leading-order

(LO), next-to-leading order (NLO) or at next-to-next-to-leading order (NNLO) in the strong coupling α_S.

3.1.4 Event Generators

The event generators are special computer programs designed to simulate the high energy collision events. The Monte Carlo method of event generation is based on randomly generating the events of the desired physics process. MC generators produce theoretical simulations of real collisions by using both the QCD perturbation theory and the phenomenological models. The perturbation theory predicts the behavior of the hard scattering interactions and phenomenological models explain the soft hadronic interactions. The physics of the generated particles, namely their evolution, their decay modes and their couplings, needs to be given as input to a MC generator. The output of MC simulations are used to validate theoretical predictions, efficiency and acceptance calculation and to correct the collision data for the detector effects.

The MC event generators are either general purpose or the specialized generators. The general purpose MC generators perform all the event generation steps, whereas, the specialized generators are dedicated to particular steps of event generation and are interfaced with general purpose event generators to obtain final state. Some generators use LO calculations while other generators provide Next-to-Leading Order (NLO) calculations. The event generators used for Drell-Yan cross section measurement are Pythia (using different tunes), Powheg, MadGraph, aMC@NLO and Resbos. FEWZ (Fully Exclusive W and Z) is used to calculate highly precise estimate of the theoretical value of the interaction cross section. Leading order predictions of the DY process are commonly extracted from matrix element (ME) plus parton shower (PS) Monte Carlo simulations. To avoid double counting in regions where the ME and PS overlap, a matching scheme is utilized. Common matching schemes are the CKKW (Catani, Kuhn, Krauss and Webber) [7] and MLM (Michelangelo L. Mangano) [8] matching schemes. The main features of these MC generators are briefly described in the next sections.

3.1.4.1 PYTHIA

Pythia [9] is a general purpose tree-level generator used in the generation of events in hadronic and leptonic collisions with CM energies greater than 10 GeV. It uses LO calculation for generation of $2 \rightarrow n$ ($n \leq 3$) hard scattering processes. However, for particles arising from resonance decays, events with higher final-state multiplicity can be generated. Pythia computes ME for a large number of processes and also implements the necessary tools to simulate ISR and FSR for complete event simulation. It also has set of utilities and various interfaces to external programs.

Two versions of the generator, Pythia 6 and Pythia 8 [10], are used for the analysis discussed in this thesis. Pythia6 is the older version written in Fortran while Pythia8 is more recent and written in C++. The underlying events can be represented in Pythia by different configurations of parameters, known as "tunes". The tunes have been chosen to correctly model the PDFs estimated from HERA and Tevatron. The Pythia6 and Pythia8 samples used in this thesis, tune Z2star [11] and tune CUETP8M1 [12] are used. Pythia6 has the options of parton showers with virtuality or transverse momentum as the evolution variable, whereas Pythia8 is based on dipole showering. Pythia samples used for this analysis are produced with CTEQ6L1 PDFs. Both versions use the Lund string model for hadronization and a highly developed multiple-interaction model for the underlying event.

3.1.4.2 POWHEG

POWHEG (Positive Weight Hardest Emission Generator) [13] is a prescription for interfacing NLO calculations with parton shower MC generators. Initially, the hard physics process is generated by POWHEG and later the shower MCs (SMC), such as, PYTHIA, MADGRAPH are used for showering and hadronization. However, the approximate SMC implementation of the NLO corrections has to be deducted from the exact NLO result in order to avoid double counting. In POWHEG algorithm, the events are generated with positive (constant) weight, and, the generator is independent of SMC program to be used for showering.

The hard-scatter part of signal has been generated at NNLO precision by POWHEG generator using CT10 [14] PDF. The Parton Showering and the hadronization were implemented using PYTHIA6 with k_T- MLM prescription. For the underlying event Z2star [11] tune has been used where the parameters required to describe the nonperturbative strong interaction are tuned to the observed characteristics of the minimum-bias events in CMS experiment at $\sqrt{s} = 7$ TeV.

3.1.4.3 MADGRAPH

MADGRAPH [15] is a MC generator providing only ME calculations and has to be interfaced with other MC generators (e.g. PYTHIA) for the remaining steps like parton showering and hadronization. It is a tree-level generator and can produce the events up to 4 partons in the final state. It generates all Feynman diagrams for the process depending on users input specifying initial and final state particles, branching fractions required in models (BSM models), masses and couplings of the particles etc. The MEs at a given phase space point are calculated and the event information is stored in Les Houches format Event (LHE) file [16], which can subsequently be used by other packages for event generation. To avoid double counting of equivalent phase space configurations during parton showering, various jet matching algorithms such as CKKW, MLM etc. are used.

An inclusive DY signal sample, was generated by the MADGRAPH using CTEQ6LI [17] PDF set. Parton shower and hadronization effects are implemented by interfacing the event generator with PYTHIA6 along with the k_T-MLM matching scheme and using the Z2star tune for the underlying event.

3.1.4.4 aMC@NLO

aMC@NLO [18] generates hard scattering events with NLO precision and has to be interfaced with other generators (e.g. PYTHIA) for hadronization and parton showering. When the MC generates events with real parton emission, it generates kinematical configurations that are also taken into account by the NLO computation: the possibility of having the same kinematical configuration from the MC and from the NLO may lead to double counting. aMC@NLO uses negatively weighted events to account for the duplicate events. Each event in aMC@NLO has either positive or negative event weight that will have to be taken into account for the distributions to be meaningful. In this analysis, aMC@NLO sample has been generated using NNPDF3.0 NLO PDF and PYTHIA 8 for the parton shower and FxFx merging scheme [19].

3.1.4.5 ResBos

ResBos (Resummation for Bosons) [20] is the analytical program used for calculating kinematic distributions for the hadronic production and vector boson decay. It utilizes the resummation method of transverse momentum to account for contributions from gluon radiations in the initial state and hence differs from fixed-order perturbation theories and Monte Carlo showering methods.

3.1.4.6 FEWZ

FEWZ (Fully Exclusive W and Z Production) [1] is a simulation code for production of lepton pairs at hadron colliders through the Drell-Yan process. It can calculate cross section at next-to-next-to-leading-order (NNLO) in the strong coupling constant.

3.2 Detector Simulation

The purpose of a detector simulation is the modeling of the passage of particles through the detector and the calculation of the associated interactions with the detector material. It allows checking and/or correcting for non-trivial or unforeseen detector or physics effects, smearing of observables such as particle energies etc. , as well as comparing detector performance with available theoretical models. The MC generators discussed in section 3.1.4 replicate physics processes only at generator level and the particle interactions with the detector material have to be simulated separately. The CMS collaboration uses the software package GEANT4 (GEometry ANd Tracking) [22] for detector modelling within the CMS software framework. For full detector simulation, following steps are performed serially :

- GEN-SIM: The hard scattering physics process is generated using one of the above listed generators. Then, the kinematical variables and the corresponding energy depositions in the detector of the final state particles (SIM hits) are simulated with GEANT4.

- RAW-DIGI: The SIM hits are then converted into the detector response. This is the raw information coming out of the detector after any internal activity, and after implementing the desired triggers.

- RECO-AOD: The detector response is then refined and different physics objects i.e. tracks, vertices, jets, electrons and muons etc. are then reconstructed. The AOD (Analysis Object Data) format is a subset of the RECO (Reconstructed) format with the information relevant for all analyses within CMS and is also smaller in size.

The analysis discussed in this thesis is done using the AOD samples which contain all the relevant information of reconstructed objects at the detector level. However, the samples produced at the intermediate steps are also very important. A GEN-SIM sample is useful in case of comparison with the data corrected to stable particle level while a RAW-DIGI sample is used to study about details of detector reconstruction or noise. CMS uses a tiered structure for the storage and the processing of the samples. MC samples are generally stored in Tier-2 centers and can be accessed for the physics analysis.

Two different versions of simulation are implemented in the CMS framework :

- Full Simulation : Full Simulation (FullSim) model uses GEANT4 toolkit for a detailed detector simulation and is interfaced to various MC generators. Four-vectors of the final state particles in HepMC format are given as inputs to the simulation program. The particle propagation through a detailed detector geometry is done by GEANT4 (version 9.3.patch01). The energy depositions in the sensitive detector volumes are then converted to electronic signals and the the format of the output from this step is kept identical to that of real LHC collision data. Further processing uses this data to simulate the formation of the Level1 Trigger and High Level Trigger decisions using the identical algorithms implemented online in the CMS Trigger system.

- Fast Simulation : Fast simulation (FastSim) model is based on rather simplified detector geometry and on parameterization of detector effects. It uses intuitive detector parameters and simulated particle decays produced by MC generators as inputs. The format of the output is kept identical to that of real LHC collision data. Event production rates are 100 times faster than the FullSim program, with accuracy equivalent to FullSim, for most of the physics objects typically considered in CMS analyses.

3.3 Event Reconstruction

During LHC data-taking period, a positive decision from HLT initiates the transfer of selected events to the storage manager that writes the data to disks. Hence, it is relevant to extract only the compact information from the huge amount of CMS recorded data related to particles which have crossed the detector. The detector detects particles with high efficiency and momentum resolution in order to perform optimal measurements but meanwhile an excellent offline reconstruction of the final objects is also needed. Particle-Flow algorithm is used in CMS for event reconstruction for producing well calibrated physics objects using electronic signals recorded by the CMS sub-detectors.

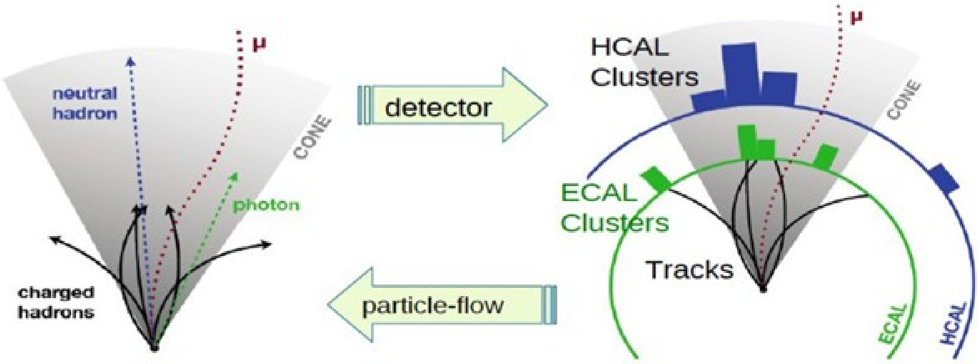

Figure 3.4: CMS Particle-Flow (PF) algorithm used for reconstructing an event by combining information for all CMS sub-detector. Figure reproduced from [24].

3.3.1 Particle-Flow Algorithm

The Particle-Flow (PF) algorithm [23] aims to identify and reconstruct all the stable and meta-stable particles from collisions at LHC, as depicted in figure 3.4. It extensively combines the information from all the sub-detectors for reconstruction of physics objects. The reconstructed PF candidates namely, electrons, muons, charged and neutral hadrons are then used for jet, missing transverse energy and tau reconstruction. It uses iterative tracker algorithm which is based on Kalman Filter method [25] for tracks reconstruction. The particle hits in the CMS calorimetry are converted to PF clusters for particle identification using calorimeter clustering algorithm. Lastly, link algorithm is used to form PF blocks by connecting pairs of elements in the event and also to avoid double counting from different detector components. The PF algorithm uses the following method for particle identification and reconstruction ;

- Photons are reconstructed from the ECAL energy deposit not linked to any track hits in the tracker. The four-momentum of the reconstructed photons is calculated based on the location of the reconstructed primary vertex.
- For electron reconstruction, a track reconstructed in the central tracker is associated with energy deposits in the ECAL. The electron trajectory is reconstructed by refitting the track position using Gaussian Sum Filter (GSF)

model [26].

- Charged hadrons are identified from the remaining tracks which are identified neither as electrons nor muons. Momentum for each hadron is obtained from the track under the pion hypothesis.
- Neutral hadrons are identified as energy deposits in the HCAL not linked to any charged hadron trajectory.
- Muons are identified as tracks in the central tracker consistent with either a track or several hits in the muon system, associated with an energy deficit in the calorimeters.

3.3.2 Primary Vertex Reconstruction

The primary-vertex reconstruction [27] aims to determine the coordinates of collision points and the associated uncertainty of the hadronic collisions. The main interaction vertex per event and the vertices due to pileup collisions are determined by two step process :

- Vertex Finding : A quality selection criterion is applied on the tracks for the vertex reconstruction. The tracks passing the conditions listed below are selected for vertex reconstruction :
  - Consistent with being produced in the primary interaction region.
  - At least two pixel layers, minimum five pixel and strip layers are associated with the track.
  - χ^2 per degree of freedom for the track fit should be less than 20.
- Vertex Fitting : The selected tracks are then clustered together into vertices based on a deterministic annealing (DA) algorithm [27]. For each selected track, the z-coordinate of the point of closest approach z_i to the beam-line is measured with an uncertainty σ_i and an anonymous number of vertices

is assigned at position z$_j$. For events with only one vertex per track, the probability p$_{ij}$ will be 1 if track i is assigned to vertex j, and 0 otherwise. For tracks with more than one vertex assigned, the probability p$_{ij}$ ranges from 0 to 1, that can be inferred as the probability of the assignment of track i to vertex j in a large ensemble of possible assignments. Hence, the clustering performance metric χ^2 is :

$$\chi^2 = \sum_{ij} p_{ij} \cdot \frac{(z_i - z_j)^2}{\sigma_i^2}$$

For a given value of χ^2, the DA algorithm finds the most likely distribution of p$_{ij}$ and tends to decrease χ^2 until a good reliable minimum is found. The vertex candidates are then characterized by the tracks clustered within d$_z \leq 1$ cm with respect to their nearest neighbor, where d$_z$ represents the longitudinal position of the extrapolated impact parameter.

After the designation of vertex candidates, a three dimensional fit is performed using the Adaptive Vertex Fitter (AVF) [28]. It is a robust fitter that efficiently down-weights outlier tracks by assigning a weight (between 0 and 1) to the tracks. The fitting is done for calculating the vertex parameters (x,y,z coordinates), the number of degrees of freedom for the vertex. The sum of weights estimates the effective number of tracks accepted by the fitter and corresponds to the number of degrees of freedom (ndf) assigned to the vertex. A quality selection is applied to consider only vertices with ndf > 4, which corresponds here to having at least four tracks assigned to the vertex. All the reconstructed vertices are $\sum p_T^2$ ordered.

As shown in figure 3.5, primary vertex reconstruction efficiency for CMS data collected at $\sqrt{s} = 7$ TeV is close to 100% when more than 2 tracks are used to reconstruct the vertex. figure 3.6 shows the primary vertex resolution in z for both minimum-bias and jet-enriched samples. The resolutions in z and x are less than 25 μm and 20 μm for minimum-bias samples and less than 12 μm and 10 μm for jet-enriched samples [27].

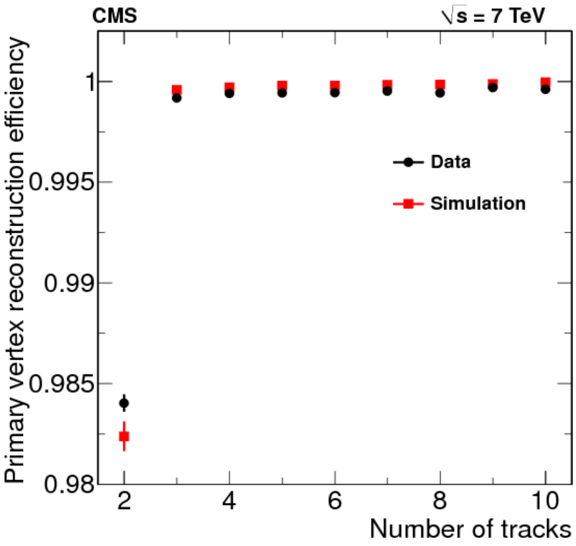

Figure 3.5: Primary vertex reconstruction efficiency measured in data and MC simulation at $\sqrt{s} = 7$ TeV. Figure reproduced from [27].

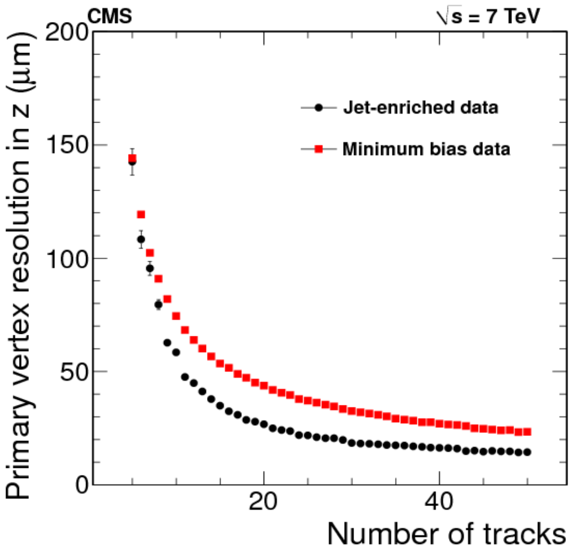

Figure 3.6: Primary vertex resolution in z for two kinds of events with different average track p_T values as a function of the number of tracks. Figure reproduced from [27].

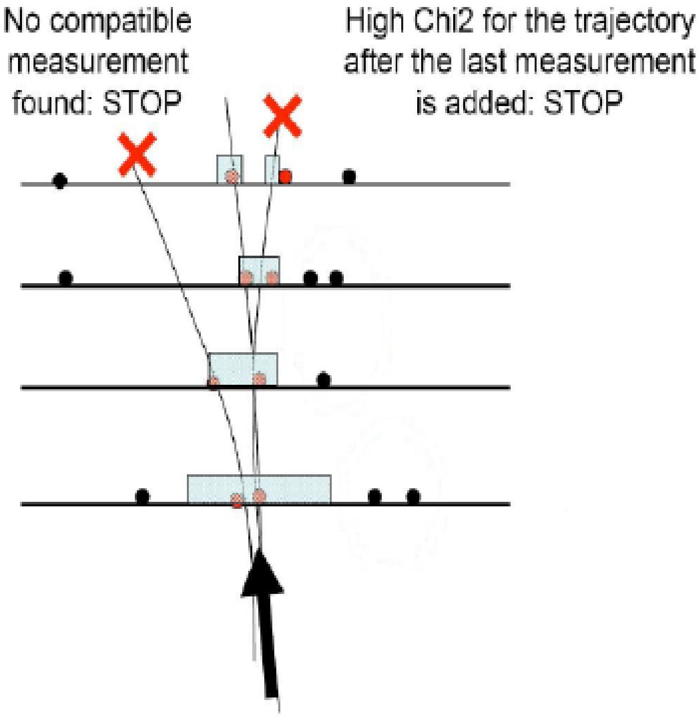

Figure 3.7: The Kalman Filter based CTF track pattern recognition. Figure reproduced from [29].

3.3.3 Track Reconstruction

The CMS silicon tracker is used to detect and measure trajectories of charged particles produced in the pp collisions. The charged particles while traversing through, deposit their energies through ionization in the tracker material and leave the so-called hits. To reconstruct the trajectories of these particles, the hits inside the tracker sub-detectors are then linked together, and are referred to tracks, of the particles. Due to strong magnetic field, every charged particles traverse the detector following a curved path and this curvature is proportional to its transverse momentum.

The Combinatorial Track Finder (CTF) based on combinatorial Kalman Filter is used for measuring the trajectory and other track parameters as depicted in figure 3.7. The CTF alogorithm uses an iterative approach for particle recognition. For each iteration, the pixel and strip hits assigned to good tracks are eliminated from the input lists of the successive iterations to streamline the trajectory building. The complete track reconstruction is done in following steps :

- Local reconstruction : The digitized hits in the tracker are transformed into tracks in a local coordinate system of the CMS tracker. The position along with certain uncertainty is estimated independently in pixel and strip detectors and the information is then gathered for the track seed generation.
- Seed finding : The preliminary trajectory candidates or “seeds” are obtained using very few hits for the full track reconstruction. At least two hits compatible with the hypothesis of a track coming from the interaction region are used for seed generation (figure 3.7).
- Pattern recognition : The seeds are propagated outwards by the Kalman filter to find hits that coincide with the predicted trajectory of the charged particle. The trajectory is built iteratively by extrapolating it to the subsequent layers until the outermost layer of tracker is reached. To avoid biasing, the trajectory building is done in parallel.
- Final fit : The selected hits are fitted using Least Square Method for the best estimation of the trajectory parameters with high precision.
- Track cleaning : To avoid duplication in track counting, the track collection is filtered by selecting the track with lowest value of χ^2. Further, to avoid fakes, certain quality cuts are applied on the tracks that pass the cleaning process.

For low p_T well isolated muons, the global tracking efficiency is more than 99%, as can be observed in figure 3.8, in the full η range of the Tracker acceptance and is independent of the ϕ direction.

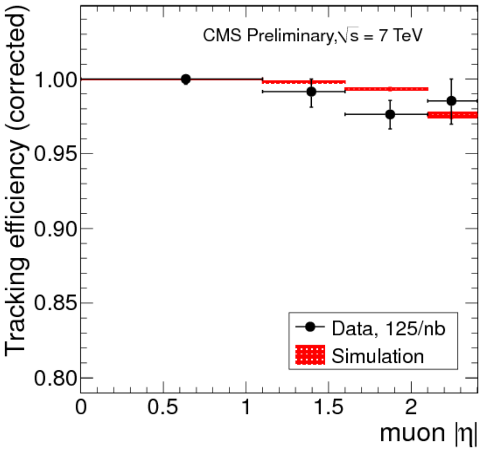

Figure 3.8: Corrected tracking efficiency as a function of η for muons. Figure reproduced from [27].

3.3.4 Muon Reconstruction and Identification

The CMS detector has been designed to have an excellent muon identification efficiency and momentum resolution. Muons can penetrate more in detector regions without being absorbed by interaction with the detector material. They cross the iron return yoke and are not stopped by the calorimeters. Furthermore, its mass of 105 MeV makes the radiation loss very small. As they dispose only a small amount of energy in the calorimeters hence muons are known as the minimum-ionizing particles (MIP).

3.3.4.1 Muon Reconstruction

For reconstructing muons in CMS, the particle signatures from the tracker and muon subsystems are used [30]. The transverse view of a collision event in which four muons were reconstructed is shown in figure 3.9. The muon reconstruction involves three stages :

- **Local Reconstruction** : The initial reconstruction takes place at the level of individual muon subsystems [31]. For the collision data, the output from the DAQ is unpacked to create digital signals and, the simulated samples rely on

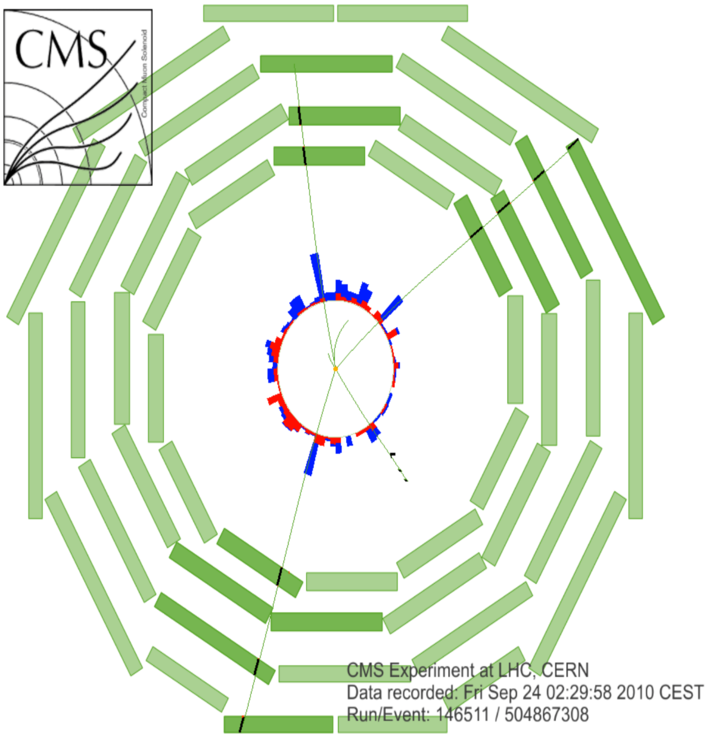

Figure 3.9: The transverse view of a collision event in which four muons were reconstructed. The tracks of charged particles are represented by green (thin) curves in the inner cylinder; muon tracks extends to the muon system. Three muons are identified by the DTs and RPCs, the fourth one by the CSCs. Short black stubs in the muon system show fitted muon-track segments; Short red (light) horizontal lines indicate positions of RPC hits; energy depositions in the ECAL and HCAL are shown as red (light) and blue (dark) bars, respectively. Figure reproduced from [30].

digitization procedure for creation of digis by the GEANT simulation. These digis are then clustered together to build RecHits, which are further grouped using pattern recognition algorithm to form segments. The muon segments give the straight-line parameters of a candidate - muon, producing those hits.

For the segment reconstruction in Drift tubes, the initial parameter is the muon drift time stored in digis. The drift time is extracted from the digis and using the Look Up Table algorithm, the muon hit position is measured. Then, for each collection of hits, a linear fit is performed using the hit positions and measured errors. The muon segment with the maximum number of hits and the minimum χ^2 is retained.
In case of CSC chambers, the detected signals from the cathode strips and anode wires are the inputs for segments reconstruction. The pulse height in each strip of endcap CSCs is obtained and then clustering of neighbouring strips is performed to determine the probable position of incidence of the incident muon, considering all 6 layers of a chamber independently. A 2D RecHit is created at each intersection of a 3-strip cluster and a wire group. Finally, the RecHits in the all the layers of a chamber are fitted to form a track segment.

For the RPC segment reconstruction, the hits are obtained by clustering the adjacent fired strips. After the strip clustering, the center of gravity i.e the area covered by the cluster of strips is obtained. In the barrel region with rectangular strips, the center of gravity is the center of a rectangle. However, for the endcap region, the computation is more complex as the area covered by the clusters is trapezium of varying shape.

- **Standalone Reconstruction** : This level of the reconstruction uses the information from the muon subsystems alone. The track parameters associated with the segments found in the innermost chambers from local reconstruction are taken as seed for trajectory building. The seeds are propagated to the innermost compatible muon detector layer and are used for reconstructing muons using Kalman filter [25] in the inside-out direction. To reject fake hits due to showering, delta rays and pair production, a suitable cut on χ^2 is applied. The trajectory parameters are updated after each step. Once the hits are fitted and the fake trajectories removed, the remaining tracks are extrapolated to the point of closest approach to the beam line. Only around 1% of the total reconstructed muons from pp collisions fall under this category. However, misidentification rate for this reconstruction method is 10^4 -10^5 larger than other methods due to high contamination from the cosmic or collision muons.

- **Global Reconstruction** : The global reconstruction of muons is done by elongating their trajectories to include hits in the tracker system (silicon strip and silicon pixel detectors). The best matching track from the inner detector is then fitted along with the standalone muon track to form a global muon track. This is also known as the outside-in method. The global muon refit has better momentum resolution at higher transverse momenta i.e. $p_T > 200$ GeV/c than the tracker muon reconstruction.

- **Tracker Muon Reconstruction** : Possible muon candidates are selected from every track starting from the inner tracker with $p_T >$ 0.5 GeV/c and $|p| >$ 2.5 GeV/c. An extrapolation to the muon system is performed taking into account loss of energy and uncertainties from multiple scattering. A track hit in the inner tracker is tagged as tracker muon, if any muon segments exist in the muon system within the extrapolated track position. This is also known as the inside-out method. This procedure is slightly more efficient for muon track momentum of below 5 GeV/c.

About 99% of high p_T muons from collisions are reconstructed either as Global or Tracker muons [30], owing to high tracker track efficiency and the reconstructing segments efficiency in the muon system (figure 3.10).

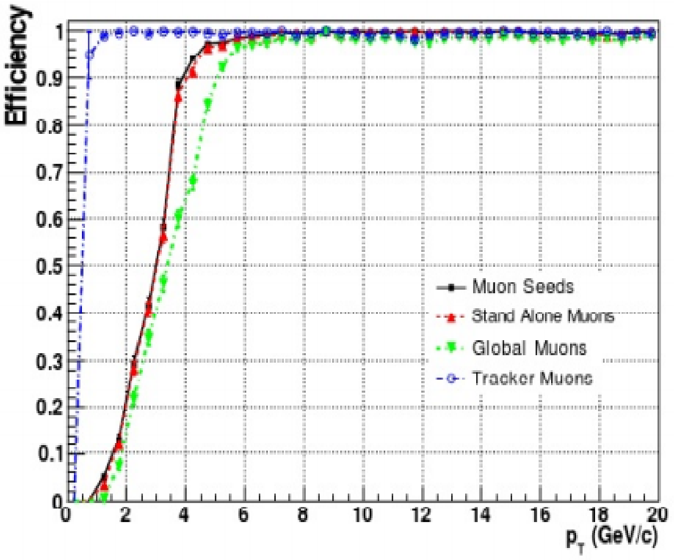

Figure 3.10: Efficiencies of the different muon reconstruction steps as a function of muon p_T. Figure reproduced from [33].

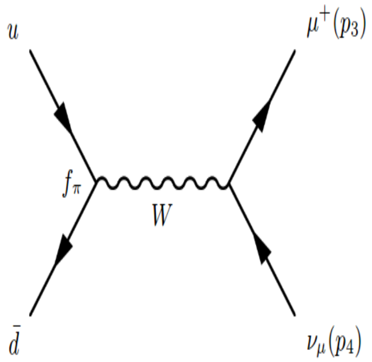

Figure 3.11: Light quarks decay into a pair of muon and its neutrino.

3.3.4.2 Muon Identification

Muon reconstruction with very high efficiency is obtained using the combination of above algorithms. However, the reconstructed muons from the kaon (K^0) decay, pion (π) decay and from the light quarks decay, as shown in figure 3.11, along with the cosmic muons serve as background. Following are some of the basic muon identification algorithms used in various physics analyses:

- **Soft Muon Selection** : The muon candidates reconstructed as tracker muons are considered. Additionally, the muon segment must be compatible with the

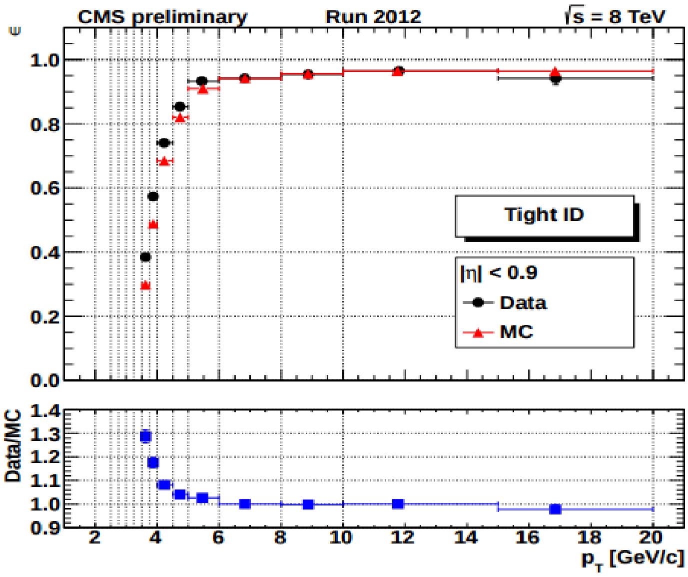

Figure 3.12: Identification efficiencies for tight muons as function of muon p_T for $|\eta| < 0.9$ determined in data and MC simulations. Figure reproduced from [34].

extrapolated tracker track both in x and y coordinate.

- **Loose Muon Selection** : Every muon candidate must be reconstructed either as global muon or tracker muon passing the PF muon identification requirements. The PF requirements impose following selection cuts on the muon hits and their p_T :

  1. The candidate should have at-least one hit in the muon subsystems
  2. The transverse sum of all the neighboring tracks and calorimetric cells around a cone of $R = 0.3$ centered on the muon itself, should be less than 10% of the muon p_T.

- **Medium Muon Selection** : The muon candidate satisfying the “Loose” muon identification criteria are considered. The additional cuts imposed are :

  1. The fraction of valid hits should be more than 0.8.
  2. Additionally, for good global muons, the segment compatibility[1] of the

---

[1] Muon Segment Compatibility evaluates data on which crossed stations have matching muon segments.

   muon track in the muon stations should be greater than 0.303 and should be greater than 0.451 for remaining candidates.

3. The χ^2/d.o.f. should be less than 3 for good global muons and for standalone and tracker muon, should be less than 12. Additionally, χ^2 from the kink-finder on the inner track hits should be less than 20.

- **Tight Muon Selection** : For this selection, following cuts are applied :

  1. The candidate must be reconstructed as global and PF muon.
  2. The normalized χ^2 of global-muon track fit should be less than 10 and at least one muon chamber hit included in the fit.
  3. The corresponding tracker track is required to match a muon segment in at least two muon stations and using more than 10 inner-track hits
  4. The candidate has transverse impact parameter less than 2 mm with respect to the primary vertex.

The efficiency of the muon selection algorithms is studied with the tag-and-probe method [35]. A very well identified muon which triggered the event is taken as the tag, while the probe is a tracker muon or a loosely-identified muon matched with the tag. The efficiency is estimated by simultaneously fitting the tag-probe invariant mass distributions for the probes passing and failing the selection requirements (listed in table 3.1). For low p_T muons, the efficiencies are measured with the J/ψ resonance and with Z resonance at higher values of p_T. Figure 3.12 shows the single muon efficiencies for the Tight Muon selection algorithms determined with the J/ψ resonance at $\sqrt{s} = 8$ TeV as a function of muon p_T.

3.3.5 Muon Isolation

Muons are required to be well isolated from energy deposits and other charged particles in its vicinity. This condition imposed on the muons reduce the fake muon contributions coming from heavy flavour and hadronic decays. It also help to discriminate between the leptons coming from high p_T process from the leptons produced

	Tracking	**Reconstruction**	**Identification**
Tag	Global Muon event triggered with $p_T >$ 3 GeV/c	Global Muon event triggered with $p_T >$ 3 GeV/c	Global Muon event triggered with $p_T >$ 3 GeV/c
Probe	Si-Track $p_T >$ 3 GeV/c	Muon Si-Track $p_T >$ 3 GeV/c	Muon Si-Track matched to Standalone Muon $p_T >$ 3 GeV/c
Passing Probe	Probe matched to Muon Si-track	Probe matched to StandAlone Muon	Probe is also Global Muon

Table 3.1: Criteria for the selection of tags and probes for each efficiency measurement.

copiously due to various QCD processes e.g muons from heavy mesons decay. For calculating muon isolation, the particle's activity in three sub-detectors : Tracker, ECAL and HCAL is studied. There are different isolation algorithms available in CMS:

- Tracker relative isolation : For all the reconstructed tracks in the tracker, the scalar sum of the p_T is calculated. The tracks, except the muon tracks, lying in a cone of radius $\Delta R < 0.3$ centred around the muon track direction are considered. The candidates with the ratio of the p_T sum to the muon track p_T below a certain threshold are considered as isolated. The muon isolation cone is illustrated in figure 3.13.

- Combined relative isolation : The isolation variable is calculated using the hits in the tracker along with the energy deposits in the electromagnetic and hadronic calorimeters. The sum of energies is considered within a cone of radius 0.3 centred on the muon track direction. The candidate with the ratio of the p_T sum to the muon track p_T below a certain threshold is isolated muon.

- PF relative isolation : The isolation variable is calculated by taking the scalar sum of the transverse energies of all photons, all neutral hadrons along with

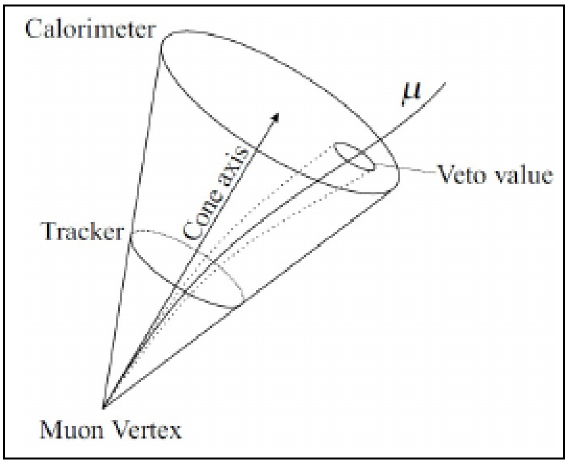

Figure 3.13: Pictorial representation of the isolation cone.

the p_T of all charged hadrons contained within a cone with $\Delta R < 0.4$. The discriminating (isolation) variable for muons (R^{μ}_{Iso}) is required to be less than 0.12 :

$$R^{\mu}_{Iso} = (\sum p_T^{charged} + max(0, \sum p_T^{neutral} + \sum p_T^{\gamma} - 0.5 \sum p_T^{PU}))/p_T^{\mu}$$

where, $\sum p_T^{charged}$, $\sum p_T^{neutral}$ and $\sum p_T^{\gamma}$ represent the scalar sum of transverse momenta of charged, neutral particles and the photons. The energy of the neutral particles is corrected by subtracting the energy deposited by the charged particles not associated with the primary vertex ($\sum p_T^{PU}$) in the isolation cone multiplied by a factor of 0.5 ($\Delta\beta$ -correction factor). The $\Delta\beta$ correction is applied to the isolation variable to account for effects of additional interactions (i.e. pileup) and is computed using reconstructed tracks and primary vertices.

3.3.6 Muon Trigger

The basic tasks of CMS Muon Trigger are: muon identification, transverse momentum measurement and bunch crossing identification, which are done by two trigger division explained below:

- **First level muon trigger** : The First Level Muon Trigger of CMS uses all three kinds of muon detectors: Drift Tubes (DT), Cathode Strip Chambers (CSC) and Resistive Plate Chambers (RPC). DT and CSC electronics first process the information from each muon chamber locally, hence are called local triggers. These local triggers deliver a vector (position and angle) per muon station for each muon crossing the station. Then, the vectors from different stations are collected by the *Track Finder*, (TF), which combines them to form a muon track and assign a transverse momentum value. This information is sent to the Muon Sorter. In the case of RPCs there is no local processing apart from synchronization and cluster reduction. Hits from all stations are collected by the PACT logic. If they are aligned along a possible muon track, a p_T value is assigned and the information is sent to the Muon Sorter. The Muon Sorter selects the four highest p_T muons from each subsystem in several detector regions and sends them to the Global Muon Trigger which compares the information from Track Finder (DT/CSC) and PACT (RPC). Finally, transverse momentum thresholds are applied by the Global Trigger for all trigger conditions.

- **Global Muon Trigger** : The purpose of the Global Muon Trigger (GT) is to combine information from both systems i.e. TF and PACT, explained above in order to improve the overall muon trigger efficiency and rate capability. The GT algorithm makes use of the complementarity of the subsystems, and is not a simple AND/OR combination of both. The information from the RPC system arrives before that of the DT/CSC and the synchronization logic aligns the two. The next step of the Global Muon Trigger algorithm is to convert the η, ϕ and p_T values of the tracks from the RPC and DT/CSC systems to comparable units, which is done with look-up tables. Then for every possible combination of muons, matching logic calculates the match quality to get a measurable criterion for the determination of whether muon candidates seen in both systems come from the same physical muon or not. First the differences in η and ϕ ($\Delta\eta$, $\Delta\phi$) are calculated. If one of the RPC or DT/CSC channels is empty, the difference is set to a maximum value. Then a function in (η, ϕ)-space is calculated to determine the *(match quality)*, which is defined as a distance in (η, ϕ)-space where η carries a weight w which may differ from one. Sometimes, the weights are defined as a function of η to take into account the different resolutions of the different muon chamber systems.

The next step is the pair logic which uses the match qualities MQ_{ij} to find pairs of muon candidates. If MQ_{ij} is higher than that of its vertical and horizontal neighbors and if it exceeds a programmable threshold, then it represents the best match of two muon candidates. Only muons that are not disabled by one of their neighbors are included in this comparison. This last condition is necessary to find more pairs and therefore to suppress a small fraction of ghost muons in the output.

Bibliography

[1] S. H$\ddot{o}$che, “Introduction to parton-shower event generators”, arXiv:1411.4085, 2014.

[2] B. R. Webber, “Hadronization”, no. hep-ph/9411384. CAVENDISH-HEP-94-17, 1994.

[3] B. R. Webber, “Fragmentation and hadronization”, Int. J. Mod. Phys., vol. A15S1, pp. 577-606, 2000.

[4] ATLAS Collaboration, “Measurement of dijet cross sections in pp collisions at $\sqrt{s} = 7$ TeV centre-of-mass energy using the ATLAS detector”, arXiv:1312.3524, 2014.

[5] T. H1 and Z. Collaborations, “Combined Measurement and QCD Analysis of the Inclusive ep Scattering Cross Sections at HERA”, arXiv:0911.0884, 2010.

[6] P.Z.Quintas (D0 Collaboration), “Measurement of W and Z production cross-sections in p collisions at s = 1.8 TeV”, arXiv:hep-ex/9412016, 1994.

[7] F. Krauss, “Matrix elements and parton showers in hadronic interactions”, JHEP, vol. 2002, no. 08, pp. 015, 2002.

[8] M. L. Mangano, “Matching matrix elements and shower evolution for top-quark production in hadronic collisions”,JHEP, vol. 2007, no. 01 , pp. 013, 2007.

[9] T. Sjostrand, S. Mrenna, and P. Z. Skands, “PYTHIA 6.4 Physics and Manual”, JHEP, vol. 2006, no. 05, pp. 026, 2006.

[10]] T. Sjostrand et al., “An Introduction to PYTHIA 8.2”, Comput. Phys. Commun., vol. 191, pp. 159-177, 2015.

[11] R. Field, “Early LHC Underlying Event Data - Findings and Surprises”, arXiv:1010.35582010.

[12]] CMS Collaboration, “Underlying Event Tunes and Double Parton Scattering”, Technical Report CMS-PAS-GEN-14-001, CERN, Geneva, 2014.

[13] P. Nason, “A new method for combining NLO QCD with shower Monte Carlo algorithms”, JHEP, vol. 2004, no. 11, pp. 040, 2004.

[14] J. Gao et al., “CT10 next-to-next-to-leading order global analysis of QCD”, Phys.Rev. D, vol. 89, issue 3, issue 3, pp. 033009, 2014.

[15] J. Alwall et al., “MadGraph 5 : Going Beyond”, JHEP 1106 (2011) 128, doi:10.1007/JHEP06(2011)128, arXiv:1106.0522.

[16]] J. Alwall et al., “A Standard format for Les Houches event files”, Comput. Phys. Commun., vol. 176, pp. 300304, 2007.

[17] P. Nadolsky et al., “Progress in CTEQ-TEA PDF Analysis”,doi:10.3204/DESY-PROC-2012-02/301, arXiv:1206.3321.

[18] J. Alwall et al., “The automated computation of tree-level and next-to-leading order differential cross sections, and their matching to parton shower simulations”, JHEP 07 (2014) 079, doi:10.1007/JHEP07(2014)079, arXiv:1405.0301.

[19]] R. Frederix and S. Frixione, “Merging meets matching in MC@NLO”, JHEP 12 (2012) 061, doi:10.1007/JHEP12(2012)061, arXiv:1209.6215.

[20] G. Ladinsky and C. Yuan, “The Nonperturbative regime in QCD resummation for gauge boson production at hadron colliders”, Phys.Rev. D50 (1994) 4239, doi:10.1103/PhysRevD.50.R4239, arXiv:hep-ph/9311341.

[21] Y. Li and F. Petriello, “Combining QCD and electroweak corrections to dilepton production in FEWZ”, Phys.Rev. D86 (2012) 094034, doi:10.1103/PhysRevD.86.094034, arXiv:1208.5967.

[22] GEANT4 Collaboration, “GEANT4: A simulation toolkit”, Nucl. Instrum. Meth. A506 (2003) 250303, doi:10.1016/S0168-9002(03)01368-8.

[23] CMS Collaboration,“Particle-Flow Event Reconstruction in CMS and Performance for Jets, Taus, and MET”, Tech. Rep. CMS-PAS-PFT-09-001, CERN, 2009. Geneva, Apr 2009.

[24] Joe Candela, “Status of the CMS Higgs Search”, UCSB/CERN July 4,2012.

[25] R. Fr*ü*hwirth,et al., Application of Kalman Filtering to Track and Vertex Fitting, Nucl.Instrum. and Methods A262 (1987) 444; doi:10.1016/0168-9002(87)90887-4.

[26] W. Adam et al., “Reconstruction of electrons with the Gaussian-sum filter in the CMS tracker at LHC”, J. Phys. G 31 (2005) N9, doi:10.1088/0954-3899/31/9/N01.

[27] CMS Collaboration, “Description and performance of track and primary-vertex reconstruction with the CMS tracker”, JINST, vol. 9, no. 10, p. P10009, 2014.

[28] R. Fruewirth, et al., “Adaptive Vertex Fitting”,CMS Analysis Note, CMS-AN-2007/008 (2008).

[29] P.Lenzi, et al., “Track reconstruction of real cosmic muon events with CMS tracker detector”,doi:10.1088/1742-6596/119/3/032030 (2008).

[30] CMS Collaboration, “Performance of CMS muon reconstruction in pp collision events at $\sqrt{s} = 7$ TeV”, JINST, vol. 7, p. P10002, 2012.

[31] G. Bruno, et al., Local reconstruction in the muon detectors, CMS Analysis Note CMS-AN-2002/043 (2002).

[32] R. Frühwirth,et al., Application of Kalman Filtering to Track and Vertex Fitting, Nucl.Instrum. and Methods A262 (1987) 444; doi:10.1016/0168-9002(87)90887-4.

[33] http://people.na.infn.it/ noli/Tesi/Capitolo3.pdf.

[34] I. Krätschmer,“Muon reconstruction and identification in CMS Run I and towards Run II”, Nuclear and Particle Physics Proceedings 273275, 25002502 (2006).

[35] CMS Collaboration, “Measurements of Inclusive W and Z Cross Sections in pp Collisions at $\sqrt(s)$=7 TeV”, JHEP 01 (2011) 080.

Chapter 4

HCAL Calibration Studies

During the LS1 phase of the LHC, various parts of CMS detector were improved for better performance at higher luminosity and pileup. The Hadron Outer (HO) sub-detector of Hadron Calorimeter (HCAL) was upgraded [1] in which, the Hybrid Photodiodes (HPD), used as photo-detectors for the outer part of the HCAL were replaced by Silicon PhotoMultipliers (SiPM) [2,3] due to serious disadvantages of the former. Hamamatsu SiPMs of 3x3 mm^2 area 50 μm pitch MPPC were the drop-in replacement for the HPDs. In this chapter, the work done on the HO upgrade will be discussed. The second part of the chapter will be dedicated to studies related to the calibration of HCAL for 13 TeV data.

4.1 Hadron Outer Calorimeter

The Outer Hadronic Calorimeter (HO) [4] is located outside the solenoid coil. It acts as an additional absorber ensuring the sufficient sampling depth for $|\eta| < 1.3$. The purpose of the HO is to measure any energy from the hadronic showers, due to the particles hitting the HB, that leaks out of the backend of the HB. It increases the effective thickness of the hadron calorimetry to over 10 interaction lengths, thus reducing the tails in the energy resolution function except at the boundary of barrel and endcap. The HO layers are mounted within magnetic field returning iron

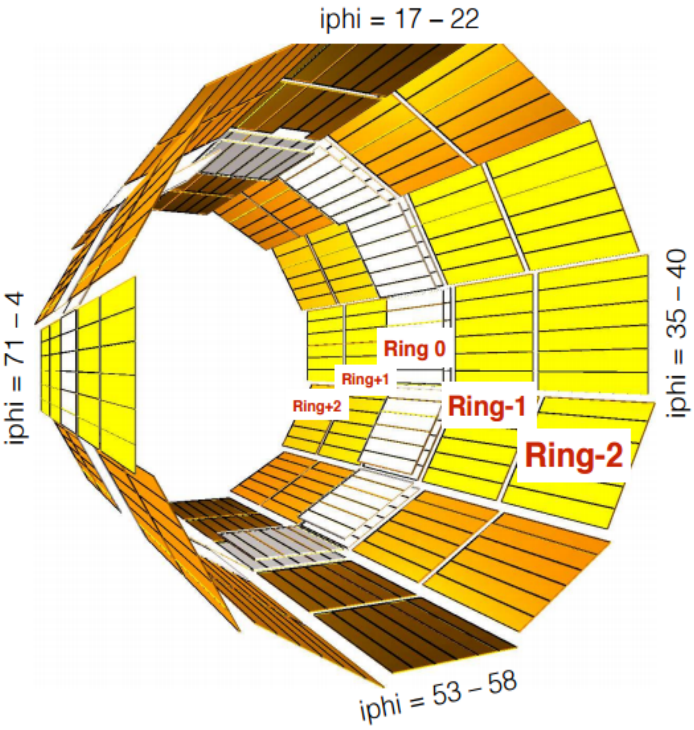

Figure 4.1: Layout of five HO rings in iϕ coordinate system. iϕ corresponds to an integer index for defining HCAL detector volumes as a function of azimuthal angle ϕ. In the transverse plane HO is split thereby in 72 iϕ sections, figure reproduced from [4].

yoke and are the first sensitive layers in each of the five rings of the yoke. The 10 mm thick scintillator tiles made up of Bicron BC408 act as the active material for sub-detector. The HO is divided into 5 rings as shown in figure 4.1 in z : ±1, ±2 (referred as YB±1, YB±2) and 0 (YB0). The rings are segmented in 12 sectors and are 2.5 m wide along the z-axis with inner and outer radii of 4 and 8 m, correspondingly.

HO uses plastic scintillators as the active material. The outgoing hadronic particles interact with absorber plates resulting in the production of innumerable secondary particles. The cascade or shower of particles is formed when these secondary particles traverse through successive layers of absorber. The shower particles traverse through the alternating layers of active scintillation material emitting blue-violet light. This emitted light is later absorbed by tiny optical Wavelength-Shifting

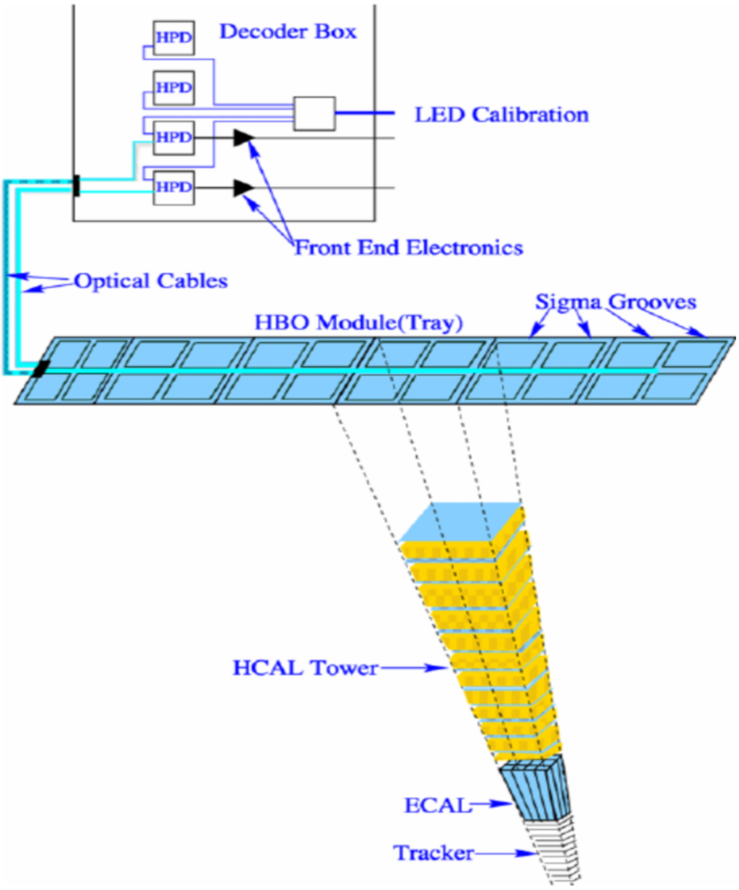

Figure 4.2: A single HO tray with individual tiles and the WLS fibres. Each HO tile is mapped to a HB tower for particle identification, figure reproduced from [4].

Fibres (WLS) and blue-violet light is shifted to the green region of the spectrum. The clear optic cables then carry the green light away to readout boxes (RBX) located within the HCAL volume. The optical signals arrive at the readout boxes from megatile layers and the signals from successive tiles, one behind the other, are then added optically to form “towers”. This optical summation is a measure of its energy and/or can be an indicator of particle type. These summed optical signals are converted into fast electronic signals by photosensors called Hybrid Photodiodes (HPDs). Special electronics then integrates and encodes these signals and sends them to the data acquisition system for purpose of event triggering and event reconstruction. Figure 4.2 shows the illustrative outline of a HO tray along with the decoder box equipped with photo-detector and readout electronics.

4.1.1 HO upgrade

After three years of very successful operation that led to discovery of the Higgs boson in 2012, the LHC was scheduled for a series of upgrades to enhance the experimental potential to study the nature of the new particle, and to extend the searches for new physics beyond the Standard Model. CMS decided to replace the HPD sensors from the Readout Modules (RMs) in the HO detector with magnetic field resistive Silicon Photomultipliers (SiPM) due to the following reasons :

- The HPDs produce large noise pulses when operated in magnetic field ranging from 0.2-0.3 T at the 3.8T operating field of the CMS magnet. A large fraction of HPDs (10 % or more) produce large discharges leading to their permanent damage.

- Large electric field of 8 kV across a gap of 3 mm required for HPDs operation. When high voltage is applied across the device, electrical discharges occur. This effect is enhanced by particular orientations and strengths of the magnetic field relative to the HPD device and is particularly severe for the HO calorimeter, requiring significant reductions in voltage (from 8 kV to 6.5 kV) in much of the detector.

- The total gain of HPDs is measured in terms of electron bombardment gain and avalanche diode gain. The measured total gain of HPDs is of the order of ~ 5 X 10^3. Due to low gain of HPDs, the separation of the signal from noise is difficult in case of HPDs, due to large contribution from electrical noise.

- No separation between signal and noise of the HPDs is shown in figure 4.3.

4.1.2 Silicon PhotoMultipliers

SiPMs are pixelated Avalanche Photo Diodes that operate in Geiger mode under bias voltage of few volts ($\sim$ 70 volts) above the breakdown voltage, so each electron hole pair generated by photons gives rise to a Geiger type discharge. The absorption of a photon of proper wavelength can excite an avalanche that causes the struck pixel to discharge. The firing of a pixel causes its capacitor to discharge, creating a quantized charge output from the SiPM depending on the number of pixels that discharge. SiPMs are inherently magnetic field insensitive and hence can be designed easily to operate in the 0.2T return magnetic field. The SiPMs have a relatively high photon-detection efficiency and high gain.

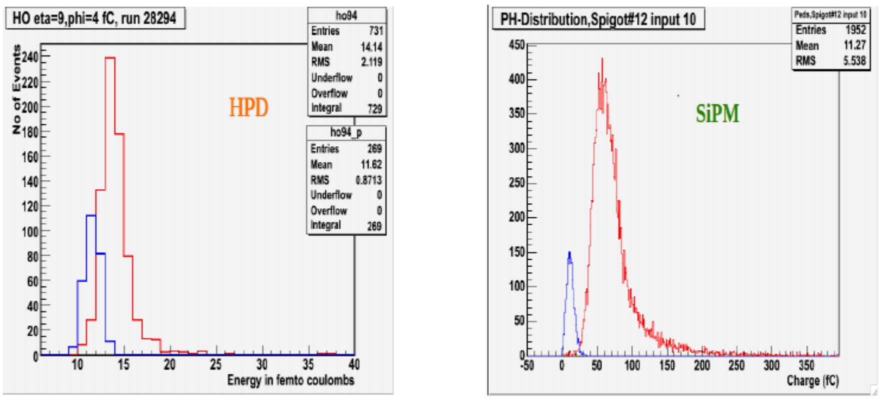

Figure 4.3: Comparison of muon response in HO for HPD and SiPM. For HPDs there is substantial overlap between muon signal and the pedestal. For SiPMs the signal and pedestal are well separated, figure reproduced from [2].

Hamamatsu SiPMs of 3x3 mm^2 area 50 m pitch Multi-Pixel Photon Counter (MPPC) are the drop-in replacement for the HPDs. These devices have 3600 micro-pixels and good dynamic range of 2500 photo-electrons (pe). At 500 nm, the MPPC has a photon detection efficiency (PDE) between 25% and 30%. The photo-detector and front end electronics are housed in Readout boxes (RBXs) that are installed inside the magnet return yoke. Electronics and photo-detectors are arranged inside the RBX into independent Readout Modules (RMs), as shown in figure 4.4 currently containing one HPD each.The drop-in replacement needs to match this physical layout as well as the existing front-end ADC. Each RM consists of 3 circuit boards, the Mounting Board (MB), the Control Board (CB), and the Bias Board (BB). The array of 18 SiPMs is mounted on one side of the MB. On the other side a Peltier cooler is placed to regulate SiPM temperature. The CB is connected on the Peltier side to the MB. The control board shapes the SiPM signals and sends them to the 40 MHz ash front end ADC. It also regulates the bias voltages, reads out the leakage currents, measures the temperatures and voltages of the system, and supplies the power to the Peltier system.

4.1.2.1 Peltier Cooling System

The Peltier System is used to stabilize the temperature of the SiPMs. As shown in figure 4.5, it consists of two plates and a set of four Peltier-effect [1] One hot plate is thermally coupled to the RBX cooling system which receives heat from four Peltier devices. On the other side of the Peltiers is the cold plate which is thermally coupled to the SiPM mounting board. The maximum power that can be supplied to the Peltier system is 15 W. In a test setup, it was found that a total of 8 W could be removed from the SiPM mounting board.

The mounting board has arrays of perforations around the SiPM area to provide a better thermal isolation. The temperature of the SiPM area is read out using a precision platinum resistor. The measured temperature is taken as input by the CMS slow control system which in turn generates a correction voltage. The new correction voltage is downloaded into a SiPM control board register and a DAC (Digital to Analog Converter) generates Peltier voltages. When a direct current is passed through a Peltier Module, the low temperature side absorbs heat and the high temperature side emits heat, so that a temperature difference exists across the surfaces. The heat emitted is more sensitive to the voltage applied across the module, than the heat absorbed. Hence, if a direct current is continuously passed through the module the emitted heat will exceed the absorbed heat and both sides of the unit will become hot. Hence, it is necessary to connect the module to a radiator such as aluminum fins to efficiently disperse the emitted heat.

---

[1] The creation of temperature difference between the electrodes by supplying voltage to the electrodes is referred as Peltier effect. The phenomena was first observed by French experimentalist Peltier in 1834. The process is extensively used to transfer heat from one medium to another on a small scale.

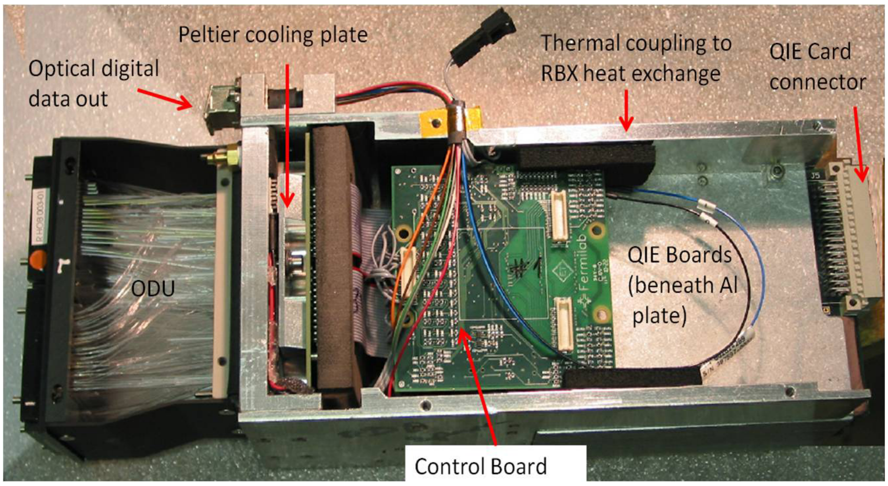

Figure 4.4: Outer HCAL readout module (RM), figure reproduced from [5].

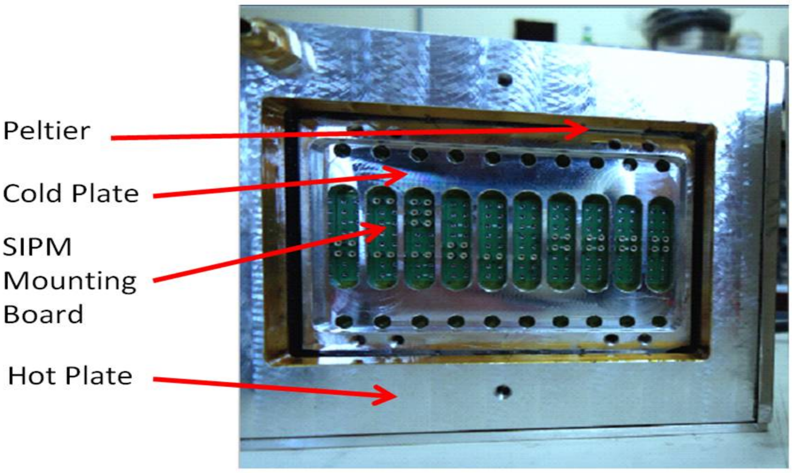

Figure 4.5: SiPM cooling and SiPM Mounting board, figure reproduced from [5].

Installation	Mean Temperature	Mean Dynamic Range	Mean Mid Temperature
Before	21.11	6.305	3.152
After	21.38	6.299	3.15

Table 4.1: Measured values of SiPMs parameters before and after block installation.

4.1.2.2 Peltier Data Analysis

We performed an analysis of the Peltier data to see the effect of installation of the aluminum block on the thermal stability of the Peltier Cooling System. The block was installed between the Readout Modules (RM) and the Readout Boxes (RBX) for their better thermal contact. Two Readout Boxes : HO1MO4 and HO1MO2 were installed with 8 Readout Modules in each RBX. We analyzed particular run-type in the CMS build framework, before and after installation of the aluminum block. To check the thermal stability, we studied the temperature versus voltage plots for each run and measured the following parameters for each run :

- Mean temperature
- Middle of the temperature range
- Dynamic range

The results for the 3 parameters are shown in figures 4.6 to 4.8 and the mean values are listed in table 4.1. From the data analyzed, it was concluded that the installation of the aluminum block has no significant effect on the observables studied.

As a second part of this analysis, we performed the linear fitting of current versus voltage plots for the Peltier data and extracted the slope of the curve. The aim was to define a range which covers the 3σ region [2], which will be used to define the normal operating I-V slope to differentiate between the good and bad SiPM card packs. The slope of all the SiPMs tested was found to lie between 0.145 to 0.176,

---

[2] The term σ refers to the amount of variability in a given set of data: whether the data points are all clustered together, or very spread out. Three-sigma limits (3-sigma limits) are used to set the upper and lower control limits of the data and is the significance with which scientists believe a result to be real as opposed to a random fluctuation in the background signal (the noise).

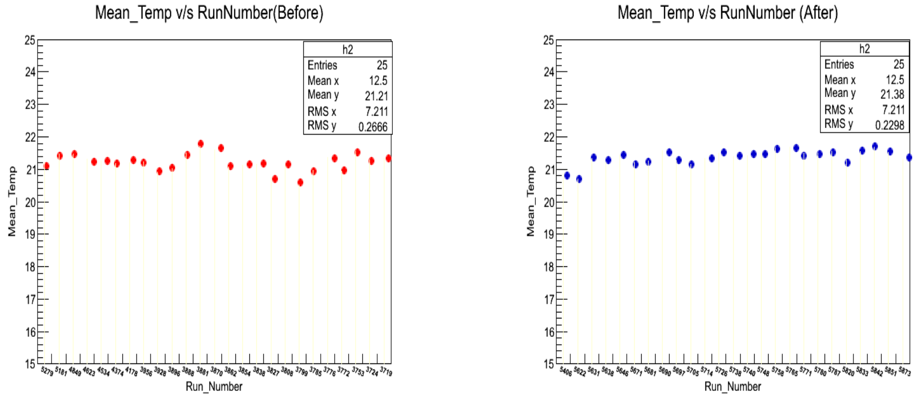

Figure 4.6: Mean Temperature of all Runs before (left) and after (right) the installation of the block.

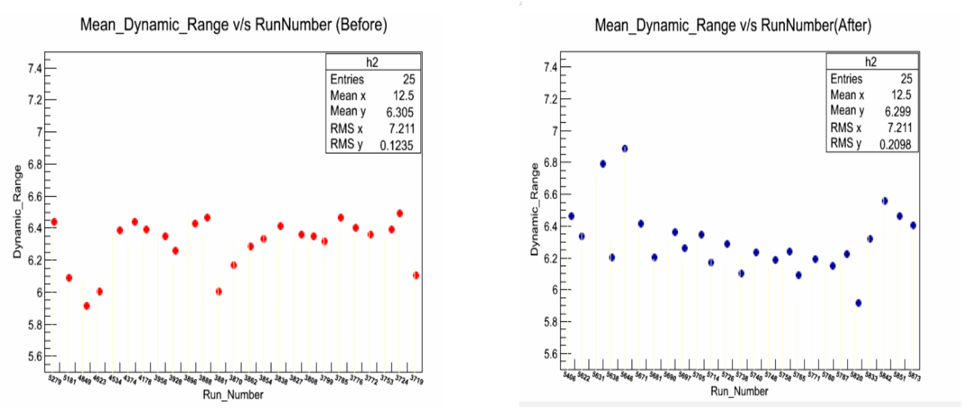

Figure 4.7: Mean Dynamic range of all Runs before (left) and after (right) the installation of the block.

as shown in figure 4.9. The outliers from this range signified a bad SiPM and they were not used for installation on the detector.

4.1.2.3 RMs installation and Performance Study

During Sept-Nov, 2013 at CERN, I participated in the following hardware related activities :

- Installation of the tested SiPMs on the YB-1 and YB-2 ring of the detector. The Readout Modules (RMs) with HPDs were removed from the detector and

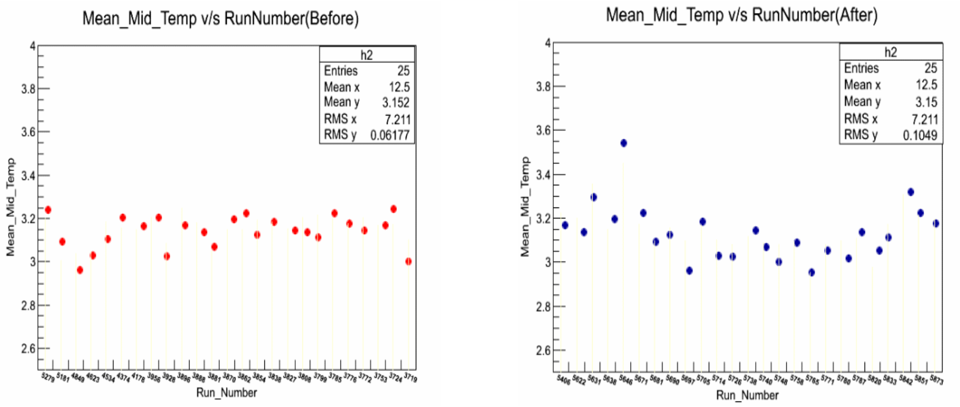
Mean_Mid_Temp v/s RunNumber(Before)

Mean_Mid_Temp v/s RunNumber(After)

Figure 4.8: Mean mid-temperature of all Runs before (left) and after (right) the installation of the block. The plots clearly show that the mean value of the variable studied remains same even after installation of box.

new RMs with SiPMs were installed. After installation LED runs were taken to check the performance of new RMs. Then, light tightening was performed for each sector and other runs were taken to study and compare SiPM characteristic with the result obtained earlier at the test stand. Figure 4.10 shows a readout module with SiPMs mounted in the RMs before the installation.

- For the Rings YB0, YB+1 and YB+2, SiPMs were tested at the SX5 test stand at P5 (figure 4.11). I participated in these test stand operations, where a set of 8 RMs were changed every week and tested by taking HO runs. I monitored these test stand operations during data-taking.

- To study the pedestal properties of the SiPMs being tested at P5, we studied the SiPM behaviour when LED was switched off. In this analysis, following properties of SiPMs were studied for each channel (for each SiPM card-pack there are 18 channels):
  - **Gain** : The charge distribution in pedestal events is fitted to determine the gain from the separation between the main pedestal peak and the first thermal avalanche peak.
  - **Avalanche Rate** : It is the rate at which the thermal avalanches occur

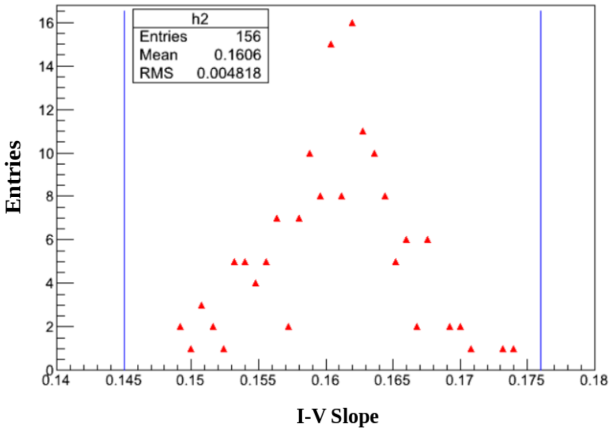

Figure 4.9: Slope of I-V plot was calculated for 156 SiPMs before their installation at detector site. The blue line indicate the range for linear fit of I-V i.e. 0.145 -0.176.

in 4 time samples, with 25 ns bunch spacing of the CMS DAQ system.

- **Cross talk** : It is the rate that an avalanche in one pixel of a SiPM causes a second avalanche in that SiPM and is derived from the parameters of the pedestal fit.

and these parameters were expected to be in 3σ region, results for one random run are shown in figure 4.12. The outliers from this region indicated a bad SiPM channel.

4.2 Performance of Isolated track Trigger

The hadron calorimeter (HCAL) has a nonlinear energy response, and must be calibrated to increase the energy response to one for the charged hadrons of energy around 50 GeV. The absolute calibration is done regularly using the isolated charged hadrons from the collision data. Dedicated HCAL calibration triggers have been set up to provide adequate number of charged hadrons to calculate the correction factors. To avoid any bias in the set of tracks used for calibration, two dedicated High Level Triggers (HLT) in the commissioning stream are used for this purpose :

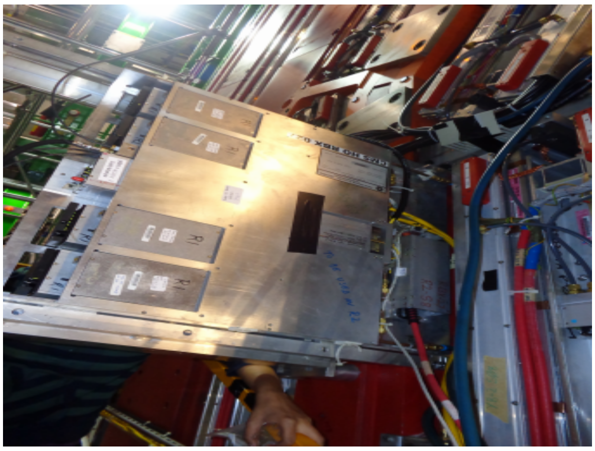

Figure 4.10: The readout module with tested SiPMs before installation in the HO ring YB+1.

Figure 4.11: Test stand set-up at CMS detector site for SiPMs testing.

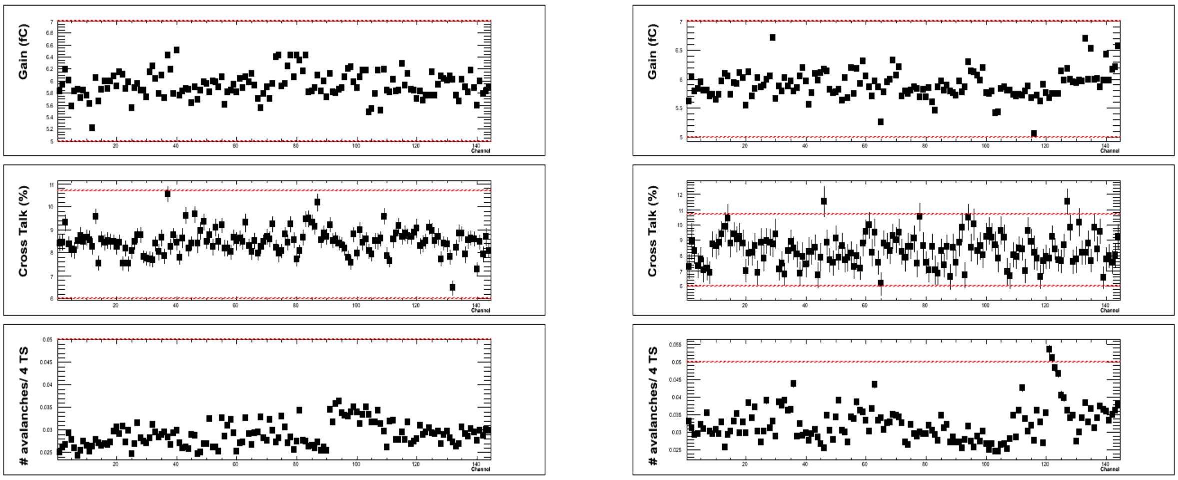

Figure 4.12: The left plot shows the results of the above mentioned SiPM properties for two random runs. Every point is in range (within the red line) and for the right plot there are various outliers for the the cross-talk and avalanche rate for SiPM channels. Hence, these SiPMs can not be further used in installation.

- **HLT_IsoTrackHB** for the barrel region ($|\eta| < 1.15$)
- **HLT_IsoTrackHE** for the endcap region ($1.1 < |\eta| < 2.2$)

4.2.1 Modified HLT Path

Figure 4.13 shows the structure of the old HLT path which was used during Run-I operation. It utilized four parts : reconstruction of pixel tracks, identification of isolated pixel track candidates, complete reconstruction of isolated pixel tracks and final selection based on complete reconstruction results. The performance of these two triggers was studied using 2012 collision data and the major drop in efficiency of track selection was encountered due to Minimum-Ionization Particle (MIP) cut on the tracks. The MIP cut on the reconstructed tracks reduced the efficiency from 0.520 to 0.156. Hence, it was suggested to move the MIP cut at the trigger level.

For data-taking at $\sqrt{s} = 13$ TeV, these two triggers were re-developed to enhance the efficiency of finding isolated charged hadrons. Figure 4.14 demonstrates

Figure 4.13: HLT_IsoTrackHB(HE) path for Run-I data-taking period.

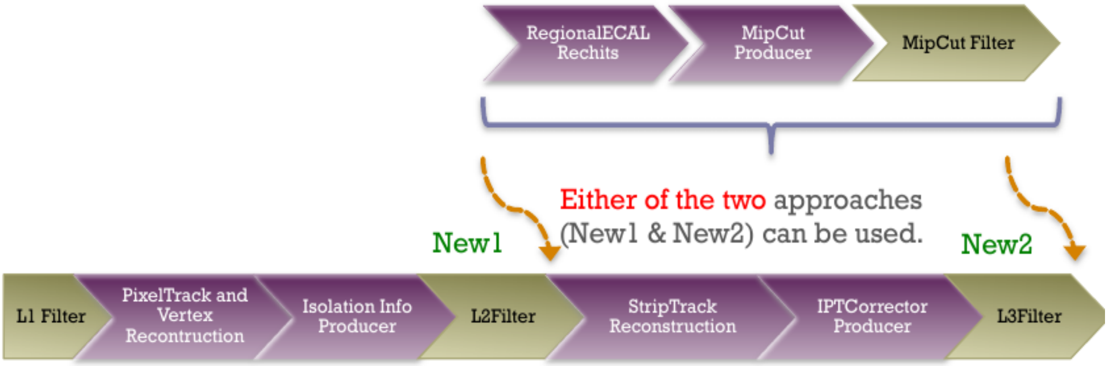

Figure 4.14: The new trigger paths to enhance isolated track selection by HCAL.

the new trigger path where additional checks are introduced to estimate energy deposited by the isolated track in the electromagnetic calorimeter (ECAL) :

- A change in the isolated pixel track producer was done to improve the HLT timing.
- Scenario 1 : Add a MIP cut filter just after L2 filter.
- Scenario 2 : Add the MIP cut filter just after L3 filter.

For LHC Run-II operations, Scenario 1 was implemented in both the isolated track triggers. Inclusion of the MIP Filter in the HLT paths improved the efficiency of the HLT paths.

4.2.2 Pileup dependence

The effect of pileup on the isolated track trigger efficiency was studied using simulation samples generated with 13 TeV data-taking scenario. The selection cuts used for offline track selection are :

- Tracks are required to have an associated primary vertex and to have the track quality bit set to “high purity”.

- Tracks are selected on the basis of proximity of the track to the primary vertex in the transverse (xy) plane as well as along the beam axis and the χ^2. [3] The cuts chosen are (a) 200 μm for proximity to event vertex, for transverse as well as longitudinal direction; (b) normalized χ^2 to be smaller than 5; (c) minimum number of layers to be crossed by the track is 8.

- Tracks do not interact before reaching the calorimeter surface. This is checked by looking at the number of missing hits in the inner and outer hit patterns of the reconstructed hits. All tracks with missing hits in the inner and outer hit patterns are rejected.

- For each HCAL cell, the intersection point of the line running through the center of the cell with the plane perpendicular to the track momentum is determined. If the distance between this point and the point where the isolated track candidate impacts the HCAL is less than a certain threshold (R_{cone} , the cone radius) the energy from the HCAL cell is included in the cluster. Signal is measured in a cone of radius 35.0 cm which contains on average more than 99% of the energy deposited by a hadron of energy 50 GeV.

- The tracks are considered to be isolated from other charged particles, if there are no hits in 4 layers of the tracker by any other good or bad track with p > 2 GeV/c in a radius of 63.9 cm around the impact point of the isolated track candidate.

- Tracks are required not to undergo inelastic interaction in the electromagnetic calorimeter. This is ensured by requiring energy measured in the ECAL in a

---

[3] The χ^2 between track and vertex is calculated as : $\chi^2 = \sum_{ik} c_{ik} \frac{(z_i - z_k)^2}{\sigma_i^2}$, where, the z-coordinates of the points of closest approach to the beam-line are called z_i , their measurement uncertainty σ_i. The tracks must be assigned to an unknown number of vertices at positions z_k. The term c_{ik} represents a track vertex assignment and are 1 when track i is assigned to the vertex k and 0 otherwise.
The normalized χ^2 is defined as the ratio of χ^2 and number of degrees of freedom : χ^2/ndof

PU Events	20-30 GeV/c	30-40 GeV/c	40-60 GeV/c	60-100 GeV/c
20-30	0.046	0.026	0.013	0.003
30-40	0.029	0.015	0.009	0.004
>40	0.019	0.009	0.006	0.003

Table 4.2: Fraction of events (in %) with well isolated tracks for different momentum bins in event sample with different number of pileup events.

cone of radius 14 cm around the impact point of the track to be less than 1 GeV.

- The track should be away from the L1 object in a cone of $\Delta R = 1$.
- The total momentum of the tracks should lie between 40 to 60 GeV/c.

Following two MC samples generated and hadronized with Pythia 8, with 2 different pileup scenarios were used :

- QCD_Pt-5to3000_Tune4C_Flat_13TeV_pythia8/Spring14dr-PU20bx25_POSTLS170_V5-v2/GEN-SIM-RECO
- QCD_Pt-5to3000_Tune4C_Flat_13TeV_pythia8/Spring14dr-PUS14_POSTLS170_V5-v2/GEN-SIM-RECO

The fraction of well isolated tracks in various track momentum bins for different pileup events were calculated. The results are shown in table 4.2. As can be seen from the table, there is a clear pileup dependence on the trigger efficiency. The fraction of events with well isolated tracks is large in case of low pileup events for all momentum range considered for this analysis. Hence, a larger bandwidth for data transfer at lower luminosity (or at low PU events) will benefit the overall rate of isolated track event selection.

4.2.3 Data Quality Monitoring

The next step was to develop specific softwares for monitoring the two isolated track trigger paths for data quality monitoring (DQM). The online Data Quality monitoring system receives a prescaled set of data from the "all" stream and from the calibration stream. The specific software for DQM, runs on this subset of events, and produces the monitoring and diagnostic histograms for various trigger parameters : the trigger rates, distribution of momentum, η, ϕ of the isolated track at different stages of the trigger along with a few other quantities relevant for future analysis. Figure 4.15 shows typical plots from one collision run during 2015. Momentum distributions of the isolated pixel track at L2 level and of the final selected track at L3 level are displayed in the figure and they are found to be as expected.

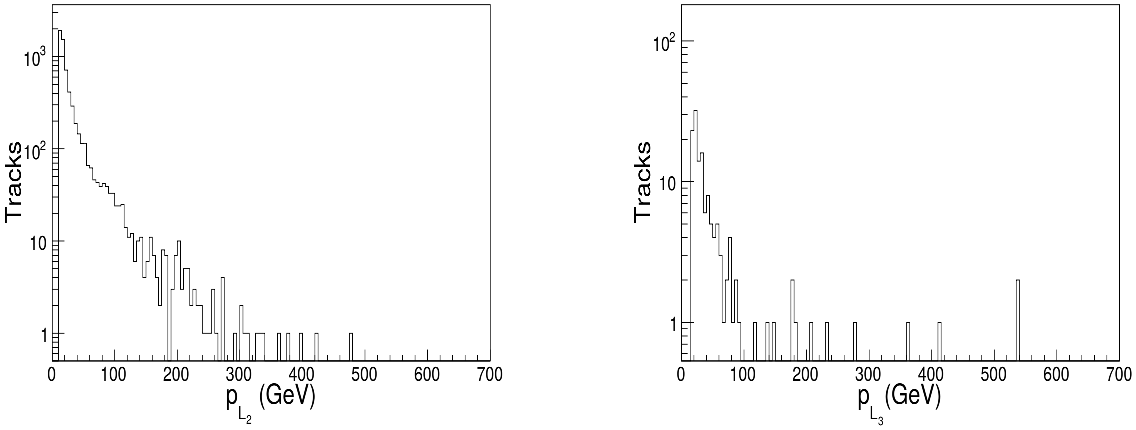

Figure 4.15: Output of the DQM package for a specific run which shows momentum distribution of the isolated track at L2 (left) and L3 (right) levels respectively.

Figure 4.16 shows a distribution of the ratio $\mathrm{E}_{HCAL}/(\mathrm{p}_{Track}\quad \mathrm{E}_{ECAL})$ for well isolated tracks in the calorimeter surface coming from a sample triggered by the new HLTs. E_{HCAL} is the energy of the isolated track measured in HCAL within a cone of 35 cm radius around the impact point of track on HCAL while E_{ECAL} is the energy measured in the ECAL within a cone of radius 14 cm around the impact point in ECAL [6]. The most probable value from the Gaussian fit is used to determine the η-dependent correction factors for the HCAL towers. These triggers produce sufficient statistics which enables calibration of the HCAL.

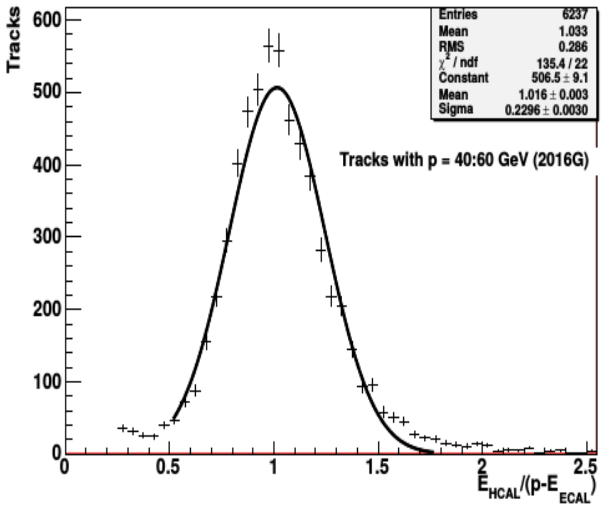

Figure 4.16: Distribution of the ratio $E_{HCAL}/(p_{Track} - E_{ECAL})$ for events selected by strong charge isolation in events selected by IsoTrackHB(HE) trigger.

4.3 HCAL Calibration with Isolated Charged Hadrons

Isolated charged hadrons are excellent tool for performing energy calibration of the HCAL in the areas covered by the tracking system. The momenta of the charged particles are measured in the tracking system with a very high degree of precision and that can be associated to the energy deposition in the calorimeter. However, these particles can interact and deposit a substantial part of the energy in the ECAL. Hence, the hadrons which have not undergone inelastic collision before reaching the hadron calorimeter, should be used for calibration. The particles used for calibration are required to be isolated from other particles to ensure minimal contamination from unrelated energy depositions. The threshold on momentum is chosen depending on the selection efficiency and purity of the measurement.

To calibrate a region of HCAL channels, the energy response of the isolated cluster is calculated for each event. The response is computed as the sum of hits in the cone around the impact point of the selected track, with added contribution from the MIP-like cluster in the ECAL The calculated energy response is compared to the particle momentum and ideally, their ratio is expected to be unity. The goal of the calibration is to obtain the correction factors ci for each HCAL sub-detector, which get the MPV of response equal to 1 in the rapidity range covered by the HCAL barrel and endcap. The counter 1 ≤ i ≤ I, where I is the number of sub-detectors.

4.3.1 L3 iterative method

To calibrate a region of HCAL channels, for each event j the energy response of the isolated cluster, E$_j$,calculated as the sum of hits in the cone around the impact point of the selected track and is compared to the particle momentum p$_j$ (after subtracting the energy deposit in ECAL):

$$\sum_{i=1}^{n} c_i \cdot E_i^j = E_{input}^j \tag{4.1}$$

where c_i is the inter-calibration constant for the i-th HCAL cell in the cluster (cone with n cells) around the hot cell (hit by the track) for each event, E_i^j is the energy response of this cell for the jth event, and E_{input}^j is the particle momentum after subtracting out the energy deposit in the ECAL.

The L3 method can be used to get the coefficients and is based on an iterative approach. At m-th iteration, the new correction factor c$_i^{m+1}$ is calculated using one of two possible options:

$$c_i^{(m+1)} = c_i^{(m)} \left(1 + \frac{\sum_j w_{ij}^{(m)} \cdot \left(\frac{p_j}{E_j^{(m)}} - RR \right)}{\sum_j w_{ij}^{(m)}} \right) \tag{4.2}$$

$$c_i^{(m+1)} = c_i^{(m)} \left(1 - \frac{\sum_j w_{ij}^{(m)} \cdot \left(\frac{E_j^{(m)}}{p_j} - RR \right)}{\sum_j w_{ij}^{(m)}} \right) \tag{4.3}$$

where the sum is done over J_i events, which contribute to the i^{th} sub-detector, RR is the reference response, to which the mean response should be equalized, p_j is the track momentum, $w_{ij}^{(m)}$ is the weight of the particular sub-detector in the cluster energy $E_j^{(m)}$:

$$w_{ij}^{(m)} = \frac{c_i^{(m)} \cdot e_{ij}}{E_j^{(m)}}, \qquad E_j^{(m)} = \sum_{i=1}^{n_j} c_i^{(m)} \cdot e_{ij} \tag{4.4}$$

As follow from equations (4.2) and (4.3), the iterative procedure results in equalization of the mean response of the detector around the value RR, which equals 1 by default. If the most probable value for the sample, MPV_{sample}, differs from the sample mean, $MEAN_{\text{sample}}$, the reference response should be set to $RR = \frac{MEAN_{\text{sample}}}{MPV_{\text{sample}}}$.

The statistical uncertainty of the correction factor $\Delta C_i^{(m+1)}$ can be estimated from the known r.m.s. of the response distribution $\Delta R_i^{(m)}$ for the subsample used for the i^{th} sub-detector.

$$\Delta C_i^{(m+1)} = \Delta R_i^{(m)} \frac{\sqrt{\sum_j (w_{ij}^{(m)})^2}}{\sum_j w_{ij}^{(m)}} \tag{4.5}$$

The procedure is reiterated until the difference between the coefficients (given in equation 4.4) at the subsequent steps become three times smaller than the statistical uncertainty. This corrected calibration constant is applied to the energy deposition in each cell and the procedure is reiterated until the coefficients converge. It has been demonstrated that the first method, equation (4.2) causes a small bias and the second method, equation (4.3) is more stable.

4.3.2 Event Selection

In absence of sufficient bandwidth given to dedicated trigger while data-taking, the isolated track events are selected from specific data stream using offline filters with or without any pre-defined level 1 triggers. Two options are used for the data selection:

- JetHT data stream is used and the events satisfying any single jet trigger at level 1 are used.
- Double eγ data stream is used where no preselection of level 1 trigger is used.

Events are selected to have at least one well reconstructed primary vertex which is close to the nominal interaction point, namely, r ($\sqrt{x^2 + y^2}$) < 2 cm and $|z| < 15$ cm. “Good” track selection is ensured by following the criteria discussed in section 4.2.2.

4.3.3 Results

The following data sets are used from JetHT data set for the 2015B, C and D periods, corresponding to center of mass energy $\sqrt{s} = 13$ TeV :

1. /JetHT/CMSSW_7_4_11-patch1-Run2015B_HLTnewcondition0_74X_dataRun2_Prompt_v3_v1/RECO,
2. /JetHT/CMSSW_7_4_11-patch1-Run2015C_HLTnewcondition0_74X_dataRun2_Prompt_v3_v1/RECO,
3. /JetHT/Run2015D-PromptReco-v3/RECO,
4. /JetHT/Run2015D-PromptReco-v4/RECO

Good runs are selected using CMS recommended JSON files. The data set corresponds to integrated luminosity of 0.85 fb^{-1}. Events satisfying any of the single jet L1 trigger condition are selected. 1684 well isolated tracks are obtained in the momentum region between 40 and 60 GeV/c. Figure 4.17 shows the energy response measured for these tracks. The distribution is fitted with a Gaussian function which gives the mean as 1.064 ± 0.006.

Figure 4.18 shows the mean energy response as a function of the distance of the track from the L1 trigger object measured in the $(\eta - \phi)$ plane. d_{L1} is measured as $\sqrt{(d\eta)^2 + (d\phi)^2}$. As can be seen from the figure, there is a strong trigger bias, namely the tracks close to the L1 trigger object have significantly larger response than the tracks away from the trigger object. So tracks close to the L1 trigger objects are removed using a cut on d_{L1} at 0.5.

Figure 4.19 shows the distribution of energy response after removing tracks close to the L1 object. 1181 tracks remain after the cut and the mean response drops to 1.032 ± 0.007.

Single jet sample with cut on closeness to L1 trigger object and the double eγ data set with no cut on L1 trigger can be combined to have an enlarged statistics. This sample has a very small overlap (only 14 tracks in the momentum range between 40 and 60 GeV/c). A fit to a Gaussian distribution gives the mean value of 1.036 ± 0.003. Figure 4.20 shows a comparison of the response measured with the data and Monte Carlo. The two sets of data measurements peak at 1.032 while the Monte Carlo peaks at 1.022.

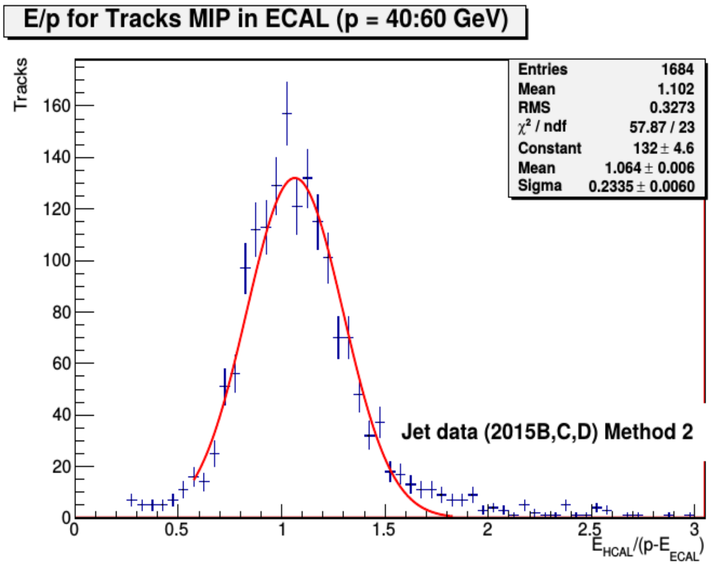

Figure 4.17: Energy response defined as the ratio of energy measured in the HCAL to the difference between track momentum and energy measured in the ECAL for all isolated track candidates satisfying L1 single jet trigger condition .

The L3 iterative method is applied to the 2015 data set from JetHT and Double eγ data stream with the silver JSON file. Figure 4.21 shows the correction factors as a function of iη for different depths from this procedure.

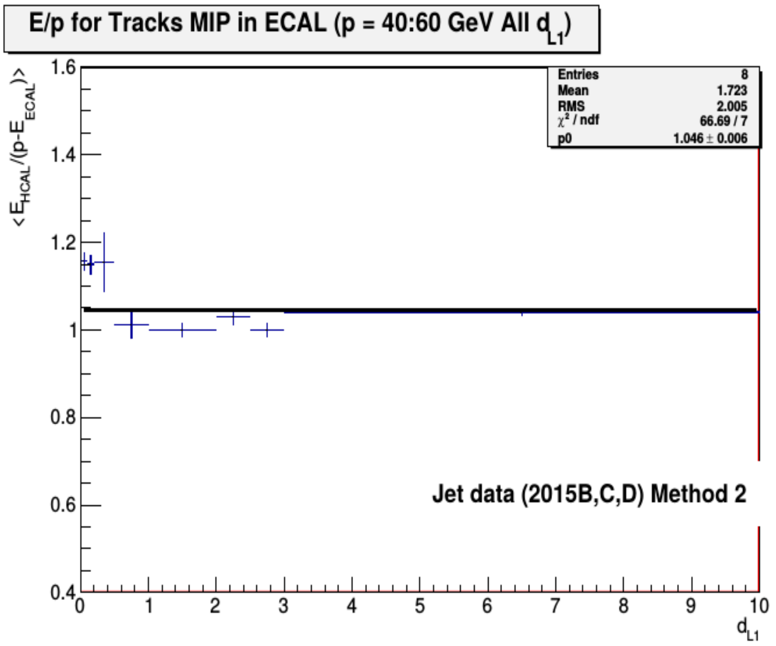

Figure 4.18: Mean energy response as a function of distance of the track from the L1 trigger object in the $(\eta - \phi)$ plane.

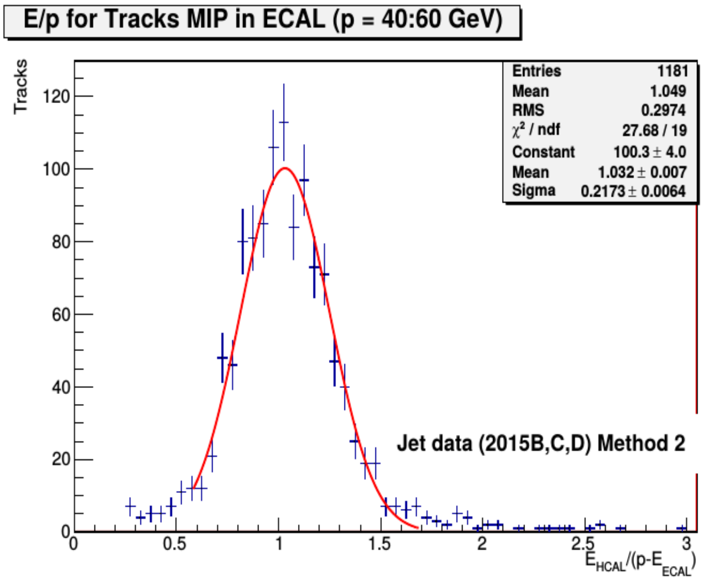

Figure 4.19: Energy response defined as the ratio of energy measured in the HCAL to the difference between track momentum and energy measured in the ECAL for isolated track candidates satisfying L1 single jet trigger criteria but away from the trigger object with $d_{L1} > 0.5$.

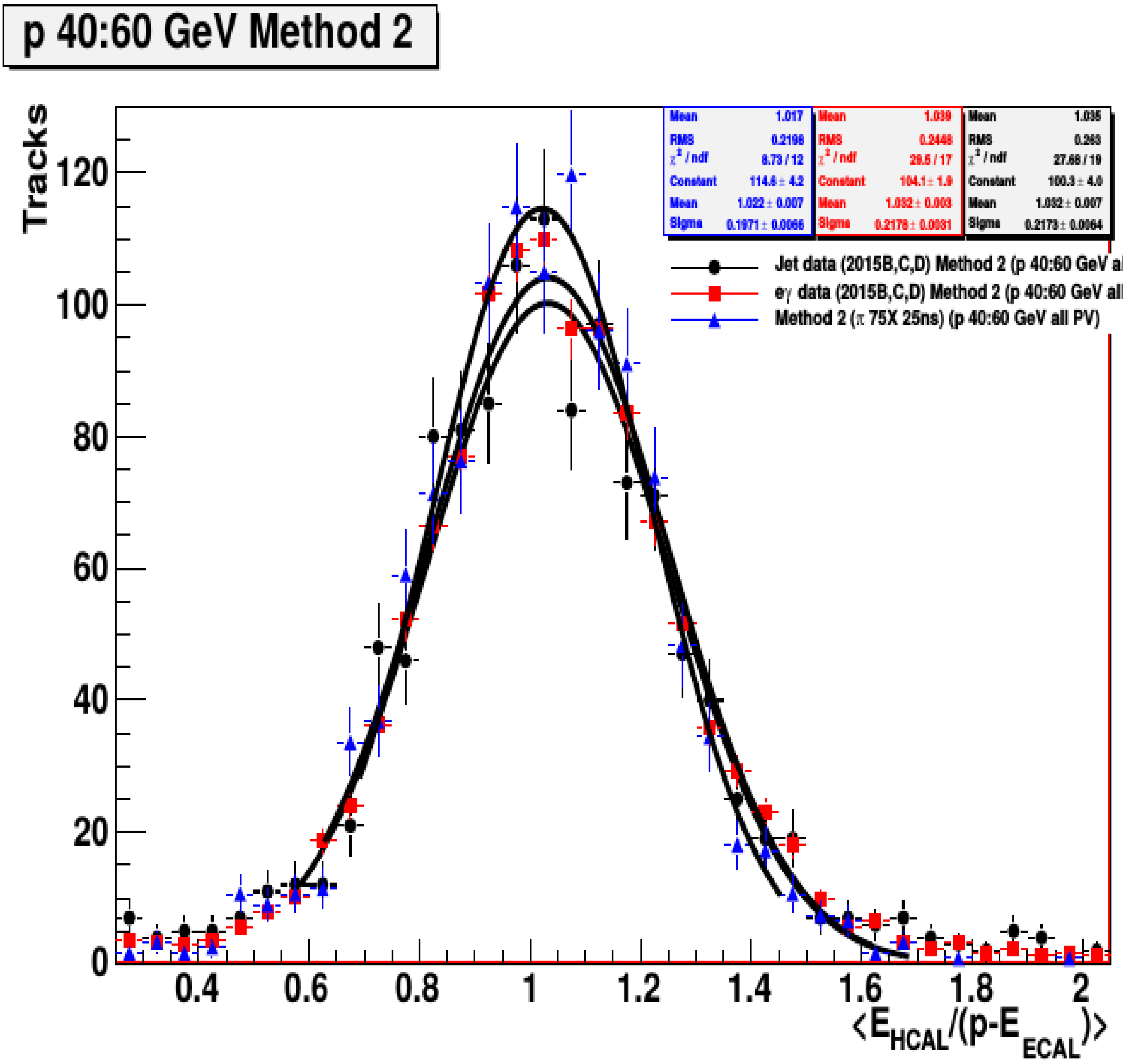

Figure 4.20: Distribution of energy response measured from two sets of data (single jet and from double $e\gamma$ sample) as well as from Monte Carlo sample.

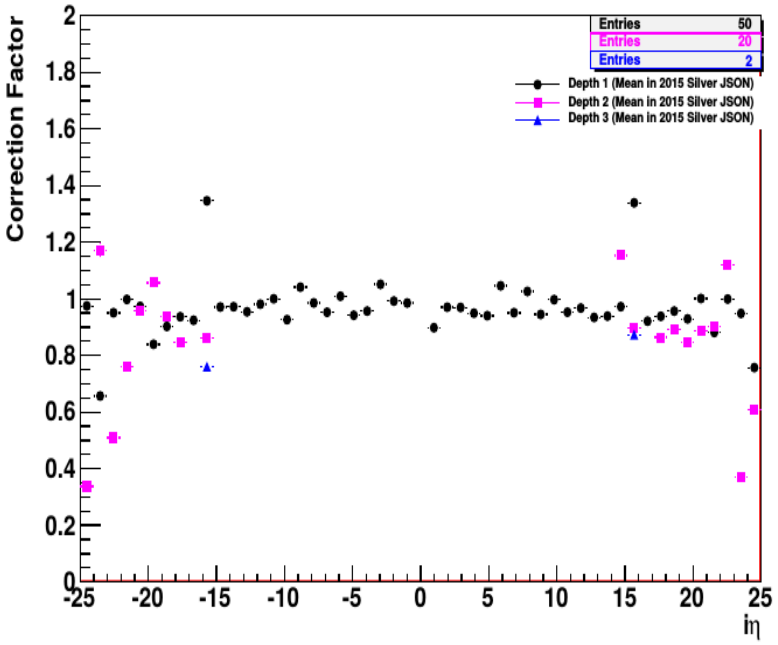

Figure 4.21: Distribution of energy response measured from two sets of data (single jet and from double $e\gamma$ sample) as well as from Monte Carlo sample.

4.4 Other Activities

I have worked for one year as the SMP-PdMV validator. Whenever new releases of CMSSW are available results from this new release are compared with the previous "validated" release. The purpose of this is to be aware of the changes being made in CMSSW and to ensure that there are no errors in it that can affect data analysis. A report is prepared to highlight in particular the salient features of the comparison, based on the validation which involves a manual, visual inspection of physical quantities of interest reconstructed in the two releases.

The CMS detector must be constantly monitored in order to ensure optimal operation and performance. For this purpose, when the detector is running or in commissioning phase, there is always a member of the shift crew monitoring the online DQM system, DAQ and DCS (Detector Control System). If problems arise in the DQM system, shifters will contact experts, or Detector On-Calls (DOCs), who will be able to diagnose and solve the problem in a timely fashion to reduce detector down time as far as possible. DCS is an automated system that controls the safe, correct and efficient operation of the detector. I have taken HCAL DOC shifts, HCAL shifts to monitor collision run remotely and on Computing CSP offline shifts during my visits to CERN.

Bibliography

[1] CMS Collaboration , “CMS physics : Technical Design Report for the Phase 1 upgrade of the Hadron Calorimeter” , CERN-LHCC-2012-015.

[2] J. Freeman, “Silicon photomultipliers for the CMS hadron calorimeter”, Nuclear Instruments and Methods in Physics Research Section A: Accelerators, Spectrometers, Detectors and Associated Equipment 617 (2010), no. 13, 393 395, doi:http://dx.doi.org/10.1016/j.nima.2009.10.132. 11th Pisa Meeting on Advanced Detectors Proceedings of the 11th Pisa Meeting on Advanced Detectors.

[3] CMS Collaboration, B. Lutz, “Upgrade of the CMS Hadron Outer Calorimeter with SiPM sensors”, in 15th International Conference on Calorimetry in High Energy Physics (CALOR 2012), volume 404, p. 012018. 2012. doi:10.1088/1742-6596/404/1/012018.

[4] CMS HCAL Collaboration, “Design, performance, and calibration of the CMS Hadron-outer calorimeter”, Eur. Phys. J. C57 (2008) 653663, doi:10.1140/epjc/s10052-008-0756-6.

[5] P.de Barbaro, “CMS Technical Design Report for the Phase 1 Upgrade of the Hadron Calorimeter”, CERN-LHCC-2012-015 (2012).

[6] S.Banerjee, “Calibration of the CMS Hadron Calorimeter with Isolated Charged Hadrons for 2016 Data”, CMS-DN-2016/029.

Chapter 5

Cross section measurements at $\sqrt{s} = 8$ TeV and final results

As described in Chapter 1, the Drell-Yan (DY) process is the annihilation of a quark-antiquark pair $q\bar{q}$ resulting in either a virtual photon γ^* or Z boson which further decays into a lepton- antilepton ($l\bar{l}$) pair. The DY process is well suited for study at LHC owing to its clean final state and large production cross section. The constraints on the Parton Distribution Functions (PDFs) can be well modeled by DY measurements, since the DY differential cross section depends on the PDFs of the colliding protons. Also, the theoretical predictions for the process calculated using FEWZ [1], being available at NNLO level, permits to study the validation of the perturbative QCD.

In this study, measurements of single and double-differential cross sections for the DY process have been done using the LHC data collected by CMS at $\sqrt{s} = 8$ TeV, corresponding to an integrated luminosity of 19.7 fb^{-1}. The study is focused on inclusive Z boson production with a subsequent decay into a pair of oppositely charged muons. The single-differential cross section has been measured with respect to phistar (ϕ^*), a kinematical variable which has better experimental resolution than p$_T$.For the double-differential measurements the dependence of the cross sections on Z boson rapidity $|y|$ has also been taken into account, by taking $|y|$ as the second independent variable.

5.1 ϕ^* variable

5.1.1 Motivation

At the energy scale of TeV, the W and Z/γ^* are produced copiously during the hadronic collisions. A good fraction of the Drell-Yan events have the dilepton system boosted in the transverse direction due to the QCD radiation in the initial state of the hard scattering in the s-channel as well as due to the underlying event activities accompanying the hard interaction. Consequently, the dilepton system has a non-zero component of the transverse momentum (q_T), which can be calculated using the gluon resummation or perturbative QCD techniques for low and high values of q_T respectively [2].

The Z boson production cross section is dominated by the low q_T spectrum which is explained by transverse-momentum resummation formalism. Furthermore, the theoretical calculation of the transverse momentum distribution for Higgs bosons produced in gluon-gluon fusion involve Sudakov form factors, which are related to the form factors used in calculations for vector bosons [3], so the measurements of vector boson production at low q_T are important for validating theoretical calculations of Higgs boson production. The correct modelling of the vector boson q_T distribution is important in many physics analyses at the LHC for which the production of W or Z bosons constitutes a significant background. Moreover, the W boson mass is dependant on the uncertainties in p_T^W, hence detail knowledge of the p_T^Z spectrum is essential for high precision measurement of W boson mass. The transverse momentum spectra of W and Z/γ^* bosons produced via the Drell-Yan mechanism have been extensively studied by the Tevatron [4–8] and the LHC [9, 10] collaborations. However, low p_T^Z measurements at these experiments were dominated by uncertainties in experimental resolutions and event selection efficiency, which had direct implication on the precision of p_T^Z measurement by constraining the bin width selection for the measurements. Hence, additional observables with lesser sensitivity to experimental uncertainties and with refined experimental resolution were investigated. One such optimal experimental observable to probe the low-p_T^Z domain of Z/γ^* production was found to be the ϕ^* [11].

5.1.2 Mathematical Formulation

The ϕ^* [12] is defined as :

$$\phi^* = \tan(\phi_{\text{acop}}/2)\sin(\theta^*_\eta) \tag{5.1}$$

where, ϕ_{acop} = π-$\Delta\phi$, $\Delta\phi$ is the azimuthal opening angle between the two leptons, and θ^*_η is the scattering angle of the leptons with respect to the proton beam direction in the rest frame of the dilepton system. θ^*_η is defined in terms of lepton variables :

$$\cos(\theta^*_\eta) = \tanh((\eta^- - \eta^+)/2) \tag{5.2}$$

where, η^- and η^+ is the pseudorapidity of the negatively and positively charged lepton, respectively. This ϕ^* variable has following advantages :

- Since ϕ_{acop} and θ^*_η depend exclusively on the directions of the two leptons, which are measured with a precision of a milliradian or better, ϕ^*_η is experimentally very well measured as compared to any other quantity that relies on the momenta of the leptons.

- ϕ^* is correlated to the quantity q_T/m_{ll} , where m_{ll} is the invariant mass of the lepton pair and q_T represents the tranverse momentum of dilepton pair, and therefore probes the same physics as the transverse momentum p_T^Z. Figure 5.1 displays the direct correlation between the variables ϕ^* and q_T as expected.

- Values of ϕ^* ranging from 0 to 1 probe the q_T distribution mainly up to ~100 GeV/c. In the present analysis, the ϕ^* ranging from 0 to 3.277 have been considerred for single differential measurement. For the double differential case, two additional bins ranging from 3.277 to 10 has been taken into account.

Owing to lesser statistics, the for the final measurements, the cross sections in these bins were not summed up to the total fiducial cross section.

- The experimental resolution for ϕ^* is significantly better than the one for q_T, which enables the possibility to better test theoretical ideas and constrain non-perturbative effects [13].

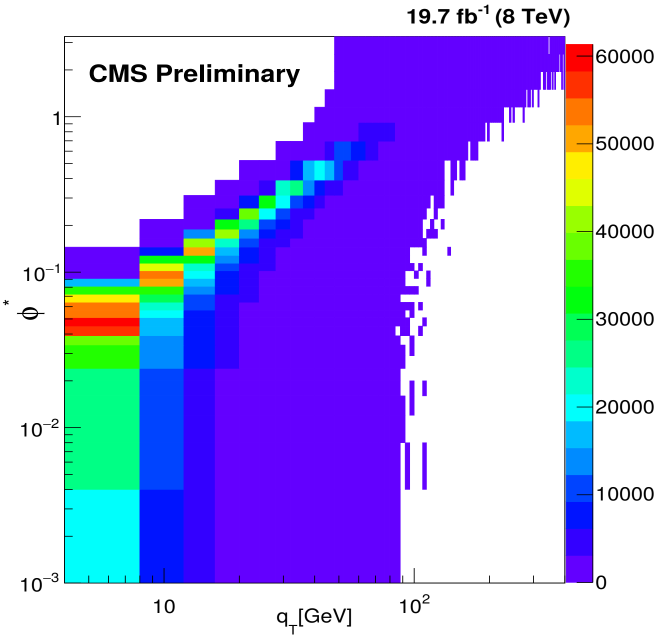

Figure 5.1: Correlation between ϕ^* and q_T(p_T of the Z), shown for Madgraph signal sample, used for the analysis.

5.1.3 Theoretical and Experimental Results

The theoretical predictions for ϕ^* variable were calculated using resummation technique [11]. The predictions were compared with the data collected by ATLAS and CMS at $\sqrt{s} = 7$ TeV within the fiducial volume mentioned in figure 5.2.

The first experimental results for ϕ^* distribution were provided by DØ collaboration [14] from a study of $p\bar{p}$ collisions of $\sqrt{s} = 1.8$ TeV corresponding to integrated luminosity of 7.3 fb^{-1}. The theoretical predictions from ResBos were compared with measured ϕ^* results in various $|y|$ bins, as shown in figure 5.3.

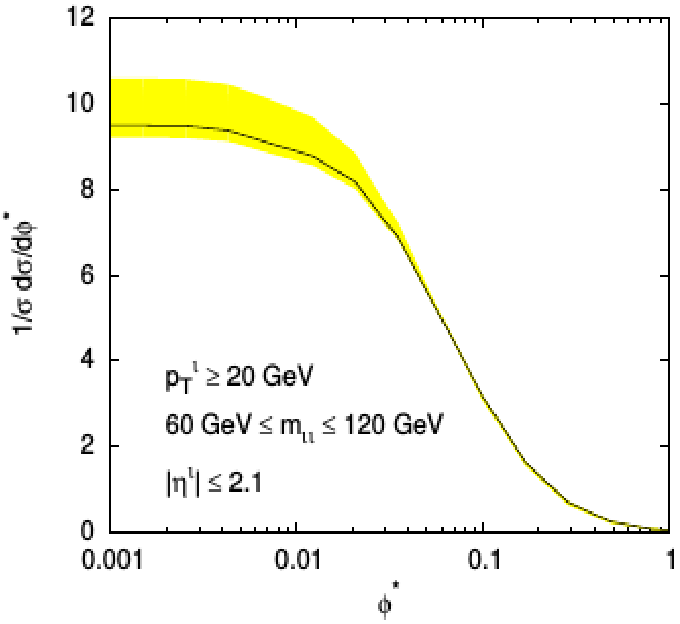

Figure 5.2: Theoretical predictions at NNLL+NLO for the normalised $\phi*$ distribution in pp collisions at 7 TeV. Figure reproduced from [11].

At the LHC, the ATLAS collaboration has published measurements of this special angular variable by measuring the $Z/\gamma^* \to e^+e^-$ and $Z/\gamma^* \to \mu^+\mu^-$ decays produced in proton-proton collisions at a center-of-mass energy of $\sqrt{s} = 8$ TeV. The data were collected with the ATLAS detector at the LHC and correspond to an integrated luminosity of 20.3 fb^{-1}. Normalized differential cross sections as a function of ${\phi_\eta}^*$ were measured separately for electron and muon decay channels. The double differential cross section was also measured as a function of ${\phi_\eta}^*$ for three independent bins of the Z boson rapidity [15]. Figure 5.4 shows the single differential ϕ^* results as compared with ResBos, using the leptons immediately after their production (referred to as Status 3 or "Born" leptons).

For the CMS experiment, the single differential DY cross section measurements have been performed at the center-of-mass energy of $\sqrt{s} = 8$ TeV, as shown in figure 5.5. The combined dielectron and dimuon cross section was compared to theory predictions from Madgraph, Powheg and Resbos [16] and results were made public in CMS document CMS-SMP-PAS-15-002.

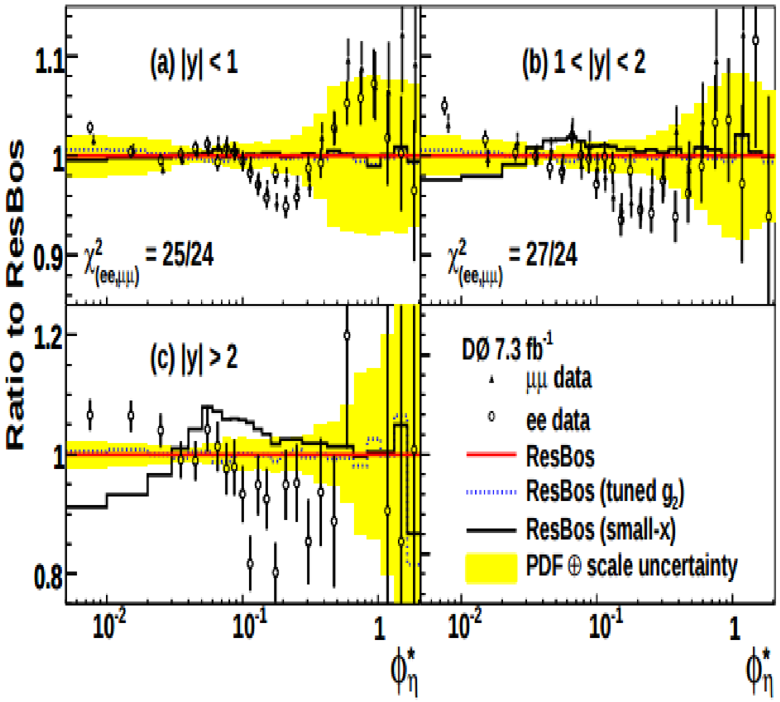

Figure 5.3: Ratio of the ϕ^* normalized data distributions to ResBos for: (a) $|y| < 1$, (b) $1 < |y| < 2$ and (c) $|y| > 2$ from DØ collaboration. The yellow band around the ResBos prediction represents the quadrature sum of uncertainty due to PDFs and QCD scale. Figure reproduced from [14].

5.1.4 ϕ^* binning

In the present analysis, the single and double differential cross section measurements have been performed in the following thirty four bins of ϕ^* :

0.0, 0.004, 0.008, 0.012, 0.016, 0.020, 0.024, 0.029, 0.034, 0.039, 0.045, 0.051, 0.057, 0.064, 0.072, 0.081, 0.091, 0.102, 0.114, 0.128, 0.145, 0.165, 0.189, 0.219, 0.258, 0.312, 0.391, 0.524, 0.695, 0.918, 1.153, 1.496, 1.947, 2.522, 3.277.

The selection of bin width for ϕ^* was done on the following basis :

- For ease of direct comparison with ATLAS analysis [15], the bin edges used

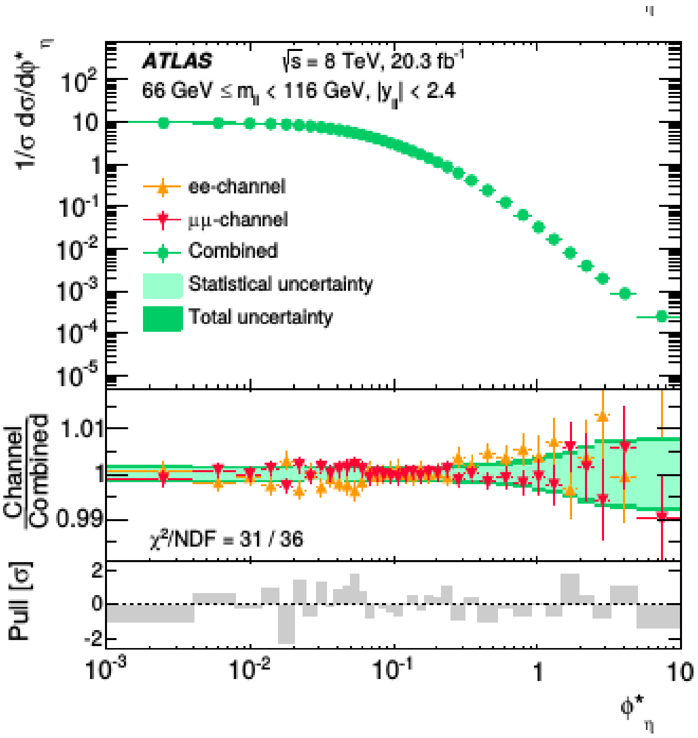

Figure 5.4: The measured normalized differential cross section $1/\sigma^{fid}$ $\mathrm{d}\sigma^{fid}/\mathrm{d}\phi_{\eta}{}^{*}$ as a function of ϕ^* $Z/\gamma^*{\to}e^+e^-$ for (closed dots) and $Z/\gamma^*{\to}\mu^+\mu^-$ (open dots) channels. The measurements as compared to ResBos predictions are represented by a line. Figure reproduced from [15].

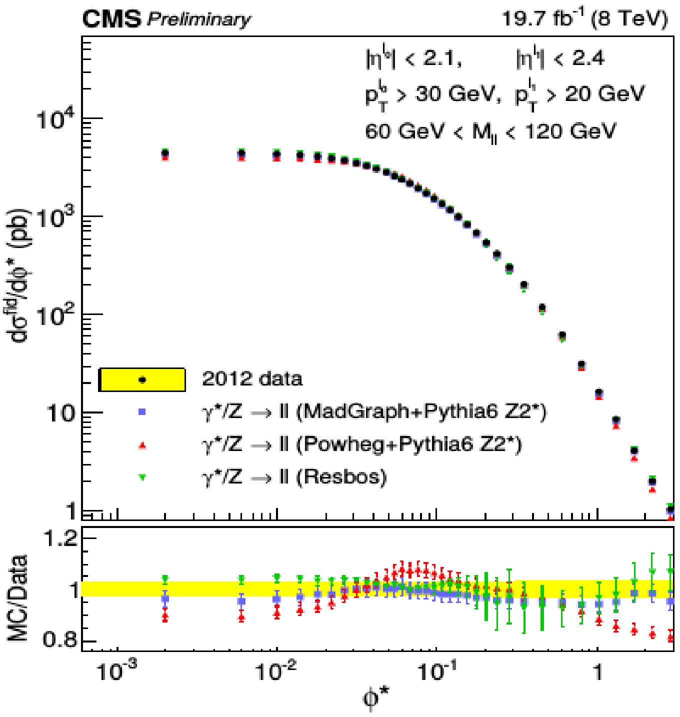

Figure 5.5: The measured absolute differential cross section $\mathrm{d}\sigma^{fid}/\mathrm{d}\phi^*$ as a function of ϕ^* for the dielectron and dimuon combined results. Figure reproduced from [16].

by ATLAS, have been taken for this measurement.

- The bin purity is evaluated and is expected to be at least 50% in each bin of ϕ^*.
- The bin resolution is each ϕ^* bin is expected to $\geq 1\sigma$.

5.2 Double Differential Measurement

Since the rapidity ($|y|$) of the dilepton system depends on the difference in the boost of the initial partons, a differential distribution in rapidity is an important input for global extraction of parton density functions. Double differential cross section $\mathrm{d}^2\sigma/\mathrm{d}\phi^*\mathrm{d}|y|$, within the fiducial volume given in table 5.2, has been measured in terms of absolute rapidity $|y|$ and ϕ^*. This measurement has been carried out using the same 2012 single muon data and simulated samples as listed in tables 5.3 and 5.4, corresponding to an integrated luminosity of 19.7 fb^{-1}.

The differential ϕ^* distribution has 36 bins, as opposed to 34 bins for 1D measurement for ease of direct comparison with ATLAS analysis. The binning has been kept the same as for 1D analysis, but two additional bins have been added corresponding to ranges ϕ^* = [3.277-5.0] and [5.0-10.0]. There are 6 rapidity bins $|y|$= [0.0-0.4], [0.4-0.8], [0.8-1.2], [1.2-1.6], [1.6-2.0] and [2.0-2.4].

5.3 Signal and Potential Backgrounds

5.3.1 Drell-Yan Signal

The work presented in this thesis is based on the DY cross section measurement in the dimuon final state. In the muon final state, the signal is divulged by the presence of oppositely charged muons, coming from the same primary vertex. An inclusive DY signal sample generated by Madgraph event generator has been used as signal sample. The details about the DY signal selection are discussed in section 5.4, whereas, the details of the signal and background samples are discussed in section 5.5 .

5.3.2 Background Processes

There are various physical processes that can mimic the Drell-Yan signal signature and are considered as backgrounds are listed in table 5.4 and are discussed below ;

- **DY → $\tau^+\tau^-$+X** process has the potential of mimicking the signal events, specially when there is no constraint on missing energy during event selection. This process will be dominant in the low and intermediate invariant mass region, ~15 GeV/c^2<$M_{\mu\mu}$<70 GeV/c^2.

- **$t\bar{t}$+jets** process can be another source of dimuons where muons are mainly due to the leptonic decays of W-bosons produced in top and anti-top decays, as shown in figure 5.6. This background region is dominant in the high-mass region of the DY mass spectrum as the muons from a top-cascade decay is highly boosted.

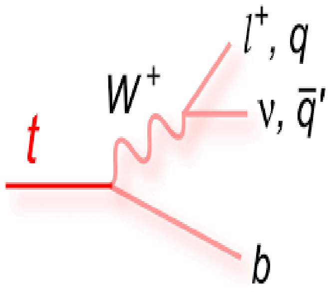

Figure 5.6: Feynman diagram depicting top quark decay into W boson. Source : https://www.quantumdiaries.org/2014/04/30/so-many-top-quarks/

- **Dibosons Production (WW, WZ and ZZ)** Among these processes, following decay modes can lead to two muons in the final state : Z→ $\mu\mu$, W→$\mu\nu$, hence WW decay can produce two muons along with two neutrinos. A fraction of dimuons coming from the processes ZZ and WZ pair decays may form same sign pairs also and these pairs can be easily removed by the opposite sign muon selection criteria.

- **W + jets** process with W→$\mu\nu$ having branching ratio of about 11%, can pose as a background, when one of the associated jets, mostly the leading one, fakes as muon, though the probability for the jet faking as muon is small $\sim 10^{-5}$. However the production rate of W+jets events is large at the LHC energy.

5.4 Event Selection

The detector signature of the DY process includes events with two oppositely charged high p_T muons. As mentioned in 5.2, several SM processes give same signature as the signal process. Hence, event selection criteria have been devised aiming to select most of the signal events with efficient rejection of background events. The event selection criteria for selecting signal events are discussed below.

5.4.1 Primary Vertex Selection

Each event is required to contain at least one well reconstructed primary vertex in order to select the good collision events. So, fake events such as those from beam-gas interactions or beam-scraping in the transport system near the interaction point are rejected using CMS recommended selection criteria for good primary vertex selection : The distance of the vertex from the nominal interaction point is required to be smaller than 24 cm in z and smaller than 2 cm in the transverse plane. The number of degrees of freedom of the vertex fit is required to be larger than 4. Out of the selected vertices, the one with the largest summed squared p_T of the tracks associated to it, is chosen as the event vertex corresponding to the hard scattering process. The selection criteria have an overall efficiency of $\approx$ 99% and is imposed on the simulated samples as well, to remove the detector noise and the beam background.

5.4.2 Trigger Requirement

During 2012 data taking period, the inclusive single muon events were collected online by using HLT_IsoMu24_eta2p1 unprescaled trigger path. The trigger requires at least one muon with transverse momentum of at least 24 GeV/c and pseudorapidity (η) of 2.1 : ($p_T \geq 24$ GeV/c and $|\eta| \leq 2.1$). The Level-1 trigger (L1) seed for the HLT is L1 SingleMu16, which has lower p_T threshold of 16 GeV/c. The efficiency of this HLT path as a function of muon p_T and η was studied by Muon POG, as shown in figure 5.7.

5.4.3 Muon Identification

The muons are reconstructed from the particle flow (PF) algorithm. Muon candidates are required to satisfy the standard CMS muon "TIGHT" identification and quality criteria as defined by the Muon POG [17]. The details of the identification algorithm are discussed in Section 3.3.5 and listed in table 5.1. In general, the muon identification is based on the number of hits found in the tracker, the response of the muon chambers, and a set of matching criteria between the muon track parameters determined by the inner tracker section of the detector and as measured in the muon chambers. To suppress the contamination of muons contained in jets, the CMS recommended PF relative isolation (details in section 3.3.5) selection is imposed on all muon candidates. The efficiency of the muon identification and isolation selection applied as a function of muon p_T and η was studied by Muon POG, as shown in figure 5.8.

5.4.4 Z Boson Reconstruction

The Z boson candidates are reconstructed from events satisfying the following conditions offline :

- Inclusive dimuon events with two oppositely charged and well isolated muons are selected. Both the muons should have passed CMS recommended

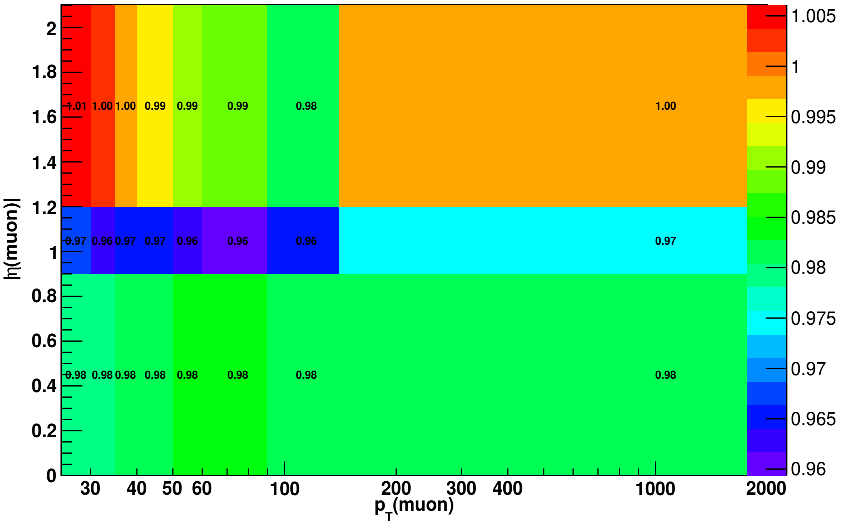

Figure 5.7: Muon selection efficiency of HLT_IsoMu24_eta2p1 trigger.

Variable	**Cut**
isGlobal	$= 1$
isPFMuon	$= 1$
global track χ^2	< 10
number muon hits	> 0
number matched stations	> 1
number pixel hits	> 0
number tracker layers with hits	> 5
|dxy| (cm)	< 0.2
dz (cm)	< 0.5

Table 5.1: List of CMS recommended selection cuts applied on various muon identification and reconstruction variables, for identification of "good" (TIGHT) muons.

"TIGHT" identification and isolation requirements.

- The transverse momentum p_T of leading muon should be greater than 30 GeV/c and pseudorapidity (η) should be less than 2.1. The sub-leading muon should have $p_T > 20$ GeV/c and $\eta < 2.4$.
- The leading muon should match to the muon used for triggering the event. The events are selected if the separation between leading muon and trigger object $\Delta R = \sqrt{\Delta\eta^2 + \Delta\phi^2} < 0.4$.

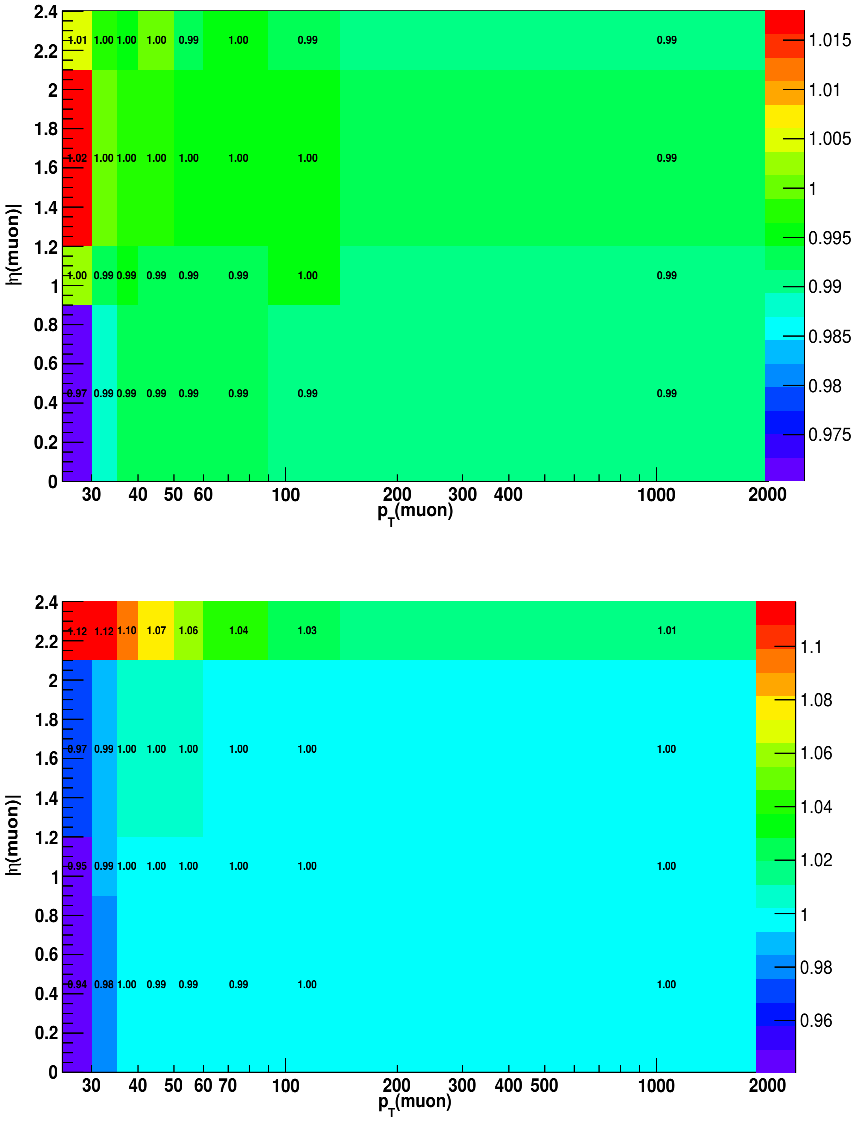

Figure 5.8: Efficiency for muon identification and isolation criteria as a function of muon transverse momentum and pseudorapidity.

- The invariant mass of the chosen pair ($M_{\mu\mu}$) should lie in the range 60 to 120 GeV/c^2. Table 5.2 gives the detail of fiducial region defined for the measurement.

$60 < M_{\mu\mu}(GeV/c^2) < 120$
$p_{T_{\mu_1}} > 30$ GeV/c , $\|\eta_{\mu_1}\| < 2.1$
$p_{T_{\mu_2}} > 20$ GeV/c, $\|\eta_{\mu_2}\| < 2.4$
$\phi^* < 3.277$

Table 5.2: The fiducial volume of the analysis, where $M_{\mu\mu}$ and p_{T_μ} are in GeV/c^2 and GeV/c, respectively.

5.5 Data and Simulation samples

The CMS experiment has collected a large sample of pp collisions data at a centre of mass energy of 8 TeV from the Large Hadron Collider (LHC). The Single Muon dataset corresponding to the entire 8 TeV proton-proton run period of 2012 is used in the present study. The analysis is based on the dataset collected when all sub-detectors of the CMS experiment have been functioning optimally and corresponds to an integrated luminosity of 19.7 fb^{-1}. The details of the dataset are listed in table 5.3.

Several Monte Carlo samples, as listed in table 5.4, are used for estimating contributions from various background processes which can mimic our signal process. An inclusive DY sample (Z/γ^* + jets), having only Z+4 hard jets events considered for NLO calculations, is used as signal sample. The sample has been generated using Madgraph event generator using CTEQ6L1 PDF set. PYTHIA6 is used for parton showering and hadronization and to account for underlying events, Z2star tune is used. The effect of FSR, i.e., photon bremsstrahlung off a muon, is implemented using PYTHIA.

Data Samples	**Run-Range**	$\mathcal{L}$ (fb^{-1})
/SingleMu/Run2012A-22Jan2013-v1/AOD	190456-193621	0.876
/SingleMu/Run2012B-22Jan2013-v1/AOD	193833-196531	4.412
/SingleMu/Run2012C-22Jan2013-v1/AOD	198022-203742	7.055
/SingleMu/Run2012D-22Jan2013-v1/AOD	203777-208686	7.369

Table 5.3: Collision data used in the analysis.

All the MC samples have been processed with a detailed simulation of the CMS detector using the GEANT4 framework.

5.5.1 Corrections on Data and Simulation

The data and simulation need to be corrected for various detector inefficiencies and misalignment. The data and the signal MC have been corrected for the tracker misalignment by applying CMS recommended Rochester corrections [18]. These corrections are applied on the transverse momentum of each of the muons in an event in both data and MC. The correction factors are calculated for each muon, by considering the charge (Q),η, and ϕ dependence in the reconstruction of the muon momentum for both samples.

The number of pileup events varies in both data and signal MC. To account for this difference, the pileup in signal MC is reweighted to pileup in data collected at $\sqrt{s}$ = 8 TeV, to replicate the same distribution as in the data. The fraction of events with "k" vertices in the data is compared to fraction of events with "k" vertices in the simulated sample. Pileup weight factor (WF) is extracted from the ratio :

$$\mathrm{WF} = \frac{\mathrm{N_k^{data}}}{\mathrm{N_k^{MC}}} \tag{5.3}$$

and is subsequently applied to all events with "k" number of vertices in the simulated sample.

To compensate for the difference in identification and isolation of the muons in the data and the MC, efficiency corrections are applied to the simulated events at reconstruction level. Similarly, the differences in Single Muon trigger efficiencies

Dataset	**Event statistics**	**Cross section** (pb)	**Kinematical selection**
Drell–Yan (Signal Madgraph)	30459503	3531.9	$M_{\mu\mu}$> 50GeV/c
Drell–Yan (Signal Powheg)	48079142	1966.7	$M_{\mu\mu}$>20 GeV/c
$t\bar{t}$+Jets	36842585	132.9	no cuts
$Z \rightarrow \tau\tau$	48079421	1966.7	$M_{\tau\tau}$> 20 GeV/c
W+Jets	75322433	37509	no cuts
WW	9976539	54.838	no cuts
WZ	9978840	33.2	no cuts
ZZ	9976144	17.7	no cuts
tW	497658	11.1	no cuts
$\bar{t}W$	493460	11.1	no cuts
QCD (15–20 GeV/c)	1722326	7.022E8	μ-enriched
QCD (20–30 GeV/c)	8484987	2.87E8	μ-enriched
QCD (30–50 GeV/c)	9557271	6.609E7	μ-enriched
QCD (50–80 GeV/c)	10359290	8082000	μ-enriched
QCD (80–120 GeV/c)	9228248	1024000	μ-enriched
QCD (120–170 GeV/c)	8484014	157800	μ-enriched
QCD (170–300 GeV/c)	7640592	34020	μ-enriched
QCD (300–470 GeV/c)	7767143	1757	μ-enriched
QCD (470–600 GeV/c)	3733404	115.2	μ-enriched
QCD (600–800 GeV/c)	4053456	27.01	μ-enriched
QCD (800–1000 GeV/c)	4031950	3.57	μ-enriched
QCD(1000 GeV/c –∞)	3794205	0.77	μ-enriched

Table 5.4: Summary of analyzed MC samples for the signal and various background processes.

between data and simulation are corrected for simulation by the corresponding scale factors. The scale factor is the ratio of muon identification (isolation/trigger) efficiency in data to the efficiency in MC and is estimated as a function of muon p$_T$ and η. The simulation is then reweighted by the ratio :

$$\mathrm{SF} = \frac{\epsilon_{\mathrm{data}}}{\epsilon_{\mathrm{MC}}} \tag{5.4}$$

These scale factors (SFs) are recommended by the Muon POG and applied on the two muons used for Z boson reconstruction. The identification and isolation scale factors are listed in tables 5.5, 5.6 and 5.7.

$\boldsymbol{p_T}$ (GeV/c)	$\mathbf{0 < \|\eta\| \leq 0.9}$	$\mathbf{0.9 < \|\eta\| \leq 1.2}$	$\mathbf{1.2 < \|\eta\| \leq 2.1}$	$\mathbf{2.1 < \|\eta\| \leq 2.4}$
$20 < p_T \leq 25$	0.989 ± 0.002	0.994 ± 0.002	1.000 ± 0.001	0.998 ± 0.003
$25 < p_T \leq 30$	0.992 ± 0.001	0.995 ± 0.001	0.998 ± 0.001	0.996 ± 0.002
$30 < p_T \leq 35$	0.993 ± 0.001	0.993 ± 0.001	0.997 ± 0.001	1.001 ± 0.002
$35 < p_T \leq 40$	0.994 ± 0.000	0.992 ± 0.001	0.996 ± 0.001	0.993 ± 0.001
$40 < p_T \leq 50$	0.992 ± 0.000	0.992 ± 0.000	0.996 ± 0.000	0.995 ± 0.001
$50 < p_T \leq 60$	0.991 ± 0.001	0.995 ± 0.001	0.995 ± 0.001	0.994 ± 0.003
$60 < p_T \leq 90$	0.989 ± 0.001	0.990 ± 0.002	0.992 ± 0.002	0.989 ± 0.005
$90 < p_T \leq 140$	1.004 ± 0.003	1.009 ± 0.006	1.023 ± 0.005	1.060 ± 0.013
$140 < p_T \leq 300$	1.019 ± 0.017	1.011 ± 0.033	0.975 ± 0.030	0.891 ± 0.142

Table 5.5: Muon Identification scale factors (Data/MC) for Tight ID.

$\boldsymbol{p_T}$ (GeV/c)	$\mathbf{0 < \|\eta\| \leq 0.9}$	$\mathbf{0.9 < \|\eta\| \leq 1.2}$	$\mathbf{1.2 < \|\eta\| \leq 2.1}$	$\mathbf{2.1 < \|\eta\| \leq 2.4}$
$20 < p_T \leq 25$	0.977 ± 0.002	0.986 ± 0.003	0.990 ± 0.002	1.116 ± 0.004
$25 < p_T \leq 30$	0.996 ± 0.001	1.000 ± 0.002	1.003 ± 0.001	1.097 ± 0.003
$30 < p_T \leq 35$	0.993 ± 0.001	1.000 ± 0.001	1.004 ± 0.001	1.075 ± 0.002
$35 < p_T \leq 40$	0.994 ± 0.001	0.999 ± 0.001	1.002 ± 0.001	1.061 ± 0.002
$40 < p_T \leq 50$	0.994 ± 0.000	0.999 ± 0.000	1.001 ± 0.000	1.038 ± 0.001
$50 < p_T \leq 60$	0.996 ± 0.000	0.998 ± 0.001	1.000 ± 0.000	1.025 ± 0.002
$60 < p_T \leq 90$	0.999 ± 0.001	0.999 ± 0.001	1.001 ± 0.001	1.015 ± 0.002
$90 < p_T \leq 140$	1.000 ± 0.001	1.001 ± 0.002	0.999 ± 0.001	1.008 ± 0.005
$140 < p_T \leq 300$	0.999 ± 0.003	1.002 ± 0.005	0.996 ± 0.003	1.011 ± 0.018

Table 5.6: Muon Isolation scale factors (Data/MC).

$\boldsymbol{p_T}$ (GeV/c)	$\mathbf{0 < \|\eta\| \leq 0.9}$	$\mathbf{0.9 < \|\eta\| \leq 1.2}$	$\mathbf{1.2 < \|\eta\| \leq 2.1}$
$30 < p_T \leq 35$	0.984 ± 0.001	0.965 ± 0.002	1.001 ± 0.001
$35 < p_T \leq 40$	0.984 ± 0.000	0.967 ± 0.001	0.996 ± 0.001
$40 < p_T \leq 50$	0.983 ± 0.000	0.967 ± 0.001	0.994 ± 0.001
$50 < p_T \leq 60$	0.984 ± 0.001	0.963 ± 0.002	0.991 ± 0.002
$60 < p_T \leq 90$	0.985 ± 0.001	0.960 ± 0.003	0.988 ± 0.003
$90 < p_T \leq 140$	0.981 ± 0.003	0.964 ± 0.010	0.982 ± 0.008
$140 < p_T \leq 500$	0.980 ± 0.008	0.971 ± 0.026	0.994 ± 0.028

Table 5.7: Muon trigger scale factors (Data/MC) for HLT_IsoMu24_eta2p1.

5.6 Data and Simulation Comparison

It is mandatory to investigate the compatibility between the 2012 data and simulation samples (listed in table 5.4) for each of the Z boson variables to check the reliability of the detector simulation. Data need to be described as good as possible by the simulation. After applying the respective corrections, the reconstructed kinematic distribution in the data are compared with the prediction from the simulated DY Madgraph signal and the simulated background processes. The signal and various background samples used within the fiducial volume are listed in table 5.4. The event yield for MC simulated samples are normalized to their respective production cross section (σ, listed in table 5.4) and luminosity ($\mathrm{L} = 19.7\ \mathrm{fb}^{-1}$) of the collision data using the weight factor (w) which is calculated as:

$$\mathrm{w} = \frac{\sigma \cdot \mathrm{L}}{\mathrm{N}} \tag{5.5}$$

To quantify possible disagreements between the data and the MC, for each reconstructed distribution, the ratio of the data to the simulated prediction is presented. The error bars on the histograms correspond to the error on the ratio of the data/MC and are calculated by combining statistical errors on the data and the simulation by simple error propagation. The kinematic variables for leading and subleading muons are shown in figures 5.9, 5.10 and 5.11. The overall disagreements between the data and the MC are within statistical uncertainty.

The reconstructed data-MC comparison for ϕ^* dependent variables : $\tan(\phi_{acop}/2)$ and $\Delta\phi$ are depicted in figure 5.12. Similarly, for Z reconstructed from two oppositely charged muons, the mass, p_T, η and ϕ are shown in figures 5.13 and 5.14. The invariant mass distribution underlines reasonable overall agreement within 3% between the data and simulation. The dip around M_Z value is due to different muon momentum resolutions in the data and MC. The p_T distribution shows an excellent agreement of the order of 98%, for $\mathrm{p}_T < 150$ GeV/c, but for higher values of p_T, the disagreement increases to 5% between the data and MC. Similarly, the figure 5.15 shows the data-MC comparison for ϕ^* variable before the removal of the detector effects from the data. Overall agreement between the data and MC is at the level of 95 % for low range of ϕ^* and for higher range of ϕ^* the agreement decreases to 90%.

The event yield in the data and MC after applying all the selection cuts is given in table 5.8. Table also lists the number of events surviving after each se-

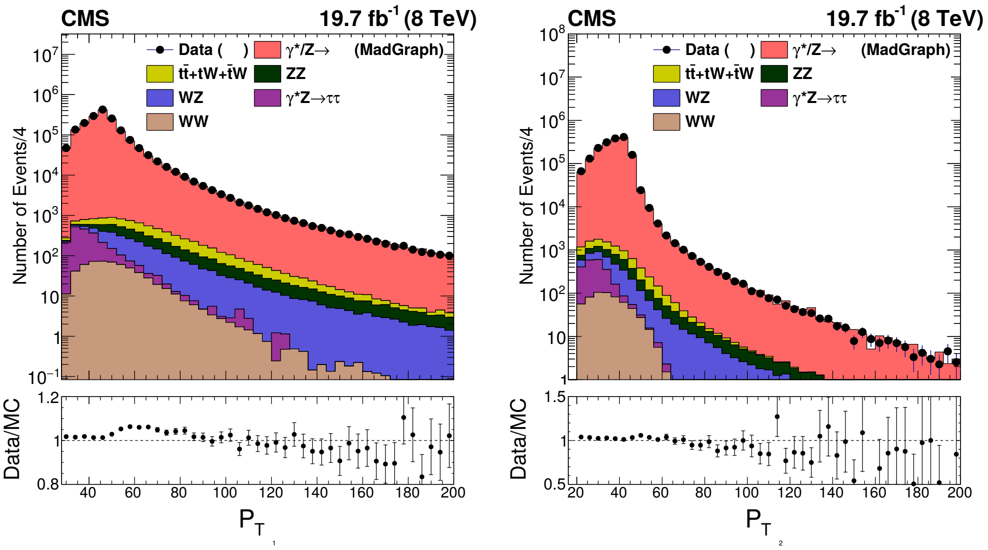

Figure 5.9: Data and MC comparison of the Leading muon p_T (left) and Subleading muon p_T(right).

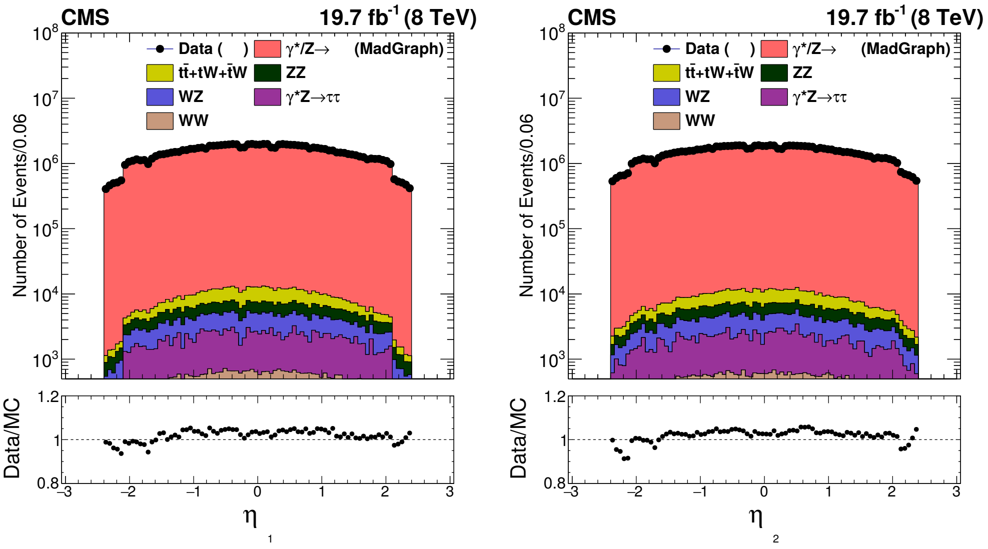

Figure 5.10: Data and MC comparison of the Leading muon η (left) and Subleading muon η(right).

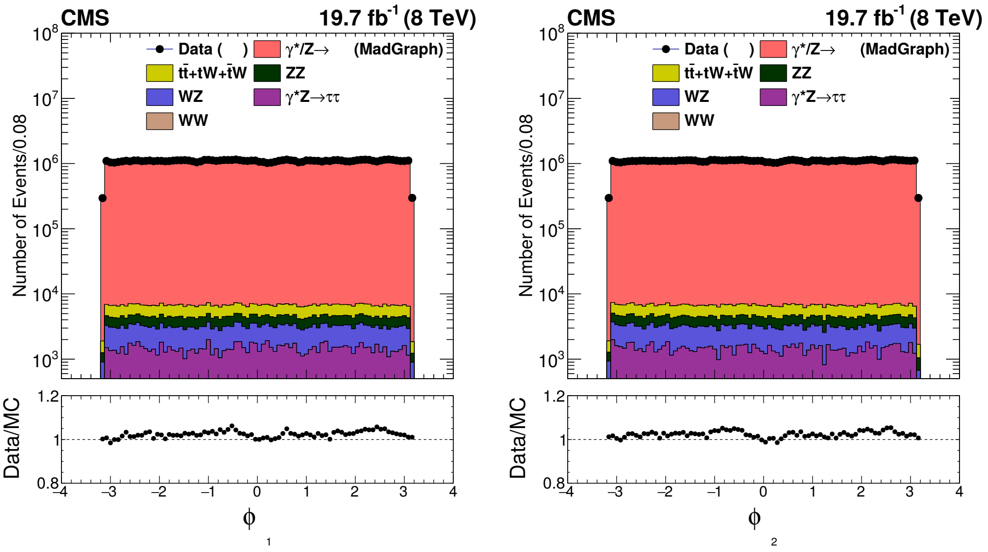

Figure 5.11: Data and MC comparison of the Leading muon ϕ (left) and Subleading muon ϕ (right).

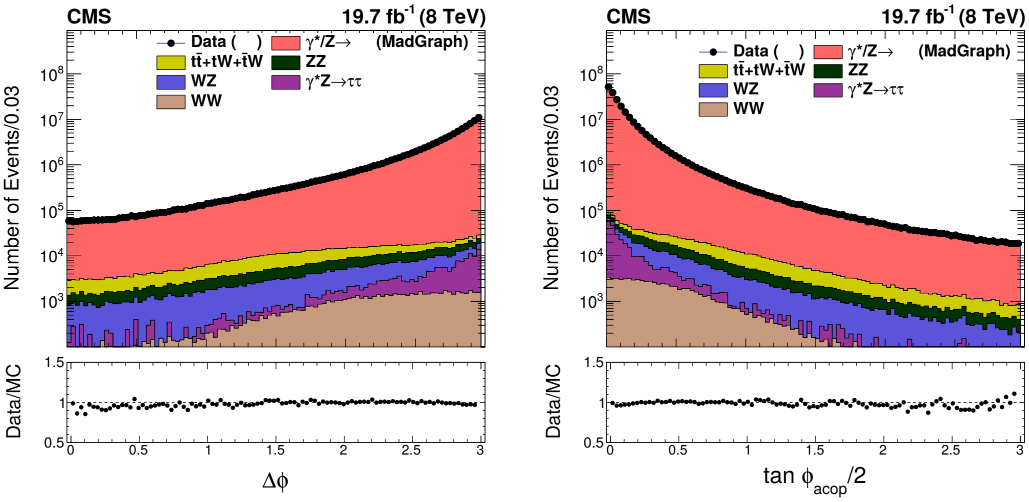

Figure 5.12: Data and MC comparison of the azimuthal opening angle between two muons $\Delta\phi$ (left) and $\tan(\phi_{acop}/2)$ for Madgraph sample.

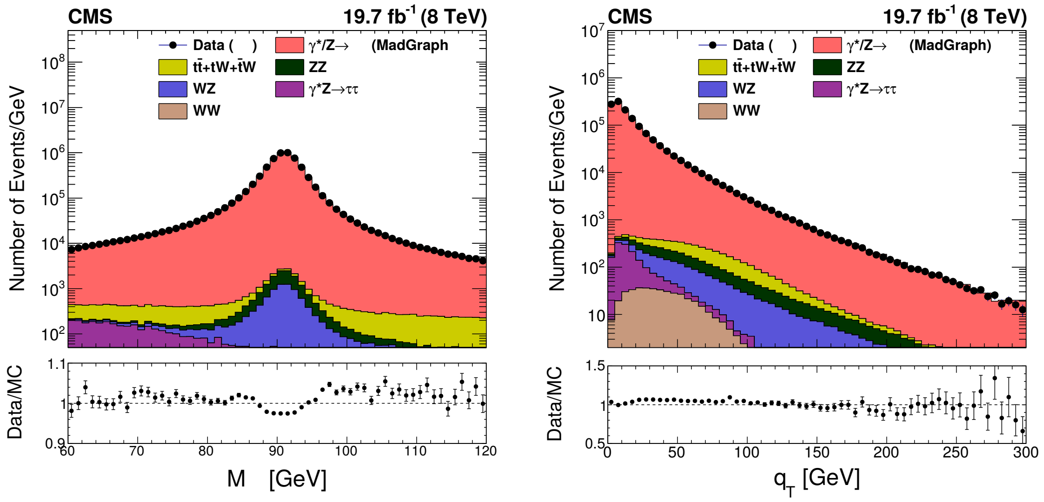

Figure 5.13: The dimuon invariant mass spectrum (left) and dimuon transverse momentum (right).

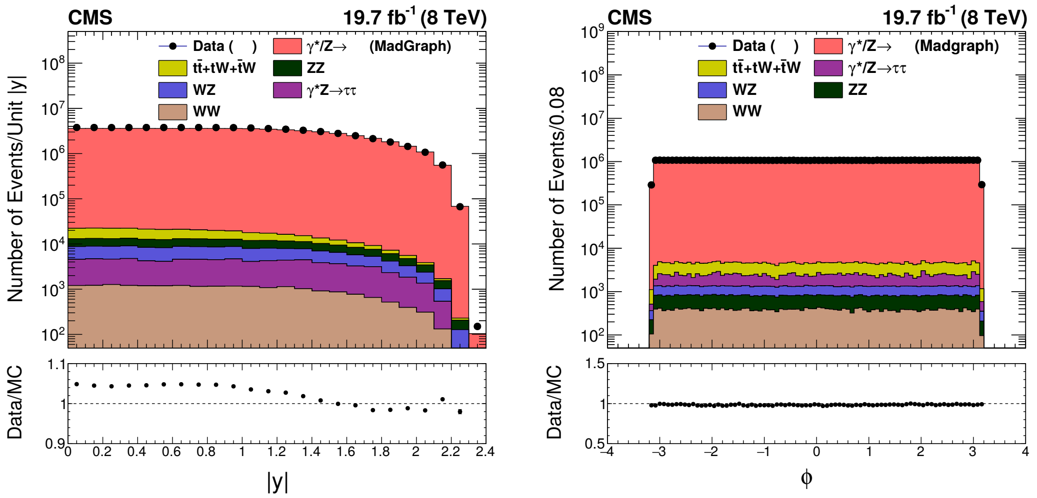

Figure 5.14: Left: Rapidity distribution of Z. Right: ϕ distribution of Z for Madgraph sample.

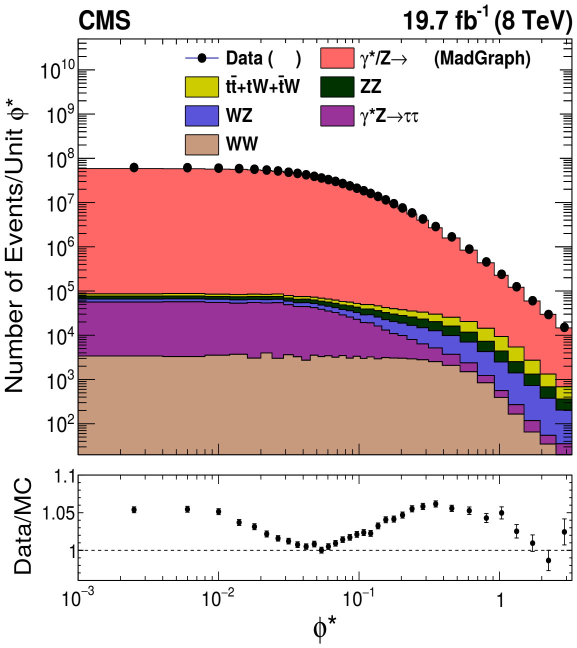

Figure 5.15: Data and MC comparison for ϕ^* variable in logarithmic scale.

lection cut imposed on both the data and simulation. A total of 6.7 million events survive after final event selection in the data. However, the total event yield from simulation is less than that from data, which clearly signifies the insufficient events generated in signal sample. All the numbers for the simulation listed in the table have been normalized to the luminosity using equation 5.5.

The data and simulation samples have been compared in various bins of $|y|$, after applying relevant corrections as discussed in Section 5.5.1. Figures 5.16 to 5.21 show the comparison of ϕ^* distribution reconstructed in the data and all simulated samples in 6 bins of $|y|$. The ratio of the data to the simulated prediction is shown. The error bars in the lower panel correspond to statistical errors coming from both the data and the simulation.

For first two $|y|$ bins [0.0-0.4] and [0.4-0.8], disagreement between the data and MC is of the order of 10% in the lower ϕ^* bins and increases to 20% in the higher ϕ^* region. The order of discrepancy for next $|y|$ bins [0.8-1.2] and [1.2-1.6]

Event Sample	**muon ID + ISO**	**ID + ISO + Trig.**	**Trig. + ISO+kine.**	**Trig.+ID+ISO kine.+ mass**
DY→ $\mu\mu$ (MadGraph)	8638644	7731117	6847546	6716901
DY→ $\mu\mu$ (Powheg)	10745260	7898541	6827558	6671730
DY→ $\tau\tau$	110280	41650	9670	6290
$t\bar{t}$ ($\ell\ell$)+ Jets	35394	35321	26913	11531
$t\bar{t}$ (ℓ)+Jets	370	366	63	41
Total $t\ \bar{t}$ +Jets	35764	35687	26976	11572
W+Jets	1423	1413	20	20
WW	6389	6378	4795	2271
WZ	3843	3804	3229	3077
ZZ	3182	3165	2664	2516
tW	1710	1706	1309	557
$\bar{t}W$	1708	1704	1310	557
QCD(50-80) multijets	896894	608064	-	-
QCD(120-170) multijets	8698	6886	1812	-
QCD(170-300) multijets	1648	1301	521	-
Total background	1008043	747445	79282	38432
Total Signal+back.	9646687	8478562	6926828	6755333
Collision Dataset A	393027	392347	315821	304857
Collision Dataset B	1962291	1958302	1571409	1517510
Collision Dataset C	3153672	3150715	2529530	2442693
Collision Dataset D	3170337	3168184	2551498	2463397
Full Collision Dataset	8679327	8669548	6968258	6728457

Table 5.8: Cumulative event yields after applying selection criteria from MC samples, normalized to integrated lumi of 19.7 fb^{-1}, and comparison with yield in the collision data.

increases upto 15% in the lower ϕ^* bins and to 20% in the higher ϕ^* region. In the last two $|y|$ bins corresponding to values [1.6-2.0] and [2.0-2.4], higher discrepancies are observed; 20% in the lower ϕ^* bins and up to 40% in the higher ϕ^* region, owing to lower statistics.

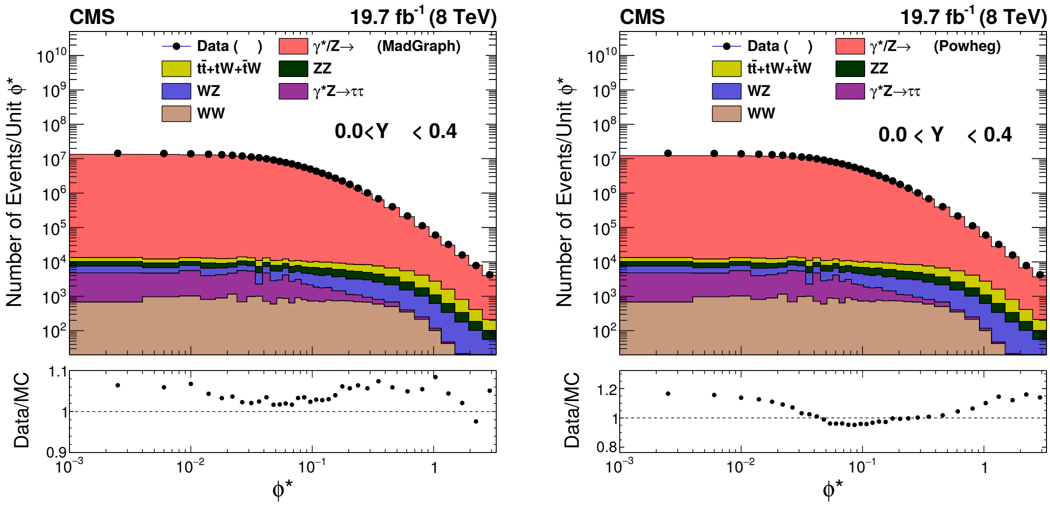

Figure 5.16: Data and MC comparison for ϕ^* variable in logarithmic scale for the $|y|$ range of [0.0-0.4] for Madgraph (left) and Powheg (right) signal samples.

5.7 Background Estimation

The overall background contribution from the processes discussed in Section 5.3 is of the order of 0.5%. Table 5.9 lists the individual contribution from each source with respect to data and total backgrounds considered in the analysis. Over 40% of the background comes from events where a Z-boson was produced in association with another Z- or W-boson. We consider these events as part of the background due to their different production mechanism compared to single Z-boson events. The rest of the background is dominated by $t\bar{t}$ production. For the double differential measurement, the backgrounds have been estimated in all bins of $|y|$ using the same procedure as followed for single differential measurement, since the overall background contribution is same as in the single differential measurement.

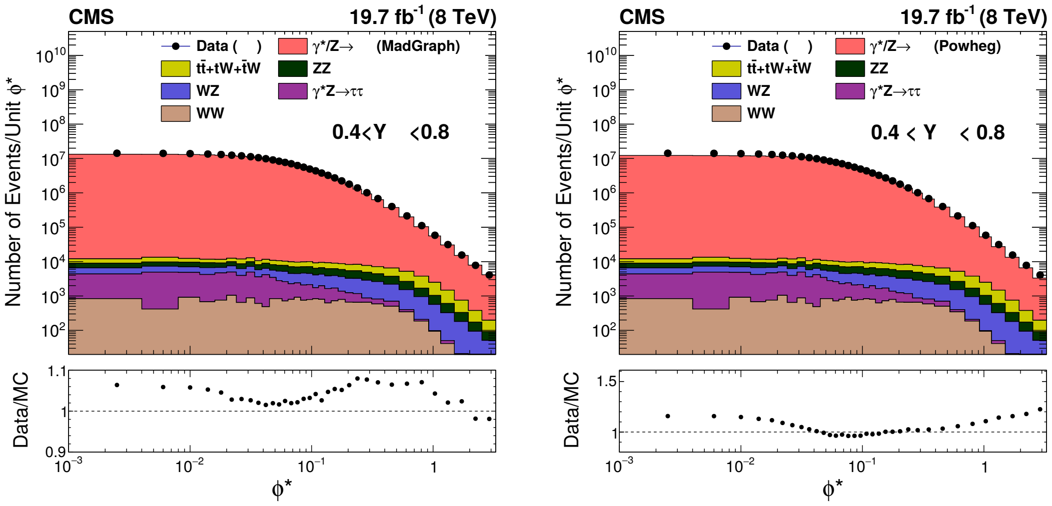

Figure 5.17: Data and MC comparison for ϕ^* variable in logarithmic scale for the $|y|$ range of [0.4-0.8] for Madgraph (left) and Powheg (right) signal samples.

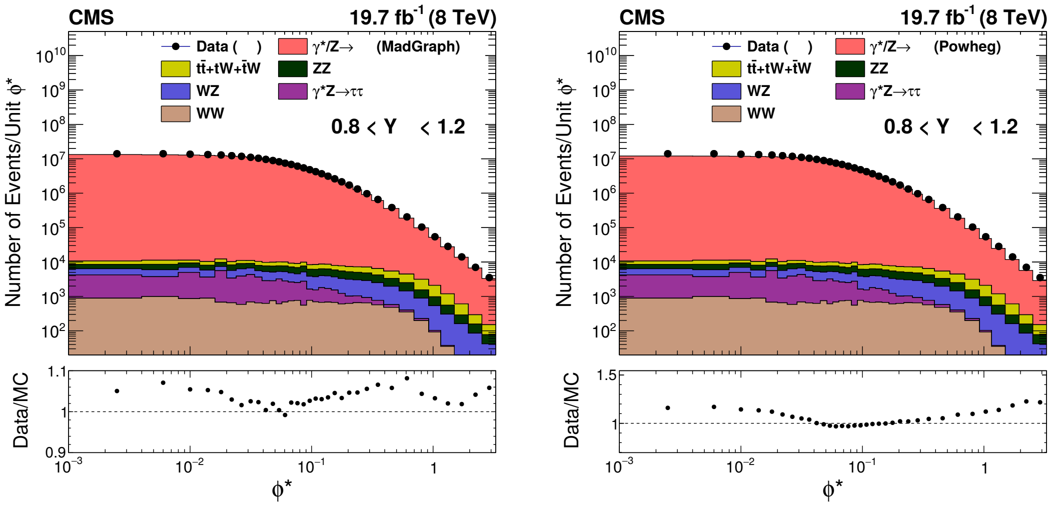

Figure 5.18: Data and MC comparison for ϕ^* variable in logarithmic scale for the $|y|$ range of [0.8-1.2] for Madgraph (left) and Powheg (right) signal samples.

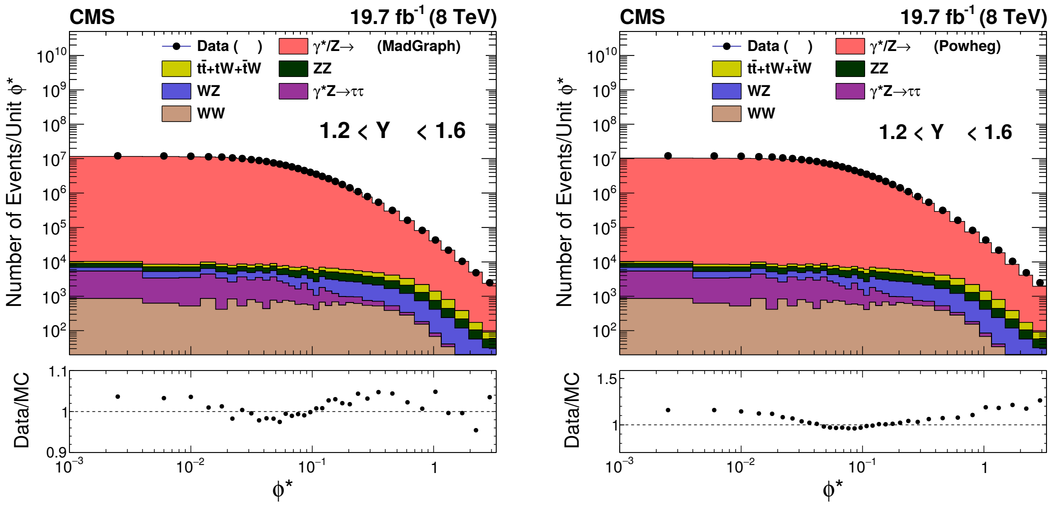

Figure 5.19: Data and MC comparison for ϕ^* variable in logarithmic scale for the $|y|$ range of [1.2-1.6] for Madgraph (left) and Powheg (right) signal samples.

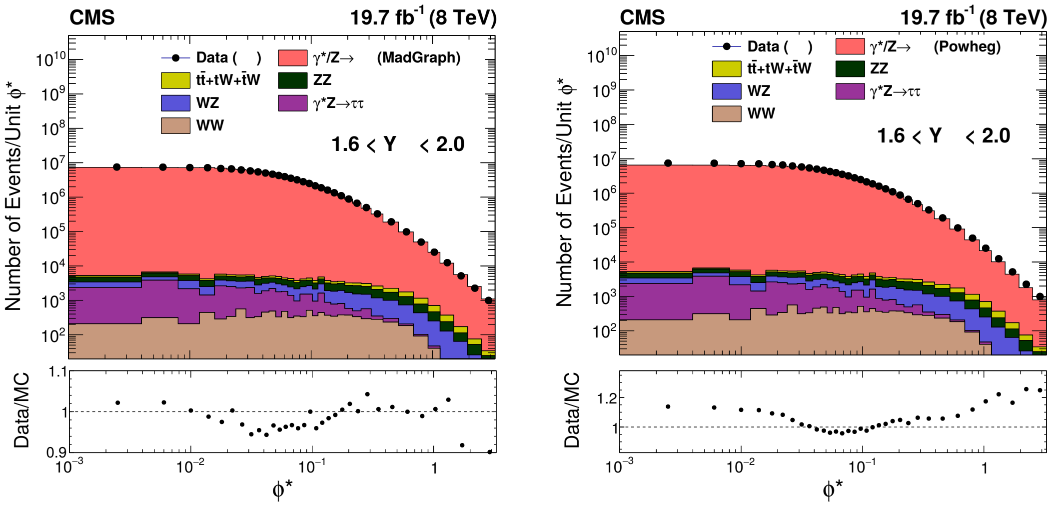

Figure 5.20: Data and MC comparison for ϕ^* variable in logarithmic scale for the $|y|$ range of [1.6-2.0] for Madgraph (left) and Powheg (right) signal samples.

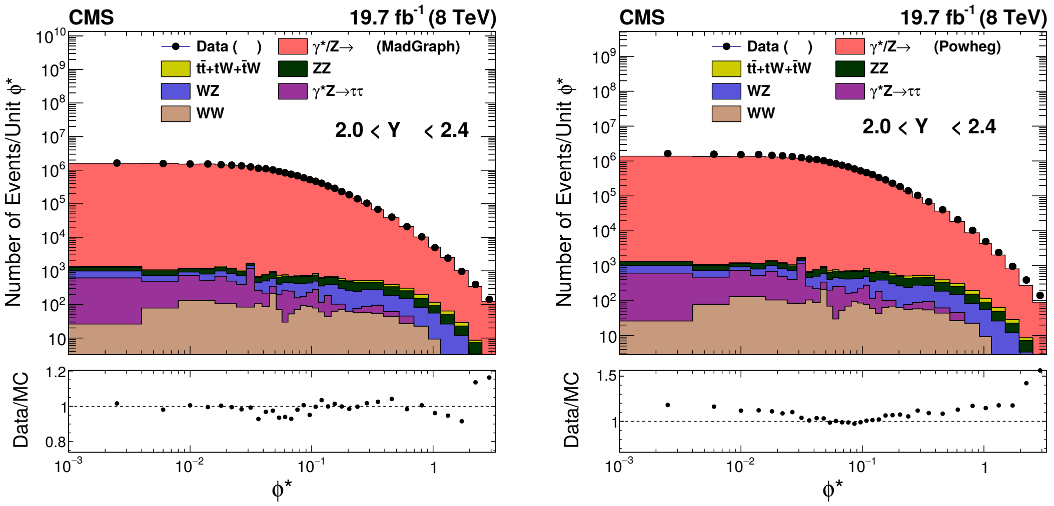

Figure 5.21: Data and MC comparison for ϕ^* variable in logarithmic scale for the $|y|$ range of [2.0-2.4] for Madgraph (left) and Powheg (right) signal samples.

Process	**percentage of data**	**percentage of background**
Signal: $Z \to \mu^+\mu^-$	99.4725	N.A.
$t\bar{t}$	0.16	30.8183
ZZ	0.11	21.2529
$W^\pm Z$	0.11	21.0196
$Z \to \tau^+\tau^-$	0.09	17.8509
W^+W^-	0.03	6.09806
$tW^-\&\bar{t}W^+$	0.0275	2.96024

Table 5.9: Data sample composition as a percentage of the total and as a percentage of just the backgrounds.

The flavour symmetric backgrounds, $t\bar{t}$, inclusive Z→ $\tau\tau$, and WW, are estimated using data driven approach which is based on lepton universality. The contributions coming from flavour symmetric background processes are estimated using the information solely from the data. [1]. An eμ control sample is produced for the estimation, since the ratio of e$^\pm$ $\mu^\mp$ to $\mu^\pm\mu^\mp$ events is the same. From the collision data, an eμ pair is selected per event and the background yield in data $(\text{Data yield})_{\mu\mu}$ is estimated as :

$$(\text{Data}\,\text{yield})_{\mu\mu} = \frac{(\text{Data}\,\text{yield})_{e\mu}}{(\text{MC}\,\text{yield})_{e\mu}} \cdot (\text{MC}\,\text{yield})_{\mu\mu} \tag{5.6}$$

---

[1] Data-driven means that progress in an activity is compelled by data, rather than by intuition or by personal experience.

where $(\mathrm{Data\,yield})_{e\mu}$ refers to the event yield obtained in data, $(\mathrm{MC\,yield})_{e\mu}$ is the sum of the event yields obtained in the MC for the flavour symmetric processes (i.e, for $\mathrm{t\bar{t}}$, inclusive $Z \rightarrow \tau\tau$, and the dibosons WW) for eμ final state. Finally, $(\mathrm{MC\,yield})_{\mu\mu}$ is the sum of event yields obtained in the same backgrounds for $\mu\mu$ final state.

The event selection for the muon leg of the eμ final state is similar to that of the signal $\mu\mu$ process. Explicitly, the following event selection criteria are applied on the electron and muon.

- The trigger selection is exactly the same, except that the muon must be matched to the trigger. The muon in the control sample is required to be matched to the HLT muon object within a δR <0.5.
- Using the official muon POG tight identification and tight isolation criteria, the muon is selected which must have a transverse momentum p_T> 30 GeV/c and pseudorapidity $|\eta|$< 2.1 .
- The electron selected using the electron-POG recommended identification and isolation criteria, must have a transverse momentum p_T> 20 GeV/c and pseudorapidity $|\eta|$< 2.4.
- If more than one $\mathrm{e}^{\pm}\mu^{\mp}$ combination are possible in an event, the pair whose invariant mass is closer to the nominal PDG value of $\mathrm{M}_{e\mu}$ is selected.
- The invariant mass of the $\mathrm{e}^{\pm}\mu^{\mp}$ pair is required to lie within 60 and 120 GeV/c^2 .

Figure 5.22 (left) shows the ϕ^* distribution in eμ final state, after applying above listed selection requirements. The $t\bar{t}$ production process populate the higher ϕ^* region, as the resulting leptons are highly energetic and boosted. The bottom panel of the plot shows the data to MC ratio for the eμ final state and agreement between them is within the statistical errors. The data-MC ratio is used as “scale factor” for each ϕ^* bin to normalize the content of the corresponding bin in the

$\mu\mu$ final state, as explained in equation 5.6. The flavour symmetric backgrounds as estimated by using the data driven method are compared to the different background components in figure 5.22 (right) and the total estimate from this method is consistent with the data.

However, it is evident from figure 5.22 (left) that contribution for the signal DY sample to the eμ final state is quite high. The reason for this strange behavior was investigated and it was found that muons were being mis-identified as electrons. This is due to the fact that the muon track is bent by the strong magnetic field which results in photon emission by brehmsstrahlung. Hence, during object reconstruction, an electromagnetic shower gets linked with each muon track and gets mis-identified as an electron. Thus the same object gets counted as an electron as well as a muon. However, the total background contribution is less than 1%, hence the backgrounds were estimated from simulation. Table 5.10 shows the results from both the approaches and the difference is found to be negligible.

The bin wise event yield in the data and MC is given in table 5.11 for $\mu\mu$ final state. The total background (except column 3 of the table), is subtracted bin-wise from the data yield before the data unfolding.

Bkg. processes	**Estimation from simulation**	**Data driven estimation**
$t\bar{t}$	11678	11126
DY$\rightarrow \tau\tau$	6861	6732
WW	2388	2284
tW	565	540
$\bar{t}$W	563	538
WZ	3138	-
ZZ	2581	-
W+jets	22	21
QCD	-	-

Table 5.10: Comparison of background rates estimated from simulation and using a data-driven method.

ϕ^* range	**Data yield**	**DY→ $\mu\mu$**	**DY→ $\tau\tau$**	**$t\bar{t}$**	**Dibosons**	**Single Top**	**Net Bkg**
0.000-0.004	247296	219231	234.03	35.97	44.29	5.30	219551
0.004-0.008	245547	217916	226.49	36.41	43.76	7.52	218230
0.008-0.012	239799	216107	231.52	35.71	45.05	2.65	216422
0.012-0.016	233888	213188	183.70	35.97	46.86	4.86	213460
0.016-0.020	226423	208851	231.52	36.86	41.89	4.86	209166
0.020-0.024	217065	204811	186.22	34.16	48.05	4.42	205084
0.024-0.029	258488	248763	266.75	46.14	54.64	7.95	249138
0.029-0.034	242108	239284	279.33	44.23	57.36	4.85	239670
0.034-0.039	227837	228274	183.70	46.83	54.70	4.85	228564
0.039-0.045	254467	259882	269.27	54.14	63.56	5.74	260274
0.045-0.051	234561	243875	223.97	54.48	68.65	4.42	244226
0.051-0.057	215201	228091	198.8	55.95	65.54	6.17	228417
0.057-0.064	230891	245427	236.55	63.69	79.39	5.73	245812
0.064-0.072	240225	254701	203.84	73.49	85.45	5.74	255069
0.072-0.081	241801	257756	206.35	82.62	98.71	6.62	258150
0.081-0.091	237938	253554	259.20	90.52	107.97	9.28	254021
0.091-0.102	231928	245527	203.84	101.72	120.60	7.06	245960
0.102-0.114	221958	232995	166.09	114.98	125.99	11.91	233414
0.114-0.128	224674	234352	256.68	133.84	152.53	12.81	234908
0.128-0.145	233308	241210	249.13	162.35	176.84	18.53	241817
0.145-0.165	229893	236248	226.48	185.14	210.12	18.09	236888
0.165-0.189	226007	229813	213.90	221.55	247.46	22.96	230519
0.189-0.219	226260	228361	181.19	278.84	297.91	22.53	229141
0.219-0.258	227082	227788	229.00	360.25	376.16	30.88	228784
0.258-0.312	229091	228189	218.94	498.64	495.78	66.69	229469
0.312-0.391	225988	222310	239.07	728.56	653.25	63.58	223994
0.391-0.524	222467	216213	296.95	1186.4	903.99	109.07	218719
0.524-0.695	151403	142569	135.89	1419.4	861.78	138.64	145124
0.695-0.918	101232	92375.6	88.07	1494.04	699.18	139.99	94797
0.918-1.153	56057	48794	40.26	1106.19	432.92	98.45	50472
1.153-1.496	42803	36112.2	25.16	955.74	344.87	75.96	37524
1.496-1.947	27162	22674.5	27.68	595.03	230.24	57.83	23585
1.947-2.522	16884	13720.4	7.55	343.76	153.62	37.54	14263
2.522-3.277	11364	9096.17	12.58	224.21	104.38	25.18	9462

Table 5.11: Bin-wise event yield for 2012 Data, signal and the various background processes in the $\mu\mu$ final state.

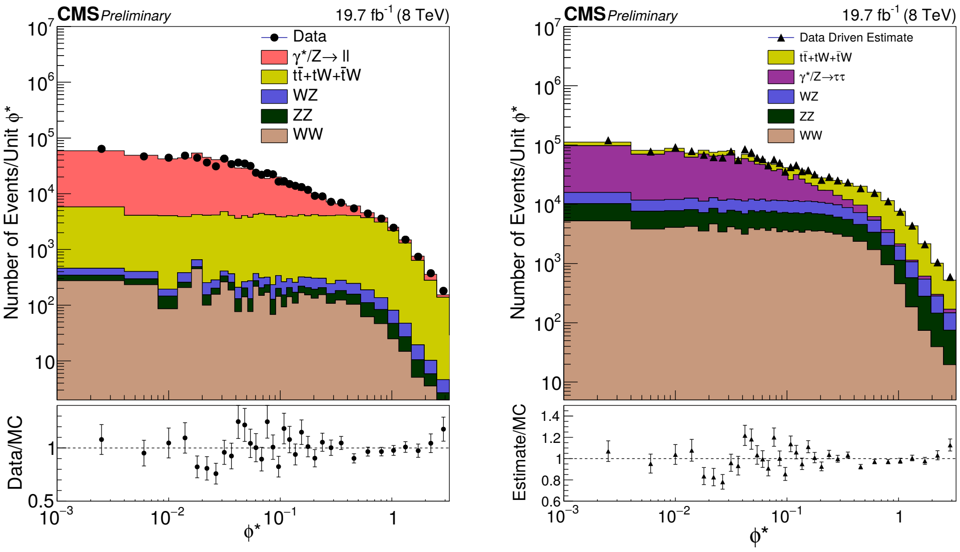

Figure 5.22: Left : ϕ^* distribution for the eμ final state obtained from the data and compared with the estimate from MC (before unfolding). Right : ϕ^* distribution in $\mu\mu$ final state from background processes including bin-wise scale factors.

5.8 Unfolding

The measured observables presented in this analysis differ from the corresponding true observables due to the finite detector resolution and acceptance. Hence, detector level distributions have to be corrected for these detector effects in order to compare the measured observables to the theoretical predictions. Therefore, after removing the estimated background contribution, the data is unfolded from the reconstructed ϕ^* distribution to the production level ϕ^* distribution. Here, the true quantity refers to the ϕ^* at generator level while the measured quantity to the ϕ^* at reconstruction level. The measured ϕ^* value in ith bin is given as :

$$\mathrm{x_i^{measured}} = \Sigma_\mathrm{k} \mathrm{R_{ik} x_k^{true}} \tag{5.7}$$

R$_{ik}$ is the square matrix which represents the order of bin migration for the ϕ^* variable and is known as the Response Matrix. An element R$_{ik}$ of the matrix refers to the probability of ϕ^* being reconstructed in a certain bin i, given that the corresponding true value lies in some other bin k. The matrix is evaluated within the fiducial region given in table 5.2 using the signal Madgraph sample. The response matrices for the DY Madgraph and Powheg signal samples are shown in figure 5.23. The order of bin migration is $\approx 1\%$ and the matrix is diagonal for the DY Madgraph and Powheg signal samples.

The information contained in the Response Matrix along with the reconstructed and generated ϕ^* distribution for the signal MC is used for unfolding the measured ϕ^* distribution in data. Iterative Bayesian Method, used to remove the detector effects, is implemented in the RooUnfold package [19]. This method uses an iterative approach and requires the number of iterations as an input parameter. In this analysis, the iteration procedure continues until the new unfolded distribution is compatible with the one obtained from the previous step. For each iteration, the unfolded distribution is multiplied by the response matrix to get back the reconstructed distribution which is then compared to the original reconstructed distribution. The number of iterations are tuned according to the sample statistics and binning. In practice, the results are fairly insensitive to the precise setting used and four iterations are sufficient.

5.8.1 Closure Tests

A closure test is the process of unfolding the reconstructed MC distributions and then comparing the resulting distribution to the corresponding generator level distribution. The different cross closure tests have been tried in order to check the performance of the unfolding procedure in various observables and with different settings, as listed below :

- **Same Sample Closure** : The measured ϕ^*distribution from Madgraph is unfolded and compared with the generated spectrum from Madgraph itself. Figure 5.24 illustrates results of this trivial closure test. Ideally, after unfolding, the ratio of corrected (or unfolded) to the generated should be 1, if all detector effects have been removed from the resulting distribution post unfolding. The closure test was also performed for Powheg DY signal sample.

- **Different Sample Closure** : The response matrix from one MC generator (Madgraph or Powheg) is used to unfold the measured ϕ^* distribution in second MC generator. For instance, figure 5.25 (left) shows the ratio of the unfolded ϕ^* distribution to the generated distribution for the Madgraph sample, by using the response matrix evaluated from the Powheg MC generator. The ratio deviates from 1 due to difference in level of acceptance for both generators.

- **Half Sample Closure** : For this closure, each simulated sample was divided into two statistically independent samples of equal size. One half was used to unfold the reconstructed ϕ^* distribution of the second half and vice versa. The resulting two correlated unfolded distributions for each sample are shown in figure 5.26.

For all the closure tests performed, the Bayesian unfolding method was able to reproduce the generated distribution within the assigned uncertainties. Hence, these tests validated the method used for unfolding the data.

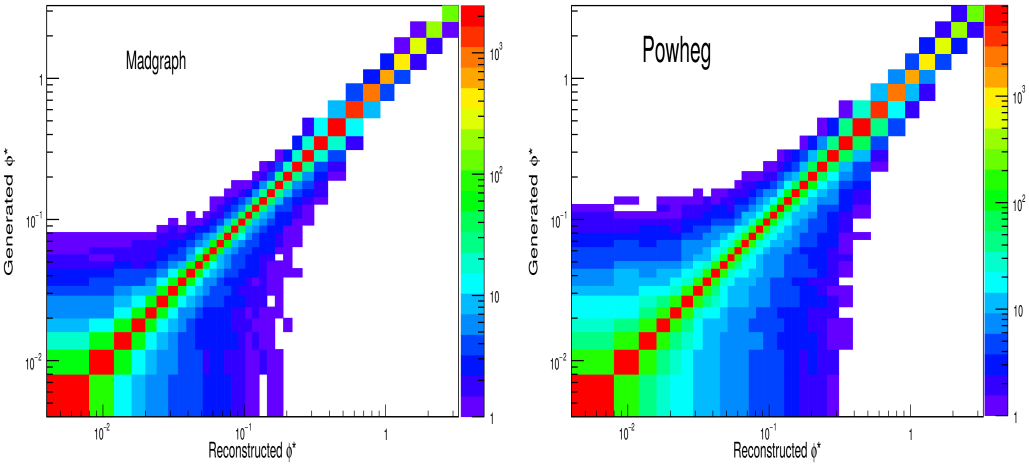

Figure 5.23: Response matrix: reconstructed ϕ^* as a function of generated ϕ^* for Madgraph (Left) and Powheg (Right) samples.

A total of 216 (ϕ^*, y) bins have been considered for double differential measurement to facilitate unfolding and to consider intermediate results. Table 5.12 lists all (ϕ^*, y) bins and their respective ϕ^* and $|y|$ ranges.

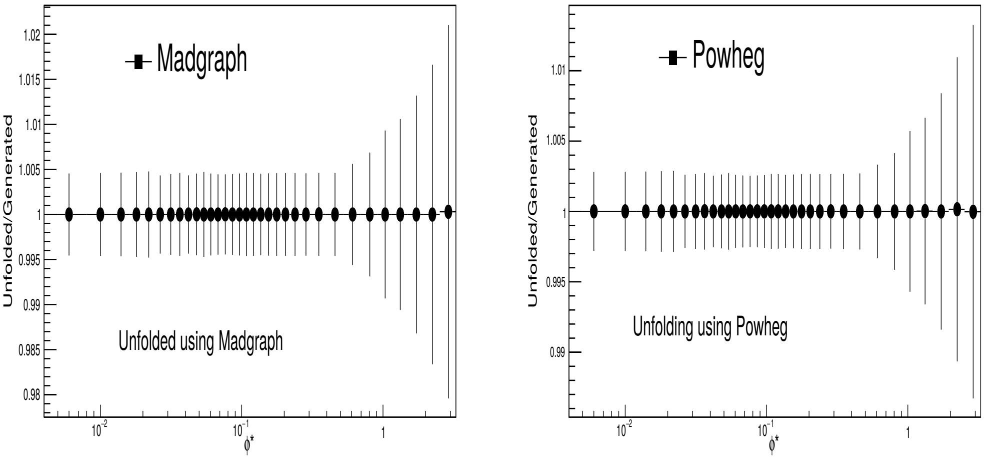

Figure 5.24: Closure test with unfolded ϕ^* distribution from Madgraph (Left) and Powheg (Right) reconstructed sample and the same from generator level information using the sample of full statistics.

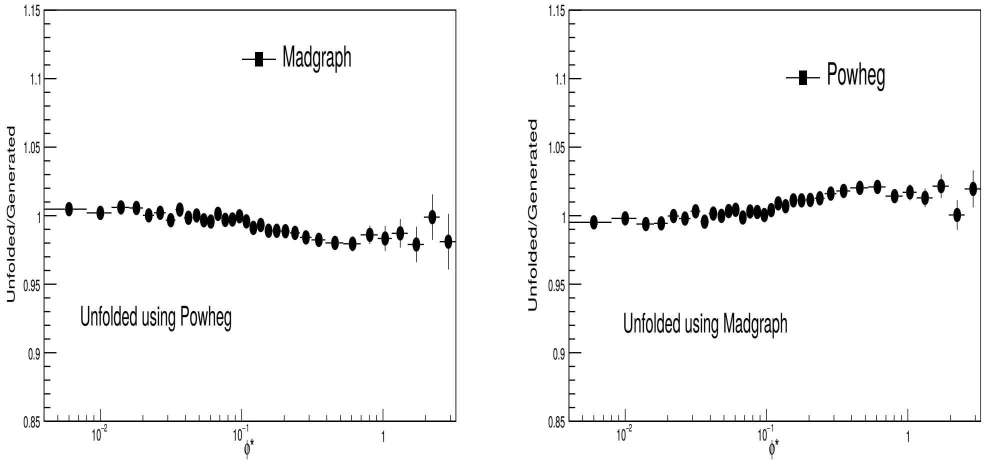

Figure 5.25: Closure test with unfolded ϕ^* distribution from Madgraph (Left) and Powheg (Right) reconstructed sample and the from different generator level information using the sample of full statistics.

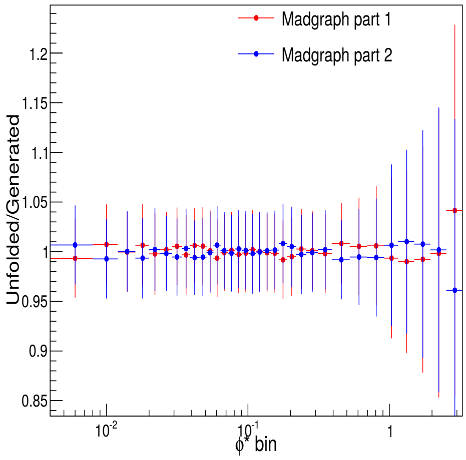

Figure 5.26: Closure test with unfolded ϕ^* distribution from Madgraph reconstructed sample and the same from generator level information using a sample of half statistics for unfolding.

Due to the finite detector resolution in muon angular reconstruction, the resolution of the reconstructed $|y|$ and ϕ^* is limited. The reconstruction resolution of ϕ^* is evaluated as :

$$\text{resolution} = \frac{\delta_{\text{diff}}}{\phi^*_{\text{generated}}} \tag{5.8}$$

where,

$$\delta_{\text{diff}} = \phi^*_{\text{generated}} - \phi^*_{\text{reconstructed}} \tag{5.9}$$

Similarly, the reconstruction resolution of $|y|$ is defined in terms of its reconstructed and generated values. The ϕ^* and $|y|$ resolutions are shown in figure 5.27 and 5.28 for Madgraph and Powheg signal samples. This finite resolution results in some events being reconstructed in a different ϕ^* and y bins than they originated.

The variation of reconstructed (ϕ^*, y) as a function of generated (ϕ^*, y) is illustrated in figure 5.29. The bin migration, which is defined in terms of diagonal and off-diagonal (ϕ^*, y) elements is of the order of about 6% for both signal samples. The iterative Bayesian method [19] is used with 4 iterations for correcting the bin migration. The same set of closure tests, discussed in section 5.8.1, are performed for the double differential measurement and for all tests done, the unfolding method was able to reproduce the generated distribution within assigned uncertainties. Results from various closure tests are shown in figures 5.30, 5.31 and 5.32.

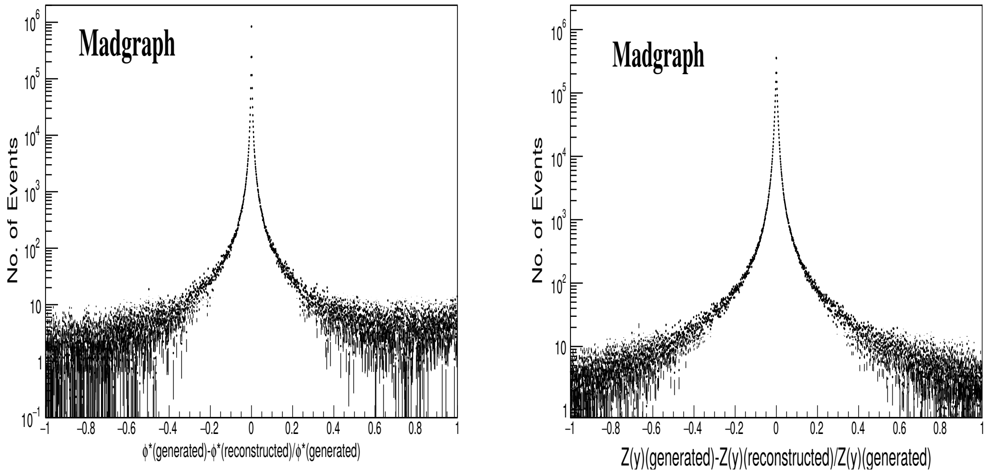

Figure 5.27: The resolutions measured using events generated with Madgraph for ϕ^* (left) and $|y|$ (right).

5.9 Systematic Uncertainties

For any physics analysis involving measurements, it is mandatory to evaluate the accuracy of results to extract meaningful conclusions. This accuracy can be quantified as an *error* or *uncertainty* on a measurement. These are the bounds around the measured value within which the true value lies. The sources of uncertainty are divided into two categories: *statistical* and *systematic*. Statistical errors arise from the fluctuations due to number of events used while the systematic uncertainties arise due to various reasons, e.g due to detector effects, specific choice of the models used for the correction of data and the possible biases inherent in reconstruction or identification algorithms. The systematic uncertainties are obtained by repeating all of the analysis steps with systematic variations (up and down) corresponding to their sources. The unfolded results with the variations are then compared to the unvaried

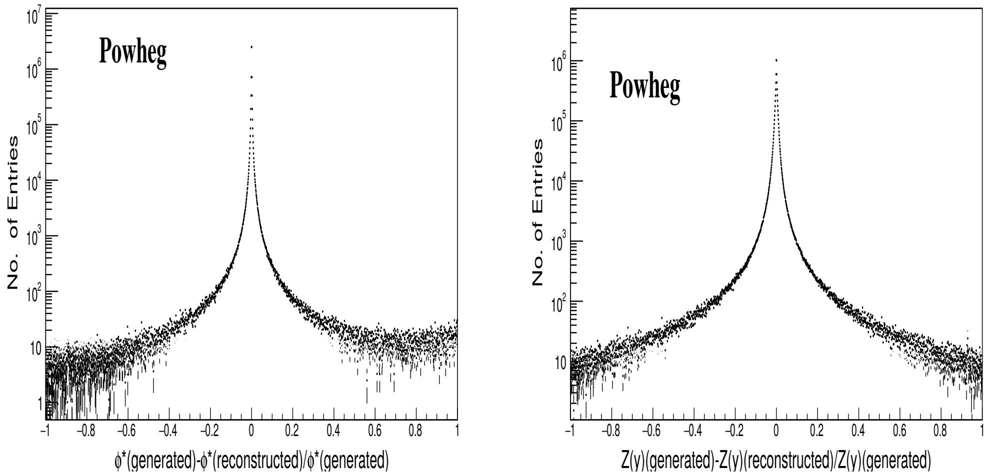

Figure 5.28: The resolutions measured using events generated with Powheg for ϕ^* (left) and $|y|$ (right).

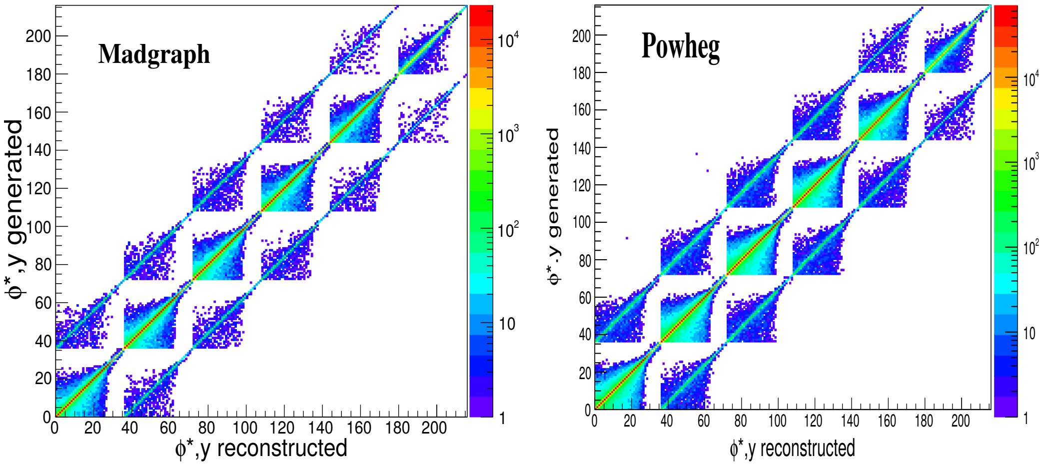

Figure 5.29: Response matrix: reconstructed ϕ^*, $|y|$ as a function of generated ϕ^*, $|y|$ for the Madgraph signal sample (left) and for the Powheg signal sample (right).

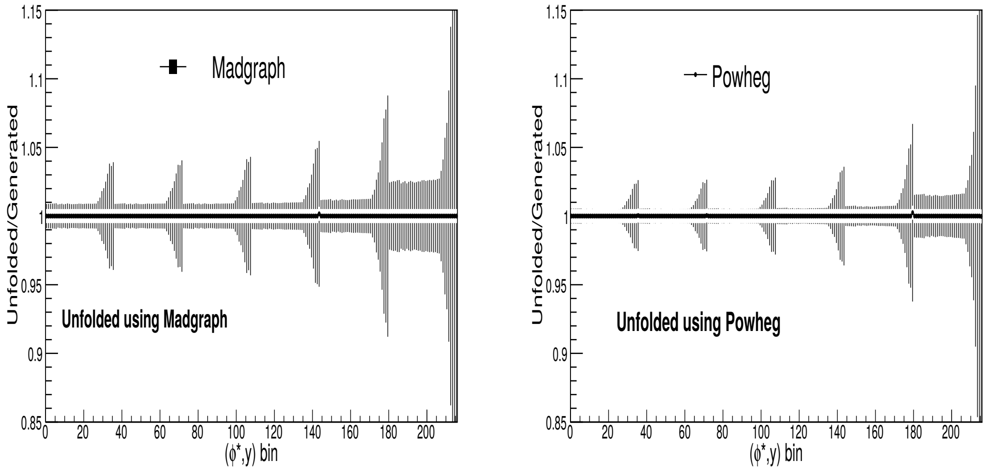

Figure 5.30: Closure test with unfolded ϕ^*, $|y|$ distribution from a given reconstructed sample and the same from generator level information using the sample of full statistics; left:Madgraph and right:Powheg.

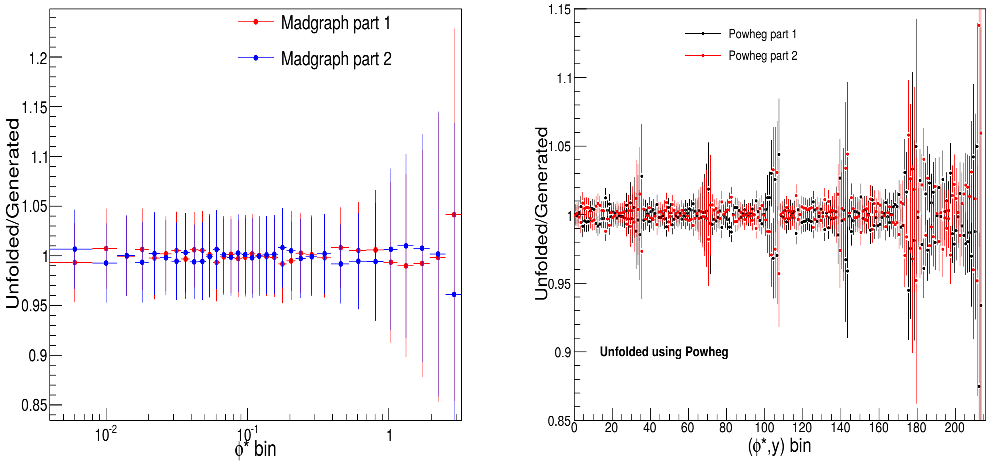

Figure 5.31: The ratio between the unfolded reconstructed (ϕ^*,$|y|$)-bin distribution and the true generated (ϕ^*,$|y|$)-bin distribution in two statistically independent samples of events generated: (left) Madgraph and (right) Powheg signal samples.

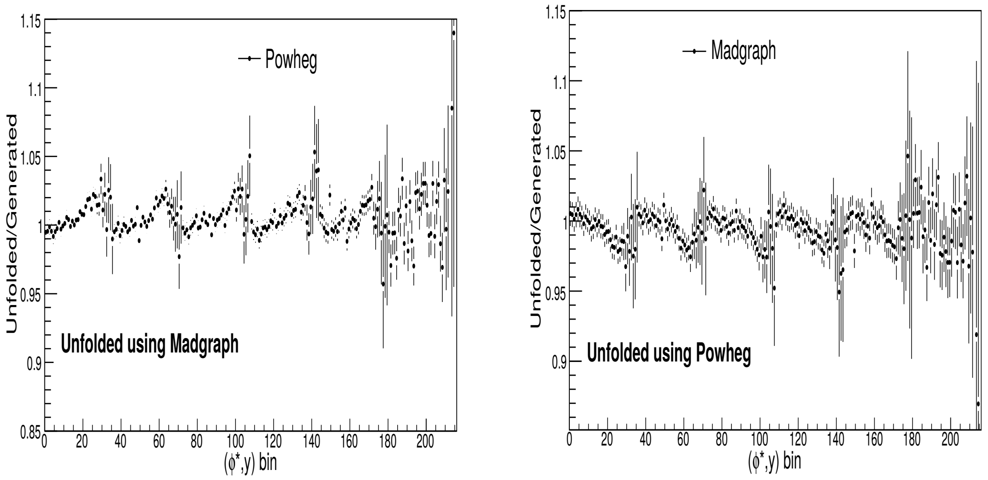

Figure 5.32: Closure test: (left) with unfolded ϕ^*, $|y|$ distribution from Madgraph reconstructed sample, using Powheg response matrix for unfolding and (right) with unfolded ϕ^*, $|y|$ distribution from Powheg reconstructed sample, using Madgraph response matrix for unfolding.

result post-unfolding and the difference between them is quoted as an estimation of systematic uncertainty. The sources of systematic uncertainties considered in this analysis are described below:

- **Luminosity** : The integrated luminosity of a data sample in CMS is known with a precision of 2.6% [20] at $\sqrt{s} = 8$ TeV. This uncertainty is taken as highly correlated and symmetric in all ϕ^* bins.
- **Pileup** : An uncertainty in the modelling of pileup in simulation is determined by varying the minimum bias cross section by ±5% to account for the uncertainty in the total inelastic cross section [21]. The largest deviation from the nominal pileup scenario is quoted as uncertainty.
- **Background subtraction** : This systematic uncertainty is determined by varying the background cross sections within their uncertainty. The cross sections of the two dominant backgrounds : $t\bar{t}$ and dibosons are varied up and down. The cross section is varied by ±10% for $t\bar{t}$ and by ±20% for diboson (WZ and ZZ) backgrounds. The uncertainty due to the other backgrounds

is found to be negligible. The total background uncertainty is obtained by adding these two uncertainties in quadrature.

- **Muon Momentum Scale** : The uncertainty due to Rochester corrections is estimated by varying the correction factors. The central value of the correction is varied within 1 σ using 1000 pseudo-experiments and the root mean square (RMS) is quoted as the uncertainty.

- **Muon identification, isolation, and trigger** : The uncertainties in the efficiencies due to trigger, isolation and identification are evaluated by varying them randomly within their errors using 500 toy samples. The RMS of the these toys is quoted as the corresponding uncertainty. In addition, the uncertainty on these efficiencies as recommended by Muon POG are also taken into account.

- **Final State Radiation** : This uncertainty is calculated by re-weighting events to account for some missing effects in the QED FSR calculations in PYTHIA, as recommended in [22]. The difference between the measurements with and without the re-weighting is assigned as an uncertainty.

- **MC statistics** : The limited statistics of the signal Madgraph sample affects the results of the unfolding. It is taken into account via 500 pseudo-experiments. The response matrix is varied within the statistical uncertainties and the RMS of these unfolded distributions is taken as the uncertainty.

- **Statistical** : The statistical uncertainty from the data distribution is propagated through the unfolding procedure. The uncertainty is based on the diagonal elements of the covariance matrix. Due to the relative low amount of bin migration the matrix provides an adequate description of the propagated statistical uncertainty of the data distribution.

- **Total** : All the uncertainties described above are added in quadrature in order to get the total systematic uncertainty. The total uncertainty is the sum in quadrature of all the contributions assuming each uncertainty source independent.

The relative systematic uncertainties (in %) for sources discussed above are given in tables 5.13 and 5.14 for the Madgraph sample. For the absolute measurement, total uncertainty is dominated by the luminosity uncertainty, followed by the muon identification and trigger uncertainty. Typically, at low values of ϕ^*, the total uncertainty for the absolute measurement is of the order of $\sim 3\%$ which increases to 3.5% at higher values of ϕ^*. For the normalized measurement, the statistical uncertainty dominates in all ϕ^* bins and the total uncertainty is of the order of 0.3% for $\phi^* < 1$ and gradually increases upto 1.5% for $\phi^* > 1$. The impact of these sources of systematic uncertainty varies with ϕ^*, as shown in figure 5.33 for signal sample, and is different for the measurement of absolute and normalised cross sections.

The resulting uncertainty per ϕ^* bin in 3 representative bins of $|y|$ for the absolute and normalized case is shown in figure 5.34. The contributions from each uncertainty component considered for each bin of ϕ^* in 6 $|y|$ bins are listed in tables 5.15 to 5.20 for the absolute measurement. Similarly, for the normalised measurement, the identical uncertainties are quoted in tables 5.21 to 5.25.

5.10 Covariance Matrices

A term covariance refers to the measure of how two random variables will change together and is used to calculate the correlation between these variables. Specifically, covariance measures the degree to which two variables are linearly associated. A positive covariance means that both variables move together, while a negative covariance means variables move inversely. The diagonal elements of the covariance matrix contain the variances of the variables and the off-diagonal elements contain the covariances between all possible pairs of variables.

In this analysis, for each of the systematic and statistical uncertainties, the

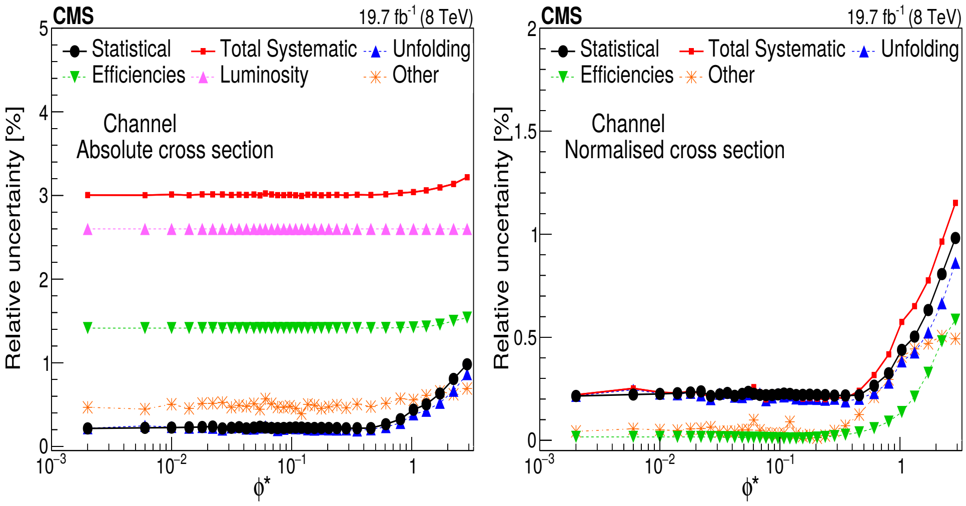

Figure 5.33: The variation of statistical and systematic uncertainties with ϕ^*. The left plot shows the relative uncertainty for the absolute cross section, and the right plot shows the relative uncertainty for the normalised cross section.

covariance matrix is calculated and is used to combine the results of this analysis with the equivalent result of our sister analysis in the dielectron channel. The individual covariance matrices are added to form the total covariance matrix for our measurement. The covariance matrix for each source of uncertainty is computed over the entire ϕ^* range (34 bins) for single differential and in 34 ϕ^*nd 6 $|y|$ bins for double differential measurement. In this section, the covariance matrices for major sources are shown :

- **Luminosity uncertainty** : Since the CMS recommended luminosity uncertainty on 2012 data is 2.6%, hence, the covariance matrix for this case is given by $\mathrm{M}_{ij} = 2.6^2 \times \mathrm{x}_i \times \mathrm{x}_j$ where x_i (x_j) is the absolute cross section in bin i(j). This matrix is shown in figure 5.35 ad 5.40 for single and double differential measurement respectively. The covariance matrix is fully correlated in all ϕ^* bins. This uncertainty has no significant effect on the obtained normalized differential cross section results, as this uncertainty in the integrated luminosity only affects the subtraction of some of the background samples, which is negligible next to the background subtraction uncertainty.

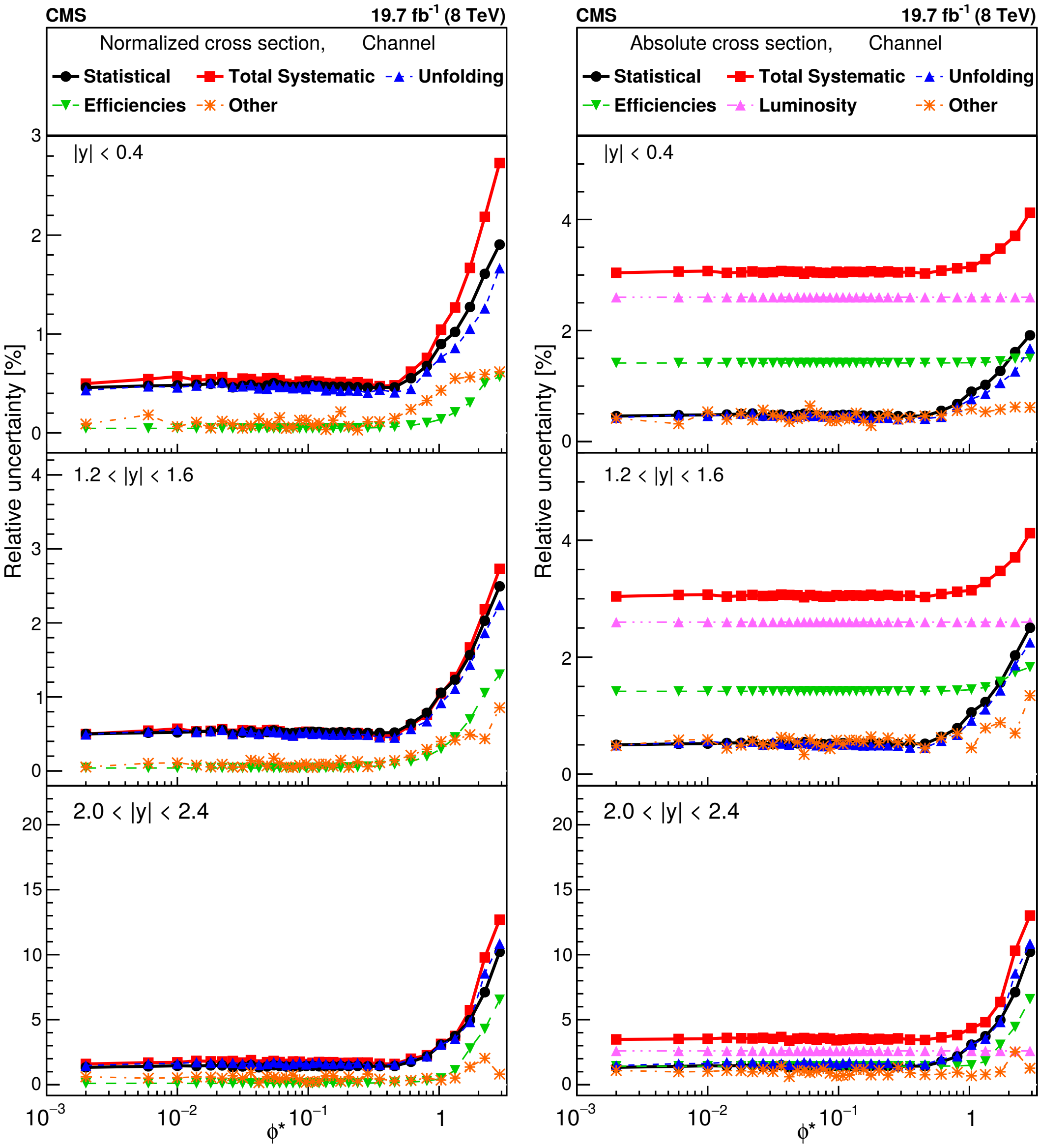

Figure 5.34: The variation of statistical and systematic uncertainties, for different $|y|$ bins, for the normalised (left) and absolute (right) double differential cross section measurement. The main components are shown individually while uncertainties from the background, pileup, the electron energy scale and from QED FSR are combined under the label "Other".

- **Statistical uncertainty** : The covariance matrix for the statistical uncertainty after unfolding is provided by RooUnfold. The covariance matrix is corrected bin by bin for the bin width for the absolute case and for the overall normalization in the case of the normalized distribution. The statistical uncertainty is uncorrelated between ϕ^* bins. The covariance matrix for the statistical uncertainty of the absolute and normalized differential cross section to ϕ^* are shown in the left and right plot of figure 5.36 and respectively. Similarly, for double differential measurement, matrices are shown in figure 5.41.

- **Pileup uncertainty** : As already discussed in section 5.9, this uncertainty is calculated by varying the event weight of simulated events by ±5%. For x_i , d_i and u_i being the values of bin i in the nominal, pileup reduced and pileup enriched distributions respectively, the covariance matrix is given by :
$$\frac{((\mathrm{x_i} - \mathrm{d_i}) \times (\mathrm{x_j} - \mathrm{d_j})) - ((\mathrm{x_i} - \mathrm{u_i}) \times (\mathrm{x_j} - \mathrm{u_j}))}{2} \tag{5.10}$$
This variation is fully correlated between ϕ^* bins for the absolute and normalised distributions. These matrices for the absolute and normalized differential cross section are shown in the left and right plot of figure 5.37 respectively. Similarly, for double differential measurement, matrices are shown in figure 5.42.

- **Muon reconstruction uncertainty** : The efficiency uncertainty for the dimuon channel contains two components, corresponding to the scale factors which calculated by toy MCs, as discussed in sec 5.9 and the uncertainty on muon identification and isolation efficiencies as recommended by Muon POG. The covariance matrices of each component are added to form the covariance matrix for the efficiency uncertainty. The matrices are shown in figure 5.38 for the absolute and normalized differential cross section respectively. Similarly, for double differential measurement, matrices are shown in figure 5.43.

- **Total uncertainty** : The covariance matrix for the total uncertainty, obtained by adding the matrices of all the individual uncertainties, for the absolute and normalized single differential cross section are shown in figure 5.39. Similarly, for double differential measurement, matrices are shown in figure 5.44.

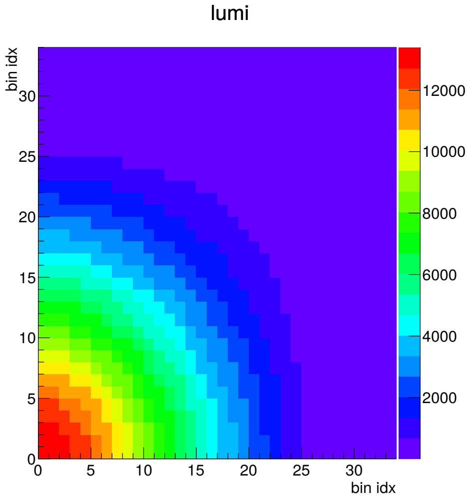

Figure 5.35: Covariance matrix for the luminosity uncertainty of the absolute differential cross section measurement.

5.11 Final Results

This section presents the measurements of the single- and double-differential cross sections for Z-boson decaying to a dimuon pair within a fiducial region defined by the kinematics of the muons, one of which has $p_T > 30$ GeV/c and $|\eta| < 2.1$ and the second muon has $p_T > 20$ GeV/c and $|\eta| < 2.4$. For the single differential case, the absolute and normalised differential cross sections are measured as a function of ϕ^*. For double differential cross section, both the absolute and normalised differential cross sections as a function of ϕ^* and the dimuon rapidity, $|y|$ are measured. The measured single- and double-differential cross sections are compared with various theoretical predictions. Discussion of the results is presented at the end of the chapter.

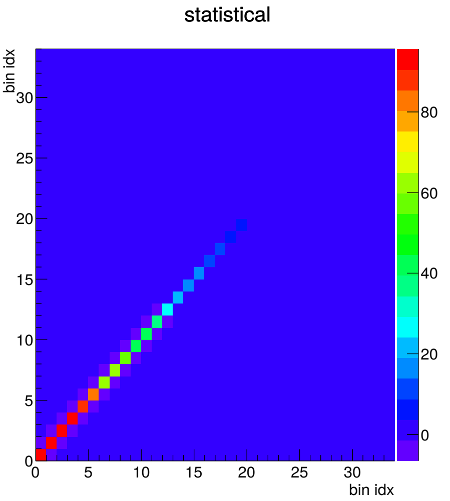

Figure 5.36: Covariance matrix for the statistical uncertainty for the absolute (left) and normalised (right) differential cross section measurements.

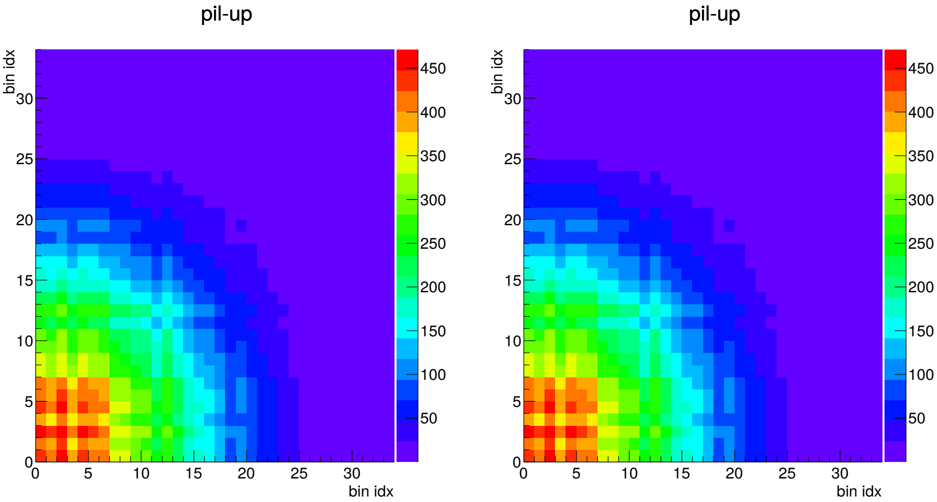

Figure 5.37: Covariance matrix for the pile up uncertainty for the absolute (left) and normalised (right) differential cross section measurements.

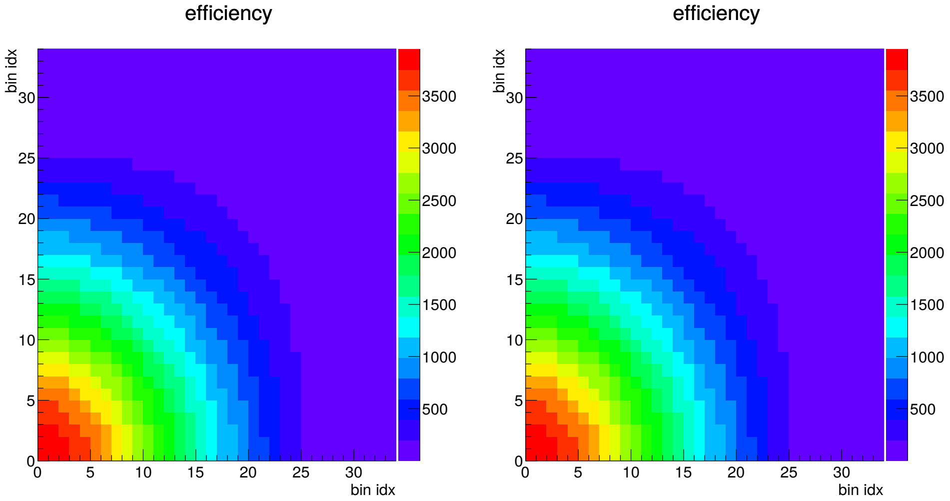

Figure 5.38: Covariance matrix for the total efficiency uncertainty for the absolute (left) and normalised (right) differential cross section measurements.

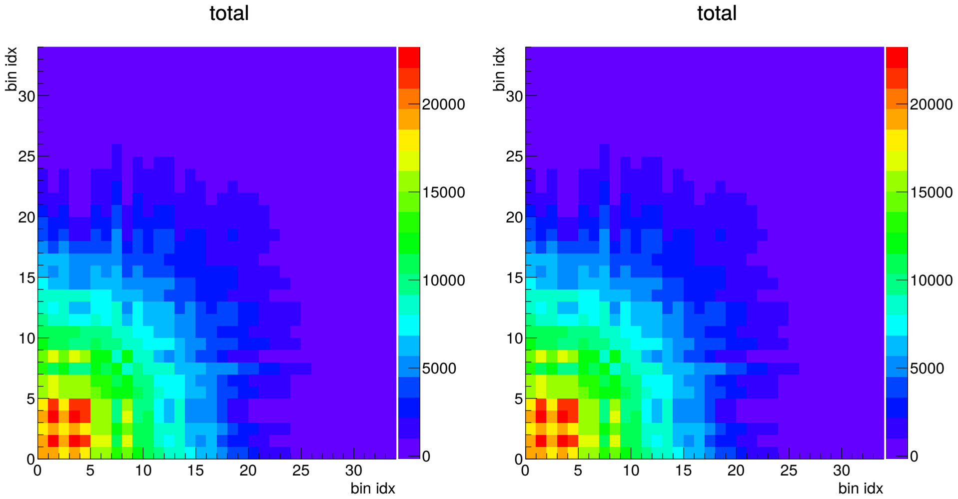

Figure 5.39: Covariance matrix for the total uncertainty for the absolute (left) and normalised (right) differential cross section measurements.

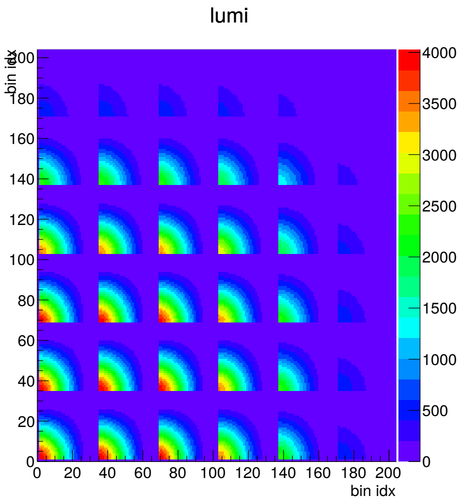

Figure 5.40: Covariance matrix for the luminosity uncertainty of the absolute differential cross section measurement.

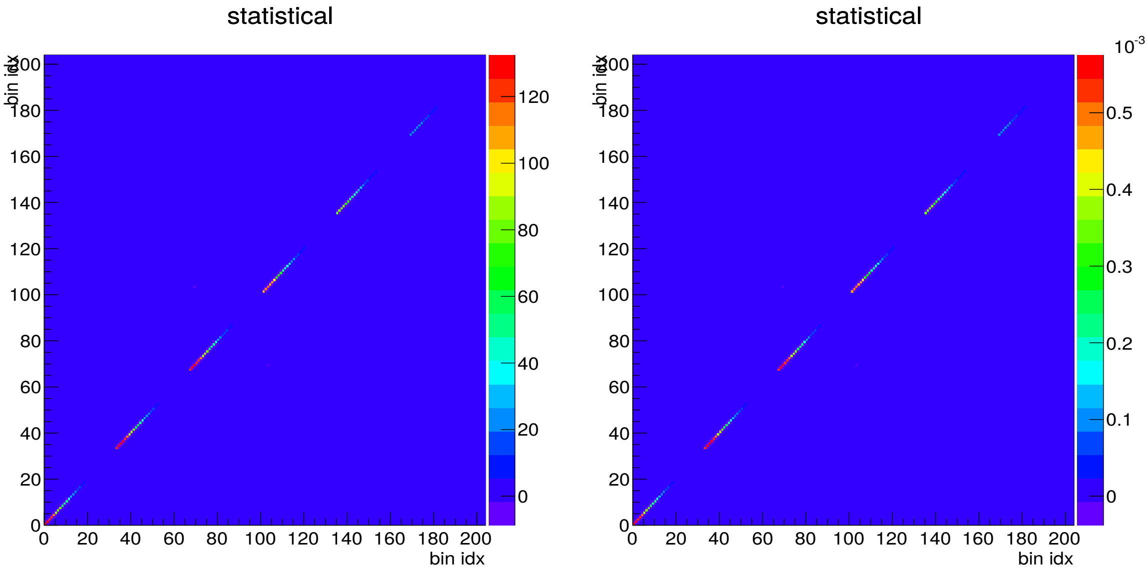

Figure 5.41: Covariance matrix for the pileup uncertainty of the absolute (left) and normalized (right) differential cross section measurements.

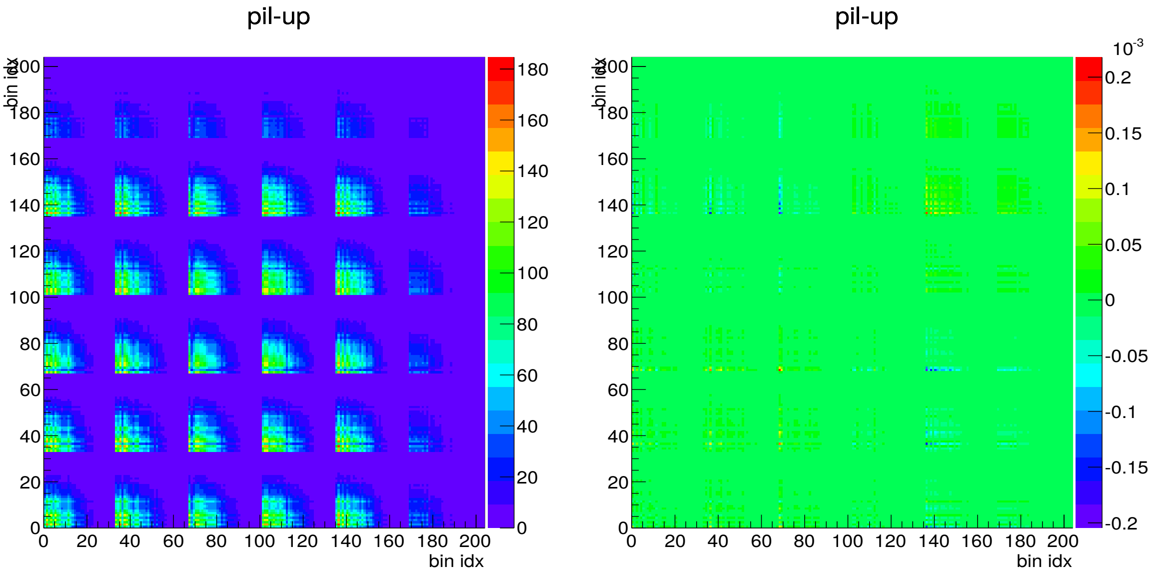

Figure 5.42: Covariance matrix for the pileup uncertainty of the absolute (left) and normalized (right) differential cross section measurements.

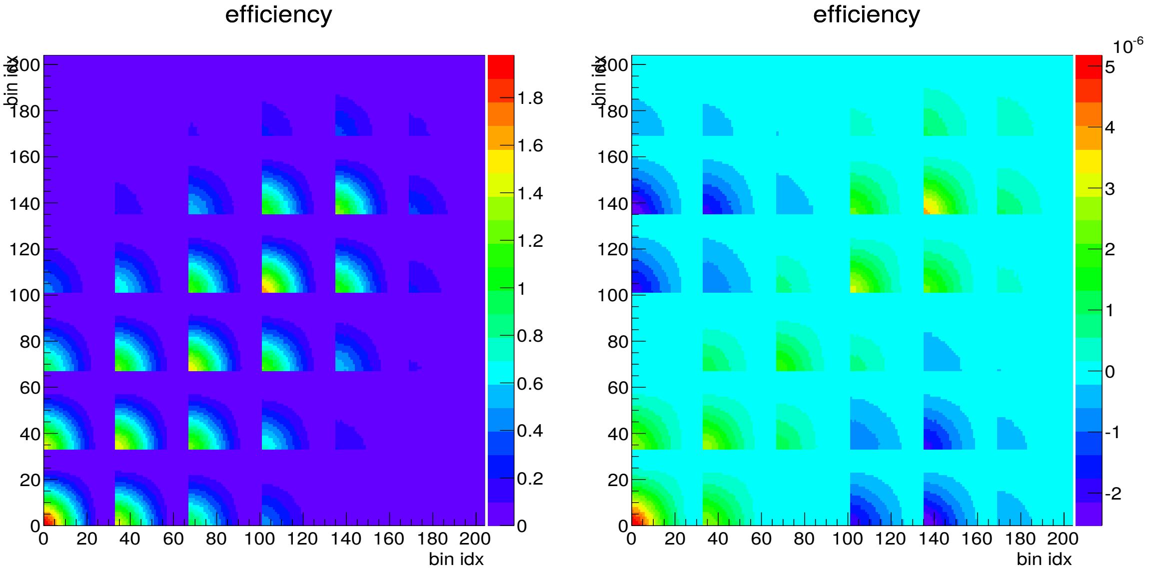

Figure 5.43: Covariance matrix for the total efficiency uncertainty for the absolute (left) and normalised (right) differential cross section measurements.

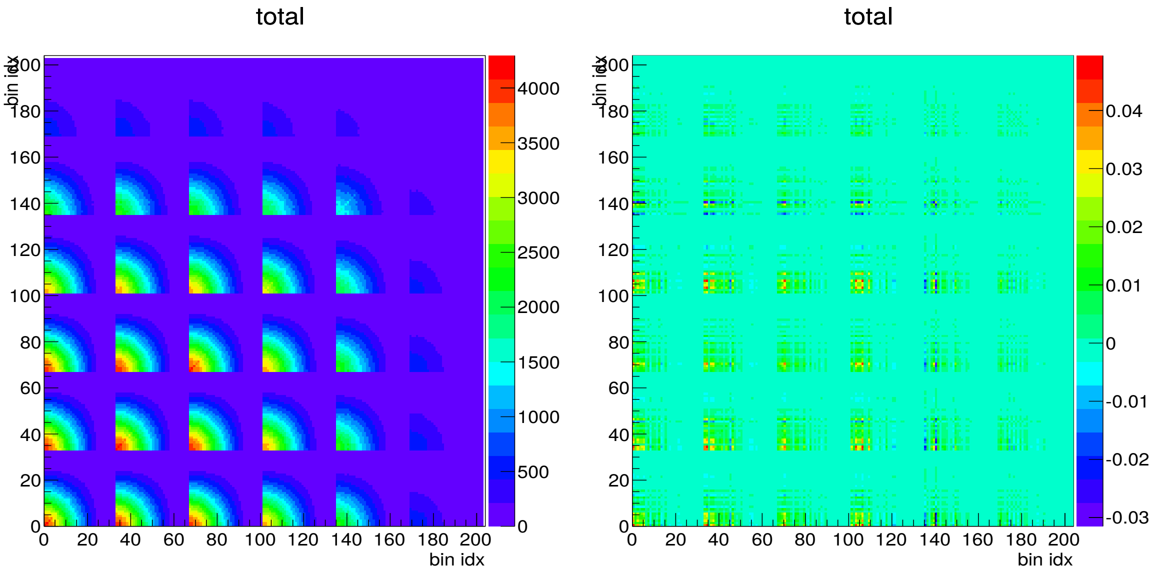

Figure 5.44: Covariance matrix for the total uncertainty of the absolute (left) and normalized (right) differential cross section measurements.

5.11.1 Single Differential Measurement

The following expression describes the absolute differential cross section, pre-unfolding (shown in figure 5.15), as a function of ϕ^*, in the ith bin and is defined as:

$$[\frac{\mathrm{d}\sigma}{\mathrm{d}\phi^*}]_{\mathrm{i}} = \frac{\mathrm{N_i} - \mathrm{B_i}}{\mathcal{L}\,\epsilon_{\mathrm{i}}\,\Delta\phi^*_{\mathrm{i}}} \tag{5.11}$$

where N_i, B_i, ϵ_i, $\Delta\phi^*_i$, and $\mathcal{L}$ are the number of selected events in data, the estimated number of background events, the overall efficiency, the width of the i^{th} bin of ϕ^* and the total integrated luminosity, respectively. The cross section measurements have been made in 34 bins of ϕ^*, as listed in section 5.1.4. Since we are reporting fiducial cross sections which, by definition, are independent of the acceptance, hence, there no acceptance systematic uncertainty is reported.

The number of signal events in each ϕ^* bin are obtained by subtracting the corresponding number of background events, B_i from the total number of events N_i in each bin of ϕ^*. Then, the background subtracted data is unfolded using response matrix and the generator level ϕ^* distribution obtained from the signal

Madgraph sample. The total fiducial cross section obtained for the single differential measurement in the dimuon final state is :

$$480.0 \pm 0.2(\text{stat}) \pm 7.2(\text{syst}) \pm 12.5(\text{lumi})\ \text{pb}$$

and

$$478.5 \pm 0.2(\text{stat}) \pm 3.6(\text{syst}) \pm 12.4(\text{lumi})\ \text{pb}$$

in the dielectron-dimuon combined case. These results have been obtained by combining the results from dielectron and dimuon channel using the BLUE method [23,24][2]. For the signal, Madgraph sample with (M(ll)>50 GeV/c), the FEWZ[3] cross section at NNLO level, for the dimuon final state is 1177.3 pb [25]. The measured and FEWZ cross section are quite different because the measurement is done within the fiducial volume of this analysis (given in table 5.2), whereas, the FEWZ cross section is calculated for the complete phase space, by only requiring the mass of Z-boson to be greater than 50 GeV/c^2.

The normalised cross section is defined as the absolute cross section calculated in each bin divided by the total fiducial cross section. The total normalised cross section is calculated as unity, using following expression:

$$\text{Total normalised cross section} = \sum (\text{normalised differential cross section in each bin of } \phi^* \times \text{ bin width of each bin of } \phi^*)$$

The individual absolute and normalised cross sections in each bin of ϕ^* along with the systematic and statistical uncertainties is given in table 5.27.

---

[2] The BLUE method is a simple and powerful tool to combine measurements using the uncertainties and their correlation between the measurements

[3] FEWZ is a tool to calculate simultaneously QCD corrections up to NNLO and EW corrections at NLO

5.11.2 Double Differential Measurement

The absolute double differential cross section, pre-unfolding, as a function of ϕ^* and dimuon rapidity $|y|$, is defined as:

$$\left[\frac{d^2\sigma}{d\phi^* d|y|}\right]_{ij} = \frac{\mathcal{N}_{ij} - \mathcal{B}_{ij}}{\mathcal{L}\, \epsilon_{ij}\, \Delta\phi_i^*\, \Delta|y|_j} \tag{5.12}$$

where, i and j represents the ϕ^* and d$|y|$ bins. The N$_i$, B$_i$, ϵ_i and $\Delta\phi_i^*$, Δy ,$\mathcal{L}$ are the number of selected events in data, the estimated number of background events, the overall efficiency, the width of the i^{th} bin of ϕ^*, the width of the j^{th} bin of $|y|$ and the total integrated luminosity, respectively. When measuring the double-differential cross section, six bins in $|y|$ of constant width $\Delta|y| = 0.4$ covering the range $\Delta|y| < 2.4$ are used.

The bulk of the ϕ^* distribution for 2012 data, falls in the range $\phi^* < 1$. The absolute and normalised double differential results for dimuon final state w.r.t. ϕ^*, in each bin of dimuon rapidity, within the fiducial volume, are listed in tables 5.28 to 5.33.

5.11.3 Comparison with Theoretical Predictions

The measured DY production cross section has been compared with various theoretical predictions, available at LO or NNLO level :

(i) Madgraph interfaced with PYTHIA 6 using CTEQ6L1 LO PDF
(i) Powheg interfaced with PYTHIA 6 and Z2star tune using CT10NLO PDF
(ii) Powheg interfaced with PYTHIA 8 and CUETP8M1 tune using NNPDF2.3 LO PDF
(iii) ResBos
(iv) aMC@NLO interfaced with PYTHIA 8 using NNPDF3.0 NLO PDF

The uncertainties of the Madgraph sample have been calculated with FEWZ and are $\sim$ 3.3%. The uncertainties for other theoretical models include statistical, PDF and scale uncertainties. The PDF uncertainty is calculated using the recommendations of Ref. [26], and the scale uncertainties are evaluated by varying the renormalisation and the factorization scales independently by factors of ±2 and ±1/2. The largest variations of the renormalisation and the factorization scales w.r.t nominal values are taken as the uncertainty.

5.11.3.1 Single Differential Measurement

The absolute and normalised differential cross sections for Z-boson decaying to an oppositely charged dimuon pair in the fiducial region are shown as a function of ϕ^* in figures 5.45 and 5.46 . The uncertainty of the normalised differential cross section measured is dominated by the statistical uncertainty of the data distribution, as shown in table 5.14. All other uncertainties are small in comparison. Similarly, the uncertainty on the measured absolute cross section is dominated by the fully correlated uncertainty on the integrated luminosity of the data sample. While the uncertainty on the Madgraph distribution is dominated by the PDF uncertainty (±38.8 pb [25]) of the FEWZ. For Powheg sample, the uncertainty is dominated by the PDF uncertainty calculated by varying the CT10 PDF within its given uncertainty bands.

5.11.3.2 Double Differential Measurement

Using the procedure described in the previous sections we measure the differential cross section for Z-boson decaying to a pair of oppositely charged dimuons within the fiducial region. In this section we present both the normalized and the absolute differential cross sections as a function of ϕ^* and dimuon rapidity $|y|$. As discussed earlier, the data was unfolded, using a Madgraph simulated signal sample, to the (ϕ^*, y)-bin defined by the generated “born” muons.

The normalized 2D differential cross section for Z-boson decaying to an oppositely charged dimuon pair in our fiducial region is shown as a function of ϕ^* for all the six y bins in figure 5.48. The statistical uncertainty of the data distribution remains the major source of uncertainty in double differential measurements with

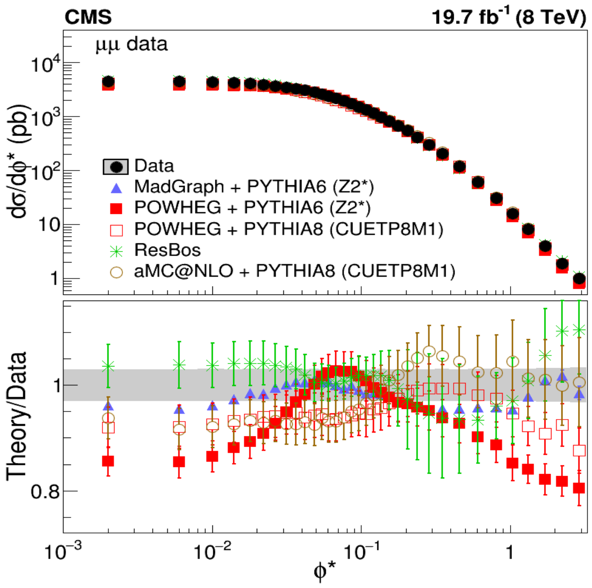

Figure 5.45: Absolute differential cross section with respect to ϕ^* of $\mathrm{Z} \to \mu^+\mu^-$ in our fiducial region in data and generated by Madgraph, Powheg + PYTHIA6, Powheg + PYTHIA8, RESBOS and aMC@NLO. The ratio of these distributions with respect to the measured data is also shown.

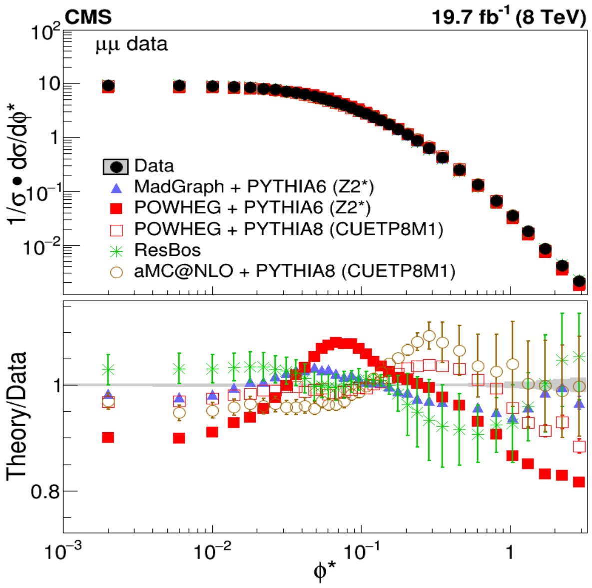

Figure 5.46: Normalised differential cross section with respect to ϕ^* of $\mathrm{Z} \to \mu^+\mu^-$ in our fiducial region in data and generated by Madgraph, Powheg + PYTHIA6, Powheg + PYTHIA8, RESBOS and aMC@NLO. The ratio of these distributions with respect to the measured data is also shown.

very less much smaller contributions from other uncertainties. The uncertainties for the theoretical predictions are calculated as discussed in previous section and the uncertainty on the simulated distribution is mostly determined by the statistical uncertainty of the samples.

The shape of the ϕ^* distribution varies with dilepton rapidity. In order to emphasize this feature, ratios of cross sections as functions of ϕ^* for bins of $|y|$ relative to the central bin $|y| < 0.4$ are presented in Fig. 5.49, where they are compared to the predictions from theoretical calculations and models. All of the theoretical predictions provide a fairly good description of the shape of the ϕ^* distribution with $|y|$.

5.12 Discussion

Measurements of the single- and double differential cross sections in dimuon channel have been presented. The measurements are based on 19.7 fb^{-1} of proton-proton collision data at $\sqrt{s} = 8$ TeV collected with the CMS detector at the LHC. They provide a sensitive test of theoretical predictions. The normalised cross section $(1/\sigma)d\sigma/d\phi^*$, is precise at the level of 0.24 to 1.2%. The measured ϕ^* distribution has been compared with various theoretical predictions. For the ϕ^* range considered in this thesis, none of the theoretical predictions matches perfectly with the measurements from the data. For the normalised cross section, Madgraph + PYTHIA 6 provide the best description of the new measurements in the whole range with a disagreement of at most 5% over the entire ϕ^* range. ResBos, aMC@NLO + PYTHIA8 and Powheg + PYTHIA8 are similarly precise at describing the data at low ϕ^* but they disagree with the measurements by by about 10% for ϕ^*>0.1. For higher values of ϕ^* the differences are larger, roughly by 5%, 15%, 8%, 9%, and 10%, respectively. These observations suggest that more advanced calculations (e.g. at the NLO and NNLO level) of the hard-scattering process reproduce the data better. At the same time, the large difference in theoretical predictions from a single Powheg sample interfaced with two different versions of PYTHIA, i.e. PYTHIA6

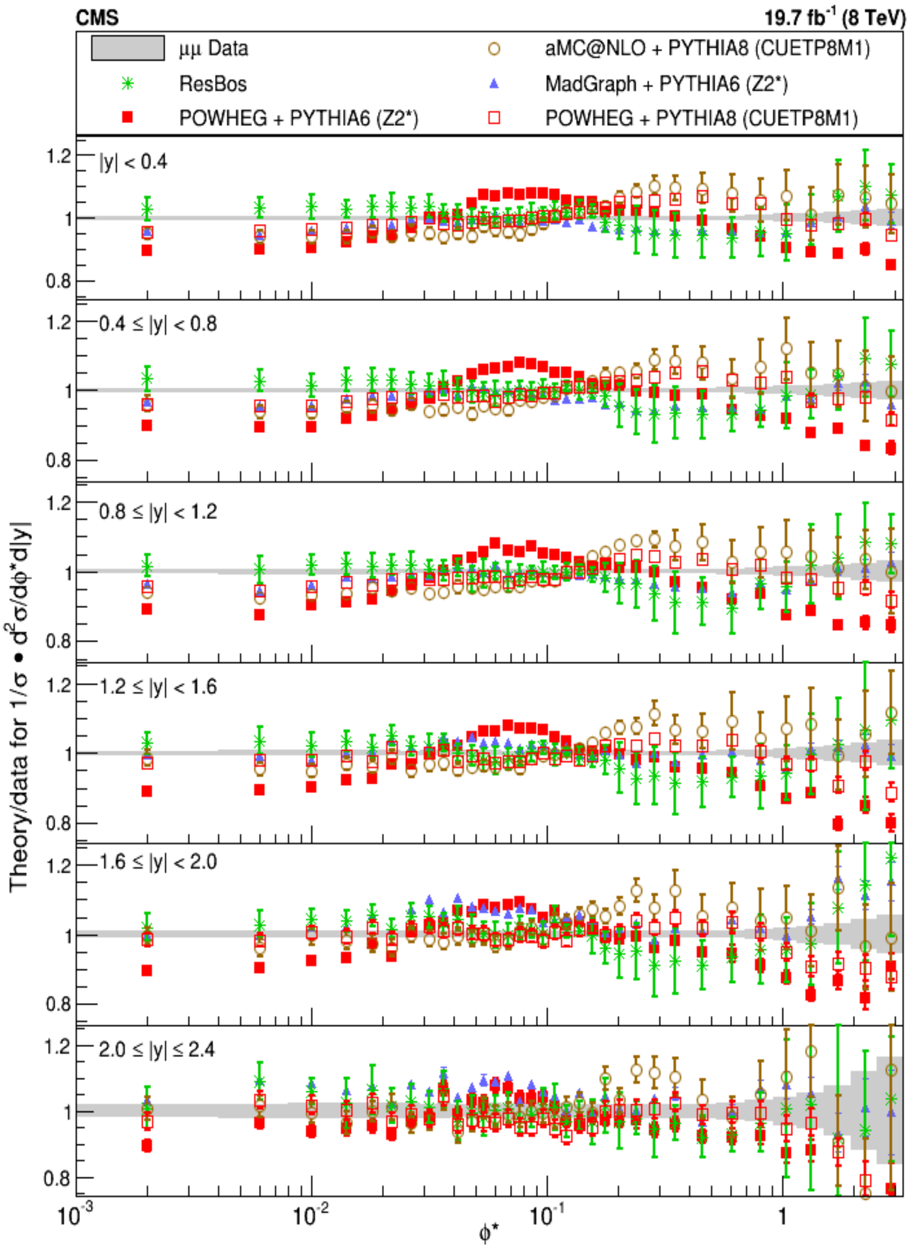

Figure 5.47: Ratio of measured normalised double-differential cross section with respect to ϕ^* of $Z \to \mu^+\mu^-$ in our fiducial region in data to the various theoretical models considered.

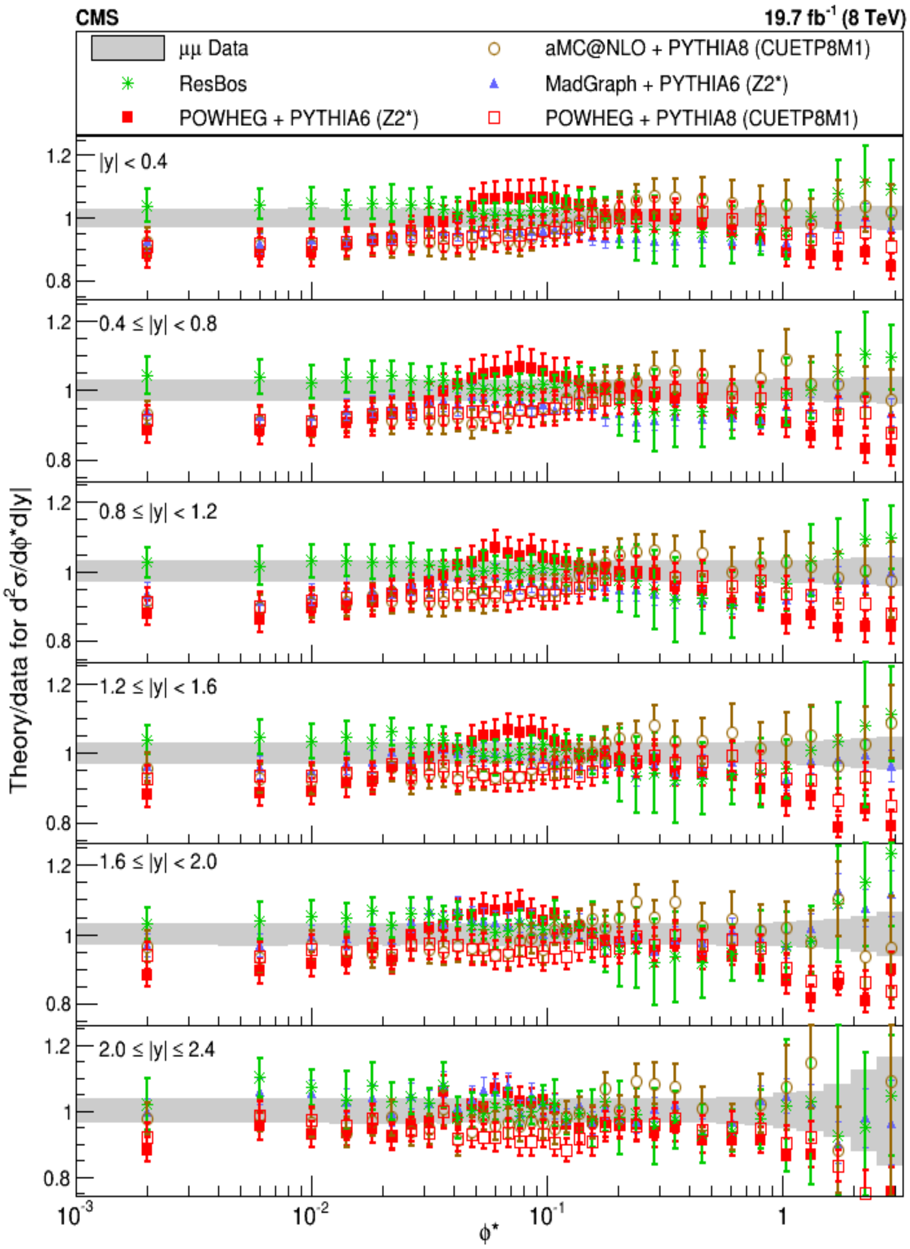

Figure 5.48: Ratio of measured absolute double-differential cross section with respect to ϕ^* of $Z \to \mu^+\mu^-$ in our fiducial region in data to the various theoretical models considered.

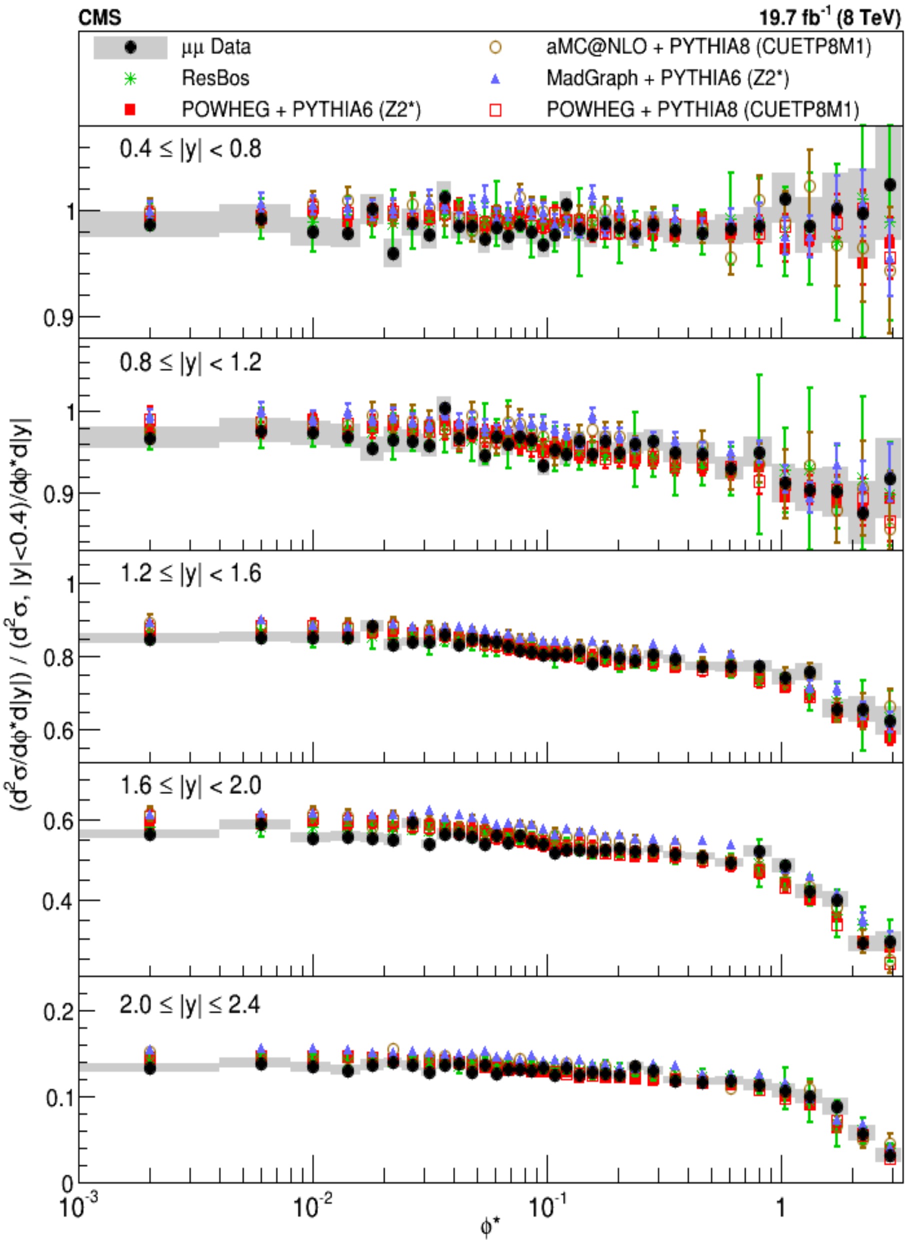

Figure 5.49: The ratio of double differential cross section for higher rapidity bins normalised to the values in most central bin. The theoretical predictions from Madgraph + PYTHIA 6, Powheg + PYTHIA 6, Powheg + PYTHIA 8, ResBos, and aMC@NLO + PYTHIA 8 are also shown.The uncertainties for the theoretical predictions are mainly statistical.

and PYTHIA8, and underlying event tunes, indicates the combined importance of showering method, non-perturbative effects and the need for soft-gluon resummation on the predicted values of cross sections reported. The variation of the cross section with $|y|$ is reproduced by ResBos within 1%, while Madgraph+ PYTHIA6 differs from the data by 5%, comparing the most central and most forward rapidity bins. The other theoretical predictions deviate from the measurement by $\sim$2%.

This analysis validates the overall theoretical description of inclusive production of a vector boson at the LHC energies by the perturbative formalism of the Standard Model. Nevertheless, further tuning of the description of the underlying event is necessary for an accurate prediction of the kinematics of the Drell-Yan production of lepton pairs.

ϕ^* range	**$\vert y\vert$ range**					
	0.0-0.4	**0.4-0.8**	**0.8-1.2**	**1.2-1.6**	**1.6-2.0**	**2.0-2.4**
0.000-0.004	0	36	72	108	144	180
0.004-0.008	1	37	73	109	145	181
0.008-0.012	2	38	74	110	146	182
0.012-0.016	3	39	75	111	147	183
0.016-0.020	4	40	76	112	148	184
0.020-0.024	5	41	77	113	149	185
0.024-0.029	6	42	78	114	150	186
0.029-0.034	7	43	79	115	151	187
0.034-0.039	8	44	80	116	152	188
0.039-0.045	9	45	81	117	153	189
0.045-0.051	10	46	82	118	154	190
0.051-0.057	11	47	83	119	155	191
0.057-0.064	12	48	84	120	156	192
0.064-0.072	13	49	85	121	157	193
0.072-0.081	14	50	86	122	158	194
0.081-0.091	15	51	87	123	159	195
0.091-0.102	16	52	88	124	160	196
0.102-0.114	17	53	89	125	161	197
0.114-0.128	18	54	90	126	162	198
0.128-0.145	19	55	91	127	163	199
0.145-0.165	20	56	92	128	164	200
0.165-0.189	21	57	93	129	165	201
0.189-0.219	22	58	94	130	166	202
0.219-0.258	23	59	95	131	167	203
0.258-0.312	24	60	96	132	168	204
0.312-0.391	25	61	97	133	169	205
0.391-0.524	26	62	98	134	170	206
0.524-0.695	27	63	99	135	171	207
0.695-0.918	28	64	100	136	172	208
0.918-1.153	29	65	101	137	173	209
1.153-1.496	30	66	102	138	174	210
1.496-1.947	31	67	103	139	175	211
1.947-2.522	32	68	104	140	176	212
2.522-3.277	33	69	105	141	177	213
3.277-5.000	34	70	106	142	178	214
5.00-10.000	35	71	107	143	179	215

Table 5.12: (ϕ^*, $|y|$) bin number corresponding to each considered ϕ^* and $|y|$ range.

ϕ^* range	MC stat.	Pile-up	Bkg.	pt scale	Eff.	Total syst.	Stat.	Total
0.000-0.004	0.22	0.47	0.01	0.02	1.41	3.00	0.22	3.01
0.004-0.008	0.25	0.45	0.01	0.02	1.41	3.00	0.22	3.01
0.008-0.012	0.23	0.50	0.01	0.02	1.41	3.01	0.23	3.02
0.012-0.016	0.22	0.45	0.01	0.02	1.41	3.00	0.23	3.01
0.016-0.020	0.23	0.51	0.01	0.02	1.41	3.01	0.23	3.02
0.020-0.024	0.22	0.51	0.01	0.02	1.42	3.01	0.24	3.02
0.024-0.029	0.20	0.53	0.01	0.02	1.41	3.01	0.22	3.02
0.029-0.034	0.23	0.47	0.01	0.02	1.41	3.00	0.22	3.01
0.034-0.039	0.23	0.49	0.01	0.02	1.41	3.01	0.23	3.02
0.039-0.045	0.21	0.48	0.01	0.02	1.41	3.01	0.22	3.01
0.045-0.051	0.21	0.51	0.01	0.02	1.41	3.01	0.23	3.02
0.051-0.057	0.23	0.44	0.01	0.02	1.41	3.00	0.23	3.01
0.057-0.064	0.24	0.57	0.01	0.02	1.41	3.02	0.23	3.03
0.064-0.072	0.23	0.51	0.01	0.02	1.41	3.01	0.22	3.02
0.072-0.081	0.20	0.47	0.02	0.03	1.41	3.00	0.22	3.01
0.081-0.091	0.21	0.47	0.02	0.03	1.41	3.00	0.22	3.01
0.091-0.102	0.23	0.48	0.02	0.02	1.41	3.01	0.22	3.02
0.102-0.114	0.22	0.45	0.02	0.02	1.41	3.00	0.23	3.01
0.114-0.128	0.22	0.39	0.03	0.02	1.41	2.99	0.23	3.00
0.128-0.145	0.20	0.50	0.03	0.02	1.41	3.01	0.22	3.02
0.145-0.165	0.20	0.49	0.04	0.02	1.42	3.01	0.22	3.02
0.165-0.189	0.21	0.45	0.04	0.02	1.41	3.00	0.22	3.01
0.189-0.219	0.20	0.47	0.05	0.02	1.41	3.00	0.22	3.01
0.219-0.258	0.20	0.49	0.07	0.02	1.41	3.01	0.22	3.02
0.258-0.312	0.20	0.45	0.09	0.02	1.41	3.00	0.22	3.01
0.312-0.391	0.19	0.49	0.12	0.02	1.42	3.01	0.22	3.02
0.391-0.524	0.20	0.44	0.17	0.02	1.41	3.01	0.22	3.01
0.524-0.695	0.23	0.45	0.25	0.02	1.42	3.01	0.27	3.03
0.695-0.918	0.28	0.46	0.34	0.02	1.42	3.03	0.33	3.05
0.918-1.153	0.38	0.35	0.43	0.02	1.42	3.04	0.44	3.07
1.153-1.496	0.43	0.38	0.48	0.02	1.43	3.06	0.50	3.10
1.496-1.947	0.52	0.41	0.51	0.03	1.46	3.10	0.63	3.16
1.947-2.522	0.67	0.33	0.53	0.02	1.50	3.14	0.81	3.24
2.522-3.277	0.86	0.44	0.53	0.02	1.54	3.22	0.98	3.36

Table 5.13: Systematic errors (in %) for absolute cross section in different ϕ^* bins due to various sources. The total value includes the uncertainty of 2.6% due to luminosity for signal sample.

ϕ^* range	**MC stat.**	**Pile-up**	**Bkg.**	**pt scale**	**Eff.**	**Total syst.**	**Stat.**	**Total**
0.000-0.004	0.22	0.01	0.04	0.00	0.02	0.22	0.22	0.31
0.004-0.008	0.25	0.04	0.04	0.00	0.02	0.25	0.22	0.34
0.008-0.012	0.23	0.03	0.04	0.00	0.02	0.23	0.23	0.32
0.012-0.016	0.22	0.02	0.04	0.00	0.02	0.23	0.23	0.32
0.016-0.020	0.23	0.04	0.04	0.00	0.02	0.24	0.23	0.33
0.020-0.024	0.22	0.04	0.04	0.00	0.02	0.23	0.24	0.33
0.024-0.029	0.20	0.05	0.04	0.00	0.02	0.21	0.22	0.30
0.029-0.034	0.23	0.01	0.04	0.01	0.02	0.23	0.22	0.32
0.034-0.039	0.23	0.01	0.04	0.00	0.01	0.24	0.23	0.33
0.039-0.045	0.21	0.02	0.04	0.00	0.01	0.22	0.22	0.31
0.045-0.051	0.21	0.03	0.04	0.00	0.01	0.22	0.23	0.31
0.051-0.057	0.22	0.03	0.04	0.00	0.01	0.23	0.23	0.33
0.057-0.064	0.24	0.09	0.04	0.00	0.01	0.26	0.23	0.34
0.064-0.072	0.23	0.03	0.04	0.00	0.01	0.23	0.22	0.32
0.072-0.081	0.19	0.01	0.03	0.01	0.01	0.20	0.22	0.30
0.081-0.091	0.21	0.01	0.03	0.01	0.01	0.21	0.22	0.30
0.091-0.102	0.22	0.01	0.03	0.01	0.01	0.23	0.22	0.32
0.102-0.114	0.21	0.02	0.03	0.00	0.01	0.22	0.23	0.31
0.114-0.128	0.22	0.09	0.02	0.00	0.01	0.24	0.23	0.33
0.128-0.145	0.20	0.03	0.02	0.01	0.01	0.21	0.22	0.30
0.145-0.165	0.20	0.01	0.01	0.00	0.01	0.20	0.22	0.30
0.165-0.189	0.20	0.02	0.01	0.00	0.01	0.20	0.22	0.30
0.189-0.219	0.20	0.01	0.01	0.01	0.01	0.20	0.22	0.30
0.219-0.258	0.20	0.01	0.02	0.00	0.02	0.20	0.22	0.30
0.258-0.312	0.20	0.02	0.04	0.00	0.02	0.21	0.22	0.30
0.312-0.391	0.19	0.01	0.07	0.00	0.03	0.20	0.22	0.30
0.391-0.524	0.20	0.03	0.12	0.01	0.04	0.24	0.22	0.32
0.524-0.695	0.23	0.05	0.20	0.01	0.06	0.32	0.27	0.41
0.695-0.918	0.28	0.04	0.29	0.01	0.09	0.42	0.33	0.53
0.918-1.153	0.38	0.14	0.38	0.01	0.14	0.57	0.44	0.72
1.153-1.496	0.43	0.10	0.43	0.01	0.21	0.65	0.50	0.82
1.496-1.947	0.52	0.08	0.46	0.02	0.33	0.78	0.63	1.00
1.947-2.522	0.67	0.16	0.48	0.02	0.48	0.96	0.81	1.26
2.522-3.277	0.86	0.08	0.49	0.02	0.59	1.15	0.98	1.51

Table 5.14: Systematic errors (in %) for normalized cross section in different ϕ^* bins due to various sources, using Madgraph sample.

ϕ^* range	**MC stat.**	**Pile-up**	**Bkg.**	**pt scale**	**Eff.**	**Total syst.**	**Stat.**	**Total**
0.000-0.004	0.43	0.42	0.01	0.03	1.42	3.02	0.46	3.06
0.004-0.008	0.47	0.32	0.01	0.04	1.42	3.02	0.48	3.05
0.008-0.012	0.46	0.54	0.01	0.04	1.42	3.04	0.48	3.08
0.012-0.016	0.48	0.40	0.01	0.03	1.42	3.03	0.49	3.06
0.016-0.020	0.51	0.51	0.01	0.04	1.42	3.05	0.50	3.09
0.020-0.024	0.51	0.39	0.01	0.05	1.42	3.03	0.51	3.07
0.024-0.029	0.47	0.57	0.01	0.03	1.42	3.05	0.46	3.09
0.029-0.034	0.47	0.48	0.01	0.04	1.42	3.04	0.48	3.07
0.034-0.039	0.48	0.44	0.01	0.04	1.42	3.03	0.49	3.07
0.039-0.045	0.45	0.36	0.01	0.03	1.42	3.02	0.46	3.05
0.045-0.051	0.45	0.41	0.01	0.03	1.42	3.02	0.48	3.06
0.051-0.057	0.49	0.44	0.01	0.04	1.42	3.03	0.50	3.07
0.057-0.064	0.46	0.64	0.01	0.03	1.42	3.07	0.48	3.10
0.064-0.072	0.47	0.52	0.01	0.03	1.42	3.04	0.47	3.08
0.072-0.081	0.45	0.45	0.02	0.03	1.42	3.03	0.46	3.06
0.081-0.091	0.46	0.37	0.02	0.04	1.42	3.02	0.47	3.06
0.091-0.102	0.44	0.37	0.02	0.03	1.42	3.02	0.47	3.05
0.102-0.114	0.47	0.43	0.03	0.04	1.42	3.03	0.48	3.07
0.114-0.128	0.47	0.40	0.03	0.03	1.42	3.02	0.48	3.06
0.128-0.145	0.43	0.51	0.03	0.03	1.42	3.04	0.47	3.07
0.145-0.165	0.44	0.37	0.04	0.03	1.42	3.02	0.47	3.05
0.165-0.189	0.43	0.28	0.04	0.03	1.42	3.00	0.47	3.04
0.189-0.219	0.43	0.43	0.05	0.03	1.42	3.02	0.47	3.06
0.219-0.258	0.43	0.49	0.07	0.03	1.42	3.03	0.46	3.07
0.258-0.312	0.40	0.39	0.09	0.03	1.42	3.01	0.46	3.05
0.312-0.391	0.44	0.41	0.12	0.03	1.42	3.02	0.46	3.06
0.391-0.524	0.41	0.43	0.18	0.03	1.42	3.02	0.46	3.06
0.524-0.695	0.45	0.39	0.26	0.03	1.42	3.03	0.55	3.08
0.695-0.918	0.63	0.42	0.36	0.03	1.42	3.08	0.68	3.15
0.918-1.153	0.76	0.37	0.45	0.05	1.42	3.12	0.90	3.24
1.153-1.496	0.86	0.19	0.50	0.06	1.43	3.14	1.02	3.30
1.496-1.947	1.06	0.22	0.53	0.06	1.45	3.21	1.27	3.45
1.947-2.522	1.26	0.24	0.57	0.09	1.49	3.31	1.61	3.68
2.522-3.277	1.68	0.22	0.56	0.12	1.52	3.50	1.91	3.99

Table 5.15: Systematic and Statistical errors (in %) for absolute cross section as a function of ϕ^* and in the $|y|$ range [0.0-0.4]. The total value includes the uncertainty of 2.6% due to luminosity.

ϕ^* range	MC stat.	Pile-up	Bkg.	pt scale	Eff.	Total syst.	Stat.	Total
0.000-0.004	0.45	0.45	0.01	0.04	1.42	3.03	0.46	3.06
0.004-0.008	0.47	0.39	0.01	0.04	1.42	3.02	0.48	3.06
0.008-0.012	0.47	0.53	0.01	0.03	1.41	3.04	0.48	3.08
0.012-0.016	0.51	0.27	0.01	0.04	1.42	3.02	0.49	3.06
0.016-0.020	0.51	0.54	0.01	0.04	1.42	3.05	0.50	3.09
0.020-0.024	0.52	0.51	0.01	0.04	1.42	3.05	0.51	3.09
0.024-0.029	0.45	0.41	0.01	0.03	1.42	3.02	0.46	3.06
0.029-0.034	0.46	0.37	0.01	0.05	1.42	3.02	0.48	3.06
0.034-0.039	0.51	0.31	0.01	0.04	1.42	3.02	0.49	3.06
0.039-0.045	0.47	0.44	0.01	0.04	1.42	3.03	0.46	3.07
0.045-0.051	0.48	0.51	0.01	0.04	1.42	3.04	0.48	3.08
0.051-0.057	0.50	0.37	0.01	0.04	1.42	3.02	0.50	3.07
0.057-0.064	0.45	0.39	0.01	0.04	1.42	3.02	0.48	3.06
0.064-0.072	0.49	0.39	0.01	0.04	1.42	3.03	0.47	3.06
0.072-0.081	0.50	0.41	0.02	0.05	1.42	3.03	0.47	3.07
0.081-0.091	0.45	0.54	0.02	0.04	1.42	3.04	0.47	3.08
0.091-0.102	0.47	0.38	0.02	0.04	1.41	3.02	0.47	3.06
0.102-0.114	0.47	0.40	0.02	0.05	1.41	3.02	0.48	3.06
0.114-0.128	0.48	0.23	0.03	0.03	1.42	3.01	0.48	3.05
0.128-0.145	0.44	0.55	0.03	0.03	1.42	3.04	0.47	3.08
0.145-0.165	0.43	0.39	0.04	0.03	1.42	3.02	0.47	3.05
0.165-0.189	0.46	0.40	0.04	0.03	1.42	3.02	0.47	3.06
0.189-0.219	0.43	0.41	0.05	0.03	1.42	3.02	0.47	3.06
0.219-0.258	0.43	0.38	0.07	0.03	1.42	3.02	0.47	3.05
0.258-0.312	0.44	0.32	0.09	0.03	1.42	3.01	0.46	3.05
0.312-0.391	0.41	0.48	0.12	0.03	1.42	3.03	0.46	3.06
0.391-0.524	0.42	0.36	0.17	0.03	1.42	3.02	0.46	3.05
0.524-0.695	0.49	0.38	0.25	0.04	1.42	3.04	0.56	3.09
0.695-0.918	0.61	0.38	0.34	0.03	1.42	3.07	0.68	3.14
0.918-1.153	0.76	0.46	0.43	0.06	1.42	3.12	0.92	3.26
1.153-1.496	0.88	0.20	0.48	0.07	1.43	3.14	1.04	3.31
1.496-1.947	1.06	0.09	0.51	0.09	1.45	3.20	1.28	3.45
1.947-2.522	1.32	0.12	0.52	0.10	1.48	3.31	1.62	3.69
2.522-3.277	1.65	0.35	0.52	0.16	1.52	3.50	1.96	4.01

Table 5.16: Systematic and Statistical errors (in %) for absolute cross section as a function of ϕ^* and in the $|y|$ range [0.4-0.8]. The total value includes the uncertainty of 2.6% due to luminosity.

ϕ^* range	**MC stat.**	**Pile-up**	**Bkg.**	**pt scale**	**Eff.**	**Total syst.**	**Stat.**	**Total**
0.000-0.004	0.44	0.48	0.01	0.03	1.42	3.03	0.47	3.07
0.004-0.008	0.48	0.20	0.01	0.04	1.42	3.01	0.48	3.04
0.008-0.012	0.51	0.33	0.01	0.04	1.42	3.02	0.49	3.06
0.012-0.016	0.50	0.48	0.01	0.04	1.42	3.04	0.49	3.08
0.016-0.020	0.49	0.50	0.01	0.04	1.42	3.04	0.50	3.08
0.020-0.024	0.50	0.44	0.01	0.04	1.42	3.04	0.51	3.08
0.024-0.029	0.46	0.47	0.01	0.04	1.42	3.03	0.46	3.07
0.029-0.034	0.49	0.46	0.01	0.04	1.42	3.04	0.48	3.07
0.034-0.039	0.51	0.41	0.01	0.04	1.42	3.03	0.49	3.07
0.039-0.045	0.47	0.41	0.01	0.04	1.42	3.03	0.47	3.06
0.045-0.051	0.51	0.44	0.01	0.03	1.42	3.04	0.49	3.07
0.051-0.057	0.52	0.48	0.01	0.04	1.42	3.04	0.51	3.09
0.057-0.064	0.46	0.48	0.01	0.04	1.42	3.04	0.49	3.07
0.064-0.072	0.44	0.42	0.01	0.04	1.42	3.02	0.48	3.06
0.072-0.081	0.45	0.43	0.01	0.03	1.42	3.02	0.47	3.06
0.081-0.091	0.45	0.32	0.02	0.03	1.42	3.01	0.48	3.05
0.091-0.102	0.46	0.42	0.02	0.03	1.42	3.03	0.48	3.06
0.102-0.114	0.45	0.35	0.02	0.04	1.42	3.02	0.49	3.05
0.114-0.128	0.50	0.30	0.03	0.04	1.42	3.02	0.49	3.06
0.128-0.145	0.46	0.35	0.03	0.03	1.42	3.02	0.47	3.05
0.145-0.165	0.46	0.42	0.04	0.03	1.42	3.03	0.48	3.06
0.165-0.189	0.47	0.45	0.04	0.03	1.42	3.03	0.48	3.07
0.189-0.219	0.45	0.46	0.05	0.03	1.42	3.03	0.48	3.07
0.219-0.258	0.44	0.42	0.07	0.04	1.42	3.02	0.48	3.06
0.258-0.312	0.43	0.39	0.09	0.03	1.42	3.02	0.47	3.05
0.312-0.391	0.43	0.43	0.12	0.04	1.42	3.02	0.47	3.06
0.391-0.524	0.42	0.47	0.16	0.03	1.42	3.03	0.47	3.07
0.524-0.695	0.52	0.42	0.24	0.04	1.42	3.05	0.57	3.10
0.695-0.918	0.63	0.40	0.31	0.04	1.42	3.07	0.70	3.15
0.918-1.153	0.83	0.19	0.40	0.07	1.43	3.11	0.95	3.25
1.153-1.496	0.90	0.58	0.45	0.06	1.44	3.19	1.08	3.37
1.496-1.947	1.21	0.63	0.47	0.08	1.48	3.32	1.35	3.58
1.947-2.522	1.54	0.44	0.49	0.11	1.54	3.46	1.70	3.85
2.522-3.277	1.96	0.28	0.48	0.12	1.59	3.67	2.08	4.22

Table 5.17: Systematic and Statistical errors (in %) for absolute cross section as a function of ϕ^* and in the $|y|$ range [0.8-1.2]. The total value includes the uncertainty of 2.6% due to luminosity.

ϕ^* range	MC stat.	Pile-up	Bkg.	pt scale	Eff.	Total syst.	Stat.	Total
0.000-0.004	0.49	0.48	0.01	0.04	1.42	3.04	0.50	3.08
0.004-0.008	0.53	0.58	0.01	0.03	1.42	3.06	0.52	3.11
0.008-0.012	0.56	0.59	0.01	0.04	1.42	3.07	0.52	3.11
0.012-0.016	0.53	0.44	0.01	0.04	1.42	3.04	0.53	3.08
0.016-0.020	0.54	0.49	0.01	0.04	1.42	3.05	0.53	3.10
0.020-0.024	0.56	0.57	0.01	0.03	1.42	3.06	0.56	3.11
0.024-0.029	0.50	0.51	0.01	0.04	1.42	3.05	0.50	3.09
0.029-0.034	0.55	0.50	0.01	0.03	1.42	3.05	0.52	3.10
0.034-0.039	0.52	0.63	0.01	0.04	1.42	3.07	0.54	3.12
0.039-0.045	0.50	0.61	0.01	0.04	1.42	3.06	0.50	3.10
0.045-0.051	0.55	0.54	0.01	0.04	1.42	3.06	0.53	3.10
0.051-0.057	0.53	0.33	0.01	0.04	1.42	3.03	0.55	3.07
0.057-0.064	0.52	0.59	0.01	0.03	1.42	3.06	0.52	3.11
0.064-0.072	0.49	0.53	0.01	0.03	1.42	3.05	0.51	3.09
0.072-0.081	0.48	0.48	0.02	0.04	1.42	3.04	0.51	3.08
0.081-0.091	0.51	0.43	0.02	0.03	1.42	3.04	0.52	3.08
0.091-0.102	0.52	0.58	0.02	0.04	1.42	3.06	0.53	3.11
0.102-0.114	0.50	0.51	0.02	0.03	1.42	3.05	0.53	3.09
0.114-0.128	0.51	0.58	0.03	0.03	1.42	3.06	0.53	3.10
0.128-0.145	0.50	0.58	0.03	0.03	1.42	3.06	0.52	3.10
0.145-0.165	0.49	0.55	0.04	0.03	1.42	3.05	0.52	3.10
0.165-0.189	0.49	0.64	0.04	0.03	1.42	3.07	0.52	3.11
0.189-0.219	0.49	0.53	0.05	0.03	1.42	3.05	0.52	3.09
0.219-0.258	0.49	0.62	0.06	0.03	1.42	3.06	0.51	3.11
0.258-0.312	0.48	0.53	0.08	0.03	1.42	3.05	0.51	3.09
0.312-0.391	0.46	0.58	0.11	0.03	1.42	3.05	0.51	3.10
0.391-0.524	0.45	0.42	0.16	0.03	1.42	3.03	0.52	3.07
0.524-0.695	0.57	0.57	0.24	0.04	1.42	3.08	0.64	3.15
0.695-0.918	0.67	0.62	0.30	0.05	1.43	3.12	0.78	3.22
0.918-1.153	0.92	0.26	0.36	0.07	1.45	3.14	1.06	3.32
1.153-1.496	1.11	0.66	0.42	0.06	1.48	3.29	1.23	3.51
1.496-1.947	1.43	0.75	0.45	0.11	1.58	3.48	1.57	3.81
1.947-2.522	1.86	0.51	0.46	0.13	1.74	3.71	2.03	4.23
2.522-3.277	2.25	1.24	0.49	0.13	1.83	4.12	2.50	4.82

Table 5.18: Systematic and Statistical errors (in %) for absolute cross section as a function of ϕ^* and in the $|y|$ range [1.2-1.6]. The total value includes the uncertainty of 2.6% due to luminosity.

ϕ^* range	MC stat.	Pile-up	Bkg.	pt scale	Eff.	Total syst.	Stat.	Total
0.000-0.004	0.64	0.54	0.01	0.04	1.42	3.08	0.62	3.14
0.004-0.008	0.68	0.97	0.01	0.04	1.42	3.19	0.65	3.25
0.008-0.012	0.74	0.61	0.01	0.04	1.42	3.11	0.66	3.18
0.012-0.016	0.74	0.84	0.01	0.04	1.42	3.17	0.67	3.24
0.016-0.020	0.75	0.57	0.01	0.04	1.42	3.11	0.69	3.18
0.020-0.024	0.75	0.84	0.01	0.04	1.42	3.17	0.69	3.24
0.024-0.029	0.72	0.76	0.01	0.04	1.42	3.14	0.63	3.21
0.029-0.034	0.68	0.60	0.01	0.04	1.42	3.10	0.66	3.17
0.034-0.039	0.71	0.77	0.01	0.04	1.42	3.14	0.68	3.21
0.039-0.045	0.68	0.80	0.01	0.04	1.42	3.14	0.64	3.21
0.045-0.051	0.73	0.77	0.01	0.04	1.42	3.14	0.66	3.21
0.051-0.057	0.71	0.67	0.01	0.05	1.42	3.12	0.69	3.19
0.057-0.064	0.69	0.96	0.01	0.04	1.42	3.19	0.66	3.26
0.064-0.072	0.71	0.85	0.01	0.04	1.42	3.16	0.65	3.23
0.072-0.081	0.66	0.69	0.01	0.04	1.42	3.11	0.65	3.18
0.081-0.091	0.68	0.88	0.02	0.04	1.42	3.16	0.66	3.23
0.091-0.102	0.72	0.91	0.02	0.04	1.42	3.18	0.66	3.25
0.102-0.114	0.71	0.77	0.02	0.04	1.42	3.14	0.68	3.21
0.114-0.128	0.68	0.58	0.03	0.04	1.42	3.09	0.67	3.16
0.128-0.145	0.68	0.56	0.03	0.03	1.42	3.09	0.65	3.16
0.145-0.165	0.68	0.91	0.03	0.03	1.42	3.17	0.66	3.24
0.165-0.189	0.66	0.68	0.04	0.04	1.42	3.11	0.66	3.18
0.189-0.219	0.66	0.56	0.05	0.03	1.42	3.08	0.65	3.15
0.219-0.258	0.68	0.69	0.07	0.04	1.42	3.12	0.66	3.19
0.258-0.312	0.64	0.78	0.08	0.04	1.42	3.13	0.64	3.19
0.312-0.391	0.68	0.69	0.11	0.05	1.42	3.12	0.66	3.19
0.391-0.524	0.67	0.69	0.15	0.04	1.42	3.12	0.66	3.19
0.524-0.695	0.76	0.58	0.23	0.05	1.43	3.13	0.81	3.23
0.695-0.918	0.94	0.52	0.29	0.06	1.44	3.17	1.00	3.33
0.918-1.153	1.25	0.59	0.36	0.07	1.47	3.31	1.36	3.58
1.153-1.496	1.59	0.22	0.39	0.09	1.54	3.44	1.63	3.81
1.496-1.947	2.01	0.86	0.44	0.19	1.69	3.82	2.21	4.42
1.947-2.522	2.74	0.28	0.49	0.17	2.01	4.32	2.98	5.25
2.522-3.277	3.41	0.26	0.51	0.22	2.40	4.95	3.90	6.30

Table 5.19: Systematic and Statistical errors (in %) for absolute cross section as a function of ϕ^* and in the $|y|$ range [1.6-2.0]. The total value includes the uncertainty of 2.6% due to luminosity.

ϕ^* range	MC stat.	Pile-up	Bkg.	pt scale	Eff.	Total syst.	Stat.	Total
0.000-0.004	1.47	1.09	0.01	0.09	1.42	3.48	1.34	3.73
0.004-0.008	1.62	0.98	0.01	0.09	1.42	3.52	1.41	3.79
0.008-0.012	1.63	1.02	0.01	0.09	1.42	3.53	1.45	3.82
0.012-0.016	1.73	1.08	0.01	0.10	1.42	3.60	1.43	3.87
0.016-0.020	1.69	1.07	0.01	0.09	1.42	3.57	1.49	3.87
0.020-0.024	1.71	0.98	0.01	0.12	1.42	3.56	1.48	3.86
0.024-0.029	1.68	1.19	0.01	0.07	1.42	3.61	1.37	3.86
0.029-0.034	1.62	1.01	0.01	0.08	1.42	3.52	1.40	3.79
0.034-0.039	1.64	1.42	0.01	0.08	1.42	3.67	1.50	3.97
0.039-0.045	1.54	0.61	0.01	0.08	1.42	3.39	1.34	3.65
0.045-0.051	1.62	1.09	0.01	0.07	1.42	3.55	1.40	3.81
0.051-0.057	1.73	1.06	0.01	0.08	1.42	3.59	1.50	3.89
0.057-0.064	1.68	0.92	0.01	0.07	1.42	3.53	1.44	3.81
0.064-0.072	1.50	1.03	0.01	0.08	1.42	3.48	1.40	3.75
0.072-0.081	1.63	1.21	0.02	0.10	1.42	3.59	1.41	3.86
0.081-0.091	1.72	0.87	0.02	0.11	1.42	3.54	1.40	3.81
0.091-0.102	1.57	0.66	0.02	0.08	1.42	3.42	1.44	3.71
0.102-0.114	1.67	0.71	0.02	0.10	1.42	3.47	1.46	3.77
0.114-0.128	1.72	0.74	0.02	0.08	1.42	3.51	1.42	3.78
0.128-0.145	1.58	1.17	0.03	0.07	1.42	3.56	1.41	3.83
0.145-0.165	1.59	1.17	0.04	0.07	1.42	3.56	1.41	3.83
0.165-0.189	1.65	0.74	0.03	0.09	1.42	3.47	1.45	3.76
0.189-0.219	1.57	1.10	0.05	0.08	1.42	3.53	1.43	3.81
0.219-0.258	1.68	0.73	0.05	0.12	1.42	3.48	1.44	3.77
0.258-0.312	1.49	1.31	0.07	0.08	1.42	3.56	1.41	3.83
0.312-0.391	1.55	0.92	0.11	0.10	1.42	3.47	1.42	3.75
0.391-0.524	1.56	0.75	0.14	0.08	1.42	3.44	1.44	3.73
0.524-0.695	1.96	0.77	0.21	0.11	1.43	3.65	1.76	4.05
0.695-0.918	2.19	0.89	0.26	0.24	1.44	3.81	2.17	4.39
0.918-1.153	3.08	0.58	0.34	0.14	1.49	4.35	3.08	5.33
1.153-1.496	3.55	0.58	0.41	0.34	1.79	4.81	3.73	6.09
1.496-1.947	4.83	0.67	0.49	0.54	3.07	6.36	4.98	8.08
1.947-2.522	8.56	2.45	0.38	0.46	4.44	10.30	7.12	12.52
2.522-3.277	10.85	1.19	0.43	0.04	6.57	13.02	10.21	16.54

Table 5.20: Systematic and Statistical errors (in %) for absolute cross section as a function of ϕ^* and in the $|y|$ range [2.0-2.4]. The total value includes the uncertainty of 2.6% due to luminosity.

ϕ^* range	**MC stat.**	**Pile-up**	**Bkg.**	**pt scale**	**Eff.**	**Total syst.**	**Stat.**	**Total**
0.000-0.004	0.43	0.08	0.04	0.02	0.05	0.44	0.46	0.64
0.004-0.008	0.47	0.18	0.04	0.03	0.05	0.51	0.48	0.69
0.008-0.012	0.46	0.04	0.04	0.03	0.05	0.47	0.48	0.67
0.012-0.016	0.48	0.10	0.04	0.02	0.05	0.49	0.49	0.69
0.016-0.020	0.50	0.02	0.04	0.02	0.05	0.51	0.50	0.71
0.020-0.024	0.51	0.11	0.04	0.03	0.05	0.53	0.51	0.73
0.024-0.029	0.47	0.08	0.04	0.02	0.05	0.48	0.46	0.66
0.029-0.034	0.47	0.02	0.04	0.02	0.05	0.48	0.48	0.67
0.034-0.039	0.48	0.06	0.04	0.02	0.04	0.49	0.49	0.69
0.039-0.045	0.45	0.14	0.04	0.02	0.04	0.48	0.46	0.66
0.045-0.051	0.45	0.08	0.04	0.03	0.05	0.46	0.48	0.66
0.051-0.057	0.48	0.05	0.04	0.03	0.05	0.49	0.50	0.70
0.057-0.064	0.46	0.15	0.03	0.02	0.04	0.49	0.48	0.69
0.064-0.072	0.47	0.02	0.03	0.02	0.04	0.47	0.47	0.66
0.072-0.081	0.45	0.05	0.03	0.02	0.04	0.46	0.46	0.65
0.081-0.091	0.46	0.12	0.03	0.03	0.04	0.48	0.47	0.67
0.091-0.102	0.44	0.13	0.03	0.03	0.04	0.46	0.47	0.66
0.102-0.114	0.47	0.07	0.02	0.03	0.04	0.48	0.48	0.68
0.114-0.128	0.47	0.09	0.02	0.02	0.04	0.48	0.48	0.68
0.128-0.145	0.43	0.02	0.01	0.02	0.05	0.43	0.47	0.64
0.145-0.165	0.44	0.13	0.01	0.02	0.05	0.46	0.47	0.66
0.165-0.189	0.42	0.21	0.00	0.02	0.05	0.48	0.47	0.67
0.189-0.219	0.43	0.06	0.01	0.02	0.05	0.44	0.47	0.64
0.219-0.258	0.43	0.00	0.02	0.02	0.05	0.43	0.46	0.63
0.258-0.312	0.41	0.10	0.04	0.02	0.05	0.42	0.46	0.62
0.312-0.391	0.44	0.09	0.07	0.02	0.05	0.46	0.46	0.65
0.391-0.524	0.41	0.07	0.13	0.02	0.06	0.44	0.46	0.64
0.524-0.695	0.44	0.10	0.21	0.02	0.08	0.51	0.55	0.75
0.695-0.918	0.62	0.07	0.32	0.03	0.10	0.71	0.68	0.98
0.918-1.153	0.76	0.13	0.41	0.04	0.14	0.89	0.90	1.26
1.153-1.496	0.86	0.31	0.45	0.04	0.21	1.04	1.02	1.46
1.496-1.947	1.05	0.28	0.49	0.05	0.31	1.23	1.27	1.77
1.947-2.522	1.26	0.26	0.52	0.10	0.51	1.48	1.61	2.19
2.522-3.277	1.67	0.32	0.51	0.13	0.57	1.87	1.90	2.67

Table 5.21: Systematic uncertainty (in %) for normalized cross section as a function of ϕ^* for y range [0.0-0.4].

ϕ^* range	MC stat.	Pile-up	Bkg.	pt scale	Eff.	Total syst.	Stat.	Total
0.000-0.004	0.45	0.04	0.04	0.03	0.03	0.46	0.46	0.65
0.004-0.008	0.47	0.11	0.04	0.03	0.03	0.49	0.48	0.68
0.008-0.012	0.48	0.03	0.04	0.02	0.03	0.48	0.48	0.68
0.012-0.016	0.51	0.22	0.04	0.03	0.03	0.56	0.49	0.74
0.016-0.020	0.51	0.05	0.04	0.03	0.03	0.52	0.50	0.72
0.020-0.024	0.53	0.01	0.04	0.03	0.03	0.53	0.51	0.74
0.024-0.029	0.45	0.08	0.04	0.02	0.03	0.46	0.46	0.65
0.029-0.034	0.46	0.12	0.04	0.03	0.03	0.48	0.48	0.68
0.034-0.039	0.51	0.18	0.04	0.03	0.03	0.55	0.49	0.73
0.039-0.045	0.47	0.05	0.04	0.03	0.03	0.47	0.46	0.66
0.045-0.051	0.48	0.02	0.04	0.03	0.03	0.49	0.48	0.68
0.051-0.057	0.50	0.13	0.03	0.03	0.03	0.52	0.50	0.72
0.057-0.064	0.44	0.11	0.03	0.03	0.03	0.46	0.48	0.66
0.064-0.072	0.49	0.10	0.03	0.03	0.03	0.50	0.47	0.69
0.072-0.081	0.49	0.08	0.03	0.03	0.03	0.50	0.47	0.69
0.081-0.091	0.45	0.05	0.03	0.03	0.03	0.46	0.47	0.65
0.091-0.102	0.47	0.11	0.03	0.03	0.03	0.48	0.47	0.68
0.102-0.114	0.47	0.10	0.02	0.03	0.03	0.48	0.48	0.68
0.114-0.128	0.48	0.26	0.02	0.03	0.03	0.55	0.48	0.73
0.128-0.145	0.44	0.05	0.02	0.02	0.03	0.44	0.47	0.65
0.145-0.165	0.43	0.10	0.01	0.03	0.03	0.44	0.47	0.65
0.165-0.189	0.45	0.09	0.00	0.03	0.03	0.47	0.47	0.66
0.189-0.219	0.43	0.09	0.00	0.03	0.03	0.44	0.47	0.64
0.219-0.258	0.42	0.11	0.02	0.03	0.04	0.44	0.47	0.64
0.258-0.312	0.44	0.18	0.04	0.02	0.04	0.48	0.46	0.66
0.312-0.391	0.41	0.02	0.07	0.02	0.04	0.42	0.46	0.62
0.391-0.524	0.42	0.13	0.13	0.02	0.05	0.46	0.46	0.65
0.524-0.695	0.48	0.11	0.21	0.03	0.07	0.54	0.56	0.78
0.695-0.918	0.61	0.12	0.30	0.03	0.09	0.70	0.68	0.97
0.918-1.153	0.76	0.04	0.39	0.06	0.13	0.87	0.92	1.27
1.153-1.496	0.88	0.29	0.44	0.06	0.20	1.05	1.04	1.48
1.496-1.947	1.06	0.41	0.47	0.08	0.31	1.27	1.28	1.80
1.947-2.522	1.33	0.37	0.47	0.10	0.44	1.52	1.62	2.23
2.522-3.277	1.63	0.11	0.47	0.15	0.58	1.80	1.95	2.66

Table 5.22: Systematic uncertainty (in %) for normalized cross section as a function of ϕ^* for y range [0.4-0.8].

ϕ^* range	**MC stat.**	**Pile-up**	**Bkg.**	**pt scale**	**Eff.**	**Total syst.**	**Stat.**	**Total**
0.000-0.004	0.44	0.02	0.04	0.03	0.03	0.45	0.47	0.65
0.004-0.008	0.48	0.29	0.04	0.03	0.03	0.57	0.48	0.74
0.008-0.012	0.51	0.17	0.04	0.03	0.03	0.54	0.49	0.73
0.012-0.016	0.50	0.02	0.04	0.03	0.03	0.50	0.49	0.70
0.016-0.020	0.49	0.01	0.04	0.03	0.03	0.49	0.50	0.70
0.020-0.024	0.50	0.05	0.04	0.03	0.03	0.51	0.51	0.72
0.024-0.029	0.46	0.03	0.04	0.03	0.03	0.47	0.46	0.66
0.029-0.034	0.48	0.03	0.04	0.03	0.03	0.49	0.48	0.68
0.034-0.039	0.51	0.08	0.04	0.03	0.03	0.52	0.49	0.72
0.039-0.045	0.47	0.09	0.04	0.03	0.03	0.48	0.47	0.67
0.045-0.051	0.51	0.06	0.04	0.03	0.03	0.52	0.49	0.71
0.051-0.057	0.52	0.01	0.04	0.03	0.03	0.52	0.51	0.73
0.057-0.064	0.46	0.01	0.03	0.03	0.03	0.46	0.49	0.68
0.064-0.072	0.44	0.08	0.03	0.03	0.03	0.45	0.48	0.65
0.072-0.081	0.45	0.07	0.03	0.02	0.03	0.46	0.47	0.66
0.081-0.091	0.45	0.17	0.03	0.03	0.03	0.48	0.48	0.68
0.091-0.102	0.45	0.07	0.03	0.03	0.03	0.46	0.48	0.67
0.102-0.114	0.45	0.14	0.02	0.03	0.03	0.48	0.49	0.68
0.114-0.128	0.50	0.19	0.02	0.03	0.03	0.54	0.49	0.72
0.128-0.145	0.46	0.14	0.02	0.03	0.03	0.48	0.47	0.67
0.145-0.165	0.46	0.08	0.01	0.03	0.03	0.47	0.48	0.67
0.165-0.189	0.47	0.05	0.01	0.03	0.03	0.47	0.48	0.67
0.189-0.219	0.45	0.03	0.01	0.03	0.03	0.46	0.48	0.66
0.219-0.258	0.44	0.08	0.02	0.03	0.03	0.45	0.48	0.65
0.258-0.312	0.43	0.11	0.04	0.02	0.04	0.44	0.47	0.65
0.312-0.391	0.43	0.07	0.07	0.03	0.04	0.44	0.47	0.64
0.391-0.524	0.42	0.02	0.11	0.03	0.06	0.44	0.47	0.64
0.524-0.695	0.51	0.07	0.19	0.04	0.08	0.56	0.57	0.80
0.695-0.918	0.63	0.09	0.27	0.04	0.12	0.70	0.70	0.99
0.918-1.153	0.83	0.30	0.36	0.07	0.19	0.97	0.95	1.36
1.153-1.496	0.90	0.09	0.41	0.06	0.28	1.03	1.08	1.49
1.496-1.947	1.21	0.13	0.42	0.09	0.45	1.37	1.35	1.92
1.947-2.522	1.54	0.08	0.44	0.11	0.65	1.73	1.70	2.43
2.522-3.277	1.96	0.22	0.43	0.12	0.83	2.18	2.07	3.01

Table 5.23: Systematic uncertainty (in %) for normalized cross section as a function of ϕ^* for y range [0.8-1.2].

ϕ^* range	MC stat.	Pile-up	Bkg.	pt scale	Eff.	Total syst.	Stat.	Total
0.000-0.004	0.49	0.01	0.04	0.03	0.04	0.50	0.50	0.71
0.004-0.008	0.53	0.09	0.04	0.03	0.04	0.54	0.52	0.75
0.008-0.012	0.56	0.10	0.04	0.03	0.04	0.57	0.52	0.77
0.012-0.016	0.53	0.06	0.04	0.04	0.04	0.53	0.53	0.75
0.016-0.020	0.54	0.00	0.04	0.04	0.04	0.54	0.53	0.76
0.020-0.024	0.56	0.07	0.04	0.04	0.04	0.56	0.56	0.79
0.024-0.029	0.50	0.02	0.04	0.03	0.04	0.50	0.50	0.71
0.029-0.034	0.55	0.01	0.04	0.03	0.04	0.55	0.52	0.75
0.034-0.039	0.52	0.13	0.04	0.03	0.04	0.54	0.54	0.76
0.039-0.045	0.50	0.11	0.04	0.03	0.04	0.52	0.50	0.72
0.045-0.051	0.55	0.05	0.04	0.03	0.04	0.55	0.53	0.76
0.051-0.057	0.53	0.16	0.04	0.03	0.04	0.55	0.55	0.78
0.057-0.064	0.52	0.10	0.04	0.03	0.04	0.53	0.52	0.75
0.064-0.072	0.49	0.03	0.03	0.03	0.04	0.50	0.51	0.71
0.072-0.081	0.48	0.02	0.03	0.03	0.04	0.48	0.51	0.70
0.081-0.091	0.51	0.06	0.03	0.03	0.04	0.52	0.52	0.73
0.091-0.102	0.52	0.09	0.03	0.03	0.04	0.53	0.53	0.75
0.102-0.114	0.50	0.02	0.03	0.03	0.04	0.50	0.53	0.73
0.114-0.128	0.51	0.08	0.02	0.03	0.04	0.52	0.53	0.74
0.128-0.145	0.49	0.09	0.02	0.03	0.04	0.50	0.52	0.72
0.145-0.165	0.49	0.06	0.01	0.03	0.04	0.50	0.52	0.72
0.165-0.189	0.49	0.14	0.01	0.03	0.04	0.51	0.52	0.73
0.189-0.219	0.49	0.04	0.01	0.03	0.05	0.50	0.52	0.72
0.219-0.258	0.49	0.12	0.02	0.03	0.05	0.51	0.51	0.73
0.258-0.312	0.49	0.04	0.04	0.03	0.06	0.50	0.51	0.71
0.312-0.391	0.45	0.09	0.07	0.03	0.07	0.47	0.51	0.70
0.391-0.524	0.45	0.08	0.11	0.03	0.09	0.48	0.52	0.71
0.524-0.695	0.57	0.08	0.19	0.04	0.13	0.62	0.64	0.89
0.695-0.918	0.67	0.13	0.26	0.05	0.20	0.76	0.78	1.09
0.918-1.153	0.92	0.24	0.31	0.07	0.30	1.04	1.06	1.49
1.153-1.496	1.11	0.17	0.38	0.07	0.45	1.27	1.23	1.77
1.496-1.947	1.43	0.26	0.40	0.11	0.70	1.67	1.57	2.29
1.947-2.522	1.86	0.05	0.41	0.13	1.05	2.18	2.03	2.98
2.522-3.277	2.24	0.72	0.44	0.13	1.30	2.73	2.49	3.70

Table 5.24: Systematic uncertainty (in %) for normalized cross section as a function of ϕ^* for y range [1.2-1.6].

ϕ^* range	**MC stat.**	**Pile-up**	**Bkg.**	**pt scale**	**Eff.**	**Total syst.**	**Stat.**	**Total**
0.000-0.004	0.64	0.04	0.04	0.04	0.07	0.65	0.62	0.90
0.004-0.008	0.69	0.47	0.04	0.04	0.07	0.84	0.65	1.06
0.008-0.012	0.74	0.11	0.04	0.04	0.07	0.75	0.66	1.00
0.012-0.016	0.73	0.35	0.04	0.05	0.07	0.82	0.67	1.06
0.016-0.020	0.75	0.07	0.04	0.04	0.07	0.76	0.69	1.03
0.020-0.024	0.74	0.35	0.04	0.05	0.07	0.83	0.69	1.08
0.024-0.029	0.72	0.27	0.04	0.04	0.07	0.77	0.63	1.00
0.029-0.034	0.68	0.11	0.04	0.03	0.07	0.70	0.66	0.96
0.034-0.039	0.71	0.28	0.04	0.05	0.07	0.77	0.68	1.02
0.039-0.045	0.68	0.30	0.04	0.04	0.07	0.75	0.64	0.99
0.045-0.051	0.72	0.28	0.04	0.04	0.07	0.78	0.66	1.02
0.051-0.057	0.71	0.18	0.04	0.05	0.07	0.73	0.69	1.01
0.057-0.064	0.69	0.46	0.04	0.03	0.07	0.84	0.66	1.07
0.064-0.072	0.71	0.36	0.03	0.04	0.07	0.80	0.65	1.03
0.072-0.081	0.66	0.19	0.03	0.04	0.07	0.69	0.65	0.95
0.081-0.091	0.68	0.38	0.03	0.04	0.07	0.79	0.66	1.02
0.091-0.102	0.71	0.41	0.03	0.04	0.07	0.83	0.66	1.06
0.102-0.114	0.71	0.28	0.03	0.04	0.07	0.76	0.68	1.02
0.114-0.128	0.68	0.08	0.02	0.04	0.07	0.69	0.67	0.96
0.128-0.145	0.68	0.08	0.02	0.03	0.07	0.69	0.65	0.95
0.145-0.165	0.67	0.41	0.02	0.03	0.07	0.79	0.66	1.03
0.165-0.189	0.66	0.19	0.01	0.04	0.07	0.69	0.66	0.96
0.189-0.219	0.65	0.07	0.01	0.03	0.08	0.66	0.65	0.93
0.219-0.258	0.67	0.20	0.02	0.03	0.08	0.71	0.66	0.97
0.258-0.312	0.64	0.28	0.04	0.04	0.09	0.71	0.64	0.96
0.312-0.391	0.68	0.20	0.06	0.04	0.10	0.72	0.66	0.97
0.391-0.524	0.66	0.20	0.11	0.04	0.13	0.71	0.66	0.97
0.524-0.695	0.76	0.09	0.18	0.05	0.17	0.81	0.81	1.15
0.695-0.918	0.94	0.03	0.25	0.06	0.26	1.01	1.00	1.42
0.918-1.153	1.25	0.10	0.31	0.07	0.40	1.35	1.36	1.92
1.153-1.496	1.59	0.28	0.35	0.09	0.64	1.77	1.63	2.41
1.496-1.947	2.01	0.37	0.39	0.18	0.99	2.31	2.21	3.20
1.947-2.522	2.74	0.22	0.44	0.17	1.51	3.18	2.98	4.36
2.522-3.277	3.41	0.23	0.47	0.22	2.15	4.07	3.90	5.63

Table 5.25: Systematic uncertainty (in %) for normalized cross section as a function of ϕ^* for y range [1.6-2.0].

ϕ^* range	MC stat.	Pile-up	Bkg.	pt scale	Eff.	Total syst.	Stat.	Total
0.000-0.004	1.47	0.60	0.04	0.09	0.10	1.60	1.34	2.08
0.004-0.008	1.62	0.49	0.04	0.09	0.10	1.70	1.41	2.21
0.008-0.012	1.63	0.52	0.04	0.09	0.10	1.72	1.45	2.25
0.012-0.016	1.73	0.59	0.04	0.10	0.10	1.83	1.43	2.33
0.016-0.020	1.69	0.57	0.04	0.09	0.10	1.79	1.49	2.33
0.020-0.024	1.71	0.48	0.04	0.12	0.10	1.78	1.48	2.32
0.024-0.029	1.68	0.69	0.04	0.07	0.10	1.82	1.37	2.28
0.029-0.034	1.62	0.51	0.04	0.08	0.10	1.70	1.40	2.21
0.034-0.039	1.64	0.93	0.04	0.08	0.10	1.89	1.50	2.41
0.039-0.045	1.54	0.12	0.04	0.08	0.10	1.55	1.34	2.05
0.045-0.051	1.62	0.60	0.04	0.06	0.10	1.73	1.40	2.22
0.051-0.057	1.73	0.57	0.04	0.08	0.10	1.83	1.50	2.36
0.057-0.064	1.68	0.43	0.04	0.07	0.10	1.74	1.44	2.26
0.064-0.072	1.50	0.54	0.04	0.08	0.10	1.60	1.40	2.13
0.072-0.081	1.63	0.71	0.03	0.10	0.11	1.78	1.41	2.27
0.081-0.091	1.72	0.38	0.03	0.10	0.10	1.77	1.40	2.26
0.091-0.102	1.57	0.17	0.03	0.08	0.11	1.59	1.44	2.14
0.102-0.114	1.67	0.21	0.03	0.10	0.10	1.69	1.46	2.23
0.114-0.128	1.72	0.25	0.03	0.08	0.11	1.74	1.42	2.25
0.128-0.145	1.58	0.67	0.02	0.07	0.11	1.72	1.41	2.23
0.145-0.165	1.58	0.68	0.02	0.06	0.11	1.73	1.41	2.23
0.165-0.189	1.65	0.24	0.02	0.09	0.11	1.67	1.45	2.21
0.189-0.219	1.57	0.60	0.01	0.08	0.12	1.69	1.43	2.21
0.219-0.258	1.68	0.23	0.01	0.11	0.12	1.70	1.44	2.23
0.258-0.312	1.49	0.81	0.03	0.08	0.13	1.70	1.41	2.21
0.312-0.391	1.55	0.43	0.06	0.09	0.14	1.61	1.42	2.15
0.391-0.524	1.56	0.26	0.09	0.09	0.16	1.60	1.44	2.15
0.524-0.695	1.96	0.27	0.16	0.10	0.21	2.00	1.76	2.66
0.695-0.918	2.18	0.39	0.21	0.23	0.28	2.26	2.17	3.13
0.918-1.153	3.08	0.12	0.30	0.14	0.47	3.14	3.08	4.40
1.153-1.496	3.55	0.09	0.36	0.34	1.11	3.75	3.73	5.29
1.496-1.947	4.83	1.17	0.44	0.55	2.78	5.73	4.98	7.59
1.947-2.522	8.56	1.96	0.34	0.45	4.29	9.79	7.12	12.10
2.522-3.277	10.86	0.71	0.39	0.04	6.54	12.70	10.21	16.29

Table 5.26: Systematic uncertainty (in %) for normalized cross section as a function of ϕ^* for y range [2.0-2.4].

ϕ^*-bin	**Normalised Cross section**	**Absolute Cross section** (pb)
0.000-0.004	9.29±0.02±0.02	(4.437±0.010±0.067±0.115)$\times10^{3}$
0.004-0.008	9.22±0.02±0.02	(4.400±0.010±0.066±0.114)$\times10^{3}$
0.008-0.012	9.02±0.02±0.02	(4.306±0.010±0.065±0.112)$\times10^{3}$
0.012-0.016	8.76±0.02±0.02	(4.183±0.010±0.063±0.109)$\times10^{3}$
0.016-0.020	8.47±0.02±0.02	(4.045±0.009±0.062±0.105)$\times10^{3}$
0.020-0.024	8.13±0.02±0.02	(3.884±0.009±0.059±0.101)$\times10^{3}$
0.024-0.029	7.74±0.02±0.02	(3.697±0.008±0.056±0.096)$\times10^{3}$
0.029-0.034	7.27±0.02±0.02	(3.470±0.008±0.052±0.090)$\times10^{3}$
0.034-0.039	6.81±0.02±0.02	(3.249±0.007±0.049±0.084)$\times10^{3}$
0.039-0.045	6.35±0.01±0.01	(3.033±0.007±0.046±0.079)$\times10^{3}$
0.045-0.051	5.84±0.01±0.01	(2.788±0.006±0.042±0.072)$\times10^{3}$
0.051-0.057	5.37±0.01±0.01	(2.563±0.006±0.038±0.067)$\times10^{3}$
0.057-0.064	4.95±0.01±0.01	(2.362±0.005±0.036±0.061)$\times10^{3}$
0.064-0.072	4.488±0.010±0.010	(2.143±0.005±0.033±0.056)$\times10^{3}$
0.072-0.081	4.025±0.009±0.008	(1.922±0.004±0.029±0.050)$\times10^{3}$
0.081-0.091	3.564±0.008±0.008	(1.702±0.004±0.026±0.044)$\times10^{3}$
0.091-0.102	3.153±0.007±0.007	(1.505±0.003±0.023±0.039)$\times10^{3}$
0.102-0.114	2.774±0.006±0.006	(1.324±0.003±0.020±0.034)$\times10^{3}$
0.114-0.128	2.410±0.005±0.006	(1.151±0.003±0.017±0.030)$\times10^{3}$
0.128-0.145	2.059±0.005±0.004	(9.83±0.02±0.15±0.26)$\times10^{2}$
0.145-0.165	1.725±0.004±0.003	(8.23±0.02±0.12±0.21)$\times10^{2}$
0.165-0.189	1.415±0.003±0.003	(6.75±0.01±0.10±0.18)$\times10^{2}$
0.189-0.219	1.129±0.002±0.002	(5.39±0.01±0.08±0.14)$\times10^{2}$
0.219-0.258	0.869±0.002±0.002	(4.151±0.009±0.063±0.108)$\times10^{2}$
0.258-0.312	0.633±0.001±0.001	(3.023±0.007±0.045±0.079)$\times10^{2}$
0.312-0.391	0.4254±0.0009±0.0009	(2.031±0.004±0.031±0.053)$\times10^{2}$
0.391-0.524	0.2470±0.0005±0.0006	(1.179±0.003±0.018±0.031)$\times10^{2}$
0.524-0.695	0.1293±0.0003±0.0004	30.9±0.1±0.5±0.8
0.695-0.918	(6.46±0.02±0.03)$\times10^{-2}$	16.07±0.07±0.25±0.42
0.918-1.153	(3.37±0.01±0.02)$\times10^{-2}$	8.26±0.04±0.13±0.21
1.153-1.496	(1.730±0.009±0.011)$\times10^{-2}$	8.26±0.04±0.13±0.21
1.496-1.947	(8.32±0.05±0.06)$\times10^{-3}$	3.97±0.03±0.07±0.10
1.947-2.522	(4.00±0.03±0.04)$\times10^{-3}$	1.91±0.02±0.03±0.05
2.522-3.277	(2.08±0.02±0.02)$\times10^{-3}$	0.992±0.010±0.019±0.026

Table 5.27: The normalised and absolute differential cross section with respect to ϕ^* of in our fiducial region in data for the muon channel. The uncertainty for the normalised case is separated in the statistical component followed by the systematic uncertainty, whereas, the uncertainty for the absolute case is separated in the statistical component followed by the systematic uncertainty, with the luminosity uncertainty (2.6%) separate.

ϕ^*-bin	**Normalised Cross section**	**Absolute Cross section** (pb)
0.000-0.004	5.09±0.02±0.02	(2.43±0.01±0.04±0.06)×10^{3}
0.004-0.008	5.02±0.02±0.03	(2.40±0.01±0.04±0.06)×10^{3}
0.008-0.012	4.92±0.02±0.02	(2.35±0.01±0.04±0.06)×10^{3}
0.012-0.016	4.81±0.02±0.02	(2.30±0.01±0.04±0.06)×10^{3}
0.016-0.020	4.63±0.02±0.02	(2.21±0.01±0.04±0.06)×10^{3}
0.020-0.024	4.46±0.02±0.02	(2.13±0.01±0.03±0.06)×10^{3}
0.024-0.029	4.25±0.02±0.02	(2.028±0.009±0.032±0.053)×10^{3}
0.029-0.034	3.97±0.02±0.02	(1.894±0.009±0.030±0.049)×10^{3}
0.034-0.039	3.77±0.02±0.02	(1.800±0.009±0.028±0.047)×10^{3}
0.039-0.045	3.54±0.02±0.02	(1.691±0.008±0.026±0.044)×10^{3}
0.045-0.051	3.23±0.02±0.01	(1.543±0.007±0.024±0.040)×10^{3}
0.051-0.057	2.96±0.01±0.01	(1.411±0.007±0.022±0.037)×10^{3}
0.057-0.064	2.74±0.01±0.01	(1.308±0.006±0.021±0.034)×10^{3}
0.064-0.072	2.48±0.01±0.01	(1.185±0.006±0.019±0.031)×10^{3}
0.072-0.081	2.25±0.01±0.01	(1.073±0.005±0.017±0.028)×10^{3}
0.081-0.091	1.991±0.009±0.010	(9.51±0.04±0.15±0.25)×10^{2}
0.091-0.102	1.761±0.008±0.008	(8.41±0.04±0.13±0.22)×10^{2}
0.102-0.114	1.544±0.007±0.007	(7.37±0.04±0.11±0.19)×10^{2}
0.114-0.128	1.348±0.006±0.006	(6.44±0.03±0.10±0.17)×10^{2}
0.128-0.145	1.151±0.005±0.005	(5.49±0.03±0.09±0.14)×10^{2}
0.145-0.165	0.962±0.004±0.004	(4.59±0.02±0.07±0.12)×10^{2}
0.165-0.189	0.803±0.004±0.004	(3.84±0.02±0.06±0.10)×10^{2}
0.189-0.219	0.638±0.003±0.003	(3.04±0.01±0.05±0.08)×10^{2}
0.219-0.258	0.492±0.002±0.002	(2.35±0.01±0.04±0.06)×10^{2}
0.258-0.312	0.358±0.002±0.002	(1.708±0.008±0.026±0.044)×10^{2}
0.312-0.391	0.241±0.001±0.001	(1.152±0.005±0.018±0.030)×10^{2}
0.391-0.524	0.1400±0.0006±0.0006	66.8±0.3±1.0±1.7
0.524-0.695	(7.41±0.04±0.04)×10^{-2}	35.4±0.2±0.6±0.9
0.695-0.918	(3.76±0.03±0.03)×10^{-2}	17.9±0.1±0.3±0.5
0.918-1.153	(2.02±0.02±0.02)×10^{-2}	9.63±0.09±0.17±0.25
1.153-1.496	(1.05±0.01±0.01)×10^{-2}	5.01±0.05±0.09±0.13
1.496-1.947	(5.11±0.07±0.06)×10^{-3}	2.44±0.03±0.05±0.06
1.947-2.522	(2.49±0.04±0.04)×10^{-3}	1.19±0.02±0.02±0.03
2.522-3.277	(1.37±0.03±0.03)×10^{-3}	0.65±0.01±0.02±0.02

Table 5.28: The normalised and absolute differential cross section with respect to ϕ^* for the y range of [0.0-0.4], in our fiducial region in data for the muon channel. The uncertainty for the normalised case is separated in the statistical component followed by the systematic uncertainty, whereas, the uncertainty for the absolute case is separated in the statistical component followed by the systematic uncertainty, with the luminosity uncertainty (2.6%) separate.

ϕ^*-bin	Normalised Cross section	Absolute Cross section (pb)
0.000-0.004	5.04±0.02±0.02	$(2.41\pm0.01\pm0.04\pm0.06)\times10^3$
0.004-0.008	5.01±0.02±0.02	$(2.39\pm0.01\pm0.04\pm0.06)\times10^3$
0.008-0.012	4.97±0.02±0.02	$(2.37\pm0.01\pm0.04\pm0.06)\times10^3$
0.012-0.016	4.79±0.02±0.03	$(2.29\pm0.01\pm0.03\pm0.06)\times10^3$
0.016-0.020	4.63±0.02±0.02	$(2.21\pm0.01\pm0.04\pm0.06)\times10^3$
0.020-0.024	4.44±0.02±0.02	$(2.12\pm0.01\pm0.03\pm0.06)\times10^3$
0.024-0.029	4.25±0.02±0.02	$(2.028\pm0.009\pm0.031\pm0.053)\times10^3$
0.029-0.034	4.02±0.02±0.02	$(1.917\pm0.009\pm0.029\pm0.050)\times10^3$
0.034-0.039	3.74±0.02±0.02	$(1.787\pm0.009\pm0.027\pm0.046)\times10^3$
0.039-0.045	3.50±0.02±0.02	$(1.673\pm0.008\pm0.026\pm0.043)\times10^3$
0.045-0.051	3.21±0.02±0.02	$(1.532\pm0.007\pm0.024\pm0.040)\times10^3$
0.051-0.057	2.96±0.01±0.02	$(1.414\pm0.007\pm0.022\pm0.037)\times10^3$
0.057-0.064	2.76±0.01±0.01	$(1.317\pm0.006\pm0.020\pm0.034)\times10^3$
0.064-0.072	2.48±0.01±0.01	$(1.185\pm0.006\pm0.018\pm0.031)\times10^3$
0.072-0.081	2.23±0.01±0.01	$(1.063\pm0.005\pm0.017\pm0.028)\times10^3$
0.081-0.091	1.990±0.009±0.009	$(9.50\pm0.04\pm0.15\pm0.25)\times10^2$
0.091-0.102	1.760±0.008±0.009	$(8.40\pm0.04\pm0.13\pm0.22)\times10^2$
0.102-0.114	1.558±0.008±0.008	$(7.44\pm0.04\pm0.11\pm0.19)\times10^2$
0.114-0.128	1.342±0.006±0.007	$(6.41\pm0.03\pm0.10\pm0.17)\times10^2$
0.128-0.145	1.153±0.005±0.005	$(5.51\pm0.03\pm0.09\pm0.14)\times10^2$
0.145-0.165	0.971±0.005±0.004	$(4.64\pm0.02\pm0.07\pm0.12)\times10^2$
0.165-0.189	0.796±0.004±0.004	$(3.80\pm0.02\pm0.06\pm0.10)\times10^2$
0.189-0.219	0.640±0.003±0.003	$(3.06\pm0.01\pm0.05\pm0.08)\times10^2$
0.219-0.258	0.495±0.002±0.002	$(2.36\pm0.01\pm0.04\pm0.06)\times10^2$
0.258-0.312	0.359±0.002±0.002	$(1.714\pm0.008\pm0.026\pm0.045)\times10^2$
0.312-0.391	0.240±0.001±0.001	$(1.146\pm0.005\pm0.018\pm0.030)\times10^2$
0.391-0.524	0.1396±0.0006±0.0006	66.7±0.3±1.0±1.7
0.524-0.695	$(7.41\pm0.04\pm0.04)\times10^{-2}$	35.4±0.2±0.6±0.9
0.695-0.918	$(3.76\pm0.03\pm0.03)\times10^{-2}$	17.9±0.1±0.3±0.5
0.918-1.153	$(1.91\pm0.02\pm0.02)\times10^{-2}$	9.11±0.08±0.16±0.24
1.153-1.496	$(1.04\pm0.01\pm0.01)\times10^{-2}$	4.95±0.05±0.09±0.13
1.496-1.947	$(5.07\pm0.07\pm0.06)\times10^{-3}$	2.42±0.03±0.05±0.06
1.947-2.522	$(2.54\pm0.04\pm0.04)\times10^{-3}$	1.21±0.02±0.02±0.03
2.522-3.277	$(1.35\pm0.03\pm0.02)\times10^{-3}$	0.64±0.01±0.02±0.02

Table 5.29: The normalised and absolute differential cross section with respect to ϕ^* for the y range of [0.4-0.8], in our fiducial region in data for the muon channel. The uncertainty for the normalised case is separated in the statistical component followed by the systematic uncertainty, whereas, the uncertainty for the absolute case is separated in the statistical component followed by the systematic uncertainty, with the luminosity uncertainty (2.6%) separate.

ϕ^*-bin	**Normalised Cross section**	**Absolute Cross section** (pb)
0.000-0.004	5.01±0.02±0.02	$(2.39\pm0.01\pm0.04\pm0.06)\times10^{3}$
0.004-0.008	5.05±0.02±0.03	$(2.41\pm0.01\pm0.04\pm0.06)\times10^{3}$
0.008-0.012	4.87±0.02±0.03	$(2.32\pm0.01\pm0.04\pm0.06)\times10^{3}$
0.012-0.016	4.73±0.02±0.02	$(2.26\pm0.01\pm0.04\pm0.06)\times10^{3}$
0.016-0.020	4.61±0.02±0.02	$(2.20\pm0.01\pm0.03\pm0.06)\times10^{3}$
0.020-0.024	4.40±0.02±0.02	$(2.10\pm0.01\pm0.03\pm0.05)\times10^{3}$
0.024-0.029	4.19±0.02±0.02	$(2.002\pm0.009\pm0.031\pm0.052)\times10^{3}$
0.029-0.034	3.96±0.02±0.02	$(1.890\pm0.009\pm0.030\pm0.049)\times10^{3}$
0.034-0.039	3.71±0.02±0.02	$(1.771\pm0.009\pm0.028\pm0.046)\times10^{3}$
0.039-0.045	3.41±0.02±0.02	$(1.626\pm0.008\pm0.025\pm0.042)\times10^{3}$
0.045-0.051	3.17±0.02±0.02	$(1.516\pm0.007\pm0.024\pm0.039)\times10^{3}$
0.051-0.057	2.91±0.01±0.02	$(1.387\pm0.007\pm0.022\pm0.036)\times10^{3}$
0.057-0.064	2.65±0.01±0.01	$(1.265\pm0.006\pm0.020\pm0.033)\times10^{3}$
0.064-0.072	2.45±0.01±0.01	$(1.169\pm0.006\pm0.018\pm0.030)\times10^{3}$
0.072-0.081	2.19±0.01±0.01	$(1.046\pm0.005\pm0.016\pm0.027)\times10^{3}$
0.081-0.091	1.934±0.009±0.009	$(9.23\pm0.04\pm0.14\pm0.24)\times10^{2}$
0.091-0.102	1.722±0.008±0.008	$(8.22\pm0.04\pm0.13\pm0.21)\times10^{2}$
0.102-0.114	1.511±0.007±0.007	$(7.22\pm0.04\pm0.11\pm0.19)\times10^{2}$
0.114-0.128	1.310±0.006±0.007	$(6.25\pm0.03\pm0.10\pm0.16)\times10^{2}$
0.128-0.145	1.116±0.005±0.005	$(5.33\pm0.03\pm0.08\pm0.14)\times10^{2}$
0.145-0.165	0.939±0.004±0.004	$(4.48\pm0.02\pm0.07\pm0.12)\times10^{2}$
0.165-0.189	0.763±0.004±0.004	$(3.65\pm0.02\pm0.06\pm0.09)\times10^{2}$
0.189-0.219	0.610±0.003±0.003	$(2.91\pm0.01\pm0.05\pm0.08)\times10^{2}$
0.219-0.258	0.467±0.002±0.002	$(2.23\pm0.01\pm0.03\pm0.06)\times10^{2}$
0.258-0.312	0.342±0.002±0.002	$(1.635\pm0.008\pm0.025\pm0.043)\times10^{2}$
0.312-0.391	0.233±0.001±0.001	$(1.113\pm0.005\pm0.017\pm0.029)\times10^{2}$
0.391-0.524	0.1353±0.0006±0.0006	64.6±0.3±1.0±1.7
0.524-0.695	$(7.19\pm0.04\pm0.04)\times10^{-2}$	34.3±0.2±0.5±0.9
0.695-0.918	$(3.52\pm0.02\pm0.02)\times10^{-2}$	16.8±0.1±0.3±0.4
0.918-1.153	$(1.86\pm0.02\pm0.02)\times10^{-2}$	8.88±0.08±0.15±0.23
1.153-1.496	$(9.5\pm0.1\pm0.1)\times10^{-3}$	4.54±0.05±0.08±0.12
1.496-1.947	$(4.76\pm0.06\pm0.07)\times10^{-3}$	2.27±0.03±0.05±0.06
1.947-2.522	$(2.33\pm0.04\pm0.04)\times10^{-3}$	1.11±0.02±0.03±0.03
2.522-3.277	$(1.23\pm0.03\pm0.03)\times10^{-3}$	0.58±0.01±0.02±0.02

Table 5.30: The normalised and absolute differential cross section with respect to ϕ^* for the y range of [0.8-1.2], in our fiducial region in data for the muon channel. The uncertainty for the normalised case is separated in the statistical component followed by the systematic uncertainty, whereas, the uncertainty for the absolute case is separated in the statistical component followed by the systematic uncertainty, with the luminosity uncertainty (2.6%) separate.

ϕ^*-bin	**Normalised Cross section**	**Absolute Cross section** (pb)
0.000-0.004	4.38±0.02±0.02	(2.09±0.01±0.03±0.05)×10^3
0.004-0.008	4.34±0.02±0.02	(2.07±0.01±0.03±0.05)×10^3
0.008-0.012	4.27±0.02±0.02	(2.04±0.01±0.03±0.05)×10^3
0.012-0.016	4.11±0.02±0.02	(1.96±0.01±0.03±0.05)×10^3
0.016-0.020	4.03±0.02±0.02	(1.92±0.01±0.03±0.05)×10^3
0.020-0.024	3.76±0.02±0.02	(1.796±0.010±0.029±0.047)×10^3
0.024-0.029	3.67±0.02±0.02	(1.751±0.009±0.028±0.046)×10^3
0.029-0.034	3.41±0.02±0.02	(1.628±0.008±0.026±0.042)×10^3
0.034-0.039	3.16±0.02±0.02	(1.508±0.008±0.025±0.039)×10^3
0.039-0.045	2.99±0.01±0.02	(1.429±0.007±0.023±0.037)×10^3
0.045-0.051	2.72±0.01±0.02	(1.300±0.007±0.021±0.034)×10^3
0.051-0.057	2.52±0.01±0.01	(1.203±0.007±0.019±0.031)×10^3
0.057-0.064	2.32±0.01±0.01	(1.106±0.006±0.018±0.029)×10^3
0.064-0.072	2.09±0.01±0.01	(9.96±0.05±0.16±0.26)×10^2
0.072-0.081	1.869±0.010±0.009	(8.93±0.05±0.14±0.23)×10^2
0.081-0.091	1.644±0.009±0.009	(7.85±0.04±0.12±0.20)×10^2
0.091-0.102	1.435±0.008±0.008	(6.85±0.04±0.11±0.18)×10^2
0.102-0.114	1.281±0.007±0.006	(6.12±0.03±0.10±0.16)×10^2
0.114-0.128	1.108±0.006±0.006	(5.29±0.03±0.09±0.14)×10^2
0.128-0.145	0.957±0.005±0.005	(4.57±0.02±0.07±0.12)×10^2
0.145-0.165	0.797±0.004±0.004	(3.81±0.02±0.06±0.10)×10^2
0.165-0.189	0.642±0.003±0.003	(3.07±0.02±0.05±0.08)×10^2
0.189-0.219	0.511±0.003±0.003	(2.44±0.01±0.04±0.06)×10^2
0.219-0.258	0.401±0.002±0.002	(1.914±0.010±0.031±0.050)×10^2
0.258-0.312	0.286±0.001±0.001	(1.368±0.007±0.022±0.036)×10^2
0.312-0.391	0.195±0.001±0.001	93.0±0.5±1.5±2.4
0.391-0.524	0.1120±0.0006±0.0005	53.5±0.3±0.8±1.4
0.524-0.695	(5.73±0.04±0.04)×10^{-2}	27.4±0.2±0.5±0.7
0.695-0.918	(2.87±0.02±0.02)×10^{-2}	13.7±0.1±0.2±0.4
0.918-1.153	(1.50±0.02±0.02)×10^{-2}	7.16±0.08±0.13±0.19
1.153-1.496	(7.37±0.09±0.09)×10^{-3}	3.52±0.04±0.07±0.09
1.496-1.947	(3.60±0.06±0.06)×10^{-3}	1.72±0.03±0.04±0.04
1.947-2.522	(1.64±0.03±0.04)×10^{-3}	0.78±0.02±0.02±0.02
2.522-3.277	(8.5±0.2±0.2)×10^{-4}	0.41±0.01±0.01±0.01

Table 5.31: The normalised and absolute differential cross section with respect to ϕ^* for the y range of [1.2-1.6], in our fiducial region in data for the muon channel. The uncertainty for the normalised case is separated in the statistical component followed by the systematic uncertainty, whereas, the uncertainty for the absolute case is separated in the statistical component followed by the systematic uncertainty, with the luminosity uncertainty (2.6%) separate.

ϕ^*-bin	**Normalised Cross section**	**Absolute Cross section** (pb)
0.000-0.004	$2.98\pm0.02\pm0.02$	$(1.424\pm0.009\pm0.023\pm0.037)\times10^{3}$
0.004-0.008	$2.93\pm0.02\pm0.02$	$(1.401\pm0.009\pm0.026\pm0.036)\times10^{3}$
0.008-0.012	$2.84\pm0.02\pm0.02$	$(1.357\pm0.009\pm0.023\pm0.035)\times10^{3}$
0.012-0.016	$2.78\pm0.02\pm0.02$	$(1.328\pm0.009\pm0.024\pm0.035)\times10^{3}$
0.016-0.020	$2.64\pm0.02\pm0.02$	$(1.260\pm0.009\pm0.021\pm0.033)\times10^{3}$
0.020-0.024	$2.63\pm0.02\pm0.02$	$(1.257\pm0.009\pm0.023\pm0.033)\times10^{3}$
0.024-0.029	$2.41\pm0.02\pm0.02$	$(1.150\pm0.007\pm0.020\pm0.030)\times10^{3}$
0.029-0.034	$2.25\pm0.01\pm0.02$	$(1.076\pm0.007\pm0.018\pm0.028)\times10^{3}$
0.034-0.039	$2.13\pm0.01\pm0.02$	$(1.015\pm0.007\pm0.018\pm0.026)\times10^{3}$
0.039-0.045	$1.94\pm0.01\pm0.01$	$(9.25\pm0.06\pm0.16\pm0.24)\times10^{2}$
0.045-0.051	$1.81\pm0.01\pm0.01$	$(8.65\pm0.06\pm0.15\pm0.22)\times10^{2}$
0.051-0.057	$1.66\pm0.01\pm0.01$	$(7.95\pm0.06\pm0.14\pm0.21)\times10^{2}$
0.057-0.064	$1.53\pm0.01\pm0.01$	$(7.30\pm0.05\pm0.13\pm0.19)\times10^{2}$
0.064-0.072	$1.387\pm0.009\pm0.011$	$(6.62\pm0.04\pm0.12\pm0.17)\times10^{2}$
0.072-0.081	$1.220\pm0.008\pm0.008$	$(5.82\pm0.04\pm0.10\pm0.15)\times10^{2}$
0.081-0.091	$1.084\pm0.007\pm0.009$	$(5.18\pm0.03\pm0.09\pm0.13)\times10^{2}$
0.091-0.102	$0.972\pm0.006\pm0.008$	$(4.64\pm0.03\pm0.08\pm0.12)\times10^{2}$
0.102-0.114	$0.831\pm0.006\pm0.006$	$(3.97\pm0.03\pm0.07\pm0.10)\times10^{2}$
0.114-0.128	$0.733\pm0.005\pm0.005$	$(3.50\pm0.02\pm0.06\pm0.09)\times10^{2}$
0.128-0.145	$0.617\pm0.004\pm0.004$	$(2.95\pm0.02\pm0.05\pm0.08)\times10^{2}$
0.145-0.165	$0.514\pm0.003\pm0.004$	$(2.45\pm0.02\pm0.04\pm0.06)\times10^{2}$
0.165-0.189	$0.430\pm0.003\pm0.003$	$(2.05\pm0.01\pm0.04\pm0.05)\times10^{2}$
0.189-0.219	$0.342\pm0.002\pm0.002$	$(1.63\pm0.01\pm0.03\pm0.04)\times10^{2}$
0.219-0.258	$0.256\pm0.002\pm0.002$	$(1.222\pm0.008\pm0.021\pm0.032)\times10^{2}$
0.258-0.312	$0.192\pm0.001\pm0.001$	$91.6\pm0.6\pm1.6\pm2.4$
0.312-0.391	$0.1246\pm0.0008\pm0.0009$	$59.5\pm0.4\pm1.0\pm1.5$
0.391-0.524	$(7.32\pm0.05\pm0.05)\times10^{-2}$	$34.9\pm0.2\pm0.6\pm0.9$
0.524-0.695	$(3.67\pm0.03\pm0.03)\times10^{-2}$	$17.5\pm0.1\pm0.3\pm0.5$
0.695-0.918	$(1.83\pm0.02\pm0.02)\times10^{-2}$	$8.73\pm0.09\pm0.16\pm0.23$
0.918-1.153	$(9.2\pm0.1\pm0.1)\times10^{-3}$	$4.37\pm0.06\pm0.09\pm0.11$
1.153-1.496	$(4.53\pm0.07\pm0.08)\times10^{-3}$	$2.16\pm0.04\pm0.05\pm0.06$
1.496-1.947	$(1.85\pm0.04\pm0.04)\times10^{-3}$	$0.88\pm0.02\pm0.02\pm0.02$
1.947-2.522	$(8.1\pm0.2\pm0.3)\times10^{-4}$	$0.39\pm0.01\pm0.01\pm0.01$
2.522-3.277	$(3.6\pm0.1\pm0.1)\times10^{-4}$	$0.170\pm0.007\pm0.007\pm0.004$

Table 5.32: The normalised and absolute differential cross section with respect to ϕ^* for the y range of [1.6-2.0], in our fiducial region in data for the muon channel. The uncertainty for the normalised case is separated in the statistical component followed by the systematic uncertainty, whereas, the uncertainty for the absolute case is separated in the statistical component followed by the systematic uncertainty, with the luminosity uncertainty (2.6%) separate.

ϕ^*-bin	**Normalised Cross section**	**Absolute Cross section** (pb)
0.000-0.004	0.728±0.010±0.012	(3.47±0.05±0.08±0.09)×10^{2}
0.004-0.008	0.680±0.010±0.012	(3.24±0.05±0.08±0.08)×10^{2}
0.008-0.012	0.678±0.010±0.012	(3.24±0.05±0.08±0.08)×10^{2}
0.012-0.016	0.678±0.010±0.012	(3.24±0.05±0.08±0.08)×10^{2}
0.016-0.020	0.641±0.010±0.011	(3.06±0.05±0.08±0.08)×10^{2}
0.020-0.024	0.643±0.010±0.011	(3.07±0.05±0.07±0.08)×10^{2}
0.024-0.029	0.599±0.008±0.011	(2.86±0.04±0.07±0.07)×10^{2}
0.029-0.034	0.568±0.008±0.010	(2.71±0.04±0.06±0.07)×10^{2}
0.034-0.039	0.499±0.007±0.009	(2.38±0.04±0.06±0.06)×10^{2}
0.039-0.045	0.501±0.007±0.008	(2.39±0.03±0.05±0.06)×10^{2}
0.045-0.051	0.450±0.006±0.008	(2.15±0.03±0.05±0.06)×10^{2}
0.051-0.057	0.411±0.006±0.007	(1.96±0.03±0.05±0.05)×10^{2}
0.057-0.064	0.372±0.005±0.006	(1.78±0.03±0.04±0.05)×10^{2}
0.064-0.072	0.332±0.005±0.005	(1.58±0.02±0.04±0.04)×10^{2}
0.072-0.081	0.309±0.004±0.006	(1.48±0.02±0.04±0.04)×10^{2}
0.081-0.091	0.270±0.004±0.005	(1.29±0.02±0.03±0.03)×10^{2}
0.091-0.102	0.234±0.003±0.004	(1.12±0.02±0.02±0.03)×10^{2}
0.102-0.114	0.208±0.003±0.004	100±1±2±3
0.114-0.128	0.187±0.003±0.003	89±1±2±2
0.128-0.145	0.154±0.002±0.003	74±1±2±2
0.145-0.165	0.130±0.002±0.002	61.9±0.9±1.5±1.6
0.165-0.189	0.102±0.001±0.002	48.7±0.7±1.1±1.3
0.189-0.219	(8.2±0.1±0.1)×10^{-2}	39.2±0.6±0.9±1.0
0.219-0.258	(6.28±0.09±0.11)×10^{-2}	30.0±0.4±0.7±0.8
0.258-0.312	(4.57±0.06±0.08)×10^{-2}	21.8±0.3±0.5±0.6
0.312-0.391	(2.98±0.04±0.05)×10^{-2}	14.2±0.2±0.3±0.4
0.391-0.524	(1.76±0.03±0.03)×10^{-2}	8.4±0.1±0.2±0.2
0.524-0.695	(8.9±0.2±0.2)×10^{-3}	4.27±0.08±0.11±0.11
0.695-0.918	(4.23±0.09±0.10)×10^{-3}	2.02±0.04±0.06±0.05
0.918-1.153	(2.08±0.06±0.07)×10^{-3}	0.99±0.03±0.03±0.03
1.153-1.496	(9.7±0.4±0.4)×10^{-4}	0.46±0.02±0.02±0.01
1.496-1.947	(4.0±0.2±0.2)×10^{-4}	0.192±0.010±0.011±0.005
1.947-2.522	(1.7±0.1±0.2)×10^{-4}	(8.2±0.6±0.8±0.2)×10^{-2}
2.522-3.277	(5.6±0.6±0.7)×10^{-5}	(2.7±0.3±0.3±0.1)×10^{-2}

Table 5.33: The normalised and absolute differential cross section with respect to ϕ^* for the y range of [2.0-2.4], in our fiducial region in data for the muon channel. The uncertainty for the normalised case is separated in the statistical component followed by the systematic uncertainty, whereas, the uncertainty for the absolute case is separated in the statistical component followed by the systematic uncertainty, with the luminosity uncertainty (2.6%) separate.

Bibliography

[1] Y. Li and F. Petriello, “Combining QCD and electroweak corrections to dilepton production in FEWZ”, Phys.Rev. D86 (2012) 094034, doi:10.1103/PhysRevD.86.094034, arXiv:1208.5967.

[2] G. A. Ladinsky and C. P. Yuan,“The Nonperturbative regime in QCD resummation for gauge boson production at hadron colliders”, Phys. Rev. D, vol. 50, pp.4239, 1994.

[3] A. Kulesza et. al., “Non-perturbative effects and the resummed Higgs transverse momentum distribution at the LHC”, Journal of High Energy Physics, vol. 2003, no. 12, pp. 056, 2003.

[4] CDF Collaboration, T. Affolder et al.,“The Transverse Momentum and total Cross Section of e^+e^- pairs in the Z-Boson Region from $p\overline{p}$ collisions at $\sqrt{s}$=1.8 TeV”, Phys. Rev. Lett., vol. 84, issue 5, pp. 845, 2000.

[5] DØ Collaboration, B. Abbott et al., “Differential Production Cross Section of Z Bosons as a Function of Transverse Momentum at $\sqrt{s}$=1.8 TeV”, Phys. Rev. Lett. 84, issue 13, pp. 2792, 2000.

[6] DØ Collaboration, V. M. Abazov et al.,“Measurement of the shape of the boson transverse momentum distribution in $p\overline{p}\rightarrow Z/\gamma^*\rightarrow ee+X$ events produced at $\sqrt{s}$=1.96 TeV”, Phys. Rev. Lett., vol. 100, issue 10, pp. 102002, 2008.

[7] DØ Collaboration, V. M. Abazov et al., “Measurement of the normalized $Z/\gamma^* \rightarrow \mu^+\mu^-$ transverse momentum distribution in $p\overline{p}$ collisions at $\sqrt{s}$=1.96 TeV”, Phys. Lett. B, vol. 693, issue 5, pp. 522, 2010.

[8] CDF Collaboration, T. Aaltonen et al., “Transverse momentum cross section of e^+e^- pairs in the Z-boson region from $p\overline{p}$ collisions at $\sqrt{s}$=1.96 TeV”, Phys. Rev. D, vol. 86, issue 5, pp. 052010, 2012.

[9] ATLAS Collaboration, G. Aad et al., “Measurement of the transverse momentum distribution of Z/γ^* bosons in p-p collisions at $\sqrt{s}$=7 TeV with the ATLAS detector”, Phys. Lett. B, vol. 705, issue 5, pp. 415, 2011.

[10] CMS Collaboration, S. Chatrchyan et al., “Measurement of the Rapidity and Transverse Momentum Distributions of Z Bosons in pp collisions at $\sqrt{s}$=7 TeV”, Phys. Rev. D, vol. 85, issue 3, pp. 032002, 2012.

[11] A . Banfi et al., “Predictions for Drell-Yan ${\phi_\eta}^*$ and Q_T observables at the LHC”, Phys. Lett. B, vol. 715, issue 1-3, pp. 152, 2011.

[12] A. Banfi et al., “Optimisation of variables for studying dilepton transverse momentum distributions at hadron colliders”, Eur.Phys.J.C, vol. 71, no. 3, pp. 1600, 2011.

[13] A. Banfi et al., ”Probing the low transverse momentum domain of Z production with novel variables”, Journal of High Energy Physics, no. 1, pp.1-21, 2012.

[14] V. M. Abazov et al.,“Precise study of the Z/γ^* boson transverse momentum distribution in $p\overline{p}$ collisions using a novel technique”, Phys. Lett. B, vol. 106, issue 12, pp. 122001, 2011.

[15] ATLAS Collaboration, G . Aad et al., “Measurement of angular correlations in DrellYan lepton pairs to probe Z/γ^* boson transverse momentum at $\sqrt{s}$ = 7 TeV with the ATLAS detector”, Phys. Lett. B, vol. 720, issue 1-3, pp. 32, 2013.

[16] http://cms.cern.ch/iCMS/analysisadmin/get?analysis=SMP-15-002-pas-v28.pdf.

[17] CMS Collaboration,“Performance of muon identification in pp collisions at $\sqrt{s}$ = 7 TeV”, CMS Physics Analysis Summary CMS-PAS-MUO-10-002, 2010.

[18] CMS Collaboration, “Extracting muon momentum scale corrections for hadron collider experiments”, Eur.Phys.J.C, vol. 72, no. 10, pp. 2194, 2012.

[19] G. DAgostini, “A multidimensional unfolding method based on Bayes theorem”,Nuclear Instruments and Methods in Physics Research A, vol. 362, issue 2-3, pp. 487, 1995.

[20] CMS Collaboration, “CMS Luminosity Based on Pixel Cluster Counting - Summer 2013 Update”, Technical Report CMS PAS LUM-13-001, CERN, Geneva, 2013.

[21] CMS Collaboration, “Measurement of the inelastic proton-proton cross section at $\sqrt{s} = 7$ TeV”, Phys. Lett. B, vol. 722, issue 1-3, pp. 5, 2013.

[22] The CMS Collaboration, https://twiki.cern.ch/twiki/bin/view/CMSPublic/SWGuideEWKUtilitites.

[23] A. Valassi, “Combining correlated measurements of several different physical quantities”, Nucl. Instrum. Meth., vol. 500, issue 0168-9002, pp. 391-405, 2003.

[24] R. Nisius, “On the combination of correlated estimates of a physics observable”, Eur. Phys. J. C, vol. 74, no. 08, pp. 3004, 2014.

[25] https://twiki.cern.ch/twiki/bin/viewauth/CMS/StandardModelCrossSectionsat8TeV.

[26] M. Botje et al., “The PDF4LHC Working Group Interim Recommendations”, arXiv:1101.0538.

Chapter 6

Summary and Conclusions

The Drell-Yan process unravels significant characteristics of the hadronic collisions, i.e. pp collisions at the LHC. At high energies, theoretical calculations for the DY production rate are fairly accurate, since the QCD effects dominate only at the initial state. Hence, these predictions can be used to validate the Standard Model. In addition, the Drell-Yan lepton-pair production is a major source of background for various physics analyses and for searches of new physics beyond the SM.

In this thesis, the single and double differential cross section measurements of the DY process are presented. Measurements are done using the LHC data from pp collisions, collected by the CMS experiment at $\sqrt{s} = 8$ TeV, corresponding to an integrated luminosity of 19.7 fb^{-1}. The study is focused on inclusive Z boson production with a subsequent decay into pair of oppositely charged muons. The single-differential cross section has been measured with respect to phistar (ϕ^*). For the double-differential measurements the dependence on Z boson rapidity (y) has also been taken into account. The selection criteria have been designed targeting at least two reconstructed and isolated muons, using CMS recommended quality cuts. The Z boson candidates are reconstructed selecting the oppositely charged muon pair with invariant mass lying in the range of 60-120 GeV/c^2.

The dominant background processes which can mimic the Drell-Yan signal signature are $t\bar{t}$+jets and diboson production and estimated by Monte Carlo simulation. The measured ϕ^* distributions are corrected for the detector effects by unfolding procedure and the various sources of systematic uncertainities are also considered. The absolute single differential cross section for the dimuon final state is :

$$480.0\pm0.2(\text{stat})\pm7.2(\text{syst})\pm12.5(\text{lumi})\ \text{pb}$$

Similarly, the absolute and normalised double differential results for dimuon final state in each bin of dimuon rapidity, within the fiducial volume are listed in table 6.1.

$\lvert y\rvert$-bin	**Absolute Cross section** (pb)	**Normalised Cross section**
0.0-0.4	106.48± 0.09 ± 1.58 ± 2.77	0.223 ± 0.0002 ± 0.0002
0.4-0.8	106.36± 0.09 ± 1.57 ± 2.77	0.223 ± 0.0002 ± 0.0002
0.8-1.2	103.73± 0.09 ± 1.53 ± 2.70	0.217 ± 0.0002 ± 0.0002
1.2-1.6	88.39 ± 0.08 ± 1.34 ± 2.30	0.185 ± 0.0002 ± 0.0002
1.6-2.0	58.27 ± 0.07 ± 0.93 ± 1.51	0.122 ± 0.0001 ± 0.0003
2.0-2.4	14.22 ± 0.04 ± 0.25 ± 0.37	0.030 ± 0.0001 ± 0.0002

Table 6.1: The absolute and normalised fiducial cross-section (pb) for the 2D absolute measurements. The uncertainty is separated in a statistical component, followed by systematic and luminosity uncertainty for the absolute case, whereas for normalised case, statistical and systematic components have been considered.

The measured DY production cross section using 2012 CMS data has been compared with the following theoretical predictions :

(i) MADGRAPH + PYTHIA 6

(i) POWHEG + PYTHIA 6

(ii) POWHEG + PYTHIA 8

(iii) ResBos

(iv) aMC@NLO + PYTHIA 8

The Powheg + PYHTIA 8 and aMC@NLO generators both are accurate at next-to-leading-order (NLO), whereas, Madgraph + PYTHIA 6 and Powheg + PYTHIA 6 are accurate at leading order (LO). The Madgraph + PYTHIA 6 predic-

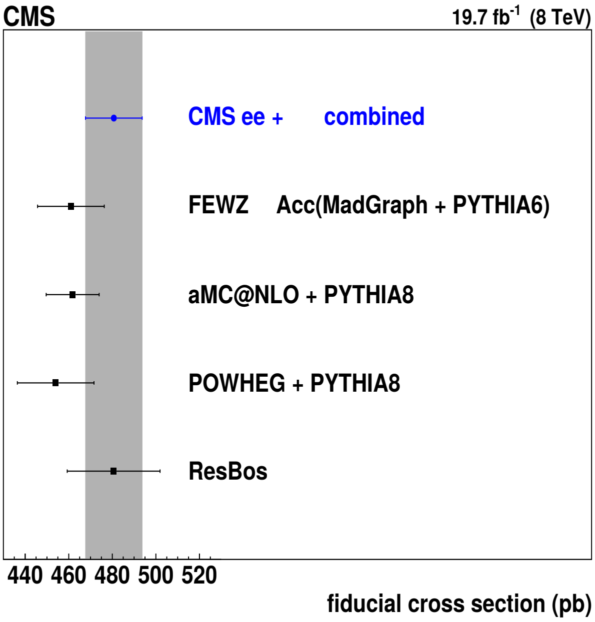

Figure 6.1: Comparison of theoretical values for the fiducial cross section with the combined dilepton cross section (Z→ e^+e^- and Z→ $\mu^+\mu^-$). The grey vertical bar represents the total experimental uncertainty for the measured value. The error bars for the theoretical values include the uncertainties due to statistical precision, the PDFs, and the scale uncertainty.

tions are normalised to the FEWZ cross section for $M_{ll} > 50$ GeV/c^2. The uncertainties of the total theoretical cross section calculated with FEWZ include those due to α_S, neglecting higher-order QCD terms beyond NNLO, the choice of heavy quark masses (bottom and charm), and PDFs, amounting to a total of $\sim$ 3.3%. The theoretical uncertainties, for Powheg, ResBos, and aMC@NLO include statistical, PDF, and scale uncertainties. The PDF uncertainty is calculated as per the official recommendations. The scale uncertainties are evaluated by varying the renormalisation and the factorization scales independently by factors of ± 2 and $\pm 1/2$. The largest variations of the renormalisation and the factorization scales w.r.t nominal values are taken as the uncertainty. The cross section calculated in dielectron and dimuon channel is combined using BLUE method and the comparison of the combined cross section with various theoretical models is shown in figure 6.1.

For the single- and double- differential measurements, the statistical uncertainty is the major source of uncertainty in all bins of ϕ^* considered in this thesis. None of the predictions matches the measurements perfectly for the entire range of ϕ^* under consideration. For the normalised cross section, Madgraph + PYTHIA 6 provides the best description over the entire ϕ^* range. ResBos, aMC@NLO + PYTHIA 8 and Powheg + PYTHIA 8 are similarly successful at describing the data at low ϕ^* but they disagree with the measurements for $\phi^* > 0.1$. The ratios of cross sections as the functions of ϕ^* for bins of $|y|$ relative to the central bin $|y| < 0.4$ were studied to verify the shape dependence of the ϕ^* distribution on the dilepton rapidity. The predictions from aMC@NLO + PYTHIA 8 and Madgraph+ PYTHIA 6 overestimate the cross section at high $|y|$ while, Powheg+ PYTHIA 6 and Powheg + PYTHIA 8 underestimate the cross section. The prediction from ResBos agrees with the $|y|$ dependence in data at the level of 1%.

This analysis validates the overall theoretical description of inclusive production of a vector boson at LHC energies by the perturbative formalism of the Standard Model. Nevertheless, further tuning of the description of the underlying event is necessary for an accurate prediction of the kinematics of the Drell-Yan production of lepton pairs.

The studies related to the phase 1 upgrade during long shutdown 1 of CMS experiment were also undertaken. After three years of very successful operation that led to the discovery of the Higgs boson in 2012, the LHC was scheduled for a series of upgrades to enhance its experimental potential necessary for the nature of the new particle, and to extend the searches for new physics beyond the Standard Model. This necessitated the upgradation of the CMS experiment as well. For instance it was decided to replace the HPD sensors from the Readout Modules (RMs) in the HO detector with magnetic field resistive SiPMs. This was due to the reason that HPDs were degrading or becoming non-functional in the magnetic field. This virtually made HO output unreliable during Run I data taking period.

To ensure the presumed performance of the HO detector during RunII of data taking at $\sqrt{s} = 13$ TeV, several properties of the SiPMs were studied before their installation. An aluminium block was inserted in the Readout boxes to get rid of Peltier effects and later the effect of block installation was studied on the SiPMs. It was concluded that block had no significant effect on the thermal stability of the SiPMs and hence it was removed from the readout boxes. Also, the RMs with HPDs were replaced with new RMs with SiPMs in the ring YB0, YB±1 and YB±2. After successful completion of the HO upgrade with SiPMs, HO commissioning with new hardware was done to assure that all optical connections were done correctly. Hence, various properties of the SiPMs were studied and HO detector was found to be $\sim$ 90% efficient.

Publications/Conferences

Publications and CMS Public Notes with Direct Contribution

1. CMS Collaboration “Measurement of differential cross sections in the ϕ^* variable for inclusive Z boson production in pp collisions at $\sqrt{s} = 8$ TeV”, arXiv:1710.07955 [hep-ex].

2. CMS Collaboration “Development of dedicated trigger for calibrating the CMS Hadron Calorimeter using isolated tracks.”, **CMS DN-2016/030**.

3. CMS Collaboration “Calibration of the CMS Hadron Calorimeter with Isolated Charged Hadrons for 2016 Data.”, **CMS DN-2016/029**.

4. CMS Collaboration “Measurements of ϕ^* differential cross sections for Drell-Yan events in pp collisions at $\sqrt{s} = 8$ TeV.”, **CMS PAS SMP-15-002** (2016).

5. CMS Collaboration “HCAL Calibration with Isolated Charged Hadrons for 2015 Data.”, **CMS DN-2015/031**.

6. CMS Collaboration “Measurement of ϕ^* variable in DrellYan events in CMS experiment at $\sqrt{s} = 8$ TeV.”, **CMS AN-2014/107** (2012).

* **CMS PAS - CMS Physics Analysis Summary**

* **CMS AN - CMS Analysis Note**

* **CMS DN - CMS Detector Note**

Conference papers in refereed journals

1. G.Walia *et. al.*,"Measurement of ϕ^* Variable in Drell-Yan Events in p-p Collisions Using CMS Detector at LHC", *Springer Proc. Phys.* **174** (2016) 591-595.
2. G.Walia *et. al.*,"Single and Double differential Drell-Yan cross section measurements using the CMS detector", *Springer Proc. Phys.*, to be published.

Papers presented in Conferences, Workshops, Symposiums

1. G.Walia *et. al.*,"Measurement of Drell-Yan cross sections at various LHC energies", **CHASCON2017: 11th Chandigarh Science Congress**, March 9-11, 2017, Panjab University, Chandigarh.
2. G.Walia *et. al.*, "Single and Double differential Drell-Yan cross section measurements using the CMS detector", **XXII DAE-BRNS High Energy Physics Symposium 2016**, December 12-16, 2016, University of Delhi, Delhi.
3. G.Walia *et. al.*, "Measurement of ϕ^* differential cross-sections for Drell-Yan events in p-p colisions at 8 TeV with CMS", **International Workshop on Frontiers in Electroweak Interactions of Leptons and Hadrons**, November 2-6, 2016, Aligarh.
4. G.Walia *et. al.*, "Study of Drell-Yan process in p-p collisions using CMS detector at LHC", **CHASCON2015: 9th Chandigarh Science Congress**, February 25-27, 2015, Panjab University, Chandigarh.
5. G.Walia *et. al.*, "Measurement of ϕ^* variable in Drell-Yan events in p-p collisions using CMS detector at LHC", **XXII DAE-BRNS High Energy Physics Symposium 2014**, December 8-12, 2014 ,Indian Institute of Technology, Guwahati.

CMS Publications

1. **“Electroweak production of two jets in association with a Z boson in proton-proton collisions at $\sqrt{s} = 13$ TeV”**, A. M. Sirunyan *et al.* [CMS Collaboration], arXiv:1712.09814 [hep-ex]
2. **“Azimuthal correlations for inclusive 2-jet, 3-jet, and 4-jet events in pp collisions at $\sqrt{s} = 13$ TeV”**, A. M. Sirunyan *et al.* [CMS Collaboration], arXiv:1712.05471 [hep-ex].
3. **“Measurement of associated Z + charm production in proton-proton collisions at $\sqrt{s} = 8$ TeV”**, A. M. Sirunyan *et al.* [CMS Collaboration], arXiv:1711.02143 [hep-ex].
4. **“Measurement of differential cross sections in the ϕ^* variable for inclusive Z boson production in pp collisions at $\sqrt{s} = 8$ TeV”**, A. M. Sirunyan *et al.* [CMS Collaboration], arXiv:1710.07955 [hep-ex].
5. **“Measurements of the pp→ ZZ production cross section and the Z→4l branching fraction, and constraints on anomalous triple gauge couplings at $\sqrt{s}$= 13 TeV”**, A. M. Sirunyan *et al.* [CMS Collaboration], arXiv:1709.08601[hep-ex].
6. **“Observation of electroweak production of same-sign W boson pairs in the two jet and two same-sign lepton final state in proton-proton collisions at $\sqrt{s} = 13$ TeV”**, A. M. Sirunyan *et al.*, [CMS Collaboration], arXiv:1709.05822 [hep-ex].
7. **“Measurement of vector boson scattering and constraints on anomalous quartic couplings from events with four leptons and two jets in proton-proton collisions at sqrt(s) = 13 TeV”**, A. M. Sirunyan *et al.*, [CMS Collaboration],arXiv:1708.02812 [hep-ex].
8. **“Measurement of the differential cross sections for the associated production of a W boson and jets in proton-proton colli-**

sions at sqrt(s) = 13 TeV", A. M. Sirunyan *et al.*, [CMS Collaboration],arXiv:1707.05979 [hep-ex].

9. **"Measurements of jet charge with dijet events in pp collisions at $\sqrt{s}$ = 8 TeV"**, A. M. Sirunyan *et al.*, [CMS Collaboration], arXiv:1706.05868 [hep-ex].

10. **"Measurement of the triple-differential dijet cross section in proton-proton collisions at sqrt(s) = 8 TeV and constraints on parton distribution functions"**, A. M. Sirunyan *et al.*, [CMS Collaboration], arXiv:1705.02628 [hep-ex].

11. **"Measurements of the pp → W$\gamma\gamma$ and pp → Z$\gamma\gamma$ cross sections and limits on anomalous quartic gauge couplings at $\sqrt{s}$ = 8 TeV"**, A. M. Sirunyan *et al.*, [CMS Collaboration], arXiv:1704.00366 [hep-ex].

12. **"Search for anomalous couplings in boosted WW/WZ → $\ell\nu$q$\bar{\text{q}}$ production in proton-proton collisions at $\sqrt{s}$ = 8 TeV"**, A. M. Sirunyan *et al.*, [CMS Collaboration], arXiv:1703.06095 [hep-ex], DOI:10.1016/j.physletb.2017.06.009, Phys. Lett. B **772**, 21 (2017).

13. **"Measurement of the cross section for electroweak production of Zγ in association with two jets and constraints on anomalous quartic gauge couplings in protonproton collisions at $\sqrt{s}$ = 8 TeV"**, V. Khachatryan *et al.*, [CMS Collaboration], arXiv:1702.03025 [hep-ex], DOI:10.1016/j.physletb.2017.04.071, Phys. Lett. B **770**, 380 (2017).

14. **"Measurement of electroweak-induced production of Wγ with two jets in pp collisions at $\sqrt{s}$ = 8 TeV and constraints on anomalous quartic gauge couplings"**, V. Khachatryan *et al.*, [CMS Collaboration], arXiv:1612.09256 [hep-ex], DOI:10.1007/JHEP06(2017)106, JHEP **1706**, 106 (2017).

15. **"Measurements of the associated production of a Z boson and b**

jets in pp collisions at $\sqrt{s}$ = 8 TeV", V. Khachatryan *et al.*, [CMS Collaboration], arXiv:1611.06507 [hep-ex].

16. **"Measurements of differential production cross sections for a Z boson in association with jets in pp collisions at $\sqrt{s}$ = 8 TeV"**,V. Khachatryan *et al.*, [CMS Collaboration], arXiv:1611.03844 [hep-ex], DOI:10.1007/JHEP04(2017)022, JHEP **1704**, 022 (2017).
17. **"Measurements of differential cross sections for associated production of a W boson and jets in proton-proton collisions at $\sqrt{s}$ = 8 TeV"**, V. Khachatryan *et al.*, [CMS Collaboration], arXiv:1610.04222 [hep-ex], DOI:10.1103/PhysRevD.95.052002, Phys. Rev. D **95**, 052002 (2017).
18. **"Measurement of the WZ production cross section in pp collisions at $\sqrt{s}$ = 7 and 8 TeV and search for anomalous triple gauge couplings at $\sqrt{s}$ = 8 TeV"**, V. Khachatryan *et al.*, [CMS Collaboration], arXiv:1609.05721 [hep-ex], DOI:10.1140/epjc/s10052-017-4730-z, Eur. Phys. J. C **77**, no. 4, 236 (2017).
19. **"Measurement and QCD analysis of double-differential inclusive jet cross sections in pp collisions at $\sqrt{s}$ = 8 TeV and cross section ratios to 2.76 and 7 TeV"**, V. Khachatryan *et al.*, [CMS Collaboration], arXiv:1609.05331 [hep-ex], DOI:10.1007/JHEP03(2017)156, JHEP **1703**, 156 (2017).
20. **"Measurement of the production cross section of a W boson in association with two b jets in pp collisions at $\sqrt{s}$ = 8 TeV"**, V. Khachatryan *et al.*, [CMS Collaboration], arXiv:1608.07561 [hep-ex], DOI:10.1140/epjc/s10052-016-4573-z, Eur. Phys. J. C **77**, no. 2, 92 (2017).
21. **"Measurement of the ZZ production cross section and Z → $\ell^+\ell^-\ell'^+\ell'^-$ branching fraction in pp collisions at $\sqrt{s}$=13 TeV"**, V. Khachatryan *et al.*, [CMS Collaboration], arXiv:1607.08834 [hep-ex],

DOI:10.1016/j.physletb.2017.09.030, 10.1016/j.physletb.2016.10.054, Phys. Lett. B **763**, 280 (2016), Erratum: [Phys. Lett. B **772**, 884 (2017)].

22. **"Measurement of electroweak production of a W boson and two forward jets in proton-proton collisions at $\sqrt{s}$ = 8 TeV"**, V. Khachatryan *et al.*, [CMS Collaboration], arXiv:1607.06975 [hep-ex], DOI:10.1007/JHEP11(2016)147, JHEP **1611**, 147 (2016).

23. **"Measurement of the WZ production cross section in pp collisions at $\sqrt(s)$ = 13 TeV"**, V. Khachatryan *et al.*, [CMS Collaboration], arXiv:1607.06943 [hep-ex], DOI:10.1016/j.physletb.2017.01.011, Phys. Lett. B **766**, 268 (2017).

24. **"Measurement of the double-differential inclusive jet cross section in protonproton collisions at $\sqrt{s} = 13\,$TeV"**, V. Khachatryan *et al.*, [CMS Collaboration], arXiv:1605.04436 [hep-ex], DOI:10.1140/epjc/s10052-016-4286-3, Eur. Phys. J. C **76**, no. 8, 451 (2016).

25. **"Measurement of the differential cross section and charge asymmetry for inclusive pp $\to$ $W^{\pm} + X$ production at $\sqrt{s}$ = 8 TeV"**, V. Khachatryan *et al.*, [CMS Collaboration], arXiv:1603.01803 [hep-ex], DOI:10.1140/epjc/s10052-016-4293-4, Eur. Phys. J. C **76**, no. 8, 469 (2016).

26. **"Measurement of the $Z\gamma \to \nu\bar{\nu}\gamma$ production cross section in pp collisions at $\sqrt{s}$ = 8 TeV and limits on anomalous $ZZ\gamma$ and $Z\gamma\gamma$ trilinear gauge boson couplings"**, V. Khachatryan *et al.*, [CMS Collaboration], arXiv:1602.07152 [hep-ex], DOI:10.1016/j.physletb.2016.06.080, Phys. Lett. B **760**, 448 (2016).

27. **"Measurement of dijet azimuthal decorrelation in pp collisions at $\sqrt{s} = 8\,$TeV"**, V. Khachatryan *et al.*, [CMS Collaboration], arXiv:1602.04384 [hep-ex], DOI:10.1140/epjc/s10052-016-4346-8, Eur. Phys. J. C **76**, no. 10, 536 (2016).

28. **“Forwardbackward asymmetry of DrellYan lepton pairs in pp collisions at $\sqrt{s}$ = 8 TeV”**, V. Khachatryan *et al.*, [CMS Collaboration], arXiv:1601.04768 [hep-ex], DOI:10.1140/epjc/s10052-016-4156-z, Eur. Phys. J. C **76**, no. 6, 325 (2016).

29. **“Measurement of the inclusive jet cross section in pp collisions at $\sqrt{s}$ = 2.76 TeV”**, V. Khachatryan *et al.*, [CMS Collaboration], arXiv:1512.06212 [hep-ex], DOI:10.1140/epjc/s10052-016-4083-z, Eur. Phys. J. C **76**, no. 5, 265 (2016).

30. **“Measurement of the W^+W^- cross section in pp collisions at $\sqrt{s} = 8$ TeV and limits on anomalous gauge couplings”**, V. Khachatryan *et al.*, [CMS Collaboration], arXiv:1507.03268 [hep-ex], DOI:10.1140/epjc/s10052-016-4219-1, Eur. Phys. J. C **76**, no. 7, 401 (2016).

31. **“Comparison of the Z/γ + jets to γ + jets cross sections in pp collisions at $\sqrt{s}$ = 8 TeV”**, V. Khachatryan *et al.*, [CMS Collaboration], arXiv:1505.06520 [hep-ex], DOI:10.1007/JHEP04(2016)010, 10.1007/JHEP10(2015)128, JHEP **1510**, 128 (2015), Erratum: [JHEP **1604**, 010 (2016)].

Complete list of the CMS Publications can be found here : *http://inspirehep.net/search?ln=en&p=genius+walia&of=hb&action_search =Search&sf=earliestdate&so=d*